

# Atomic layer deposition of Ni and $\text{Ni}_{80}\text{Fe}_{20}$ for tubular spin-wave nanocavities

Présentée le 25 juin 2021

Faculté des sciences et techniques de l'ingénieur  
Laboratoire des matériaux magnétiques nanostructurés et magnoniques  
Programme doctoral en science et génie des matériaux

pour l'obtention du grade de Docteur ès Sciences

par

**Maria Carmen GIORDANO**

Acceptée sur proposition du jury

Dr A. Hessler-Wyser, présidente du jury  
Prof. D. Grundler, Prof. A. Fontcuberta i Morral, directeurs de thèse  
Prof. M. Poggio, rapporteur  
Prof. K. Nielsch, rapporteur  
Prof. V. Michaud, rapporteuse





People have to hold on to the belief that  
the incomprehensible is understandable,  
otherwise they would not explore any further.  
— Johann Wolfgang von Goethe

To Francesca and Angelo, with love.



# Acknowledgements

I would like to thank everyone who made my PhD an enriching personal and professional experience. In particular, I deeply thank:

**Prof. Dirk Grundler**, for having given me the opportunity to join his research group and for entrusting me with an extremely interesting and challenging research project. I would like to thank you for your guidance, invaluable advices, numerous discussions and the time you have invested in shaping my scientific approach.

**Prof. Anna Fontcuberta i Morral**, for having co-supervised my project in the best possible way. I would like to thank you for giving me the right tips at the right time during all these years, directing me towards the best results and for the inspirational example you set.

**Prof. Véronique Michaud**, **Prof. Kornelius Nielsch** and **Prof. Martino Poggio** for having accepted to comprise my PhD examination committee and **Dr Aïcha Hessler-Wyser** for presiding it.

**Prof. Maartjie Bastings** and **Dr Thomas Lagrange**, who as members of the annual review board, have guided my progresses over the years.

I thank the **Deutsche Forschungsgemeinschaft** for funding via project GR1640/5-2.

The **CMI team** for maintaining a first-class cleanroom facility. A particular thank you goes to **Didier Bouvet** which has been an excellent technical support on the ALD and has worked to ensure its correct functioning from the first day of commissioning until the last day of my experiments. **Patrick Alain Madliger** and **Miguel Marmelo** for having supported with maintenance interventions my research work on ALD and for ensuring a safe working environment in the cleanroom. **Zdenek Benes** who has provided me with excellent training on e-beam lithography and SEM and supports us CMI users with patient troubleshooting whenever is needed. **Corradini Giancarlo** and **Adrien Toros** for the meticulous work of electrical bonding on my samples, which made many of my experiments possible.

**My LMGN colleagues**, for all the support received on my project, for your friendship and the good time spent outside the lab. In particular, **Korbinian Baumgaertl** for accompanying me in the development of the technical tricks necessary to perform measurements with micro-focused BLS on nanotubes, for the collaboration and many valuable discussions on BLS results. **Sho Watanabe**, for introducing me to the data analysis in Python and for the many

## Acknowledgements

---

clarifications on the use of VNA, MFM and further techniques. I am grateful for having shared the office with you. **Ping Che** for always being available when I needed help inside and outside the lab and for having often stimulated me with her goal-driven attitude. **Anna Kukolova**, for the numerous exchanges about material growth and material characterization and her inspirational ambition. **Mohammad Hamdi**, for having given with Mumax micromagnetic simulations on nanotubes a great added value to my experimental work, for all the helpful discussions and for the IT support he gave to the lab. **Andrea Mucchietto**, for his precious technical-scientific support to my latest experiments at BLS and for the incurable willpower which is of great inspiration. **Cagri Ozdilek** with whom it was a pleasure to work in the last months of my PhD. **Yuko Kagata** for the warm and friendly organizational support. **The master's students** I had the pleasure to supervise in these years (Bin Lu, Thakur Tushar Singh, Julien Gay, Martin Vuichard, Richa Agrawal) for their contribution to my work.

**Colleagues of the LMSC group**, for the good times we spent together outside the lab and in particular **Simon Escobar**, for contributing to my project with his STEM-EDX and HRTEM analysis; **Heidi Potts** for having transferred to me her knowledge on nanotubes devices fabrication at the real beginning of my PhD and **Gozde Tütüncüoglu** for providing me with batches of GaAs NWs.

My friend and former colleague at PSI **Florentina Maxim** for having encouraged me to apply to the EDMX program at EPFL.

Last but not least, I want to thank **my parents**, for having supported my every professional choice, confident in my person and in my potential. Most of all, thanks for teaching me the importance of culture and education. My brother **Salvatore** for being always there for me. **Angelo**, my husband, for all the encouragement and support in these years of challenges and learning.

*Lausanne, May 30, 2021*

M. C. Giordano.

# Abstract

Magnetic thin films and magnetic micro- and nanostructures have become essential components of modern technological applications. They are employed in data storage media, magnetic MEMS, microwave absorbers and tunable frequency filters, to name a few. Modern branches of magnetisms focus on spin-charge coupling (spintronics) and the collective excitation of spin waves in magnetically ordered materials (magnonics). In particular, spin waves represent a promising charge-free medium to encode and transmit information in the GHz frequency regime, relevant for microwaves technologies.

The ever-increasing demand for compact and portable electronic and telecommunication devices leads to the need for further miniaturization and high integration density of their functional components. These aspects have prompted nanomagnetism to venture the third dimension. This development is also motivated by novel physical phenomena and functionalities predicted to arise from three-dimensional (3D) complex magnetic configurations. Ferromagnetic nanotubes (NTs) represent the ideal 3D system for the study of shape dependent static and dynamic magnetic properties. Their magnetic configurations, as well as the spin wave confinement and propagation inside them, can be engineered by changing the three geometrical parameters: length, inner and outer radius. In order to advance the research in 3D spintronics and 3D magnonics, it will be essential on the one hand to have control over the fabrication of 3D nanoarchitectures, and on the other hand to access the new properties of individual nanostructures emerging from new complex 3D spin-textures. These two challenges are addressed in this thesis.

First, in order to fabricate 3D magnetic device architectures, we explored atomic layer deposition (ALD). The thickness and quality of the thin films deposited with ALD are irrespective of the geometry of the surface on which they are deposited. This characteristic makes it ideal to fabricate 3D nanomagnets by magnetically coating 3D nanotemplates, e.g. nanostructured surfaces or semiconductor nanowires (NWs) in the case of nanotubes. In this thesis we propose ALD processes for the conformal coating by means of two ferromagnetic materials conventionally used in planar spintronics and magnonics systems: Ni and permalloy (Py,  $\text{Ni}_{80}\text{Fe}_{20}$ ), the second material expected to have a lower spin wave damping. First, by identifying correlations between ALD process parameters and thin film properties we optimized the materials in terms of conformality, electrical resistivity, anisotropic magnetoresistance (AMR) effect, spin wave damping and, in the case of permalloy, also stoichiometry. The optimized materials were then transferred onto GaAs nanowires templates, obtaining ferromagnetic NTs with hexagonal cross sections. We achieved high quality Ni NTs with the lowest resistivity ever

## Abstract

---

reported in similar ALD-grown Ni systems and a AMR effect of about 30 % larger compared to the best low-field AMR effect of Ni NTs reported previously. We observed the lowest spin waves damping for permalloy NTs, exhibiting a value comparable with permalloy thin films achieved with conventional planar deposition techniques. To the best of our knowledge, the present study is only the second reported in literature to prepare metallic NiFe alloys by ALD and the first where spin wave damping has been quantified.

Second, we investigated magnetic states and spin waves confinement in nanotubes experimentally and via micromagnetic simulations. We combined magnetoresistance measurements with Brillouin light scattering spectroscopy (BLS) and micromagnetic simulations to study Ni and Py NTs. Consistently with the theoretical predictions, our results indicate a mixed state as ground magnetization state for both types of nanotubes suggesting a predominance of the shape anisotropy over other material contributions. These findings substantiate the good quality of the polycrystalline shells. BLS measurements, performed while irradiating NTs with microwaves, show that these nanotubes form spin-wave nanocavities which impose discrete wave vectors and confine GHz microwave signals on the nanoscale. In the case of Ni NTs magnetized along the axis we found azimuthally confined spin waves. For permalloy NTs standing spin wave properties along both the azimuthal and axial direction were measured. In the case of Py NTs a larger set of resonances was resolved due to both different boundary conditions imposed by a shorter length of the nanotubes and, above all, a lower spin wave damping compared to Ni NTs. Our study show how to manipulate the spin wave confinement in ferromagnetic NTs by changing their geometrical parameters and magnetic states.

**Key words:** Nickel, Permalloy, Atomic Layer Deposition, 3D Nanomagnets, Ferromagnetic Nanotubes, Spin Waves , Microwave Nanocavities.

# Résumé

Les couches minces magnétiques et les micro et nanostructures magnétiques sont devenus des composants essentiels des applications technologiques modernes. Ils sont utilisés dans les supports de stockage de données, les MEMS magnétiques, les absorbeurs de micro-ondes et les filtres de fréquence accordables, pour n'en nommer que quelques-uns. Les branches modernes des magnétismes se concentrent sur le couplage spin-charge (spintronique) et l'excitation collective des ondes de spin dans des matériaux magnétiquement ordonnés (magnonique). En particulier, les ondes de spin représentent un milieu sans charge prometteur pour coder et transmettre des informations dans le régime de fréquences GHz, pertinent pour les technologies à micro-ondes.

La demande toujours croissante de dispositifs électroniques et de télécommunication compacts et portables conduit à la nécessité d'une miniaturisation supplémentaire et d'une densité d'intégration élevée de leurs composants fonctionnels. Ces aspects ont poussé le nanomagnétisme à s'aventurer dans la troisième dimension. Ce développement est également motivé par de nouveaux phénomènes physiques et des fonctionnalités qui devraient résulter de configurations magnétiques complexes tridimensionnelles (3D). Les nanotubes ferromagnétiques (NT) représentent le système 3D idéal pour l'étude des propriétés magnétiques statiques et dynamiques dépendant de la forme. Leurs configurations magnétiques, ainsi que le confinement et la propagation des ondes de spin à l'intérieur de celles-ci, peuvent être conçues en modifiant les trois paramètres géométriques : longueur, rayon intérieur et extérieur. Afin de faire avancer la recherche en spintronique 3D et magnonique 3D, il sera essentiel d'une part d'avoir le contrôle sur la fabrication des nanoarchitectures 3D, et d'autre part d'accéder aux nouvelles propriétés des nanostructures individuelles émergeant de nouvelles, et plus complexes, textures de spin 3D. Ces deux défis sont abordés dans cette thèse.

Tout d'abord, afin de fabriquer des architectures de dispositifs magnétiques 3D, nous avons exploré la technique de dépôt chimique en phase vapeur par flux alternés, plus communément appelée "Atomic Layer Deposition" (ALD). L'épaisseur et la qualité des couches minces déposées à l'ALD sont indépendantes de la géométrie de la surface sur laquelle elles sont déposées. Cette caractéristique le rend idéal pour fabriquer des nanomagnets 3D par revêtement magnétique de nanotemplates 3D, par ex. surfaces nanostructurées ou nanofils semi-conducteurs (NWs) dans le cas des nanotubes. Dans cette thèse nous proposons des procédés ALD pour le revêtement conforme au moyen de deux matériaux ferromagnétiques classiquement utilisés dans les systèmes planaires de spintronique et magnonique : Ni et permalloy (Py,  $\text{Ni}_{80}\text{Fe}_{20}$ ), le second matériau censé avoir un amortissement des ondes de spin plus faible. Premièrement,

en identifiant les corrélations entre les paramètres du processus ALD et les propriétés des couches minces, nous avons optimisé les matériaux en termes de conformité, de résistivité électrique, d'effet de magnétorésistance anisotrope (AMR), d'amortissement des ondes de spin et, dans le cas du permalloy, également de stoechiométrie. Les matériaux optimisés ont ensuite été transférés sur des modèles de nanofils de GaAs, obtenant des NT ferromagnétiques avec des sections transversales hexagonales. Nous avons obtenu des Ni NT de haute qualité avec la résistivité la plus faible jamais rapportée dans des systèmes Ni de croissance ALD similaires et un effet AMR d'environ 30 % plus grand que le meilleur effet AMR à faible champ rapporté précédemment pour NTs en Ni. Nous avons observé l'amortissement des ondes de spin le plus bas pour les NT en permalloy, présentant une valeur comparable aux couches minces de permalloy obtenues avec les techniques de dépôt planaire conventionnelles. À notre connaissance, la présente étude n'est que la deuxième rapportée dans la littérature pour préparer des alliages NiFe métalliques par ALD et la première où l'amortissement des ondes de spin a été quantifié.

Deuxièmement, nous avons étudié les états magnétiques et le confinement des ondes de spin dans des nanotubes de manière expérimentale et via des simulations micromagnétiques. Nous avons combiné les mesures de magnétorésistance avec la spectroscopie de diffusion Brillouin (BLS) et des simulations micromagnétiques pour étudier les NTs en Ni et en Py. En cohérence avec les prédictions théoriques, nos résultats indiquent un état mixte comme état de magnétisation au champ zéro pour les deux types de nanotubes suggérant une prédominance de l'anisotropie de forme sur les autres contributions du matériau. Ces résultats confirment la bonne qualité de les enrobages polycristallines. Les mesures BLS, effectuées lors de l'irradiation des NT avec des micro-ondes, montrent que ces nanotubes forment des nanocavités à ondes de spin qui imposent des vecteurs d'ondes discrètes et confinent les signaux micro-ondes GHz à l'échelle nanométrique. Dans le cas des Ni NT magnétisés le long de l'axe, nous avons trouvé des ondes de spin confinées azimuthalement. Pour les NT en permalloy, les propriétés des ondes de spin stationnaires le long de la direction azimuthale et axiale ont été mesurées. Dans le cas des Py NT, un plus grand ensemble de résonances a été résolu en raison à la fois de conditions aux limites différentes imposées par une longueur plus courte des nanotubes et, surtout, d'un amortissement des ondes de spin plus faible par rapport aux Ni NT. Notre étude montre comment manipuler le confinement des ondes de spin dans les NT ferromagnétiques en modifiant leurs paramètres géométriques et leurs états magnétiques.

**Mots clés :** Nickel, Permalloy, dépôt de couche atomique, nanomagnets 3D, nanotubes ferromagnétiques, ondes de spin, nanocavités micro-ondes.



# Zusammenfassung

Magnetische Dünnschichten sowie magnetische Mikro- und Nanostrukturen sind zu wesentlichen Bestandteilen moderner technologischer Anwendungen geworden. Sie werden in Datenspeichermedien, magnetischen Mikrosystemen, Mikrowellenabsorbern und einstellbaren Frequenzfiltern eingesetzt, um nur einige Anwendungen zu nennen. Neue Forschungszweige im Magnetismus konzentrieren sich auf die Spin-Ladungs-Kopplung (Spintronik) und die kollektive Anregung von Spinwellen in magnetisch geordneten Materialien (Magnonik). Insbesondere Spinwellen stellen einen vielversprechenden ladungsfreien Informationsträger da, um Informationen in dem für die Mikrowellentechnologie relevanten GHz-Frequenzbereich zu kodieren und zu übertragen.

Die ständig steigende Nachfrage nach kompakten und tragbaren elektronischen Geräten und Telekommunikationsgeräten führt zu der Notwendigkeit einer weiteren Miniaturisierung und einer hohen Integrationsdichte der Funktionskomponenten. Diese Aspekte haben die Forschung an dreidimensionalen (3D) magnetischen Nanostrukturen angeregt. Diese Entwicklung wird auch durch neuartige physikalische Phänomene und Funktionalitäten motiviert, die für dreidimensionale komplexe magnetische Konfigurationen vorhergesagt wurden. Ferromagnetische Nanoröhren (NTs) sind das ideale 3D-System zur Untersuchung formabhängiger statischer und dynamischer magnetischer Eigenschaften. Ihre magnetischen Konfigurationen sowie die Begrenzung und Ausbreitung der Spinwellen in ihnen können durch Ändern der drei geometrischen Parameter angepasst werden: Länge, innerer und äußerer Radius. Um die Forschung in den Bereichen 3D-Spintronik und 3D-Magnonik voranzutreiben, ist es einerseits wichtig, die Herstellung von 3D-Nanoarchitekturen zu beherrschen und andererseits auf die neuen Eigenschaften einzelner Nanostrukturen zuzugreifen, die aus neuen komplexen 3D-Spin-Texturen hervorgehen. Diese beiden Herausforderungen werden in dieser Arbeit angegangen.

Um 3D-Architekturen für magnetische Bauelemente herzustellen, untersuchten wir zunächst die Atomlagenabscheidung (ALD). Die Dicke und Qualität der mit ALD abgeschiedenen Dünnschichten sind unabhängig von der Geometrie der Oberfläche, auf der sie abgeschieden werden. Diese Eigenschaft macht ALD ideal dafür geeignet, 3D-Nanomagnete durch magnetische Beschichtung von 3D-Nanotemplates herzustellen, z.B. nanostrukturierte Oberflächen oder Halbleiter-Nanodrähte bei Nanoröhren. In dieser Arbeit erarbeiten wir ALD-Verfahren für die konforme Beschichtung mit zwei ferromagnetischen Materialien, die üblicherweise in planaren Spintronik- und Magnoniksystemen verwendet werden: Ni und Permalloy (Py,  $\text{Ni}_{80}\text{Fe}_{20}$ ), wobei für das zweite Material eine geringere Spinwellendämpfung erwartet wird. Erstens

haben wir durch die Identifizierung von Korrelationen zwischen ALD-Prozessparametern und Dünnschichteigenschaften die Materialien hinsichtlich Konformität, elektrischem Widerstand, anisotropem Magnetowiderstandseffekt (AMR), Spinwellendämpfung und im Fall von Permalloy auch Stöchiometrie optimiert. Die optimierten Materialien wurden dann auf GaAs-Nanodrähte übertragen, wodurch wir ferromagnetische NTs mit hexagonalen Querschnitten erhielten. Wir erzielten hochwertige Ni-NTs mit dem niedrigsten spezifischen Widerstand, der jemals in ähnlichen ALD-basierten Ni-Systemen berichtet wurde, und mit einem etwa 30 % größerem AMR-Effekt als in zuvor bei niedrigen Feldern gemessenen Ni-NTs. Wir beobachteten die niedrigste Spinwellendämpfung für Permalloy-NTs mit einem Wert, der mit Permalloy-Dünnschichten vergleichbar ist, die mit herkömmlichen planaren Abscheidungstechniken erzielt wurden. Nach unserem besten Wissen ist die vorliegende Studie nur die zweite in der Literatur beschriebene Studie zur Herstellung metallischer NiFe-Legierungen durch ALD und die erste, bei der die Spinwellendämpfung quantifiziert wurde.

Zweitens untersuchten wir magnetische Zustände und stehende Spinwellen in Nanoröhren experimentell und über mikromagnetische Simulationen. Wir kombinierten Magnetowiderstandsmessungen mit Brillouin-Lichtstreuungsspektroskopie (BLS) und mikromagnetischen Simulationen, um Ni- und Py-NTs zu untersuchen. In Übereinstimmung mit den theoretischen Vorhersagen weisen unsere Ergebnisse auf einen gemischten Zustand als Grundmagnetisierungszustand für beide Arten von Nanoröhren hin, was darauf hindeutet, dass die Formanisotropie gegenüber anderen Materialbeiträgen überwiegt. Diese Befunde untermauern die gute Qualität der polykristallinen Beschichtungen. BLS-Messungen, die während der Bestrahlung von NTs mit Mikrowellen durchgeführt wurden, zeigen, dass diese Nanoröhren Spinwellen-Nanokavitäten bilden, die den Spinwellen diskrete Wellenvektoren auferlegen und GHz-Mikrowellensignale in den Nanobereich einschränken. Im Fall von entlang der Achse magnetisierten Ni-NTs fanden wir azimuthal diskretisierte Spinwellen. Für Permalloy-NTs wurden stehende Spinwelleneigenschaften sowohl entlang der azimuthalen als auch der axialen Richtung gemessen. Im Fall von Py-NTs wurde eine größere Anzahl an Resonanzen aufgrund von sowohl unterschiedlichen Randbedingungen, die durch eine kürzere Länge der Nanoröhren bedingt wurden, als auch vor allem einer geringeren Spinwellendämpfung im Vergleich zu Ni-NTs, aufgelöst. Unsere Studie zeigt, wie man stehende Spinwellen in ferromagnetischen NTs durch Ändern ihrer geometrischen Parameter und magnetischen Zustände manipuliert.

**Schlüsselwörter:** Nickel, Permalloy, Atomlagenabscheidung, 3D-Nanomagnete, ferromagnetische Nanoröhren, Spinwellen, Mikrowellen-Nanokavitäten.

# Contents

<b>Acknowledgements</b>	<b>1</b>
<b>Abstract (English/Français/Deutsch)</b>	<b>3</b>
<b>List of publications</b>	<b>1</b>
<b>I Introductory Chapters</b>	<b>3</b>
<b>1 Introduction</b>	<b>5</b>
1.1 Motivation and context . . . . .	5
1.2 Scope and overview of the thesis . . . . .	7
<b>2 Theoretical background</b>	<b>9</b>
2.1 Introduction to magnetism . . . . .	9
2.2 Micromagnetics: basic principles . . . . .	11
2.3 Magnetization dynamics . . . . .	15
2.3.1 Landau-Lifshitz-Gilbert Equation . . . . .	15
2.3.2 Ferromagnetic resonance . . . . .	16
2.3.3 Spin wave dispersion . . . . .	18
<b>3 Literature review</b>	<b>23</b>
3.1 Static and dynamic magnetic phenomena in ferromagnetic nanotubes . . . . .	23
3.2 Reported experiments on ferromagnetic nanotubes . . . . .	26
3.3 Atomic layer deposition of Ni and NiFe three-dimensional coatings . . . . .	29
<b>4 Methods</b>	<b>33</b>
4.1 Atomic layer deposition . . . . .	33
4.1.1 Working principle . . . . .	34
4.1.2 Beneq TFS200 ALD system . . . . .	38
4.1.3 Fabrication of ferromagnetic nanotubes . . . . .	39
4.2 Measurement techniques . . . . .	40
4.2.1 Electrical and magnetotransport characterization . . . . .	40
4.2.2 Broadband Spectroscopy . . . . .	43
4.2.3 Brillouin Light Scattering . . . . .	45

## Contents

---

4.3	Microfabrication of electrical devices . . . . .	48
4.3.1	Metallic leads on oxidized Si substrates . . . . .	49
4.3.2	Integrated coplanar wave guides on oxidized Si and transparent glass substrates . . . . .	50
<b>II</b>	<b>Results and Discussion</b>	<b>53</b>
<b>5</b>	<b>Atomic layer deposition of nickel nanotubes and thin films</b>	<b>55</b>
5.1	ALD process 1 exploiting nickelocene, ammonia and hydrogen plasma as reactants	55
5.1.1	Growth rate and resistivity of Ni as a function of the ALD process parame- ters . . . . .	56
5.1.2	Thin films annealed under reducing atmospheres . . . . .	58
5.1.3	Final morphology and properties of ALD nickel thin films and nanotubes	59
5.2	ALD process 2, exploiting nickelocene, water and hydrogen plasma as reactants	60
5.2.1	Pub. I: Plasma-Enhanced Atomic Layer Deposition of Nickel Nanotubes with Low Resistivity and Coherent Magnetization Dynamics for 3D Spin- tronic . . . . .	60
<b>6</b>	<b>Atomic layer deposition of nickel-iron nanotubes and thin films</b>	<b>77</b>
6.1	ALD process optimization for permalloy $\text{Ni}_{80}\text{Fe}_{20}$ . . . . .	77
6.1.1	Pub. II: $\text{Ni}_{80}\text{Fe}_{20}$ nanotubes with optimized spintronic functionalities prepared by Atomic Layer Deposition . . . . .	77
6.2	Static and dynamic magnetization in $\text{Ni}_{80}\text{Fe}_{20}$ nanotubes . . . . .	94
6.2.1	Pub.III: Dipolar-exchange spin waves confinement in ALD-prepared permal- loy $\text{Ni}_{80}\text{Fe}_{20}$ nanotubes . . . . .	94
6.3	Comparison between $\text{Ni}_{80}\text{Fe}_{20}$ nanotubes and Ni nanotubes . . . . .	104
<b>7</b>	<b>Summary and Outlooks</b>	<b>109</b>
<b>A</b>	<b>Appendix</b>	<b>113</b>
A.1	Supplementary information of Pub.I . . . . .	113
A.2	Supplementary information of Pub.II . . . . .	118
A.3	Supplementary information of Pub.III . . . . .	125
	<b>Bibliography</b>	<b>127</b>
	<b>Curriculum Vitae</b>	<b>147</b>

# List of publications

**Pub.I Plasma-Enhanced Atomic Layer Deposition of Nickel Nanotubes with Low Resistivity and Coherent Magnetization Dynamics for 3D Spintronic.**

M. C. Giordano, K. Baumgaertl, S. Escobar Steinvall, J. Gay, M. Vuichard, A. Fontcuberta i Morral and D. Grundler

ACS Appl. Mater. Interfaces 2020, 12, 36, 40443–40452

Publication Date: August 12, 2020

doi: 10.1021/acsami.0c06879

**Pub.II Ni<sub>80</sub>Fe<sub>20</sub> nanotubes with optimized spintronic functionalities prepared by Atomic Layer Deposition.**

M. C. Giordano, S. Escobar Steinvall, S. Watanabe, A. Fontcuberta i Morral and D. Grundler

doi: arXiv:2105.01969

Publication Date: May 5, 2021

**Pub.III Dipolar-exchange spin waves confinement in ALD-prepared permalloy Ni<sub>80</sub>Fe<sub>20</sub> nanotubes**

M. C. Giordano, M. Hamdi, A. Mucchietto and D. Grundler

Status: drafted manuscript.



# **Introductory Chapters**

## **Part I**





# 1 Introduction

## 1.1 Motivation and context

Magnetic materials play a prominent role in modern technology. They are key components of motors, generators, transformers and microwave technologies [1]. In these common applications, they are employed in the shape of laminates, bulk permanent magnets or spheres. Since the discovery of phenomena like the tunnel magnetoresistance (TMR) in 1975 [2] and the giant magnetoresistance (GMR) in 1988 [3, 4], for whose discovery Peter Grünberg and Albert Fert won the Nobel Prize in 2007 [5], spintronics has become a subject of growing interest. Here, the transfer of magnetic moment or spin by an electric current can be used in magnetic elements smaller than the spin diffusion length. Novel device concepts based on these functionalities stimulated magnetism research towards nanotechnology. Nowadays, magnetic thin films and magnetic nanostructures play an extremely important role in technologies such as data storage media [6, 7], GMR sensors [8], spin valves [9], magnetic MEMS [10, 11] and biomedical applications [12]. In the modern era, digital transformation takes place in our societies. Utility networks, industry and cities strongly depend on the wireless exchange of information. As a consequence, magnetism research has increasingly focused on optimizing the microwave properties of ferro- and ferrimagnetic materials to advance and miniaturize microwave electronics. In this context a modern branch of magnetism, Magnonics [13, 14], emerged focusing on the study of spin waves in insulating and metallic magnetic materials as a medium for information transmission and processing without moving electric charges. Spin waves, whose corresponding quasiparticles are called "magnons", are collective excitations of magnetically ordered materials excited in the technologically relevant GHz regime [15, 13]. At these frequencies, electromagnetic waves in air have wavelengths on the order of centimeters or larger, while spin waves in magnetic media exhibit significantly shorter wavelengths down to hundreds and tens of nm [16]. The enormous wavelength reduction, the low energy consumption of spin waves and the potential compatibility with next-generation circuits beyond CMOS electronics make them a promising tool for non-charge based signal processing, communication and computation [13, 17, 14, 15]. Magnonic systems investigated up to now are mainly planar systems based either on insulating magnets such as yttrium

iron garnet (YIG) or on polycrystalline metal alloys such as NiFe and CoFeB. While YIG offers the lowest spin wave damping  $\alpha$  and represents often a model system to demonstrate new magnonic functionalities, the choice of the metallic alloys NiFe and CoFeB meets better the needs for the industrial scalability of miniaturized and integrated systems [18].

The demand of high-density technologies [19] and the need of new applications drive the expansion of spintronics and magnonics towards not only miniaturization but also three-dimensional (3D) device architectures [20, 21, 18]. Here, novel physical phenomena arising from complex spin textures become possible. Special attention has been given to the propagation of spin waves in layered nanostructures, spin textures, curved surfaces, 3D nano-objects and cavity magnonics [18]. However, the measurement and interpretation of spin dynamics in complex 3D structures remain exceptionally challenging and the implementation of high-quality 3D nanomagnetic structures on large scales is lacking. A promising path is to magnetically coat 3D nanotemplates, e.g. nanostructured surfaces, porous membranes [22], polymeric scaffolds [23], self-assembled [24] or bottom-up grown [25, 26] nanostructures. Physical vapor deposition (PVD) techniques, classically favored for the fabrication of ferromagnetic thin films and planar nanostructures, are limited by shadowing effects for the coating of three-dimensional (3D) nanostructures with high aspect ratios. Therefore, a technique for conformal coatings of high-quality ferromagnetic metals is of uttermost importance to advance 3D nanomagnetism and 3D magnonics [18].

Atomic layer deposition (ALD) [27, 28] offers a great potential [29]. Here the material is deposited through self-limiting reactions between vapor phase metal-organic precursors (and co-reactants) and the exposed substrate surface, enabling conformal coatings and thickness control on the atomic scale. The deposition of high- $\kappa$  gate oxides, such as  $\text{Al}_2\text{O}_3$  has been one of the most widely examined areas of ALD and already advanced microelectronics applications like metal-oxide semiconductor field effect transistors (MOSFET) and dynamic random access memories (DRAM) [30]. The processes for depositing metal layers using this technique, including ferromagnetic metals, still present technical challenges and are the subject of extensive research [31, 32, 33, 34, 35].

Nanotubes (NTs) prepared from ferromagnets represent prototypical 3D nanomagnetic structures [21]. The properties of these nanostructures are extremely versatile for applications as they change as a function of their geometrical properties [36, 37]. NTs raised significant attention for hosting stable flux-closure magnetic states [38], which results in a fast and controllable domain wall (DW) motion when compared to magnetic stripes [39, 40]. The three geometric parameters, namely the length, the inner radius and external radius, offer the possibility to tailor and manipulate NTs ground states, DW formation via reversal mechanisms and spin-wave confinement in 3D space. Curvature-induced magnetochiral effects originating from the dipole-dipole interaction are expected to arise in such structures and are predicted to generate non-reciprocal spin-wave dispersion [41, 42]. Only recently, magnetic states and mechanisms of magnetization reversal of individual NTs were measured and controlled experimentally [43, 44]. These findings were enabled by progress in nanotechnology fabrication, nano-manipulation and measurement techniques. The importance of having a well-defined control over the material quality and morphology of the magnetic coatings of these elements

became evident when moving from theoretical predictions to experimental works. Irregularities in real NTs impacted the magnetic states predicted for ideal ones. Studies on the dynamic magnetization of individual ferromagnetic nanotubes were already presented. Still, spin waves confinement and propagation within nanotubes with small diameters ( $\sim 200$  nm or less) are an objective of experimental research. The potential of ferromagnetic NTs as 3D magnonic building blocks will materialize only when the underlying spin wave dynamics is fully understood and optimized 3D ferromagnetic coatings are achieved.

## 1.2 Scope and overview of the thesis

This thesis aims at gaining further understanding on the nanofabrication as well as the static and dynamic magnetic properties of individual ferromagnetic nanotubes (FNTs) with diameters on the order of hundreds of nanometers and hexagonal cross section. In particular, it aims at quantifying the spin wave confinement in such 3D nanocavities and relating spin waves properties to NTs geometrical parameters. At the time this thesis began, experimental work on spin waves in similar ferromagnetic NTs were limited. To the best of our knowledge, only a preliminary study presented by Daniel Ruffer in his doctoral thesis [45] existed. His work demonstrated that much more complex resonance spectra in FNTs than in simple planar films are relevant. Ruffer's simulations clearly showed that the complexity of the spectra was linked to the 3D geometry of the nanotubular cavity. However, significant discrepancies between the expected and measured resonance frequencies existed. The results were partially ambiguous and left some fundamental questions still open. For example, it was not clear if the measured discrepancy was linked to a demagnetization effect not properly taken into account by the classical micromagnetics model for the NT or if the deposited material (obtained by PVD) was compromised.

The starting objective of this thesis was the development of ALD processes which give rise to conformal ferromagnetic coatings of optimized quality. The materials addressed in this thesis are Ni and NiFe alloys. Nickel, being a single-element ferromagnetic material, provided a starting point for the optimization of ALD processes. NiFe, with the specific stoichiometry of permalloy  $\text{Ni}_{80}\text{Fe}_{20}$ , offers a lower damping for spin waves than Ni and, on the one hand, a better material platform to study FNT-based spin wave cavities. On the other hand, it imposes a technological challenge and works in the literature are still few [46]. In this thesis, we provide a throughout study on the fabrication and functional properties of ALD grown Ni and NiFe in spintronics and magnonics. The ALD process parameters have been related for both materials with their chemical, morphological and crystallographic properties by means of several characterization techniques, like scanning electron microscopy (SEM), transmission electron microscopy (TEM), X-ray diffraction (XRD), scanning transmission electron microscopy, coupled with energy dispersive X-ray imaging (STEM-EDX) and atomic force microscopy (AFM). Functional properties pertinent to the study of shape dependent static and dynamic magnetic properties were quantified by SQUID and vibrating sample magnetometry (VSM), electri-

cal resistivity, anisotropic magnetoresistance (AMR) and ferromagnetic resonance (FMR) by broadband spectroscopy measurements. Studies were performed on both planar coatings and standing GaAs nanowires serving as templates for the fabrication of NTs. The dynamic magnetization of optimized individual Ni and NiFe nanotubes was investigated by means of micromagnetic simulations and microfocused Brillouin light scattering (BLS) spectroscopy [47]. To the best of our knowledge, BLS was employed for the first time to resolve spin waves modes in small diameters FNTs.

## 2 Theoretical background

In this chapter the essential theoretical background for the presented research is introduced. In section 2.1 an introduction to the basic concepts of magnetism is given, followed by a brief overview over relevant micromagnetic aspects in section 2.2. Section 2.3 summarizes dynamic effects in magnetic materials: the fundamental equation of magnonics, the Landau–Lifshitz–Gilbert (LLG) equation, is introduced in sec. 2.3.1. Section 2.3.2 presents the LLG solution for the ferromagnetic resonance phenomenon. Lastly, in sec. 2.3.3, the spin wave dispersions analytically derived for thin films and nanotubes are presented.

### 2.1 Introduction to magnetism

The modern understanding of magnetism dates back to the establishment of quantum mechanics during the first half of the 20th century [48, 1]. The magnetism of materials is a macroscopic manifestation of quantum mechanical angular momenta associated to the electrons of the atoms. Both orbital angular momentum and spin angular momentum of the electron contribute to a microscopic magnetic moment, expressed as  $\boldsymbol{\mu}_i$  in a system of electrons. The total magnetic moment  $\boldsymbol{m} = \sum_i^N \boldsymbol{\mu}_i$  (with  $N$  being the number of electrons in an atom) is directly proportional to the total angular momentum  $\boldsymbol{J}$  via

$$\boldsymbol{m} = -\gamma \boldsymbol{J}, \quad (2.1)$$

where  $\gamma = g\mu_0 \frac{|e_0|}{2m_e}$  is the gyromagnetic ratio [49], expressed in terms of the vacuum permeability  $\mu_0 = 4\pi \cdot 10^{-7} \text{ N/A}^2$ , the electron charge  $e_0$ , the electron mass  $m_e$  and the Landé factor  $g$ . In most 3d transition metal complexes, whose d-orbital is not fully occupied, the orbital contribution is insignificant, so the magnetic moment appears due to the spins. The total angular momentum is approximated to the spin angular momentum ( $\boldsymbol{J} \approx \boldsymbol{S}$ ) and  $g \approx 2$ . The spin angular momentum of an electron projected along any given direction amounts to  $\frac{1}{2}\hbar$ , with  $\hbar$  being the reduced Planck constant. Thereby, the magnetic moment associated to the single electron results to be  $\mu_B = \frac{\hbar e_0}{2m_e} = 9.274 \cdot 10^{-24} \text{ J} \cdot \text{T}^{-1}$  and is referred to as Bohr magneton. On large length scales, the so-called ‘continuum approach’ is used where the quantized char-

## Chapter 2. Theoretical background

acter of the individual magnetic moments is neglected. The magnetization  $\mathbf{M} = \sum_{j=1}^M \mathbf{m}_j / V$  (with  $M$  being the number of atoms) is a measure of the magnetic moments per volume  $V$  and is treated as a continuous vector field over the entire magnetic body. The response of a material magnetization to an applied magnetic field  $\mathbf{H}$  is given by the relationship

$$\mathbf{M} = \hat{\chi} \mathbf{H}, \quad (2.2)$$

where  $\hat{\chi}$  is the tensor of the magnetic volume susceptibility. In free space, the magnetic flux density  $\mathbf{B}$  scales linearly with the magnetic field  $\mathbf{H}$ . In presence of a magnetic body,  $\mathbf{M}$  and  $\mathbf{H}$  add vectorially:

$$\mathbf{B} = \mu_0(\mathbf{M} + \mathbf{H}) = \mu_0(\hat{\chi} + 1) \mathbf{H}. \quad (2.3)$$

The term  $\mu_0(\hat{\chi} + 1)$  is denoted permeability  $\hat{\mu}$ . In literature often we find the relative permeability  $\mu_r = \mu / \mu_0$ .

Magnetic materials can be classified by their response to external fields [50, 51, 45]. For this classification, one usually considers the tensor components of the magnetic volume susceptibility

$$\chi_{ij} = \frac{\partial M_i}{\partial H_j}, \quad (2.4)$$

Often  $\chi_{ij}$  is considered to be a scalar  $\chi = \chi_{ij}$ . In certain materials and for sufficiently small fields, we observe a linear relation and thus  $\chi = \text{const}$ .

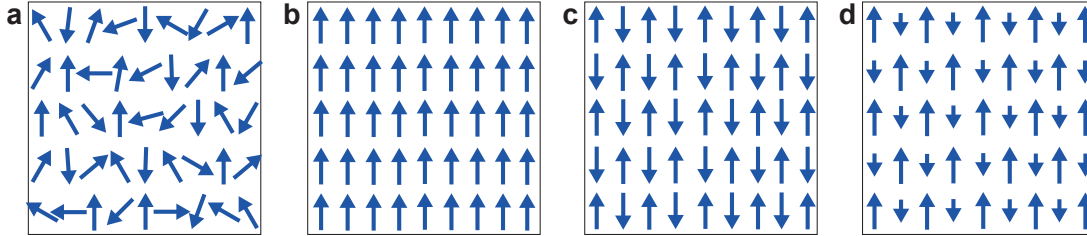


Figure 2.1 – Schematic images of magnetic moments in a (a) paramagnetic, (b) ferromagnetic, (c) antiferromagnetic and (d) ferrimagnetic material. The length of arrows represent the amplitude of magnetic moments.

If  $\chi$  is positive and small (on the order of  $10^{-4}$ ) we speak of paramagnetism. **Paramagnetic** materials possess magnetic moments which are not ordered (Fig. 2.1 a). By application of an external field the magnetic moments are aligned into the same direction, resulting in a macroscopic small magnetization.

**Diamagnetic** materials possess no permanent magnetic moments  $\mu_i$ . Their susceptibility  $\chi$  is negative and very small (on the order of  $-10^{-5}$ ). For an applied field  $\mathbf{H}$ , a weak magnetic flux density is induced pointing in the opposite direction of the external magnetic field.

A small class of materials exhibit the important property of long range magnetic order. Fundamentally, this arises because of the quantum-mechanical exchange interaction between

neighboring permanent moments [52]. In this class of materials we distinguish **ferromagnetic**, **antiferromagnetic** and **ferrimagnetic** materials, based on the order of their permanent magnetic moments in the absence of an applied external field.

In **ferromagnetic** materials the exchange interaction favors a parallel alignment of neighboring magnetic moments (Fig. 2.1 b) and exhibit spontaneous magnetization. Magnetic domains are formed due to further interactions discussed in the next section. Within each domain magnetic moments are aligned parallel. For a random alignment of the magnetic domains the remanent magnetization without external field, named remanence, is zero, while the magnetization increases significantly with an applied field. The relative susceptibility of a strong ferromagnet is on the order of  $10^6$ . When all magnetic moments are aligned in the same direction, the magnitude of the magnetization  $|M|$  reaches the saturation magnetization  $M_s$  of the material.  $M_s$  depends on the temperature  $T$ . Above the so-called Curie temperature  $T_C$  a ferromagnetic material loses its permanent magnetization and becomes paramagnetic. In the periodic table of the elements, only iron (Fe), nickel (Ni) and cobalt (Co) are ferromagnetic at room temperature (RT) [1]. NiFe and CoFeB alloys, widely used in spintronics and magnonics, also belong to the category of ferromagnetic materials.

In **antiferromagnetic** materials the exchange interaction favors an anti-parallel orientation of magnetic moments (Fig. 2.1 c) resulting in a vanishing macroscopic magnetization. The susceptibility of antiferromagnetic materials is positive but very small, as an external field has to act against the exchange interaction.

**Ferrimagnetic** materials possess two different magnetic sublattices. Neighboring magnetic moments are antiferromagnetically aligned, however their magnitude is different (Fig. 2.1 d). Hence ferrimagnets show a spontaneous magnetization and their macroscopic magnetic behavior is similar to ferromagnets. Due to the partial cancelling of magnetic moments the saturation magnetization of ferrimagnets is typically smaller than for ferromagnets. Yttrium iron garnet ( $\text{Y}_3\text{Fe}_5\text{O}_{12}$ , YIG) is a ferrimagnetic insulator widely employed in microwave components and magnonics.

## 2.2 Micromagnetics: basic principles

The challenge of micromagnetics is to develop a formalism in which the macroscopic magnetic properties of a material can be simulated including the best approximations to the fundamental atomic behavior of the material [52]. In brief, the classical approach to micromagnetics, pioneered by Brown [53, 54], replaces the spin by a vector field which initially allows the determination of magnetostatic fields within the system. In addition, the exchange interaction is formulated in a way to replace the quantum mechanical exchange interaction with a formalism appropriate for the limit of a continuous material. This, coupled with an energy minimization approach, forms the basis of classical micromagnetics. In the following relevant energy terms are introduced.

### Exchange energy

Ordering of magnetic moments is fundamentally driven by the quantum mechanical exchange energy. Following the Pauli exclusion principle, the wave functions of two electrons can only overlap if their spins  $\mathbf{S}_i$  and  $\mathbf{S}_j$  are aligned antiparallel. On the other hand, for  $\mathbf{S}_i \parallel \mathbf{S}_j$ , the electrons have to be separated in space, which lowers the repulsive electrostatic Coulomb energy. Depending on which of the two energies is larger, either an antiferromagnetic or a ferromagnetic coupling is preferred [1]. In a system with  $N$  electrons the exchange energy can be formulated by

$$E_{ex} = - \sum_{i,j}^N J_{i,j} \mathbf{S}_i \cdot \mathbf{S}_j = - \sum_{i < j}^N 2J_{i,j} \mathbf{S}_i \cdot \mathbf{S}_j, \quad (2.5)$$

where  $2J_{i,j}$  reflects the energy difference between parallel and antiparallel spin orientation of electrons  $i$  and  $j$ . In a continuum approach, changing the summation to an integral over the whole magnet body, the exchange energy can be written as:[55, 45]

$$E_{ex} = \frac{A_{ex}}{M_s^2} \int (\mathbf{M})^2 dV. \quad (2.6)$$

The parameter  $A_{ex}$  is the exchange stiffness, proportional to the exchange constant  $J_{ex}$ . The exchange stiffness constant  $A_{ex}$  sets an exchange length  $l_{ex}$  expressed as [56]

$$l_{ex} = \sqrt{\frac{2A_{ex}}{\mu_0 M_s^2}}. \quad (2.7)$$

$l_{ex}$  represents a critical length for the competition of exchange energy and dipolar energy. Over this length the direction of magnetization can adapt to a dipolar field, influencing, e.g., domain walls formations. The exchange length is typically 2-6 nm for ferromagnetic materials.

### Demagnetization field energy

The field created from a magnetic body itself is often called 'stray field' in the region outside the body and 'demagnetization field'  $\mathbf{H}_d$  inside the body. The magnetostatic energy arising from the effects of  $\mathbf{H}_d$  on  $\mathbf{M}$  is given by:

$$E_d = \frac{\mu_0}{2} \int_V \mathbf{H}_d \cdot \mathbf{M} dV. \quad (2.8)$$

In general the demagnetization field is inhomogeneous and often solved numerically in micromagnetic simulations. For the special case of uniformly magnetized elliptical bodies the demagnetization field is uniform and can be analytically calculated by

$$\mathbf{H}_d = -\hat{N}\mathbf{M} = - \begin{pmatrix} N_x & 0 & 0 \\ 0 & N_y & 0 \\ 0 & 0 & N_z \end{pmatrix} \mathbf{M} \quad (2.9)$$



where  $\hat{N}$  is denoted demagnetization tensor. The parameters on its diagonal are called demagnetization factors and fulfill the condition  $N_x + N_y + N_z = 1$ . As an approximation, the formalism of Eq. (2.9) can be applied to non-ellipsoidal magnetic bodies, assuming a uniform magnetization. In the case of a sphere we find  $N_x = N_y = N_z = \frac{1}{3}$  [57]. The demagnetization field of a magnetic thin film with a large width and length compared to its thickness is well approximated by  $N_x = N_y = 0$  and  $N_z = 1$  for  $z$  being the out-of-plane direction [58, 57]. For a magnetic cylindrical rod with length much larger than its radius, we can approximate  $N_x = N_y = \frac{1}{2}$  and  $N_z = 0$  [57] for  $z$  being the cylinder axis direction.

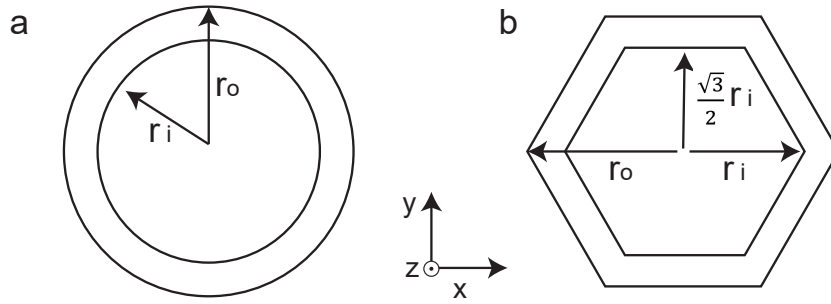


Figure 2.2 – Illustration of the geometry and the parameters for the calculation of the demagnetization factor of (a) a hollow cylinder with circular cross section and (b) a hollow cylinder with a hexagonal cross section

Because of the inhomogeneity of  $\mathbf{H}_d$  for non-ellipsoidal bodies, effective demagnetization tensors, employing some kind of averaging, are defined. For instance, the literature distinguishes between “magnetometric” and “fluxmetric” (or “ballistic”) demagnetizing factors [59]. A “magnetometric” demagnetizing factor  $N_m$  refers to an average of magnetization over the entire specimen and is appropriate for magnetometer measurements of small samples [60]. A “fluxmetric” demagnetizing factor  $N_f$  refers to an average of magnetization at the midplane of the sample [60]. Prat-Camp et al. [61] derived analytical expressions for the magnetometric  $N_m$  and fluxmetric  $N_f$  demagnetizing factors of an infinitely long hollow cylinder, which cross section is depicted in Figure 2.2a. The authors assume an infinite cylinder length in the axial direction  $z$ , with homogeneous and isotropic relative permeability  $\mu = 1 + \chi$  in the presence of a uniform field  $H$  applied transversely (e.g. along  $x$ ). The radii ratio of the hollowed cylinder is defined as [37]

$$\beta = \frac{r_i}{r_o} \quad (2.10)$$

with  $r_i$  and  $r_o$  being the inner and outer radius, respectively. For the fluxmetric and the magnetometric demagnetization tensor they obtained:

$$N_f = \frac{1 - \beta}{2} \quad (2.11)$$

and

$$N_m = \frac{1}{2} \left( 1 - \beta^2 \frac{\mu - 1}{\mu + 1} \right) \quad (2.12)$$

Whereas  $N_m$  depends on both permeability  $\mu$  and the ratio  $\beta$  of the internal and external radii of the cylinder,  $N_f$  does not depend on  $\mu$ . It has to be noted that in the absence of the hole ( $\beta \rightarrow 0$ ) the demagnetizing factors both assume the value for a cylindrical solid rod.

The demagnetization field  $\mathbf{H}_d$  and the magnetometric demagnetization factor  $N_m$  of a nanotube with hexagonal cross section (Figure 2.2b) have been determined by D. Rueffer in his PhD thesis [45] by means of micromagnetic simulations. The simulations were performed for different values of  $\beta$  and compared with the model of a cylinder with circular cross section [61]. For a hexagonal nanotube magnetized along  $y$ , thereby with an external field applied perpendicular to two facets, the results show a distribution of  $\mathbf{H}_d$  very similar to the one found for a nanotube with circular cross section. Consequently, for  $\mathbf{H}_d$  along  $y$ ,  $N_m$  shows similar dependency on the radii ratio  $\beta$  as in Eq. (2.12). The distribution of  $\mathbf{H}_d$  differs strongly for a tube magnetization along  $x$ . In this case  $N_m$  never exceeds  $\sim 0.6$  and stays almost constant for all simulated dimensions.

### Anisotropy Energy

The term magnetic anisotropy indicates that the properties of a magnetic material are dependent on the direction in which the magnetic field is applied. The energy associated to the anisotropy  $E_{ani}$  has a number of possible origins [52].

The **magnetocrystalline anisotropy** is the contribution intrinsic to the material. It originates at the atomic level and depends on the lattice structure. Due to the non-spherical shape of atomic orbitals, the orbits prefer to lie in certain crystallographic directions. The spin-orbit coupling, the strong coupling between the spin and orbital angular momenta within an atom, then assures a preferred crystallographic direction for the magnetization, which is called the easy direction. To rotate the magnetization away from the easy direction costs anisotropy energy. Easy crystallographic directions are [111] and [100] in the case of a single crystal of Ni and Fe, respectively. In the case of permalloy  $\text{Ni}_{80}\text{Fe}_{20}$  the stoichiometry of Fe and Ni was specially optimized to suppress magnetocrystalline anisotropy [62]. Furthermore, in many ferromagnetic materials, this contribution becomes negligible and averages out due to the polycrystalline nature of the films obtained.

Another origin for anisotropy is given by the demagnetization field  $\mathbf{H}_d$  discussed in the previous section and it is called **shape anisotropy**. The magnetostatic energy associated to the specific shape of the magnetic body induces an easy axis and hard axis in ferromagnetically ordered materials. The tendency of the magnetization to lie along the easy axis of a specific geometry is described by the energy density :

$$\epsilon_a = K_u \sin^2 \theta, \quad (2.13)$$

where  $K_u$  is an anisotropy constant, and  $\theta$  is the angle between magnetization  $\mathbf{M}$  and the anisotropy axis. In magnetic materials subject to the magnetostriction phenomenon, the changes in atomic structure due to the material deformation can add also a **stress anisotropy** contribution. Elemental ordering in alloys can lead to anisotropy as well

### Zeeman energy

The alignment of the magnetic moments in an external field  $H_{ext}$  is described by the Zeeman potential energy:

$$E_z = -\mu_0 \int_V \mathbf{H}_{ext} \cdot \mathbf{M} dV. \quad (2.14)$$

The Zeeman energy is minimized when the magnetization is aligned with the external field.

### Total energy and effective magnetic field

Adding all the relevant energy terms, the total energy of a system becomes:

$$E_{tot} = E_{ex} + E_d + E_{ani} + E_z. \quad (2.15)$$

To reach an equilibrium state of the static magnetization, the energy  $E_{tot}$  is minimized. It is possible to define an effective magnetic field  $\mathbf{H}_{eff}$  acting on the magnetization, as the derivative of the energy density with respect to the orientation [45]:

$$\mathbf{H}_{eff} = -\frac{1}{\mu_0} \frac{d}{d\mathbf{M}} \frac{dE_{tot}}{dV} \quad (2.16)$$

In the static limit  $\mathbf{M}$  aligns parallel to  $\mathbf{H}_{eff}$  to minimize the total energy.

## 2.3 Magnetization dynamics

### 2.3.1 Landau-Lifshitz-Gilbert Equation

In quantum mechanics, the spin intrinsically possesses an angular momentum. Therefore, the magnetic moment misaligned with an effective magnetic field  $\mathbf{H}_{eff}$  experiences a torque and starts precessing (Figure 2.3 a). This precessional motion is described in terms of the Landau-Lifshitz (LL) equation [63] proposed in 1935 :

$$\frac{d\mathbf{M}}{dt} = -\gamma\mu_0 \mathbf{M} \times \mathbf{H}_{eff}. \quad (2.17)$$

The LL equation describes a precession of the magnetization around the effective field with an angular frequency  $\omega_H = \gamma\mu_0 \mathbf{H}_{eff}$ . The gyromagnetic factor is taken as a positive value in Eq. (2.17) and in the following. Experimental observations show that eventually the precession amplitude decays until  $\mathbf{M}$  aligns parallel to  $\mathbf{H}_{eff}$  as in the static limit (Figure 2.3 a). To take

into account this energy relaxation, a phenomenological damping term was added to the Landau–Lifshitz equation, leading to the Landau–Lifshitz–Gilbert equation (LGG)[64]:

$$\frac{d\mathbf{M}}{dt} = -\gamma\mu_0\mathbf{M} \times \mathbf{H}_{eff} - \frac{\alpha}{M_s}(\mathbf{M} \times \frac{d\mathbf{M}}{dt}). \quad (2.18)$$

Here  $\alpha$  is the Gilbert damping parameter and can take values from 0 to 1. For magnonic applications, materials with small  $\alpha$  are considered to minimize damping losses. The LLG equation is the standard equation of motion and it is solved numerically in most micromagnetic simulation programs. For small precession amplitudes the equation can be linearized and analytically solved [49].

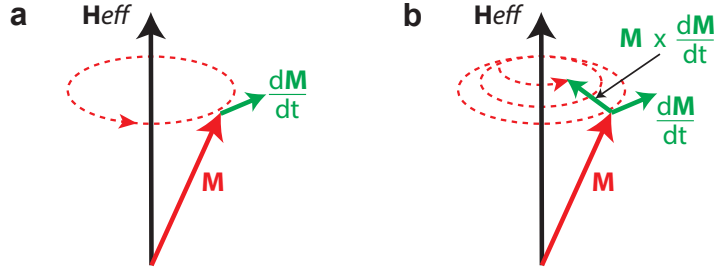


Figure 2.3 – (a) A schematic image of the magnetization  $\mathbf{M}$  precessing around the effective field  $\mathbf{H}_{eff}$  with a constant cone angle due to microwave excitation at the resonance frequency. (b) Magnetization precession around the effective field  $\mathbf{H}_{eff}$  with energy relaxation (damping).

### 2.3.2 Ferromagnetic resonance

A solution of the equation of motion was found by Kittel in 1948 [57]. This solution refers to the special case of uniform magnetization precession with all magnetic moments precessing in phase, called ferromagnetic resonance (FMR). The problem treated by Kittel considered an ellipsoid homogeneously magnetized in the direction of the static external field  $\mathbf{H}_{ext} = \mathbf{H}_0 = H_0\mathbf{e}_z$ . The exciting external radio frequency (rf) field  $\mathbf{h}_{rf} = h_{rf}\mathbf{e}_x$  is considered perpendicular to the static field. The damping is neglected, hence Eq. (2.18) simplifies to Eq. (2.17). The magnetization is assumed to be uniform in space and time for the whole sample, thus  $\mathbf{M}(\mathbf{x}, t) = \mathbf{M}$  and, according to Eq. (2.6), the exchange energy contribution vanishes. Assuming an isotropic material,  $E_{ani} = 0$  is considered. Thereby only the demagnetization field  $\mathbf{H}_d = -\hat{N}\mathbf{M}$  (Eq. (2.9)) contributes to  $\mathbf{H}_{eff}$ , which depends on the sample geometry. Considering that the field is applied along  $z$ ,  $M_x(t), M_y(t) \ll M_z \approx M_s$ . With  $|h_{rf}| \ll |H_0|$ , the  $x, y, z$  components of Eq. (2.17) can be written as follow:

$$\frac{dM_x}{dt} = \gamma\mu_0[H_0 + (N_y - N_z)M_s]M_y \quad (2.19)$$

$$\frac{dM_y}{dt} = \gamma\mu_0[h_{rf}M_s - H_0M_x - (N_x - N_z)M_x]M_s \quad (2.20)$$

$$\frac{dM_z}{dt} \approx 0 \quad (2.21)$$

On solving the set of equations with the time dependency  $M_x, M_z \sim \exp(i\omega t)$ , one finds the susceptibility  $\chi_{xx} = \frac{\partial M_x}{\partial H_x}$  equal to

$$\chi_{xx} = \frac{\chi_0}{1 - (\omega/\omega_0)^2} \quad (2.22)$$

Here,  $\omega_0 = \omega_{res}$  is the resonance frequency described by the Kittel formula:

$$\omega_{res} = 2\pi f_{res} = \gamma\mu_0 \sqrt{[H_0 + (N_y - N_z)M_s][H_0 + (N_x - N_z)M_s]} \quad (2.23)$$

with  $f_{res}$  being the frequency of the ferromagnetic resonance (FMR) and  $H_0$  pointing in the  $z$ -direction. By substituting the demagnetization constant introduced in Sec.2.2 for the planar, spherical and cylindrical geometry, the frequency of the FMR becomes  $\omega_{res} = \gamma\mu_0\sqrt{H_0(H_0 + M_s)}$  in case of a planar film,  $\omega_{res} = \gamma\mu_0 H_0$  in case of a sphere and  $\omega_{res} = \gamma\mu_0(H_0 + 1/2M_s)$  in case of a cylindrical rod. Figure 2.4a shows the calculated FMR frequency for a thin film magnetized as sketched (green curve), a cylindrical rod (red curve) and a sphere (orange curve) done out of permalloy Py (Py parameters:  $\frac{\gamma\mu_0}{2\pi} = 28 \text{ GHz T}^{-1}$  and  $\mu_0 M_s = 1 \text{ T}$ ). The relevant susceptibility in  $x$ -direction is calculated as [65, 66]:

$$Re(\chi_{xx}) = \chi'_{xx} = \frac{\omega_M(\omega_H + \omega_M)(\omega_{res}^2 - \omega^2)}{(\omega_{res}^2 - \omega^2)^2 + \alpha^2\omega^2(2\omega_H + \omega_M)^2} \quad (2.24)$$

$$Im(\chi_{xx}) = \chi''_{xx} = \frac{\alpha\omega\omega_M[\omega^2 + (\omega_M + \omega_H)^2]}{(\omega_{res}^2 - \omega^2)^2 + \alpha^2\omega^2(2\omega_H + \omega_M)^2} \quad (2.25)$$

Here, we use  $\omega_M = \mu_0\gamma M_s$  and  $\omega_H = \mu_0\gamma H_0$ . Figure 2.4b depicts the shape of  $\chi'_{xx}$  and  $\chi''_{xx}$  calculated at  $\mu_0 H_0 = 50 \text{ mT}$  for a Gilbert damping parameter  $\alpha = 0.08$ .

The linewidth of  $\chi''$  is a measure of the Gilbert damping. The line shape of  $\chi''$  can be approximated by an Lorentzian function and its linewidth is related to  $\alpha$  by [66, 67]:

$$\Delta f_{res} = \frac{|\gamma|}{2\pi} \Delta H + 2\alpha f_{res}. \quad (2.26)$$

Here  $\Delta H$  is the linewidth inhomogeneous broadening attributed to extrinsic mechanisms and film inhomogeneities.

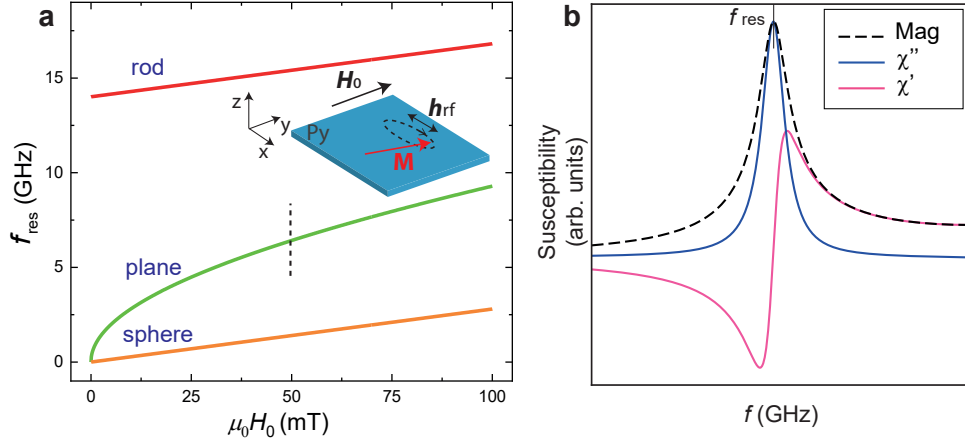


Figure 2.4 – (a) FMR frequency of a Py thin film, sphere and cylindrical rod with a magnetic field applied in-plane, along any direction and along the rod axis, respectively. The frequency is calculated with the Kittel equation [57]. (b) Real and imaginary part of the susceptibility at 50 mT (indicated by a dashed line in (a)) calculated for  $\alpha = 0.008$ . The dashed curve shows the magnitude  $\text{Mag} = \sqrt{\chi_I^2 + \chi_{II}^2}$

### 2.3.3 Spin wave dispersion

We discussed the scenario of the FMR response with uniform spin precession, caused by a uniform driving field  $\mathbf{h}_{\text{rf}}$  applied to the entire sample. The generated oscillation can be considered as a wave with infinite wavelength or, equivalently, zero wave vector  $\mathbf{k}$  ( $\lambda \rightarrow \infty$ ,  $|\mathbf{k}| = \frac{2\pi}{\lambda} = 0$ ). When the exciting field  $\mathbf{h}_{\text{rf}}$  is applied locally, the neighboring magnetic moments can precess with a phase difference, and form a wave-like excitation, called spin wave (SW, magnon). This oscillation can spread throughout the sample with a wavelength  $\lambda$  and a non-zero wave vector  $\mathbf{k} = \frac{2\pi}{\lambda}$ . SWs can be dominated by (long-range) dipolar interaction and (short-range) exchange interaction. The SW characteristics are defined by a wave vector  $\mathbf{k}$ , the magnetization configuration, as well as the angle between the magnetization  $\mathbf{M}$  and the wave vector  $\mathbf{k}$ .

#### Spin waves in thin films

Kalinikos and Slavin (K. S.) [68] established a comprehensive analytical treatment for the calculation of SW dispersion relations in a thin film with thickness  $L$ . The spin waves are confined in one dimension and the wave vector can be split into an in-plane ( $\mathbf{k}_{\text{ip}}$ ) and an out-of-plane ( $\mathbf{k}_{\text{op}}$ ) component with  $\mathbf{k} = \mathbf{k}_{\text{ip}} + \mathbf{k}_{\text{op}}$ . In the thin films  $\mathbf{k}_{\text{op}}$  represents perpendicular standing spin waves (PSSWs) along the film thickness  $t$ . The magnitude of the wave vector is calculated as  $k = \sqrt{k_{\text{ip}}^2 + k_{\text{op}}^2}$ . The K. S. formalism assumes that the magnetization  $\mathbf{M}$  in a magnetic thin film orients by an angle  $\theta$  with respect to the  $z$ -direction and forms an angle  $\varphi$ , projected in the  $x - y$  plane, with the direction of  $\mathbf{k}$ . The K.S. solution for the SW dispersion

relation reads:

$$\omega_{res} = \sqrt{(\omega_H + \omega_M l_{ex}^2 k^2)(\omega_H + \omega_M l_{ex}^2 k^2 + \omega_M F_n)} \quad (2.27)$$

with

$$F_n = 1 - P_n \cos^2(\varphi) + \frac{\omega_M P_n (1 - P_n) \sin^2(\varphi)}{\omega_H + \omega_M l_{ex}^2 k^2} \quad (2.28)$$

being the dipolar matrix element. The exact form of the matrix element depends on the pinning conditions of  $\mathbf{M}$  at the sample surfaces [68]. For the case of totally unpinned surface spins,  $P_n$  reads:

$$P_n = \frac{k_{ip}^2}{k^2} + \frac{2k_{ip}^3}{k^4 L} \left[ 1 - (-1)^n e^{-k_{ip} t} \right] \quad (2.29)$$

Knowing the dispersion relation, the SW group velocity is determined by

$$v_g = \partial \omega_{res} / \partial k. \quad (2.30)$$

SWs with  $\mathbf{k} \perp \mathbf{M}$  are called Damon–Eshbach (DE) waves (black curve in Fig. 2.5, SWs with  $\mathbf{k} \parallel \mathbf{M}$  are denoted backward-volume (BWV) waves (blue curve in Fig. 2.5). For large in-plane wave vectors the dispersion is dominated by the exchange interaction, which is isotropic. In this regime, denominated exchange regime, we find  $\omega_{res} \propto k^2$  and  $v_g \propto k$ . In contrast, for small wave vectors with  $l_{ex}^2 k^2 \ll 1$  the exchange interaction can be neglected and the dispersion relation is governed by the dipolar interaction (dipolar regime), which depends on the relative orientation of magnetic moments and it is, consequently, anisotropic.

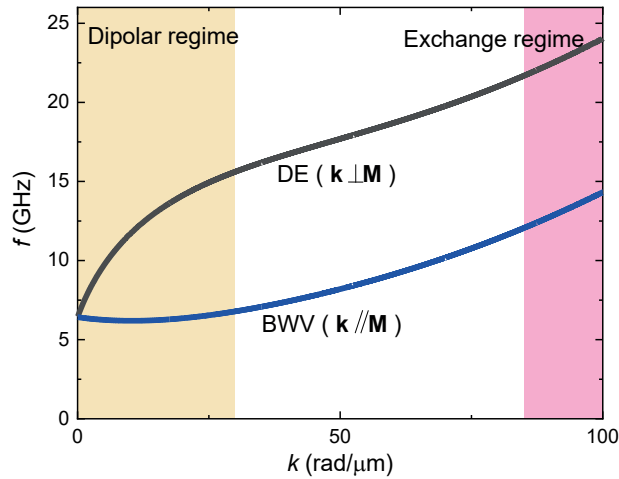


Figure 2.5 – Damon–Eshbach (DE) and backward-volume (BWV) dispersion relations for a 30-nm-thick Py film with an applied in-plane field of  $\mu_0 H = 40$  mT.

### Spin waves in nanotubes

A general analytical treatment for the calculation of SW dispersion relations in tubes with arbitrary inner radius  $r_i$  and outer radius  $r_o$  has not yet been developed up to today. Still, solutions for special cases have been discussed in literature [45]. In particular, we report an overview of the models presented in the literature for the following scenarios:

#### 1) Infinite long nanotube ( $L \rightarrow \infty$ ), with negligible thickness $t$ ( $t \rightarrow 0$ or $r_i \rightarrow r_o$ )

This model, presented by Leblond and Veerakumar [69] analyzes the dynamics of magnetization on the surface of the ferromagnetic nanotube and is based on solving the Landau-Lifshitz equation and the magnetostatic Maxwell equations. They assumed uniform axial magnetization and spin waves propagating along the axis of the tube (no azimuthal confinement is considered). Under the mentioned constraints they obtain the following dispersion relation:

$$\omega_{res} = \gamma\mu_0 \sqrt{[H_0 + l_{ex}^2 M_s(k^2 + r_o^{-2})] [H_0 + l_{ex}^2 M_s(k^2 + r_o^{-2}) + M_s]} \quad (2.31)$$

It is worth to notice that a non zero resonance frequency is obtained for  $\mathbf{k} = 0$  and  $H_0 = 0$ . This is a direct consequence of the exchange energy related to the misalignment of the spins on the curved surface of the tube. In a tube, exchange effects can only be neglected for  $l_{ex}^2(k^2 + r_o^{-2}) \ll 1$  (in a planar thin film for  $l_{ex}^2 k^2 \ll 1$ ), hence the modes become exchange dominated for much smaller  $k$  than in planar samples.

#### 2) Sufficiently large nanotube

In case the magnetic tube is large enough, so that the exchange effect of the curvature can be neglected, one can model the system using the thin film dispersion equation, Eq. (2.27), and imposing periodic boundary conditions. Balhorn et al. [70, 71] used the model to interpret the spin wave resonances found in Rolled-Up Permalloy Tubes (RUPTs) [72]. Under the experimental conditions, the magnetization was parallel to the tube axis and the spin waves propagated in DE mode azimuthally. With  $\varphi = \frac{\pi}{2}$ , considering the wave vector fully in plane  $k = k_{ip}$  and assuming unpinned surface spins, Eq. (2.28) and (2.29) simplified to

$$F_n = 1 + \frac{\omega_M P_n (1 - P_n)}{\omega_H + \omega_M l_{ex}^2 k^2} \quad (2.32)$$

$$P_n = \frac{1}{kL} \left[ 1 - (-1)^n e^{-kt} \right] \quad (2.33)$$

with  $L$  being the nanotube thickness. The periodic boundary condition demands a quantiza-



tion of the azimuthal wavevector  $k_\phi$  which is expressed as

$$n\lambda = \pi d \Leftrightarrow k_\phi = \frac{2n}{d} \quad (2.34)$$

Here  $\lambda$  denotes the wavelength of the spin wave,  $k_\phi$  the azimuthal wave vector, and  $d$  the diameter of the RUPT. This model only holds true as long as the curvature is small and the wave lengths are large, as to say for  $l_{ex}^2(k^2 + r_0^{-2}) \ll 1$ .

### 3) Nanotubes circularly magnetized

A more recent analytical approach was presented by Otalora et al.[41, 73]. The authors have derived a SW dispersion relation for an infinite long cylindrical nanotube, with arbitrary inner and outer radii  $r_i$  and  $r_o$ , magnetized circularly. The stabilization of a global vortex state is obtained by considering the application of a Zeeman field  $\mathbf{H}_\phi$  along the azimuthal direction of the cylinder. This field, together with the demagnetization and exchange term, are considered for the effective field  $H_{eff} = H_{ex} + H_{dem} + H_\phi$  entering the Landau-Lifshitz-Gilbert equation (Eq. 2.18). Small perturbations  $\mathbf{m}$  are considered applied perpendicularly to the vortex state. The analytical description is given under the framework of the micromagnetic continuum theory. The dispersion relation is calculated by (i) linearizing the LLG equation to the first order of  $\mathbf{m}$ , and (ii) solving the linear equation in terms of individual magnons described by a wave vector  $k_z$  along the nanotube axis  $z$ , with an integer wave number  $n$  characteristic of the azimuthal symmetry. The analytical derivation leads to the following dispersion relation for the coherently distributed SWs:

$$\frac{\omega_0(k_z)}{\gamma_0 \mu_0 M_s} = K_n(k_z) + \sqrt{A_n(k_z)B_n(k_z)} \quad (2.35)$$

For a detailed description of the functions  $K_n(k_z)$ ,  $A_n(k_z)$  and  $B_n(k_z)$  appearing in Eq. (2.35), the reader is referred to ref. [41]. The spin wave dispersion in Eq. (2.35) shows an asymmetry with respect to  $k_z$ , hence the direction of propagation. The origin of this asymmetric behavior can be traced back to  $K_n(k_z)$ , being the only odd function in  $k_z$  appearing in Eq. (2.35). The function comprises dynamic dipolar energy terms arising from surface and volume charges created by the propagating spin waves. The volume charges are found to be different for positive and negative values of  $k_z$ , thus also the dipolar energies are different. At a given excitation (fixed frequency) the wavelengths for both propagation directions differ such that the dynamic dipolar energy adjusts the surface and volume charges to be energetically equal. This feature, known as SWs non-reciprocity, is desirable for eventual SWs engineering in magnonic applications and here it is uniquely a dipolar effect due to the curvature of the nanotube. However, on the one hand it is worth to mention that, in absence of material anisotropies, the vortex state is not the equilibrium state for NTs with a small diameter, but rather for NT with a large diameter and a small aspect ratio[37]. On the other hand, the asymmetry in the SW dispersion is found to decrease with increasing the tube diameter, until approaches the

## Chapter 2. Theoretical background

---

reciprocal behavior for very large diameters. Hence, to practically exploit the non-reciprocity in real NTs-based devices, a current flowing in the non-magnetic core of the NT should be applied, creating an Oersted field  $H_\phi$  stabilizing the vortex state.

## 3 Literature review

In this chapter review the static and dynamic magnetic phenomena predicted theoretically in ferromagnetic nanotubes, the experiments reported to date aiming at confirming and investigating the magnetic properties of real ferromagnetic nanotubes and the current status on atomic layer deposition of ferromagnetic Ni and NiFe three-dimensional coatings.

### 3.1 Static and dynamic magnetic phenomena in ferromagnetic nanotubes

Nanometer-scale non-uniform magnetization structures such as magnetic domain walls (DWs) [74, 40], magnetic vortices [75], antivortices [76], and skyrmions [77, 78] in thin films, nanodisks and nanowires have attracted increasing attention for their potential applications in data storage and as information carriers. Magnetic nanotubes (NTs) became a prototypical 3D nanostructure for the study of non collinear magnetic spin texture [38, 43]. What makes magnetic NTs particularly interesting is the possibility to control and define their remnant state and to program the formation of DWs during their magnetization reversal processes [36, 37, 39]. This is achieved by changing their geometrical parameters (length, inner, and outer radii). Magnetic NTs distinguish themselves from magnetic nanowires in that they exhibit a core-free magnetic configuration. The Bloch point structure along the central axis is avoided. This enables the possibility in NTs to support flux-closure magnetic (vortex) states which have lower energies and, therefore, are more stable than vortexes in magnetically solid cylindrical wires. In analogy with the studies on the curling state in magnetic cylinders [79, 80], initial studies on hollow cylindrical magnetic nanotubes have focused on their reversal magnetization as a source of nucleation of vortex-like spin textures. In a pioneering work of 2007, Landeros et al. [39] introduced the notion of a domain-wall mediated reversal magnetization in magnetic nanotubes. In this model, depending on the NT geometrical parameters, the energetically more favorable DW configuration was predicted to be a vortex or a transverse DW. The DW was nucleated at the end and propagated through the tube. The approach of these works was based on both analytical and numerical studies and exploited the micromagnetics principles

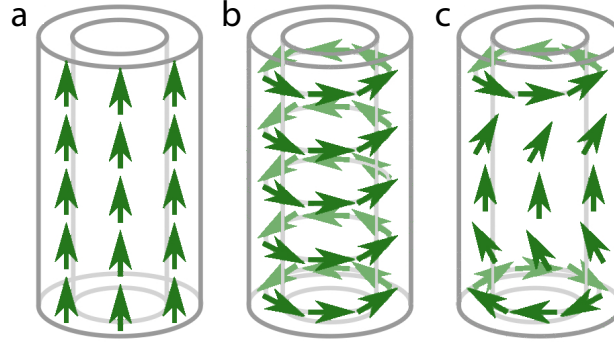


Figure 3.1 – Possible equilibrium magnetization configurations for NTs: (a) axial state, (b) vortex state and (c) mixed state.

of energy minimization discussed in section 2.2. This model was then extended to calculate nucleation fields  $H_n$  considering the dependency of the orientation of the applied field [81, 82] and the thickness  $t$  of the magnetic tube [83, 84].

The phase diagram for the static equilibrium in finite-length nanotubes has been calculated in 2007 by Escrig et al. [36] for a wide range of nanotube geometrical parameters by comparing the energies of the magnetization uniformly aligned along the NT axis (Fig. 3.1 a), and of the global vortex state, where the entire NT's magnetization is circumferentially aligned (Fig. 3.1 b). A phase diagram including also the mixed state (Fig. 3.1 c), postulated by Wang et al. [85], was developed analytically by Landeros et al. [37] shortly thereafter. In this state, depicted in Fig. 3.1 c, the magnetization curls at the ends of the tube to minimize the stray field and aligns axially in the center to minimize the exchange energy involved with the NT's curvature. The phase diagram of Landeros is reproduced in Figure 3.2. The occurrence of an axial, mixed or vortex state at remanence (ground state) is given as a function of the length  $L$  and the outer radius  $r_o$  of the NT normalized by the exchange length  $l_{ex}$  and as a function of the inner to outer radius ratio  $\beta$ , quantities discussed in detail in Chapter 2. A global vortex configuration is more likely to be found in tubes with large diameters as the curvature comprises an exchange energy penalty for the vortex configuration. The relative chirality, i.e. the rotational senses of the end-vortices, in the mixed state was found to depend on the ratio  $t/r_o$  of thickness  $t$  to the NT outer radius  $r_o$ . The reason is a stronger stray field interaction for tubes with larger  $t$ . Tubes with  $t/r_o < 0.2$  exhibit end-vortices with the same chirality and thicker tubes are predicted to show opposite rotational senses [86, 87]. Calculations suggest that for short magnetic NTs, opposing vortex states with opposite chirality and separated by a Néel domain wall, may also be stable [86, 88].

After Landeros et al. [39] proposed that vortex walls mediate the reversal of axially magnetized thick nanotubes, multiple theoretical studies on their motion were published. These works have predicted the motion of vortex DWs in NTs [89, 90, 91] to be faster and more stable than in nanostripes, due to the higher topological stability of the DWs inside the nanotube geometry. The predicted velocities of more than 1 km/s are interesting for applications as memory or

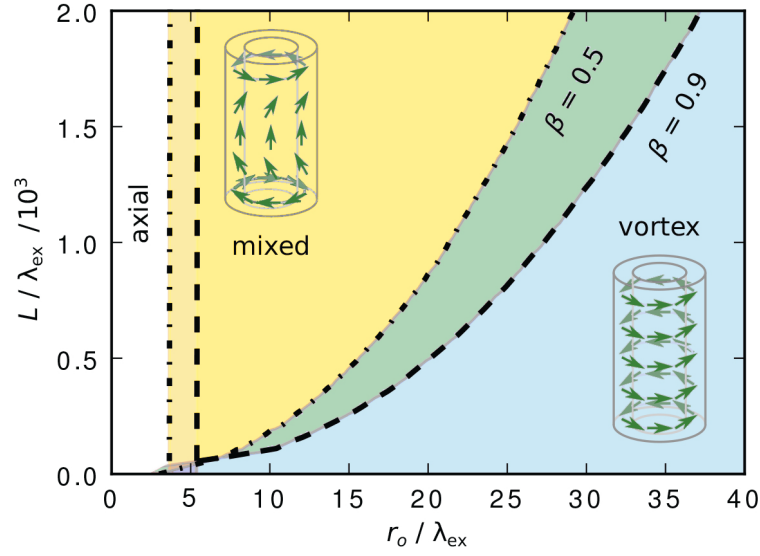


Figure 3.2 – Phase diagram for the equilibrium magnetization states in NTs. The transition from axial to mixed and finally vortex state is reported as a function of the normalized outer radius  $r_o/l_{ex}$  and the normalized tube length  $L/l_{ex}$  for radii ratios  $\beta = 0.5$  and  $0.9$  (adapted from ref. [37]).

logic devices, e.g. the racetrack memory proposed by Parkin et al. [19], where DWs can be displaced by the application of electrical currents [92, 93] or external fields [89, 40]. It is still under discussion whether a phenomenon similar to the Walker breakdown, leading to the instability and the destruction of a DW, exists in magnetic nanotubes. Analytic models by Landeros and coworkers predict a decrease in velocity after a certain threshold [89, 93, 94], while simulations by Yan et al. [40, 95] claim the suppression of the breakdown for certain geometric dimensions. They predicted a DW phase velocity regime such as to generate a Cherenkov-like spin wave emission [40], represented by a soliton strongly coupled with the DW. Furthermore it was observed that the left-right symmetry of the domain wall dynamics was broken [94, 90], resulting in different mobility for vortex walls with different rotational sense. This peculiarity might be relevant for technological applications in spintronics.

Due to the relevance of engineering the spin-wave dispersion for magnonics, research efforts have increasingly focused on the implications that curvatures, flux-closure magnetic states and their chiralities can have on spin dynamic effects. With their three geometric parameters, NTs offer the possibility to tailor and manipulate spin-wave confinement in a multiple-connected 3D configuration. The dispersion relation of axially propagating spin waves in a hollow magnetic tube was presented for the special case of a magnetic NT with negligible thickness by Leblond and Veerakumar, in 2004 [69]. Nguyen and Cottam reported results for a nanotube composed of hexagonally ordered spins [96]. They found dispersion relations for axial field comprising minima at finite wave vectors and evidenced mode-repulsion and mixing. Later, the same authors extended their numerical calculations to include dipole-exchange spin waves and radial confinement [97]. The spin wave spectra of infinitely long, cylindrical nanotubes

with or without vortex wall were calculated by Gonzalez et al. [98] by minimization of the corresponding energy functional and the linearization of the Landau-Lifshitz-Gilbert equation (Eq 2.18, Chapter 2, Section 2.3.1). They found that the spin wave dispersion is modified by the presence of the domain wall.

A model to interpret the spin waves resonances found in Rolled-Up Permalloy nanotubes (RUPTs) [72] with micrometer diameters was developed by Balhorn et al. [70]. The large diameters of the tubes cause the curvature to only influence the dipolar exchange regime of the spin waves. It is thus possible, to describe the spin wave confinement using a modified thin-film formalism [68] imposing periodic boundary conditions on the wave. More recently the focus on the spin dynamic phenomena in NTs moved to the study of small diameters, where the influence of the curvature is more significant. In the works of Otalora et al., the curvature-induced magnetochiral effects originating from the dipole-dipole interaction generate non-reciprocal spin-wave dispersion [41, 99], a feature that might be relevant for magnon-based applications. Further details on the most important models are given in Chapter 2, Section 2.3.3.

In the next paragraph, an overview on the current status of the experimental works reported in the literature is given.

### 3.2 Reported experiments on ferromagnetic nanotubes

The predictions on the equilibrium configurations and reversal modes of ferromagnetic nanotubes (FNTs) date back to more than a decade ago. Direct experimental evidence of their magnetic behavior has emerged only recently. This is partly attributed to the sensitivity of conventional magnetometry techniques, not always sufficient to measure the magnetic moment of individual magnetic nanostructures [43]. Therefore, measurements concerned only large arrays of nanomagnets for a long time [83, 84, 100, 101, 22, 102, 103]. In such ensembles they might have slightly different sizes, shapes or might interact with each other, depending on the spacing among them [83, 104]. These aspects made accurate characterization of FNTs difficult. The turning point was progress in nanofabrication and relevant measurement techniques, that made measuring of individual specimens possible. This provided a better understanding on magnetization states and reversal of individual FNTs. On the one hand, this has led to the exploration of smaller and smaller FNTs, on the other hand it has also shed light on how magnetization configurations of FNTs can be susceptible to roughness and exterior imperfections in the real samples.

The most recent experimental works on individual ferromagnetic NTs addressed magnetic states and reversal mechanisms explored by magnetoresistance (MR) measurements [25, 88, 105], anomalous Nernst effect (ANE) [105], cantilever magnetometry [106] and SQUID-on-tip sensing [107]. Direct evidence of flux closure configurations in ferromagnetic NTs was provided by X-ray magnetic imaging [108, 44, 107]. Measurements of MR monitored the change in electrical resistance of a sample as a function of the applied external magnetic field. Through the anisotropic magnetoresistance (AMR) effect, the measured resistance  $R$  can be related to

the magnetization orientation in the sample as a function of the field intensity and orientation. Early MR measurements of individual FNTs were carried out on core-shell systems consisting of hexagonal GaAs NWs cores and MnAs [109] or GaMnAs [110] shells grown by molecular beam epitaxy (MBE). The results of their MR measurements showed a magnetization behavior dominated by the magnetocrystalline anisotropy of the material, rather than the shape anisotropy. This motivated further studies on FNTs whose magnetic shells were deposited with techniques other than MBE, to favor the formation of polycrystalline materials with isotropic magnetic properties. MR measurements of ALD-grown Ni NTs on hexagonal GaAs NWs reported by Rüffer et al. [25] showed results compatible with a vortex-like magnetization state close to remanence. This result was possible thanks to the absence of magnetocrystalline anisotropy. Nonetheless the shell roughness, attributed to ALD processing limitations existing at that time, did not allow to realizing the predicted configurations of ideal NTs. Similar investigations have been conducted on CoFeB and permalloy ( $\text{Ni}_{80}\text{Fe}_{20}$ ) NTs prepared by magnetron sputtering and evaporation, respectively. A study of Baumgaertl et al. [105], combining AMR and ANE showed a preferential axial alignment and a reversal mediated by a vortex domain wall for permalloy NTs. Their data suggested a possible growth induced anisotropy in CoFeB samples. Zimmerman et al. [111] showed an MR signal consistent with the presence of a remanent vortex state in permalloy NTs grown by MBE. In this case, an appreciable growth anisotropy was measured but, interestingly, it stabilized a global vortex state as imaged by XMCD. Further developments were possible thanks to high-sensitive torque magnetometry techniques, like dynamic cantilever magnetometry (DCM), allowing to measure the hysteresis with different field orientations. A first application of DCM [106] on ALD-grown Ni NTs of Ref. [25] confirmed the presence of a multi-domain state and an onion state at remanence, confirming the previously reported MR observations. The saturation magnetization  $M_s$  of the Ni was found to be comparable within the experimental error to the one of bulk crystalline Ni. DCM has been employed also combined with a nano-meter scale superconducting quantum interference device (nanoSQUID), which was used to measure the magnetic flux originating from one end of an FNT [88, 112, 113]. The simultaneous measurement of the NT volume magnetization by the ultrasoft Si cantilevers of the DCM and the stray field of one of its ends by nanoSQUID, compared with micromagnetic simulations, allowed to accurately study the reverse process of individual the NT. By using these techniques [88] it emerged that, in the ALD Ni-grown NTs of Ref. [25] the reversal mechanism did not start from the NT end as predicted and this was again attributed to the Ni shell roughness, introducing defect sites where the magnetization was locally pinned. A reversal mechanism starting from the ends, was found by Buchter et al. [113] for the evaporated permalloy NTs originally presented in Ref. [105], exhibiting a smaller roughness. DCM/nanoSQUID studies, combined with numerical simulations based on the Landau-Lifshitz-Gilbert formalism, were performed on CoFeB nanotubes with [44] and without flat NT edges [114]. Optimized edges were achieved by focusing ion beam (FIB) etching. These studies highlighted the importance of the shape and orientation of the edges in a real FNT and their influence on the mechanism of magnetization reversal. In the earlier theories the assumption of flat NTs ends was assumed. The authors clearly saw the signatures of vortex end-domain nucleation in individual FNTs with well-defined

flat ends, absent in measurements on CoFeB FNTs with slanted ends. Imperfect ends were found to modify the nucleation fields and the reversal mechanism. For a shorter NT with low aspect ratio and flat ends, a remanent global vortex state was experimentally confirmed [44], in agreement with theoretical predictions. These results were substantiated by direct imaging of FNT magnetization configurations with soft X-rays. Here, magnetic imaging was achieved by collecting the difference in resonant absorption of  $\sigma^+$  and  $\sigma^-$  circularly polarized X-rays, due to X-ray magnetic circular dichroism (XMCD). The difference is proportional with the magnetic moment in the interaction volume projected along the beam propagation direction [43]. The imaging was achieved by photoemission electron microscopy (XPEEM). XPEEM imaging were performed on CoFeB and NiFe samples with different lengths and aspect ratios [44], where the edges were engineered with FIB. A mixed state was found as the equilibrium ground state of long FNTs, while for short FNTs both a global vortex state and a state with two vortices with opposite chirality separated by a Néel-type DW were found at remanence. Simulations suggested that this discrepancy with the predicted configuration was attributable to imperfections in the real samples. Still, these results confirmed the possibility of programming the equilibrium magnetic configuration of real FNTs by changing their geometry. Experiments on the controlled displacement of DWs and on the measurement of spin waves in FNTs are scarce in the literature. Pionering spin dynamic studies concerned either large sets of samples [85] or tubes with large diameters [71, 115]. Collective SW modes were studied in arrays of ferromagnetic rings excited by radio-frequency (rf) magnetic fields using Brillouin light scattering (BLS)[85] and broad-band microwave spectroscopy [116]. In individual rolled-up magnetic micro-tubes quantized azimuthal SW modes were resolved [71, 115]. Promising preliminary results on spin dynamic measurements of FNTs with high aspect ratios and diameters in the order of hundreds of nanometers were reported in PhD theses [45, 117] and motivated further investigations. The pionering work presented by D. Ruffer [45] was based on the excitation of spin waves in contacted NTs by microwave antennas and their detection by voltages due to spin rectification. Quantized modes could be resolved. However, a quantitative analysis remained an open task. In the PhD thesis of Zimmerman et al.[117, 42] the experimental observation of spin waves propagation in an individual permalloy nanotube hosting a global vortex state was measured by time-resolved scanning transmission X-ray microscopy. Their results suggest asymmetrical spin-wave transport. Both theses highlight that hexagonal nanotubes have a complex spin wave dispersion, which differs from the one expected for cylindrical nanotubes due to modes localised to the flat facets or to the extremely curved regions between the facets. Hexagonal nanotubes thereby open new possibilities when integrated into three-dimensional magnonic devices.



### **3.3 Atomic layer deposition of Ni and NiFe three-dimensional coatings**

#### **Metal ALD**

In metallic ALD processes, a successful combination of precursors and co-reactants in terms of reciprocal reactivity and with the deposition surface is not always a guarantee of optimized conformality in the thin films. There is a number of technical drawbacks for which attempts to develop ALD processes for elemental metal films have met only mixed success if compared to ALD processes for oxide films [31, 118, 35]. Commercially available metallorganic precursors employed in chemical vapor deposition (CVD) processes are not always suitable for ALD ones. Some precursors can lose stability under operating conditions. Many others host metals in a non-zero oxidation state with consequent difficulty to reduce the metal cations to their metallic state [35]. Ultimately, it can happen that during the deposition, the metal atoms coalesce into agglomerates [35]. The phenomenon is associated to the wetting angle of metals on different substrates [119], which is found to increase with the interface energy. The latter, in turn, scales with the lattice mismatch of the substrate and growing film [119, 120]. Even with optimized process parameters, these drawbacks can lead to the incorporation of organic precursor residues in the final thin films or compromise their roughness and conformality onto complex three-dimensional surfaces.

#### **Nickel ALD**

Due to the importance that thin nickel films possess in areas such as magnetic random access memory, contact materials, catalysis and metal–insulator–metal devices, a large number of studies can be found in literature concerning the deposition of elemental nickel Ni via ALD. In Table 3.1 we summarize the explored precursor/co-reactant(s) combinations reported so far, to our knowledge, for the deposition of ALD Ni. The table was drawn up on the basis of the review reported in ref. [121] and the information collected in the open access database of "Atomic Limits" (<https://www.atomiclimits.com/alddatabase/>). Since the Ni ALD technology is still in the exploratory phase, many of these works do not go beyond a feasibility study. Often the functional properties of the deposited Ni and its morphology on a 3D nanostructured surface are not reported. Magnetic properties are not reported in most cases. Therefore we used the electrical resistivity as one of the criteria to select possible ALD Ni processes to explore in our chamber for magnetic and spintronic functionalities. When this thesis project started in 2016 we identified two potential routes in literature to investigate: a single-step process involving ammonia as reducing reagent [32], a double-step process in which the deposition of Ni occurs through an intermediate deposition of NiO and subsequent reduction by hydrogen [122, 22]. The precursor nickelocene is suitable for both routes, quickly available on the market and easy to handle as purchased.

Recently, further processes have been developed [34, 132]. They were optimized either on Ru and Pt [34], which we do not consider here as substrates or so far had a larger specific resistivity

### Chapter 3. Literature review

Table 3.1 – Summary of Ni ALD processes.

Ni precursor	Reactant(s)	Process	Dep. T (°C)	GPC (Å/cycle)	$\rho$ ( $\mu\Omega\text{cm}$ )	Ref.
Publication year:	2002 - 2016					
Ni(dmamb) <sub>2</sub>	H <sub>2</sub>	ALD	220	1.25	NR	[123]
Ni(dmamb) <sub>2</sub>	NH <sub>3</sub>	PEALD	250	2.0	43	[124]
Ni(dmamb) <sub>2</sub>	H <sub>2</sub>	PEALD	250	0.8	75	[124]
Ni(dmamb) <sub>2</sub>	NH <sub>3</sub>	ALD	300	0.64	25	[125]
Ni(hfip) <sub>2</sub>	H <sub>2</sub>	ALD	220	1.25	NR	[126]
Ni(iPrMeCOCNtBu) <sub>2</sub>	BH <sub>3</sub> (NHMe <sub>2</sub> )	ALD	180	0.09	NR	[127]
Ni(acac) <sub>2</sub>	CH <sub>3</sub> OH	ALD	300	0.07	27	[128]
Ni(AMD(iPr) <sub>2</sub> ) <sub>2</sub>	H <sub>2</sub>	ALD	250	0.04	NR	[31]
NiCp <sub>2</sub>	H <sub>2</sub> O +H <sub>2</sub> plasma	PEALD(NiO) + reduction	165	0.19	25-30	[122, 22]
NiCp <sub>2</sub>	NH <sub>3</sub>	PEALD +annealing	280	0.2	71 11.8(ann.)	[32]
NiCp <sub>2</sub>	NH <sub>3</sub>	hot-wire ALD	250	0.63	27.9	[129]
Publication year:	2017 - 2019					
Ni(EtCP) <sub>2</sub>	N <sub>2</sub> / H <sub>2</sub>	PEALD	360	0.28	200	[130]
Ni(dpda) <sub>2</sub>	NH <sub>3</sub>	PEALD	200	2.1	87.6	[131]
Ni(tBu <sub>2</sub> DAD) <sub>2</sub>	tBuNH <sub>2</sub>	ALD	180	0.60	22.1	[34]
Ni(acac) <sub>2</sub> (tmeda)	N <sub>2</sub> H <sub>4</sub>	ALD	260	2.1	18.1	[132]
Ni(Chex)(Cp)	NH <sub>3</sub>	ALD	380	1.1	~100 44.9(ann.)	[121]

"Dep. T" = deposition temperature, "GPC"=growth per cycle, " $\rho$ " = resistivity achieved on a planar thin film , "ann." = annealed, "N.R." = not reported.

than the one achieved in this thesis [132]. In Chapter 5, Section 5.2, we will report how we improved the process of Ref. [122] to achieve beyond state-of-the art functional properties in case of ALD grown Ni films.

#### Nickel-Iron ALD

The Ni-Fe alloy with stoichiometry Ni<sub>80</sub>Fe<sub>20</sub> (red arrow in Figure 3.3 a) and crystalline FCC intermetallic phase with ordered superlattice  $L1_2$  FeNi<sub>3</sub> (Figure 3.3 b) , known as permalloy, is technologically relevant for many aspects. Among them there are the high permeability, low coercivity, near zero magnetostriction [62], significant anisotropic magnetoresistance (AMR) and its crucial role in nanomagnetism and magnonics [18]. To the best of our knowledge, the deposition of Ni-Fe metal alloys by ALD has been reported only in two publications, where cycles of nickel oxide and iron oxide were combined with a thermal [46] or plasma [66] reduction process. Nickelocene and ferrocene were chosen as metallorganic precursors, ozone as oxidant agent and hydrogen as reduction gas. In these works [46, 66] magnetic ALD

### 3.3. Atomic layer deposition of Ni and NiFe three-dimensional coatings

Ni-Fe thin films with stoichiometry close to  $\text{Ni}_{80}\text{Fe}_{20}$  were achieved. Huber et al. reported an effective magnetization of  $620 \pm 50$  kA/m (literature value for Py: 795 kA/m, 1 T) and a damping of  $0.03 \pm 0.01$  (literature value for Py: 0.008). These values, already promising, were however achieved at the expense of film conformity. In the work of Espejo et al. [46], the presence of holes in the magnetic layers is reported, with an hole area fraction of about 10% to 20%. In this sense, an optimized process for permalloy that can be deposited on high aspect ratio nanostructured surfaces, for example vertical nanowires, has not yet been reported. We here list (Tab. 3.2) a small selection of Fe precursors that, based only on the ALD deposition temperatures, were identified as comparable to the Ni processes highlighted in the previous section. Processes that are only possible by means of a catalytic metal substrate were excluded. It should be noted that, among the selected ones in Tab. 3.2, only the process of Ref. [31] led to metallic Fe deposition. In this thesis a Ni-Fe ALD process was developed that exploits nickelocene ( $\text{NiCp}_2$ ) and iron (III) tert-butoxide ( $\text{Fe}_2(\text{OtBu})_6$ ) as metallorganic precursors for Ni and Fe, based on their common reactivity with  $\text{H}_2\text{O}$  at compatible deposition temperatures. The process will be discussed in Chapter 6, Section 6.1.

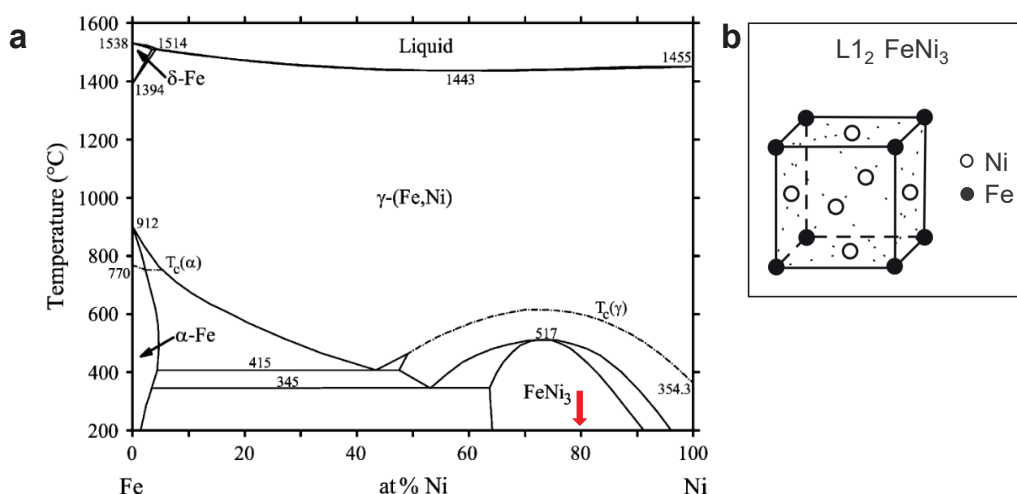


Figure 3.3 – (a) Ni - Fe phase diagram. Copyright: Cacciamani et al. [133]. (b) Intermetallic  $L1_2$   $\text{FeNi}_3$  phase.

Table 3.2 – Selection of Fe precursors.

Fe precursor	Reactant	Deposition T (°C)	Ref.
$\text{FeCp}_2$	$\text{O}_3$	200	[46, 134, 83, 66]
$\text{Fe}(\text{thd})_3$	$\text{O}_3$	186	[135]
$\text{Fe}_2(\text{OtBu})_6$	$\text{H}_2\text{O}$	140 - 180	[101, 83]
$\text{Fe}(\text{tBuAMD})_2$	$\text{H}_2\text{O}$	150	[136]
$\text{Fe}(\text{tBuAMD})_2$	$\text{H}_2$	250	[31]



## 4 Methods

This chapter intends to provide an essential description of the techniques used both for the fabrication of ferromagnetic nanotubes and for the characterization of their static and dynamic magnetization properties. Atomic layer deposition (ALD), the technique chosen for the deposition of ferromagnetic materials, is illustrated in section 4.1. A description of the general principles of operation of ALD, the specific configuration used in this thesis and its application for the fabrication of ferromagnetic nanotubes are given. It follows a description of the measurement techniques employed (section 4.2): magnetoresistance measurements of thin films and nanotubes; broadband spin wave spectroscopy of thin films and inelastic (Brillouin) light scattering (BLS) for the study of dynamic magnetization in nanotubes. The ALD deposition chamber was located at the Center of MicroNanoTechnology (CMI) at EPFL, while the setups described in section 4.2 were available on-site in the laboratories of LMGN.

### 4.1 Atomic layer deposition

Atomic layer deposition (ALD) is a chemical thin film deposition technique that can enable film thickness control on the atomic scale and conformality on 3D (nano)structures [118, 28, 137]. The peculiarity of ALD is that it is a surface-controlled deposition technique based on repeated, self-terminating gas–solid reactions [138, 28, 27]. Historically, the technique has been developed in two independent discoveries under different names: molecular layering (ML) since the 1960s in the Soviet Union and atomic layer epitaxy (ALE) since 1974 in Finland [139]. The two development paths were motivated by different reasons. In the 1960s, Stanislav Koltsov, together with Valentin Aleskovsky and colleagues of the Leningrad Technological Institute (LTI) in the Soviet Union, were involved in fundamental chemistry studies exploring the interaction of surface functional groups on silica gel with chlorides of different elements [140, 141]. The studies were not originally intended to create a thin film synthesis method to solve a particular practical problem, but a number of different synthesis processes came along to confirm experimentally the hypothesis of surface chemical transformation of the solids studied. The studies extended to different molecules and substrates and the scope of the ML research expanded from fundamental chemistry to applied research [140, 142]. The

principles of the modern ALD were developed and summarized in the doctoral thesis work of Koltsov in 1971 [140]. Different was the impulse that led to the spread of the ALE technique in Finland, initially aimed at the growth of high-quality polycrystalline ZnS thin films for electroluminescent (EL) display panels, at Instrumentarium Oy [143]. The technique was developed by the company research group led by the physicist Tuomo Suntola. The patent of Dr. Suntola [144], filed in 1974, which became public in 1977, presented ALE as an advanced thin-film technology, attracting international attention from researchers around the globe. The name "atomic layer deposition" was apparently proposed for the first time by Markku Leskelä (professor at the University of Helsinki) during the 1st international conference on atomic layer epitaxy in 1990 ( "ALE-1" Espoo, Finland) [143]. This name, suggested in analogy to chemical vapor deposition (CVD), took about a decade to get general acceptance [145]. To date, this technology is both the industrial standard for high- $\kappa$  films in the semiconductor industry, such as alumina, and the subject of basic research for numerous combinations of substrate and coating materials. For instance, since 2000, the 90-nm node DRAM and the 45-nm CMOS technology [146] were reported to use ALD for high- $\kappa$  thin films by Micron and Intel Corporation, respectively.

### 4.1.1 Working principle

Atomic layer deposition (ALD) is a vapor phase technique. The process of ALD involves the surface of a substrate being exposed to alternating gases, whose pulses do not overlap but instead are introduced sequentially [118, 28, 137]. The gaseous molecules employed in the ALD processes are often referred to as precursors and reactants (or co-reactants) or, equally, as reactant A, B, etc.. (or 1, 2 etc..), depending on the order of injection into the chamber. In this thesis, the organometallic species bearing the metal to be deposited are indicated as (metal) precursors and the gaseous species aimed at completing the decomposition of the precursor are indicated as reactants or co-reactants. Each ALD cycle consists at least of two half-cycles (but can be more complex), containing a precursor dose step and a co-reactant exposure step, separated by a purge step. In each alternate pulse, the precursor (co-reactant) molecules react with the surface in a self-limiting way. This ensures that the reaction stops once all of the reactive sites on the substrate have been used. The thickness of the thin film can be controlled performing the ALD cycle multiple times.

The surface reaction kinetics of ALD is often very complex and strongly dependent on the specific ALD process. For many processes, the reaction mechanism during an ALD cycle is not necessarily known [147]. However, the reaction chemistry can be simplified by using the irreversible Langmuir surface kinetics [148, 149]. The model, which represents an approximation, qualitatively describes many ALD existing processes. The sticking probability is introduced to describe the probability of a precursor or reactant molecule to react upon collision with the surface and contribute to the film growth [150]. It is described as:

$$s = s_0(1 - \theta), \quad (4.1)$$

with  $s_0$  being the initial sticking coefficient with a bare surface and  $\theta$  being the fraction of covered sites. The expression implies that the surface reactivity gradually decreases with the increase in the coverage and eventually becomes zero. This simple model reflects the self-limiting nature of the surface reactions during ALD, while the reaction kinetics (fast/slow) can be implemented via the initial sticking coefficient  $s_0$  (high/low values). If in the first place we consider a reversible Langmuir adsorption, the first reaction of an ALD cycle can be represented by



with  $A_g$  being the gaseous precursor,  $*$  a vacant surface site, and  $A^*$  the chemisorbed precursor A [148]. The adsorption rate  $r_{ads}$  is expressed by the product of the adsorption rate constant  $k_{ads}$ , the partial pressure of the precursor A,  $P_A$ , and the fraction of uncovered surface sites, giving the equation [148]:

$$r_{ads} = k_{ads} P_A (1 - \theta), \quad (4.3)$$

While the desorption rate  $r_{des}$  is equal to the fraction of covered sites times the desorption rate constant:

$$r_{des} = k_{des} \theta \quad (4.4)$$

The surface coverage rate  $\frac{d\theta}{dt}$  is obtained by the difference [148]:

$$\frac{d\theta}{dt} = r_{ads} - r_{des} \quad (4.5)$$

At equilibrium,  $\frac{d\theta}{dt}$  is zero. Considering that in a typical ALD process the gaseous byproducts are continuously pumped out, the reverse reactions become unlikely. Thereby, the term  $r_{des}$  in Eq. (4.5) can be ignored and the assumption of irreversibility is justified. The second reaction, with the gaseous reactant  $B_g$ , often is not modeled separately. It is only considered that the surface left behind by the exposure to reactant A, saturated with  $\theta \approx 1$ , is reactive again. The second step reaction can be described as



where  $AB^*$  is an average reaction product [148]. Another approximation used to describe ALD processes is that the total number of adsorption sites for the Langmuir adsorption model is obtained from the number of metal atoms deposited per cycle and thus from the growth per cycle (GPC). The assumptions described in this paragraph are known to be oversimplified, but they describe well the experimental observations. Experimentally speaking, a self-limiting growth is ensured by choosing a sufficiently long precursor (co-reactant) exposure time to ensure enough adsorption density and a sufficiently long purge time between different steps,

to avoid parasitic growth. The correct growth is normally assessed by determining the GPC as a function of precursors (reactants) dosing, purge times and chamber temperature. Ideally, a regime where the GPC reaches a plateau as a function of these parameters is searched. However, the constant GPC within a range of temperatures is not a necessity for an ALD process.

The 3D uniformity of a film is often discussed either in terms of step coverage or conformality (sometimes conformity) [148, 151]. Typically, step coverage (SC) is defined as the ratio of the film thickness at the bottom (or at the side wall) of a feature to the film thickness at the top of the feature and is typically expressed as percentage [148].

### Thermal ALD

In thermal ALD, the activation of the chemical reactions is achieved through thermal energy alone, by appropriately choosing the temperature of the chamber. The process generally requires relatively high temperatures (typically 150 – 350°C). Thermal ALD process often consist of four characteristic steps, which are shown in Figure 4.1 for the prototypical trimethylaluminum ( $\text{Al}(\text{CH}_3)_3$ , TMA)/ $\text{H}_2\text{O}$  process [148]:

Step 1 (Figure 4.1 a): The metallorganic precursor (TMA) is pulsed into the chamber and reacts in a self-limiting way with the available functional groups on the OH-terminated surface.

Step 2 (Figure 4.1 b): The excess of precursor (TMA) and the gaseous by-products ( $\text{CH}_4$ ) are purged or pumped away.

Step 3 (Figure 4.1 c): The co-reactant ( $\text{H}_2\text{O}$ ) is pulsed into the chamber and reacts in a self-terminating way with the adsorbed species on the surface.

Step 3 (Figure 4.1 d): The excess of co-reactant ( $\text{H}_2\text{O}$ ) and the gaseous by-products ( $\text{CH}_4$ ) are purged or pumped away.

### Plasma ALD

Chemical reactions can be enhanced by activating the precursors in plasma-enhanced ALD (PEALD) [152], radical-enhanced ALD, photo-induced ALD and ozone-based ALD processes. This paragraph will focus in particular on PEALD, being an operational mode that has been employed for the research work presented in this thesis. PEALD is an energy-enhanced ALD method in which a plasma is employed during one step of the cyclic deposition process. A plasma defines a quasi-neutral collection of free, charged particles, among other gas-phase species. This so-called quasi-neutrality means that at macroscopic length scales (typically  $> 1$  mm) the electron density is equal to the ion density, under the assumption that negative ions can be neglected. Compared with the conventional thermally-driven ALD method, the use of plasma species as reactants allows for several advantages. For example, as the result of the high reactivity provided by the plasma species, high yield of reactions can be achieved [152, 153]. Less thermal energy is required at the substrate to drive the ALD surface chemistry, hence lower substrate temperatures can be exploited than for thermal ALD. Cases exist in which the plasma species create a higher density of reactive surface sites. Consequently,



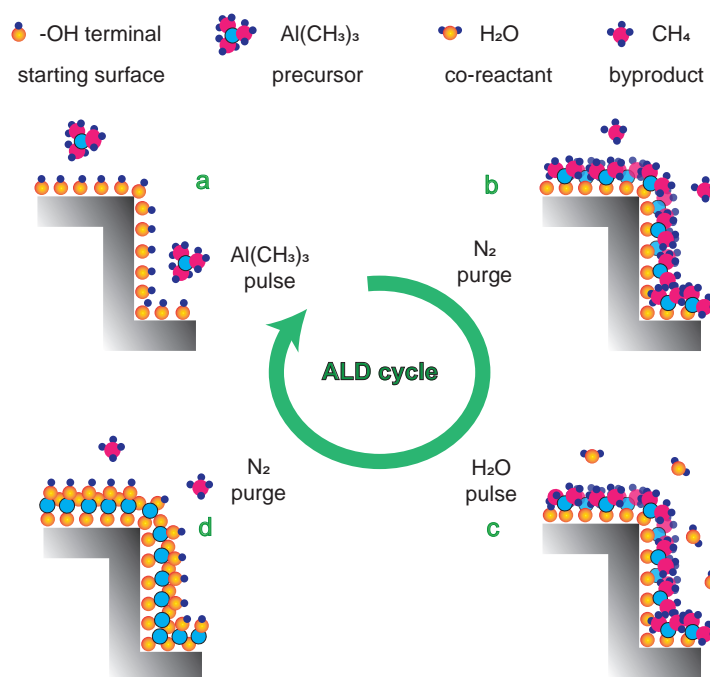


Figure 4.1 – Proposed mechanism for the  $\text{Al}_2\text{O}_3$  deposited by ALD. The ALD cycle is composed of: (a) the trimethylaluminum (TMA) pulse and reaction with the surface, (b) the purge of the chemical byproducts, (c) the water vapor  $\text{H}_2\text{O}$  pulse and reaction with the surface and (d) the purge of the chemical by products to prepare the surface for the subsequent ALD cycle.

this can lead to higher growth per cycle values [152]. The availability of a plasma source on an ALD reactor gives, in general, more processing versatility as it allows for several other in situ treatments of the starting substrate surface and deposited films. Plasmas can be used as co-reactants but also for substrate pre-treatments, post-deposition treatments and in-cycle conditioning treatments [153]. Together with the discussed benefits, there are also challenges provided with the use of the plasma species. The whole ALD process and its reaction mechanisms become more complex. Additional process variables have to be considered to fine tune the stoichiometry and composition of the films. These include the operating pressure to ignite the plasma, the plasma power, the plasma exposure time, the admixing of additional gases into the plasma and the biasing voltage [152]. Furthermore, the reactant molecules that collide with the surface can undergo recombination processes. For example, an H radical can recombine with an adsorbed H atom and form molecular  $\text{H}_2$  that leaves the surface. The probability that a species recombines during a collision with the surface is usually defined as the recombination probability  $r$  [151, 148, 153]. Although it depends on the process parameters, the recombined species can often no longer contribute to film growth, e.g., when the surface is only reactive towards H radicals and not towards molecular  $\text{H}_2$ . This might result into limited thin film conformality, especially in high aspect ratio structures where the chances of radicals recombination via surface collisions are higher [148].

## 4.1.2 Beneq TFS200 ALD system

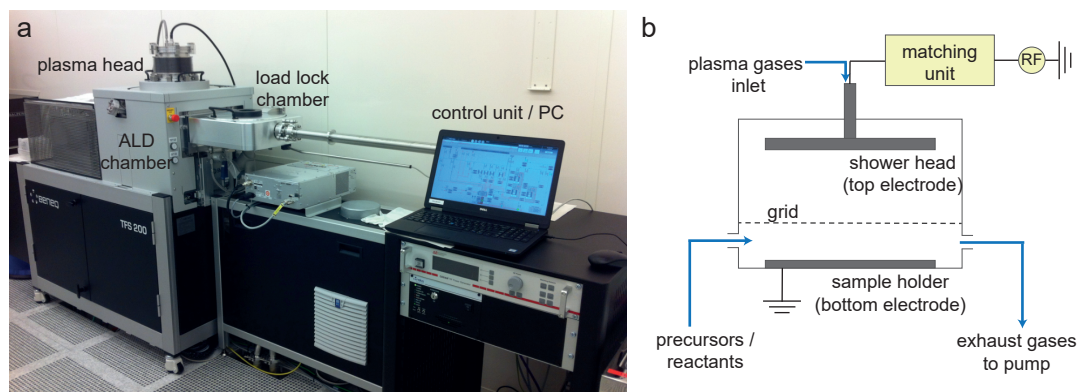


Figure 4.2 – (a) Picture of the Beneq TFS200 ALD system employed in this thesis, located at the Center of MicroNanoTechnology (CMI), EPFL. (b) Sketch of the plasma shower head integration in the chamber.

The Center of MicroNanoTechnology (CMI) at EPFL is equipped with a Beneq ALD system, model TFS200 (Figure 4.2 a). It is a hot-wall reactor chamber, provided with a plasma shower head, that can be operated both for thermal ALD and PEALD. During the deposition process, the machine operates under an adjustable constant flow of carrier gas, which is continuously pumped away. Several equipment configurations exist for assisting an ALD process by means of a plasma activation [153]. The machine model here discussed can be classified as a direct plasma ALD reactor [152]. Its operating principle is sketched in Figure 4.2 b. A capacitively-coupled plasma is generated by a radio frequency (RF) source operated at 13.56 MHz between two parallel electrodes in a so-called RF parallel plate or RF diode reactor. One electrode is powered while the other one, hosting the sample holder is grounded. This ALD reactor configuration is referred to as "direct plasma ALD" because the substrate to be coated is directly positioned at one of the electrodes which contribute to the plasma generation. In the Beneq TFS200 model, a grid can be placed between the two electrodes creating a so called triode configuration [152]. This enables a partial confinement of the plasma between the RF-driven electrode and the grid such that the exposure of the deposition surface to the plasma is mitigated. In essence, this leads to less substrate damage but also to a lower ion energy and flux towards the deposition surface and to a reduced radical density. In our machine, the gases to be activated in the plasma state are introduced through a shower head placed in the powered electrode, while the precursor vapors, the co-reactant and the carrier gases are introduced from the side of the sample holder (bottom electrode). Based on this distinction, we speak of plasma or thermal gas lines. The equipment is furnished also with an ozone generator, which was employed for nickel and iron oxides depositions, not reported in this thesis. The machine has been configured such that the plasma gas lines are the ones of  $\text{H}_2$  and  $\text{N}_2$ , while the thermal gas lines are  $\text{H}_2$ ,  $\text{N}_2$ ,  $\text{NH}_3$  and  $\text{O}_2$ . The metallorganic precursors employed in this thesis are various. We will report in particular the results achieved by exploiting nickelocene  $\text{NiCp}_2$  (Strem Chemicals, 99.9 % purity) to deposit Ni and iron(III) tert-butoxide  $\text{Fe}_2(\text{t-BuO})_6$ .

(Alpha-Chemistry - US, 99.9 % purity) for the Fe depositions. As these compounds are solid at room temperature, they are stored in stainless steel containers that can be heated, by means of an electric resistance, at temperatures sufficient to exploit their vapor pressure during the ALD process. Precursors and co-reactants with sufficient vapor pressure at room temperature, like TMA and  $\text{H}_2\text{O}$ , are stored at room temperature in a separate compartment.

#### 4.1.3 Fabrication of ferromagnetic nanotubes

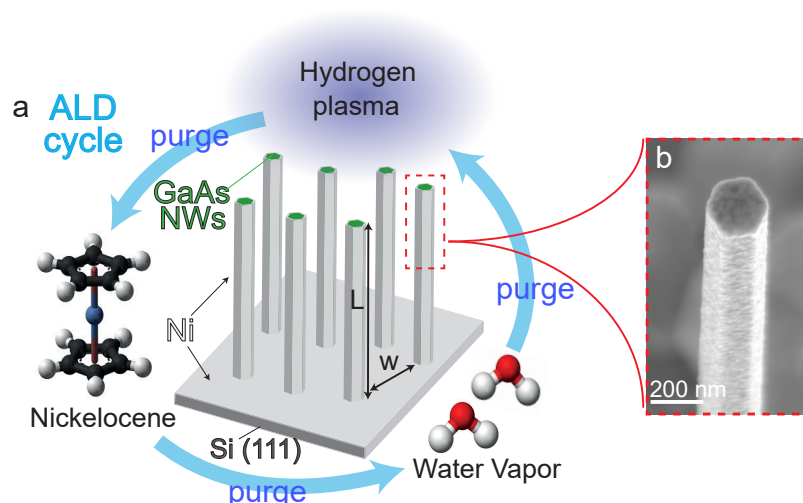


Figure 4.3 – (a) Sketch of the Si(111) substrate hosting self-assembled standing GaAs NWs. The NWs are used as template for ALD-grown ferromagnetic shells. Here we illustrate a process employed for Ni NTs. (b) SEM micrograph of an obtained NT. The polycrystalline texture of the Ni shell is visible.

For the growth of large ensembles of nominally identical magnetic nanotubes, the use of template-assisted methods has been demonstrated to be a highly efficient and low-cost fabrication procedure. The templates are often nanoporous alumina membranes [154, 155, 22] or polycarbonate membranes [156]. An inverse approach is to apply the magnetic coating onto arrays of self-assembled (semiconductor) nanowires. This strategy has been followed in previous works by either employing epitaxial growth for the entire core/ferromagnetic-shell system [157, 158], or using PVD [105, 26] or ALD [106, 26, 25] to coat polycrystalline ferromagnetic shells onto semiconductor nanowires. In this thesis the latter strategy is followed, where ALD is employed for the deposition of Ni and  $\text{Ni}_{80}\text{Fe}_{20}$  ferromagnetic shells on self-assembled vertically standing GaAs NWs used as templates. The choice of ALD is motivated by the possibility to avoid growth-induced anisotropies and obtain polycrystalline, conformal ferromagnetic shells with isotropic magnetic properties. These characteristics are ideal for the study of shape-dependent static and dynamic magnetic properties of ferromagnetic NTs. The nanowires used for this thesis were grown using the Vapor-Liquid-Solid (VLS) growth mechanism [159]. In a molecular-beam-epitaxy (MBE) system, Gallium (Ga) droplets served as catalysts and nucleation points for subsequent nanowire growth along the preferred (111)B

orientation [160]. Ga and As fluxes were optimally dosed until supersaturation was reached, GaAs precipitated and formed the mono-crystalline GaAs NW in epitaxial relation to the underlying substrate. GaAs NWs employed in this thesis were grown on Si(111) substrates. The synthesis of these nanostructures was executed by group members of the Laboratory of semiconductor materials LMSC, EPFL, and is not the subject of this thesis. Details on the NWs growth process are widely addressed in Refs. [161, 162, 163]. The advantage of using this type of nanostructures as a NT template is to have a rigid support to the magnetic shell which makes it easy to manipulate for the integration of NTs into characterization devices. Furthermore, it allows to obtain millions of nanotubes from a single deposition batch.

The procedure followed in this thesis is to employ the GaAs nanowires still standing on the substrate Si (111) as deposition surface. Throughout the thesis, GaAs NWs with average lengths ranging from  $1.5\ \mu\text{m}$  to  $15\ \mu\text{m}$  and diameters ranging from 70 nm to 250 nm were employed. As shown in Figure 4.3, the nanowires are directly exposed to the precursors and co-reactants. Here, an ALD cycle based on the exposure of the surface to three precursors interspersed with purge steps (represented by the light blue arrows) is shown. The specific ALD processes will be described in the result sections. The ALD cycle is repeated  $n$  times to increase the thickness of the ferromagnetic NT. To electrically isolate the semiconductor core from the metallic shell, we used a spacing layer of a few nanometers of the insulating material alumina. It is routinely deposited via ALD with the process described in Fig. 4.1. It is safe to assume that the diamagnetism of the semiconductor core does not affect the ferromagnetic behavior of the nanotube.

The array of standing GaAs nanowires on a Si (111) substrate represents, in the perspective of an ALD process, a nanostructured three-dimensional surface to be coated uniformly. The aspect ratio of this template can be roughly determined by comparing it with an array of square pillars, as to say dividing the average length of the NWs ( $L$ ) by the average distance between them ( $w$ ) [148]. The conformality of the coating can be assessed by measuring the ferromagnetic shell thickness at different points along the NT length, i.e. determining the ratio of the film thickness at the bottom of a feature to the film thickness at the top of the feature. Alternatively, by calculating the ratio of the film thickness at the side wall to the film thickness at the top. These values are referred as "step coverage" and are typically expressed as a percentage [148].

## 4.2 Measurement techniques

### 4.2.1 Electrical and magnetotransport characterization

Throughout the thesis, DC resistance ( $R$ ) measurements of the ALD-grown nanotubular shells and thin films have been performed. The measurements were carried out at room temperature, in a four-probe configuration to exclude the contributions of cable and contact resistances. Experiments of electrical characterization were performed both with and without an applied magnetic field. We refer to magnetotransport experiments when the change of  $R$  is determined

as a function of the applied external field  $\mu_0 H$ .

### Resistance measurement configurations in nanotubes and thin films

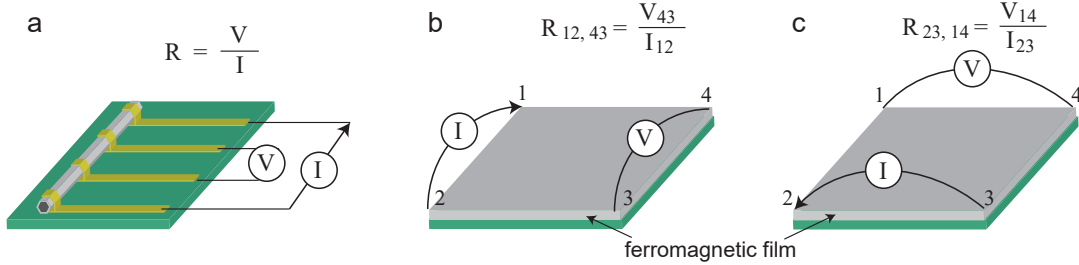


Figure 4.4 – (a) NT integrated with electric leads for the resistance measurement. (b-c) Contact configurations and edge resistance measurements in Van der Pauw configuration for a planar thin film.

Figure 4.4 shows the four-probe measurement configurations used to acquire  $R$  for a NT and a planar thin film. In the case of the NT, the electrical resistance  $R$  is determined by applying a current  $I$  between the two external electrical contacts and measuring the voltage drop  $V$  between the two inner contacts (Fig. 4.4 a). The NTs are suspended from the substrate with a microfabrication procedure described in Section 4.3.1, to have a better control on the thermal gradients. For the thin film, we exploited a Van der Pauw configuration [164], commonly used to determine the sheet resistance  $R_s$  of samples with arbitrary shapes. By applying a current along one edge of the geometry, for example  $I_{12}$ , and measuring the voltage across the opposite edge (in this case,  $V_{43}$ ) the resulting resistance  $R_{12,43}$  (Fig. 4.4 b) is calculated by using Ohm's law as:

$$R_{12,43} = \frac{V_{43}}{I_{12}} \quad (4.7)$$

The sheet resistance  $R_s$  can be determined from two resistance values - one measured along a vertical edge, such as  $R_{12,43}$  (Fig. 4.4 b), and one measured along a horizontal edge, such as  $R_{23,14}$  (Fig. 4.4 c). The sheet resistance is related to these values by the van der Pauw formula:

$$e^{-\pi R_{12,43}/R_s} + e^{-\pi R_{23,14}/R_s} = 1 \quad (4.8)$$

### Instruments

In our probe-station, the injected current  $I$  is controlled by a Keithley 2401 current source and the voltage is detected via a Keithley 2182 nanovoltmeter. The current source and the nanovoltmeter are linked with trigger lines. In order to avoid excessive heating of the nanotube, the applied current is usually kept below a few  $\mu A$ . To minimize the contribution of thermoelectric offset voltages and drifts and maximize the signal-to-noise ratio (SNR) we acquired the voltage with a "three-step delta" mode offered by the Keithley equipment. Voltage measurements are made first at a positive then at a negative test current by alternating the sign of the current as

to obtain the three voltages values  $V_1(+I)$ ,  $V_2(-I)$ ,  $V_3(+I)$ . The current source alternate with a frequency of about 25 Hz. The voltage signal is calculated by:

$$V = \frac{1}{4} [V_1 - 2V_2 + V_3] \quad (4.9)$$

and ideally does not contain voltages which do not depend on the current  $I$ . The probe-station is comprised by two perpendicularly mounted electromagnets, allowing for field application in all in-plane directions. Each of the two field axes is driven by a Kepco bipolar power supply. The power supplies support a smooth zero crossing of their output currents allowing a magnetic field sweep from positive to negative values without intermission. The probe station is located on a stabilized optical table, inside a steel cage to suppress mechanical and electrical noises.

### Anisotropic magnetoresistance

In presence of a varying external in-plane magnetic field, the resistance of a metallic ferromagnet can vary due to the phenomenon of the anisotropic magnetoresistance (AMR). The AMR effect was discovered by William Thomson over 150 years ago [165] and it connects the electrical transport to the magnetization orientation. The effect arises from the simultaneous action of magnetization and spin-orbit interaction and originates from spin-flip scattering from majority spin into the vacant minority spin states at the Fermi energy. The detailed mechanism depends on the material. In most materials, such as the 3d-ferromagnets, the density of vacant states allowing for scattering is larger in the direction of the magnetization than transverse to it and thus a higher resistance is observed for a current density  $\mathbf{J} // \mathbf{M}$ . In polycrystalline ferromagnetic materials, the AMR dependency on the angle  $\theta$  between the magnetization and current direction is described by the equation:

$$\rho(\theta) = \rho_{\perp} + (\rho_{\parallel} - \rho_{\perp}) \cos^2 \theta \quad (4.10)$$

where  $\rho$  is the longitudinal resistivity of the film and  $\rho_{\parallel}$  and  $\rho_{\perp}$  are the resistivities for  $\theta = 0^\circ$  and  $90^\circ$ , respectively. The efficiency of the effect is quantified by the AMR ratio, defined by:

$$AMR = \frac{\rho_{\parallel} - \rho_{\perp}}{\rho_{\perp}} \quad (4.11)$$

In this thesis, the AMR effect has been used to investigate the magnetization orientation inside the NT structures [25], as well as to quantify the AMR ratio in NTs and thin films to assess their quality and functionality for sensor applications [26]. The AMR of a NT and a thin film can be assessed by measuring the resistance while applying a magnetic field in different directions. For NTs, we defined the angle  $\theta$  of the external field  $\mu_0 H$  as sketched in Figure 4.5. To measure the AMR in a planar thin film, we first measure the  $R$  dependency on the field direction for the configurations sketched in Fig. 4.4 b and c ( $R_{12,43}(\theta)$  and  $R_{23,14}(\theta)$ , respectively). We then

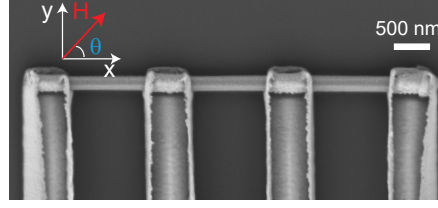


Figure 4.5 – Definition of the in-plane field orientation with respect to the NT axis.

applied the Van der Pauw condition (Eq. 4.8) to obtain the angular dependency of the film sheet resistance  $R_s(\theta)$  [166]. The angle  $\theta$  was defined along one of the two edges of the squared sample.

#### 4.2.2 Broadband Spectroscopy

In this thesis the ferromagnetic resonance (FMR) of ALD-prepared planar thin films introduced in Chap. 2, was measured by broadband spectroscopy using a measurement method where  $\mathbf{h}_{rf}$  is locally applied by a coplanar waveguide (CPW) and microwave absorption is measured by a vector network analyzer (VNA). This method is often also referred as all-electrical spin wave spectroscopy (AESWS). Here, we report a description of the configuration employed for the FMR characterization in this thesis.

A CPW is comprised by a conducting signal line and two shielding ground lines ("S" and "G", respectively, in Fig. 4.6 a). The geometrical parameters of a CPW are optimized to match the electromagnetic (EM) wave impedance of the measurement system, which is  $Z_0 = 50 \Omega$  in the case of the VNA. Details on the analytical calculation of  $Z_0$  of a CPW can be found in Ref. [167]. Due to the counter-flowing currents in the ground lines, the net current on a CPW is zero [168]. CPWs with inner conductor width of  $20 \mu\text{m}$ , ground width of  $295 \mu\text{m}$  and a gap width between them of  $12.4 \mu\text{m}$  were employed to measure FMR in squared shaped samples with a side length of about 5 mm. The thin film deposited by ALD on a Si substrate is placed on top of the CPW with the ferromagnetic material facing the signal and ground lines, in the so-called "flip chip geometry". Figure 4.6 a depicts a sketch of the executed AESWS measurement. The core tool of the setup is an Agilent PNA-X N-5242A vector network analyzer (VNA). At its two RF ports, microwaves in the frequency range from 10 MHz up to 26.5 GHz can be applied. At the same time incoming signals are detected with high sensitivity and phase resolution. The VNA measures scattering parameters between port 1 and port 2. They are defined by a scattering matrix, which can be formulated for a two-port network by [169]:

$$\begin{pmatrix} V_1^- \\ V_2^- \end{pmatrix} = \begin{pmatrix} S_{11} & S_{12} \\ S_{21} & S_{22} \end{pmatrix} \begin{pmatrix} V_1^+ \\ V_2^+ \end{pmatrix} \quad (4.12)$$

$V_1^+$  ( $V_2^+$ ) represents voltages applied by the VNA at port 1 (port 2), while  $V_1^-$  ( $V_2^-$ ) represents voltages detected at port 1 (port 2). If the output at port 2 is switched off ( $V_2^+ = 0$ ), Eq. (4.12) leads to  $S_{11} = V_1^- / V_1^+$  and  $S_{21} = V_2^- / V_1^+$ . We note that S-parameters are unitless complex



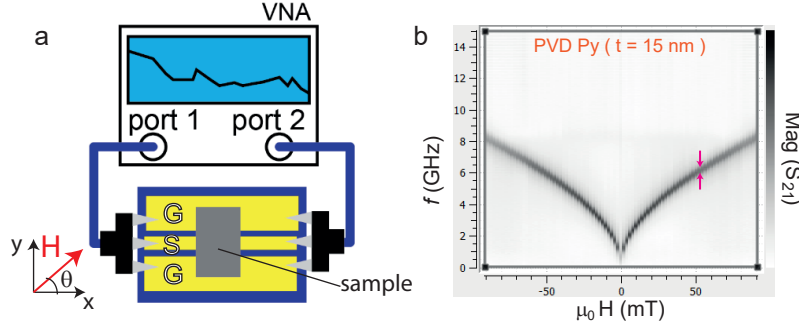


Figure 4.6 – (a) Sketch of the AESWS measurement configuration. Port 1 and 2 of a VNA are connected with RF tips to a CPW placed below the sample. Microwave absorption is characterized by measuring scattering parameters  $S_{11}$  and  $S_{21}$  with the VNA. A magnetic field  $\mu_0 \mathbf{H}$  is applied in any in-plane direction by using a two-axis electromagnet system. The field is monitored by a Hall-sensor placed directly below the sample. (b) Typical FMR absorption spectra measured on a 15-nm-thick Py thin film. The magnitude of the  $S_{21}$  scattering parameter,  $\text{Mag}(S_{21})$ , is reported as a function of the field applied along  $x$  in (a).

numbers and are either described by magnitude  $\text{Mag}(S_{ij})$  and phase  $\Phi(S_{ij})$ , or by a real part  $\text{Re}(S_{ij})$  and an imaginary part  $\text{Im}(S_{ij})$ .

In a typical FMR measurement configuration, both ports are connected via microwave cables and RF tips to the CPW. When microwaves are applied, the microwave current creates a dynamic magnetic field  $\mathbf{h}_{rf}$  in its vicinity, which exerts a torque on the sample magnetization  $\mathbf{M}$ . In a resonant condition, increased absorption is measured both in reflection  $S_{11}$  and in transmission  $S_{21}$ . The magnet system is comprised by two perpendicularly mounted electromagnets, allowing for field application in all in-plane directions  $\theta$  (see Figure 4.6 a). Each of the two field axes is driven by a Kepco bipolar power supply, respectively. The power supplies support a smooth zero crossing of their output currents allowing a magnetic field sweep from positive to negative values without intermission. The applied magnetic field is monitored by a two-axis Hall-sensor mounted directly below the sample position. The Hall voltages are amplified and fed back to the power supplies as reference values. The power supplies receive voltage values from the control computer, associated to values of  $\mu_0 \mathbf{H}$ . The power output is adjusted such that set values and reference values match. The magnet system supports a maximum field of  $|\mu_0 \mathbf{H}_{max}| = 90$  mT. The control computer allows to program automatic field sweeps and reads the measured S-parameters from the VNA.

In the FMR measurements reported in this thesis, the sample has been first saturated by applying  $\mu_0 H = 90$  mT along the  $x$ -axis. Then  $H$  is decreased in a step-wise manner and spectra are recorded. A typical resonance behavior is shown in Figure 4.6b for a 15 nm-thick Py thin film. The dependence of  $\text{Mag}(S_{21})(H)$  on the magnetic field strength  $\mu_0 H$  is reported for a field swept from + 90 mT to - 90 mT. Dark color in the gray-scale plots indicates resonant absorption. In the measurement routine followed, the field is swept from positive to negative values and the other way around to assess eventual hysteresis around zero field attributable to material anisotropies. Typical spectra of polycrystalline ferromagnetic films are symmetrical



around zero.

The field dependency of the resonant frequencies  $f_{res}(H)$  is analyzed by the discussed Kittel equation (Chapter 2, Sec. 2.3.2, Eq. (2.23)). Thereby we extract the effective magnetization  $M_{eff}$  of the thin film. The linewidth  $\Delta f$  of the imaginary component of the susceptibility  $\chi$  gives information on the Gilbert damping parameter  $\alpha$  (Chapter 2, Sec. 2.3.2, Eq. (2.26)). To extract the damping  $\alpha$  the linewidth of the microwave absorption is measured for different magnetic field values and the slope of  $\Delta f$  plotted over  $f$  is evaluated. When measurement conditions (e.g. incomplete calibration) do not allow for a clear separation of real and imaginary part of the susceptibility  $\chi$ , the linewidth  $\Delta f$  is assessed by dividing the linewidth of the  $\text{Mag}(S_{21})$  spectra (indicated by arrows in Figure 4.6b) by  $\sqrt{3}$  [13].

### 4.2.3 Brillouin Light Scattering

Brillouin light spectroscopy (BLS) is an optical spectroscopy technique. It is named after Brillouin [170], who in the 1920s predicted light scattering from acoustic phonons. The BLS technique covers the detection of inelastically scattered light with energy shifts equivalent to the GHz frequency regime [171]. Spectrometers with high frequency resolution and high contrast are needed to separately detect the GHz-shifted light from elastically scattered Rayleigh light. An optimized multipass Fabry-Pérot interferometer developed by J. Sandercock [172, 173] made BLS of magnons feasible and is widely used in BLS apparatus for the investigation of spin waves (SWs). BLS based techniques became widely used for research in magnonics. The aim of this section is to describe the basic working principles of BLS and the BLS microscopy setup used in this thesis, located in the LMGN laboratories.

#### Working principle: magnon-photon scattering

In a quantum mechanical framework, the scattering of photons with magnons is described as the interaction of quasiparticles as sketched in Fig. 4.7 [47]. An incident photon with energy  $\hbar\omega_i$  and wave vector  $\mathbf{k}_i$  either generates (Fig. 4.7a) or absorbs (Fig. 4.7b) a magnon with energy  $\hbar\omega$  and wave vector  $\mathbf{k}$ . The generation and the adsorption processes are denoted as Stokes and anti-Stokes scattering, respectively. In the first scenario the scattered photon lose energy, in the second it gains energy. Since in both cases energy and momentum are conserved, the scattered light carries information about the probed spin wave. This is described by

$$\hbar\omega_s = \hbar\omega_i \pm \hbar\omega \quad (4.13)$$

$$\mathbf{k}_s = \mathbf{k}_i \pm \mathbf{k} \quad (4.14)$$

with  $\hbar\omega_s$  and  $\mathbf{k}_s$  being the energy and the wave vector of the scattered photon, respectively. In magnetic thin films only the wave vector component parallel to the film surface ( $k_{\parallel}$ ) is conserved. The monochromatic laser light is focused on the sample with an incident angle  $\theta$  defined with respect to the surface normal of the film. Elastically scattered light is reflected on the opposite side of the surface normal with the angle between incident and elastically

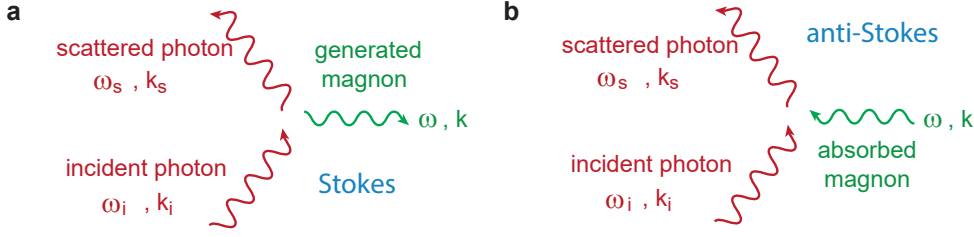


Figure 4.7 – Illustration of (a) the Stokes scattering process, in which a magnon is generated and (b) the anti-Stokes scattering process, in which a magnon is absorbed.

reflected beam amounting to  $2\theta$ . The light reflected with  $\mathbf{k}_s \parallel \mathbf{k}_i$  is collected and analyzed. Here the photon wave vector parallel to the sample surface  $k_{\parallel}$  was changed during the scattering process and the change  $\Delta k_{\parallel}$  is given by [47]

$$\Delta k_{\parallel} = 2k_i \cdot \sin \theta. \quad (4.15)$$

$\Delta k_{\parallel}$  is either transferred to or absorbed by a magnon depending on whether a Stokes or an anti-Stokes process is considered. Since a number of absorbed/created magnons correspond to the number of scattered photons, the intensity of the spin waves is quantified by counting the scattered photons. The magnitude of the wave vector of the incident light is given by  $k_i = 2/\lambda_L$ , where  $\lambda_L$  is the wave length of the laser. Measurements in this thesis were conducted with a solid-state blue laser with  $\lambda_L = 473$  nm. Photons can maximally transfer two times their wave vector which amounts to  $k_{max} = 26.6 \text{ rad}\mu\text{m}^{-1}$  for the used laser wave length.

### Brillouin light scattering microscopy setup

Extensive reviews on how the BLS principle has been integrated in setups and exploited for magnonic research are given in Refs. [174, 175]. Here we introduce the BLS setup operated at LMGN, sketched in Figure 4.8

In the BLS experiments presented in this thesis the SWs are excited by an microwave antenna in order to increase the signal strength. A coplanar wave guide (CPW) integrated on the sample is wire-bonded to an external CPW (not shown in Fig. 4.8), which is connected via a microwave cable to the signal generator (Anritsu MG 3692C). A monochromatic solid-state laser with  $\lambda_L = 473$  nm generates a linearly polarized laser beam. The laser polarization is horizontal in the beginning. The laser beam is focused to a spot diameter of around 300 – 350 nm on the surface of a sample. For measurements shown in this thesis a laser power in the range of 0.4 - 1 mW was used to avoid/reduce samples heating. The sample is mounted on a  $x, y, z$  nano-positioning stage, moving with respect to the laser spot position. An external magnetic field is applied along a fixed direction (depicted with a yellow arrow in Fig. 4.8) by means of a permanent magnet mounted on a moving stage. The magnitude of the magnetic field is adjusted by changing the distance between magnet and sample. The used objective lens (Olympus LCPLFLN100xLCD) provides a large numerical aperture of  $NA = 0.85$ , which allows

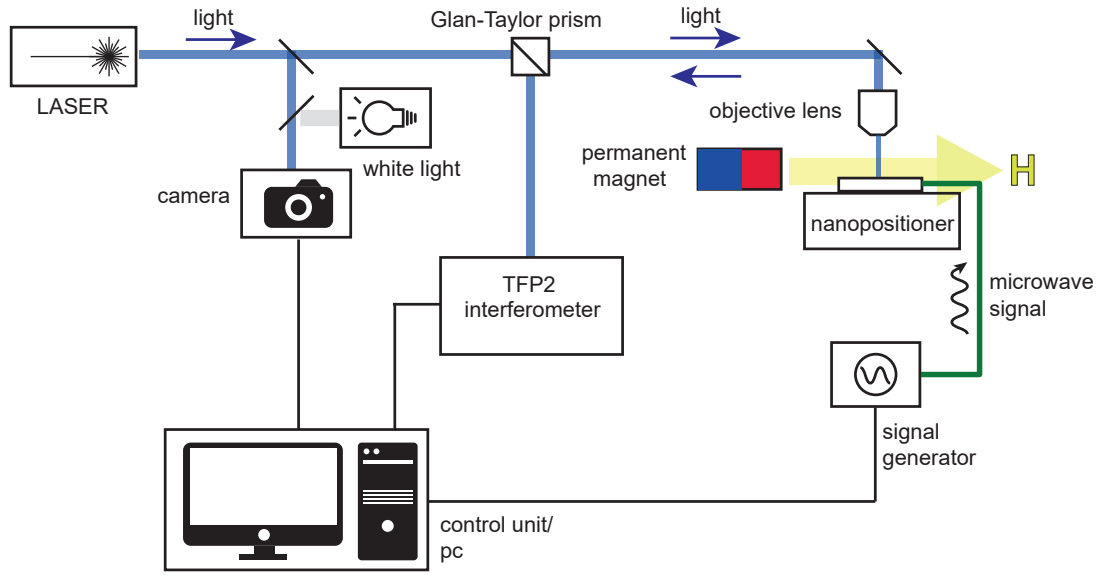


Figure 4.8 – Sketch of a BLS setup with space-resolved measurement capability. The optical beam (blue) is focuses on the sample surface with an objective lens. The sample is mounted on a nanopositioner and a magnetic field can be applied by a moving permanent magnet. The position of the laser spot on the sample is monitored with a camera. The light scattered from the sample is guided to the interferometer, where its energy shift is analyzed. Coherent SWs are excited by applying a microwave current with the signal generator to a coplanar wave guide integrated on the sample. The setup is controlled with a software package running on the control pc.

to collect photons scattered in a broad range of angles from the sample surface, suitable for the non-flat surface of nanotubes with hexagonal cross section. The light which is back-reflected is composed mostly of elastically scattered photons and a small fraction of inelastically scattered photons, which generated or absorbed magnons. In the magnon-photon scattering process, the light polarization is rotated by  $90^\circ$ . The back-reflected light passes through a Glan-Taylor prism. Horizontally polarized photons pass the prism in a straight trajectory. Via a beam splitter they are partially guided to a CCD camera, to monitor the laser spot on the sample. A white light source is used to illuminate the sample in order to localize it and, in case of large samples, to identify interesting features or structures. An optical feedback is used to focus and stabilize the laser spot on the sample surface. The inelastically scattered photons which possess the rotated polarization are reflected in the Glan-Taylor prism and leave it at a side aperture. This signal is then guided into a six-pass tandem Fabry-Pérot interferometer (Table Stable TFP-2). Photons with the matching frequency are transmitted by the interferometer and registered by a silicon avalanche photodiode detector. A software package [175] on the computer controls the interferometer. For coherent SWs the measured BLS counts are proportional to the square of the spin wave amplitude [176].

### 4.3 Microfabrication of electrical devices

In this thesis microdevices consisting of gold leads and gold coplanar wave guides (CPWs) to characterize the nanotubes were prepared by microfabrication techniques and equipments available in the cleanroom of the Center of MicroNanotechnology (CMi), at EPFL. In this section, the relevant steps to fabricate them are outlined.

The NTs were transferred from their Si(111) substrate to a 4 inch wafer serving as microfabrication support. We used Si wafers in (100) orientation oxidized with 200 nm of SiO<sub>2</sub> and transparent glass substrates. To locate the NTs and design electrical devices in their proximity, in this thesis we followed the method developed by Dr. D. Rüffer in his PhD thesis [45]. The method involves:

1. the definition of alignment markers on the target substrate,
2. the NTs distribution on the target substrate,
3. their localization via the acquisition of optical images,
4. the pattern design by means of a software tool for automatized nanotube detection and device pattern generation (GUIcontact software),
5. the electron beam lithography (EBL) of the device patterns.

The alignment markers were defined on the wafers by photolithography, evaporation of Ti/Au

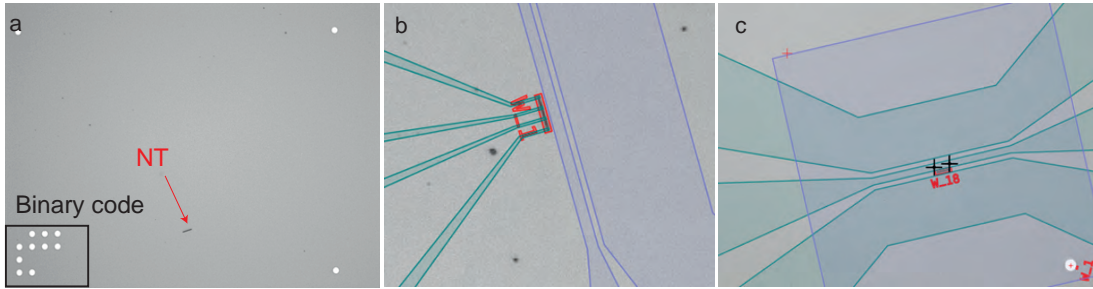


Figure 4.9 – (a) Optical micrograph showing one cell with alignment markers and a NT. Design of (b) four contact leads and (c) a CPW, oriented with respect of localized NTs.

(5 nm/100 nm) and then lift-off. An automated routine was employed for the coating and developing of the photoresists AZ1512/LOR, by using the Süss Microtech ACS200 Gen3 system. The UV exposure of the markers was done in a Süss Microtech MA6/BA6 mask aligner using a Cr mask. A gap distance of 30  $\mu\text{m}$ , exposure type "hard" and exposure time of 1.8 s for Si/SiO<sub>2</sub> and 2.1 s on glass were employed. The Cr mask was previously designed via laser-writing. The process resulted in a wafer with 128  $\times$  128 cells distinguished by a binary code. An optical image of the cell is shown in Figure 4.9 a.

The NTs, standing on their Si(111) substrate, were transferred into a isopropyl alcohol (IPA) solution by breaking them off the substrate in an ultrasonic bath. The NTs solution was then dropcasted onto the substrate with predefined markers. The NTs adhered to the surface by van der Waals forces and arranged on it in a random fashion. The NTs were then located by optical images, which needed to include the markers of one full cell (Fig. 4.9 a). The optical images were then loaded into the GUIcontact software, which automatically adjusted the rotation of

the image based on the markers. Each binary code was recognized and assigned to a specific position on the wafer. The software allowed to specify the device design for each cell and to adjust their lateral sizes. Figure 4.9 b and c show, in green, the design of four contact leads and of a coplanar wave guide (CPW), respectively, oriented with respect to the NT localized in the corresponding cell. Also the e-beam parameters, e.g. the electron beam dose and resolution, can directly be set in the software. The file with the devices pattern was exported and used as the layout for the EBL exposure process.

#### 4.3.1 Metallic leads on oxidized Si substrates

In this section, we describe the electron beam lithography process followed to contact suspended nanotubes via electrical leads (Fig. 4.10).

For surface treatment the wafer was left for 10 min at 180°C. The wafer was coated with the resist MMA EL9 at 3000 rpm and baked for 5 min at 180°C on the hot-plate. This resulted in a roughly 300 nm thick sacrificial layer that will serve to suspend the NTs and lift them from the substrate. The NTs were distributed by drop-casting the IPA solution on the surface of the

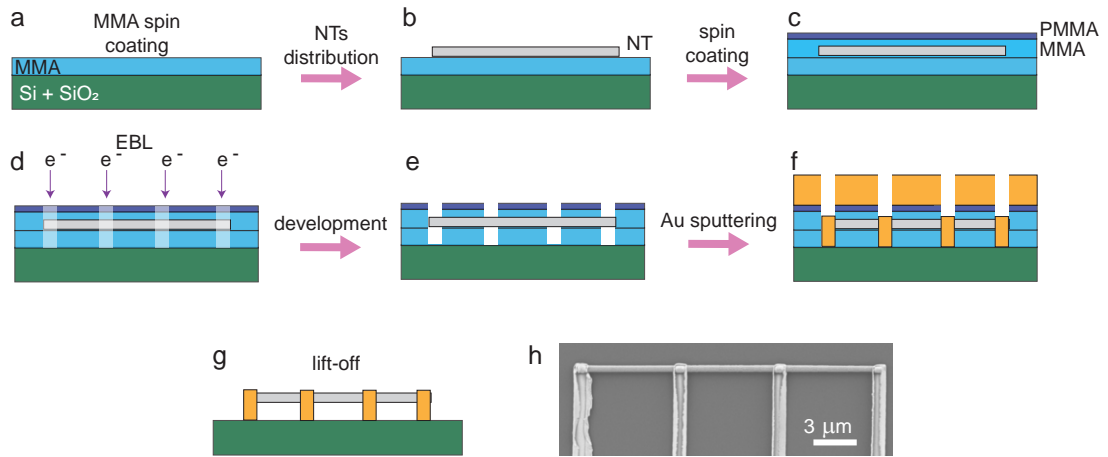


Figure 4.10 – Schematic sequence of the fabrication process for metallic leads to contact suspended NTs (cross sectional view). (a) MMA is spin-coated on the oxidized Si substrate. (b) The NTs are distributed via IPA solution drop-casting on the MMA. (c) A MMA/PMMA double layer resist is spin-coated and (d) exposed in an electron beam lithography (EBL) system. (e) The resist profile after development. (f) Au is sputtered on the resist profile. (g) Lift-off of the contact leads structures. (h) SEM image (top view) of a four-leads device after lift-off processing. The horizontal NT and the vertically displayed four Au pads are visible in light gray.

full wafer. The wafer was left again 10 min at 180°C to dry IPA residuals. In addition to the sacrificial layer, the wafer was spin-coated with a double layer of resists: MMA EL9 at 2500 rpm (400 nm) and PMMA 495K A4 at 4000 rpm (150 nm). The baking step after each coating consisted of 5 min at 180°C on the hot-plate. As PMMA is a positive e-beam resist, the exposed area will be washed away after the development. A pattern layer designed with GUIcontact

was exposed using a Vistec EPBG5000ES EBL system. A beam of 150 nA, which corresponded to a spot diameter of 75 nm, and a grid of 25 nm with a dose of  $800 \mu\text{C}/\text{mm}^2$  were utilized. For development the MiBK:IPA 1:3 solution and a development time of 1 min were used. To stop the development the wafer was left 1 min in an IPA bath and subsequently dried by nitrogen gun. For the sputtering of the contacts we used the Alliance Concept DP650 sputter system. We set a sputtering time of 12.2 s for Ti and 400 s for Au, corresponding to an average thickness of 5 nm Ti and 500 nm Au at the sputtering rates calibrated by CMI staff ( $4.1 \text{ \AA}/\text{s}$   $12.4 \text{ \AA}/\text{s}$ ). The Ti layer was used to improve the adhesion of the contacts on the substrate. One minute of RF-etch in 0.05 mbar argon atmosphere with 100 W power was performed prior to deposition to further increase the adhesion of the gold structures. Finally a lift-off process was done leaving the wafer in an acetone bath. The process lasted approximately two days. Few seconds of ultrasonic agitation helped the attacking of the resist. Long ultrasound pulses were avoided to not damage the devices fabricated.

### 4.3.2 Integrated coplanar wave guides on oxidized Si and transparent glass substrates

Coplanar wave guides (CPWs) for microwave experiments were fabricated both on oxidized Si substrates and on transparent glass. The NT was placed parallel to the signal line on oxidized Si substrates. For the glass substrates, as they were intended for  $\mu$ -BLS experiments where the laser was focused through the glass, the NT was placed below the signal line of the CPW to maximize the torque exerted by the microwave magnetic field in the measurement afterwards. The two substrates required a fabrication routine which differed in a few technical measures. We first describe the procedure to fabricate CPWs on glass (Fig. 4.11).

The wafer was left for 10 min at  $180^\circ\text{C}$  on a hot plate to treat its surface. The wafer was coated with MMA EL9 at 2500 rpm and PMMA 495K A4 at 4000 rpm, corresponding to resists thicknesses of 400 and 150 nm, respectively. The baking step after each coating consisted of 5 min at  $180^\circ\text{C}$  on the hot-plate. A 30 nm - thick Cr layer was evaporated in the LAB600H e-beam evaporating system and served as a conductive top layer to charging effects during the EBL writing. The layer pattern designed with GUIcontact for the CPWs was then exposed with the Vistec EPBG5000ES system. A beam of 150 nA, which corresponded to a spot diameter of 75 nm, a grid of 25 nm and a dose of  $1000 \mu\text{C}/\text{mm}^2$  were utilized. Before development, the Cr layer was removed by wet etching immersing the wafer in a solution of Cr etchant  $((\text{NH}_4)_2\text{Ce}(\text{NO}_3)_6 + \text{HClO}_4)$  for 1 minute. The wafer was dipped in a water bath to remove the acid etchant residuals and dried by nitrogen gun. For development the MiBK:IPA 1:3 solution and a development time of 1 min were used. For the deposition of the metal for the CPWs the LAB600H evaporator was employed. The used configuration was HRN (room temperature at high distances) and the thicknesses were 5 nm of Ti (as adhesion layer) and 120 nm of Au.

For the fabrication of CPWs on oxidized Si substrates, the same process was used with some modifications: the conductive top layer of Cr was not employed, hence also the etching step was skipped; the dose for the electron beam was  $800 \mu\text{C}/\text{mm}^2$ , instead of  $1000 \mu\text{C}/\text{mm}^2$ .

It is noted that the gold used for the device fabrication was sputtered in the case of the four

leads and evaporated in the case of the CPWs. The sputtering technique gave less sharp edges but ensured a good Au distribution under the NT, resulting in electrical leads surrounding the nanostructure and a strong contact. This expedient was not used in the fabrication of CPWs where, on the contrary, sharp edges and precise geometries were preferred.

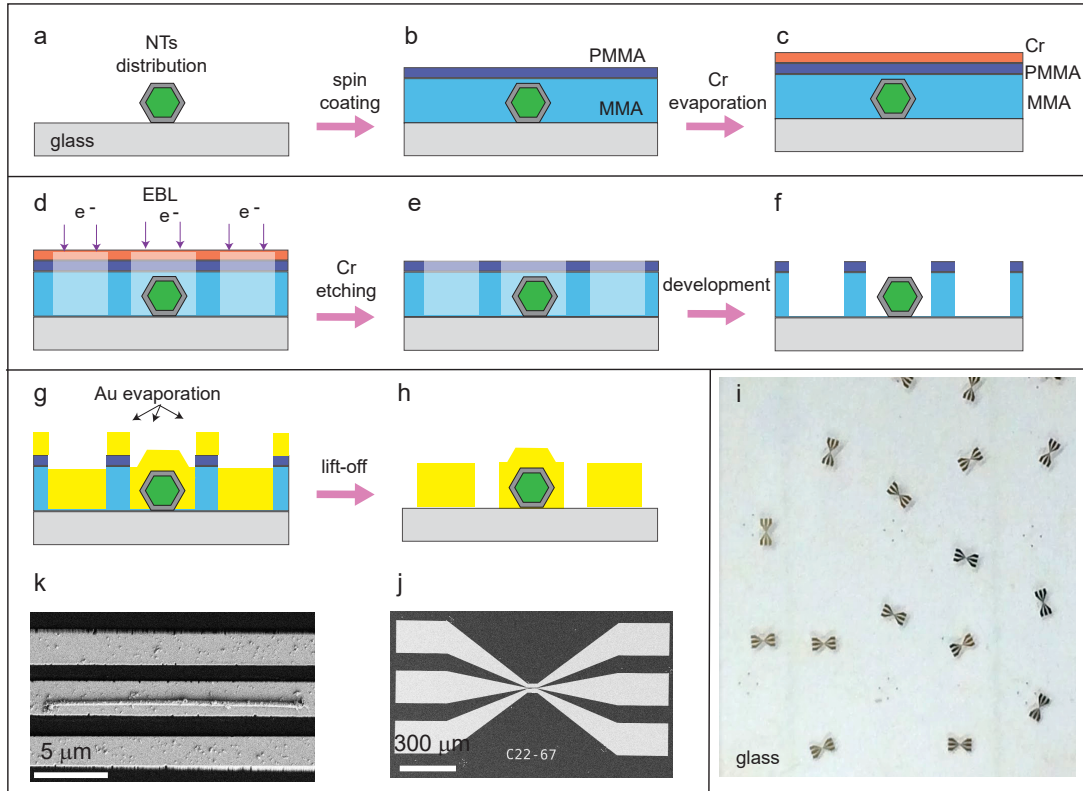


Figure 4.11 – Schematic sequence of the fabrication process for metallic CPWs integrated with individual NTs on glass substrates. (a) The NTs are distributed on the glass substrate via IPA solution drop-casting. (b) A MMA/PMMA double layer resist is spin-coated. (c) A Cr top layer serving as a electrical ground for the EBL process is evaporated. (d) The wafer is exposed in an electron beam lithography (EBL) system. (e) The Cr is etched away with an acid solution, then the MMA/PMMA is developed. (f) The resist profile after development. (g) Au is evaporated on the resist profile. (g) The lift-off process leaves the CPWs. (i) Photograph of a glass wafer area hosting gold CPWs (on a white background). (j) SEM images (top view) of a CPW. The label represents the position of the reference cell of markers on the wafer. (k) SEM images (top view) of a CPW (gray) showing a higher magnification of the grounds and the signal line of the CPW. The NT is covered by the CPW's signal line.





## **Results and Discussion Part II**



## 5 Atomic layer deposition of nickel nanotubes and thin films

This chapter reports the studies related to two different routes explored to achieve nickel (Ni) thin films in planar and nanotubular shape via atomic layer deposition (ALD). Both are based on nickelocene ( $\text{NiCp}_2$ ) as a metallorganic precursor containing Ni. At first, we investigated a one-step process leading to the direct deposition of Ni exploiting a mixture of ammonia  $\text{NH}_3$  and hydrogen plasma as co-reactant to react with  $\text{NiCp}_2$ . Secondly, we explored a two-step process where the deposition of Ni occurs via an intermediate deposition of oxidized Ni, exploiting  $\text{H}_2\text{O}$  as a co-reactant, and a subsequent reduction to metal Ni via hydrogen plasma. In both cases a post-deposition annealing step was necessary to improve the physical properties of the deposited material. The aim of the studies presented in this chapter is to identify an ALD process for Ni providing low surface roughness together with optimized physical properties, relevant for the field of 3D spintronics and magnonics. For instance, we verified that the Ni coatings are conformal on nanostructured 3D surfaces and smooth, have low electrical resistivity, low Gilbert damping and saturation magnetization close to that of nickel bulk.

### 5.1 ALD process 1 exploiting nickelocene, ammonia and hydrogen plasma as reactants

This section is dedicated to the plasma enhanced atomic layer deposition (PEALD) route where Ni thin films are achieved with a one-step process, in a planar and nanotubular shape. We exploited nickelocene  $\text{NiCp}_2$  as Ni precursor and a mixture of ammonia  $\text{NH}_3$  gas and hydrogen plasma as co-reactant. The process is similar to what reported in Ref. [32]. The deposition process provided nickel coatings with low resistivity of  $11.8 \mu\Omega\text{cm}$ . The scope of the thesis was first to reproduce the PEALD process in our ALD setup and then assess its suitability for optimized magnetic properties, not reported in literature for similar coatings [32, 124].

**5.1.1 Growth rate and resistivity of Ni as a function of the ALD process parameters****Methods**

Ni growth experiments were performed in a hot wall Beneq TFS 200 ALD reactor, operated at a pressure of 4-5 mbar, under a 200 sccm constant flow of pure nitrogen, used both as carrier and purge gas. Si (100) and GaAs NWs grown on (111) silicon substrates [161, 162] were used as substrates for planar and nanotubular Ni thin films. Both substrates were previously coated with 5 nm - thick  $\text{Al}_2\text{O}_3$  by ALD. We used nickelocene ( $\text{NiCp}_2$ ) as Ni precursor,  $\text{NH}_3$  gas and  $\text{H}_2/\text{N}_2$  plasma as reactants.  $\text{NiCp}_2$  was stored in a stainless steel container at  $80^\circ\text{C}$  to exploit its vapor pressure. In this ALD system only the  $\text{H}_2$  and the  $\text{N}_2$  gas lines enter the plasma head (see Chapter 4, Section 4.1.2). To produce a plasma-activated pulse of  $\text{NH}_3$ , we injected  $\text{NH}_3$  for 2 s into the chamber simultaneously with the existing  $\text{H}_2/\text{N}_2$  plasma. The plasma was generated in an RF parallel plate system and powered at 150 W while the  $\text{H}_2/\text{N}_2$  mixture was supplied through the plasma head with flow rates set as 50 sccm/100 sccm, respectively. After the  $\text{NH}_3$  plasma, the  $\text{H}_2/\text{N}_2$  plasma remained activated for a specific duration. The PEALD sequence can be summarized as follows: ( $\text{NiCp}_2$  pulse / purge /  $\text{NH}_3$  plasma pulse / purge)  $\times n$ , where  $n$  is the number of ALD cycles. The purge duration after the  $\text{NiCp}_2$  and  $\text{NH}_3$  steps was set as 6 s and 15 s, respectively. The number of ALD cycles  $n$  was kept at 700. Other process parameters like the chamber temperature, the durations of  $\text{NiCp}_2$  and  $\text{NH}_3$  plasma pulse were explored and optimized as reported in the following paragraph.

**Results and discussion**

In Figure 5.1 a we show the Ni growth rate as a function of the chamber temperature, which was varied from  $230^\circ\text{C}$  to  $270^\circ\text{C}$ . In Fig. 5.1 b and Fig. 5.1 c we report the growth rate and electrical resistivity dependency on the pulse duration of the  $\text{NiCp}_2$  and the  $\text{NH}_3$  plasma pulse, respectively. Figure 5.1 d shows the SEM micrographs acquired in cross-section for two specific samples of the series of Fig. 5.1 c. For a  $\text{NiCp}_2$  ( $\text{NH}_3$  plasma) pulse duration set as 2 s (2 s) we identified a growth rate plateau at  $0.4 \text{ \AA}/\text{cycle}$  in the temperature regime of  $(240 - 260)^\circ\text{C}$  (Fig. 5.1 a). We attribute this temperature regime to the ALD window. Experiments in Fig. 5.1 b and Fig. 5.1 c were thereby performed at  $T = 250^\circ\text{C}$ . By keeping the  $\text{NH}_3$  plasma pulse duration constant to 2 s in the ALD cycle, the growth rate was found to increase with the duration of the  $\text{NiCp}_2$  pulse (Fig. 5.1b), approaching a constant value of  $0.4 \text{ \AA}/\text{cycle}$  for a pulse duration  $\geq 1$  s. The resistivity was found to decrease from about  $230 \mu\Omega\text{cm}$  to about  $150 \mu\Omega\text{cm}$  and to remain constant, within an error bar of  $4 \mu\Omega\text{cm}$ , for a  $\text{NiCp}_2$  pulse duration  $\geq 2$  s. Finally, for a  $\text{NiCp}_2$  plasma pulse duration set as 2 s in the ALD cycle, we found that the growth rate increases from 0.4 to about  $0.6 \text{ \AA}/\text{cycle}$  by increasing the  $\text{NH}_3$  pulse duration from 2 to 3s. The growth rate remained constant for pulse durations greater than 3s. It is observed that the resistivity decreases monotonously with the duration of the  $\text{NH}_3$  pulse and reaches a minimum value of  $(65 \pm 5) \mu\Omega\text{cm}$  for a duration of 7 s. In Fig. 5.1 d we show the samples obtained with a

### 5.1. ALD process 1 exploiting nickelocene, ammonia and hydrogen plasma as reactants

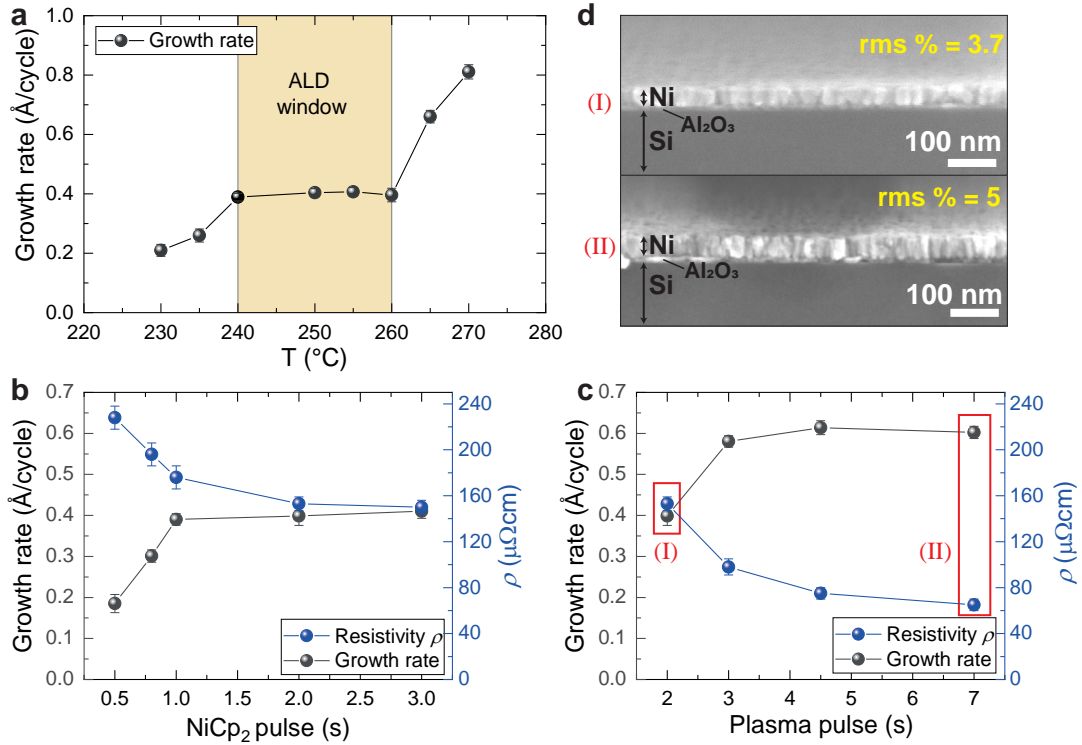


Figure 5.1 – (a) Ni growth rate dependency on the ALD chamber temperature. NiCp<sub>2</sub> and NH<sub>3</sub> plasma pulse duration are both set to 2 s. Growth rate and resistivity dependency on (b) the NiCp<sub>2</sub> and (c) NH<sub>3</sub> plasma pulse duration for a chamber temperature  $T = 250^\circ\text{C}$ . The NH<sub>3</sub> plasma pulse duration is set as 2 s in (b) and the NiCp<sub>2</sub> pulse duration is set as 2s in (c). (d) Cross-section SEM micrographs of the samples (I) and (II) highlighted in (c).

NH<sub>3</sub> pulse duration of 2 s and 7 s, respectively, as representative of the thin films obtained for this PEALD process. Generally these Ni coatings are polycrystalline with grains oriented perpendicular to the substrate, forming nanocolumns. Due to this morphology, the values of surface roughness in relation to the thickness (rms %) are 3.7 % to 5 % and are quite high. Furthermore, the rms% is found to increase in the plateau regime of the growth rate (sample (II)). On the one hand the plasma exposure promoted the reaction with the nickelocene (saturated growth rate), leading to a lower resistivity. On the other hand a column-like growth resulted which made the thin film roughness higher. The minimum value measured for the electrical resistivity (65  $\mu\Omega\text{cm}$ ) was still one order of magnitude higher than what was reported for bulk Ni [177]. We attribute this data to the incorporation of residual elements from the deposition process (N,C from precursor and reactants, O from passivation). Their presence was confirmed qualitatively by EDS analysis.

### 5.1.2 Thin films annealed under reducing atmospheres

#### Methods

Annealing treatments in a reducing atmosphere were performed to remove residual contaminants from the thin films and lower the electrical resistivity values. To do so, a mixed  $H_2/N_2$  gas with flow rates set as 50 sccm/ 300 sccm has been used as annealing atmosphere. The treatment duration and temperature were optimized as described in the following paragraph. A further experiment was carried out to verify plasma activation under the deposition conditions described previously ( $H_2/N_2$  plasma gas with flow rates set at 50sccm/100sccm in the presence of nitrogen carrier gas with flow rate 200 sccm). The test, here categorized as an annealing experiment, consists in comparing the annealing treatment in a  $H_2/N_2$  gas atmosphere with the one in an  $H_2/N_2$  plasma atmosphere with equal  $H_2$  concentration.

#### Results and discussion

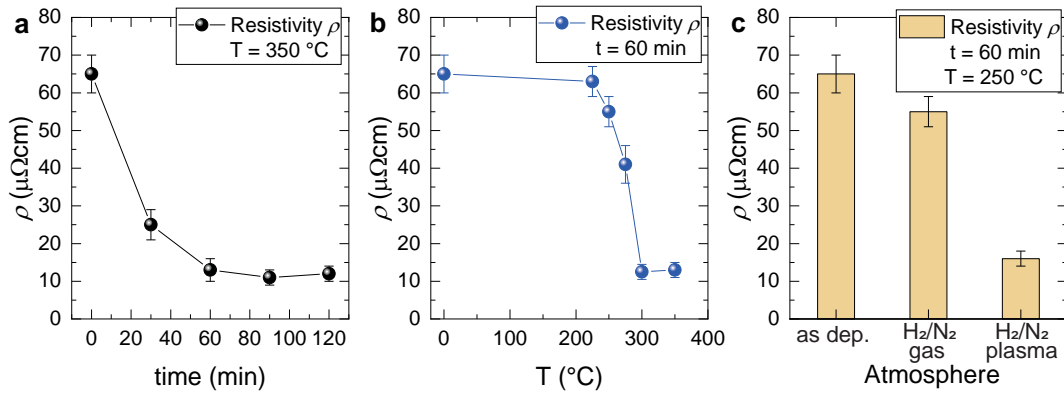


Figure 5.2 – Dependence of the Ni thin film resistivity on the following annealing treatment parameters: (a) duration, (b) temperature and (c) atmosphere. The annealing in (a) and (b) is performed in an  $H_2/N_2$  gas atmosphere. The constant treatment parameters are displayed in the top right legend of the graphs.

In Figure 5.2a and b we report on the dependency of the Ni resistivity on the duration and on the temperature of the annealing treatment, respectively. The treatments were executed in  $H_2/N_2$  gas for a chamber temperature of  $T = 350^\circ\text{C}$  in Fig. 5.2a and a duration  $t$  of 60 minutes in Fig. 5.2b. In Fig. 5.2c the effects on the electrical resistivity of the annealing treatment is shown both for a  $H_2/N_2$  gas and plasma atmosphere. We found that, for a temperature of  $T = 300^\circ\text{C}$ , the resistivity drops from 65  $\mu\Omega\text{cm}$ , measured in the as-deposited material, to a minimum of  $(11 \pm 1) \mu\Omega\text{cm}$  after an annealing time of 90 min (Fig. 5.2a). For an annealing treatment duration of  $t = 60$  min, we observe that the resistivity starts to decrease at a temperature of  $T = 250^\circ\text{C}$ , reaching a minimum of  $(12.5 \pm 0.5) \mu\Omega\text{cm}$  for  $T = 300^\circ\text{C}$  (Fig. 5.2b). The results suggest the activation of the reduction process for  $T \geq 250^\circ\text{C}$ . We show in Fig. 5.2c that for the same

## 5.1. ALD process 1 exploiting nickelocene, ammonia and hydrogen plasma as reactants

annealing temperature and duration time ( $T = 250^\circ\text{C}$ ,  $t = 60$  min) and equal  $\text{H}_2$  concentration in the annealing atmosphere, we decreased the Ni resistivity to  $(55 \pm 4) \mu\Omega\text{cm}$  and  $(16 \pm 2) \mu\Omega\text{cm}$  by performing the treatment under  $\text{H}_2/\text{N}_2$  gas and plasma, respectively. The plasma atmosphere allows more effective reducing treatments at lower temperature. The result also validated that the plasma state was correctly activated under the processing conditions (flow rates and chamber temperature) described previously for the deposition experiments. For the coatings in the form of NTs, the annealing in a gaseous atmosphere was preferred in order to avoid material re-deposition during a high energetic long plasma treatment.

### 5.1.3 Final morphology and properties of ALD nickel thin films and nanotubes

Planar and nanotubular Ni thin films have been prepared following the PEALD process of sample (II) in Fig. 5.1 c, d and annealed for 3 hours at  $300^\circ\text{C}$  under  $\text{H}_2/\text{N}_2$  gas. In the best planar sample we measure a resistivity of  $(11 \pm 1) \mu\Omega\text{cm}$  in agreement with Ref. [32] and a saturation magnetization  $M_s$  of 310 kA/m which is 37 % lower than what is expected for bulk Ni [178]. Despite the samples being magnetic, no ferromagnetic resonance (FMR) could be resolved via broadband spectroscopy for samples prepared with the process described in this section. We attributed this observation to two-magnon scattering [179, 180] arising from high roughness and surface irregularities. We here assume that this phenomena broadened the FMR signal linewidth up to the limit in which the signal was indistinguishable from the noise level. A Ni NT prepared by the same process (Fig. 5.3 a) showed a grainy shell with large roughness. A Ni NT with comparable diameter and Ni thickness, prepared with the two-step PEALD process based on the intermediate oxidation with  $\text{H}_2\text{O}$  (Fig. 5.3 b) resulted to have a smooth and homogeneous ferromagnetic shell. Here, a better surface roughness is obtained. The process leading to smooth ferromagnetic Ni shells is described in detail in the Section 5.2, which follows.

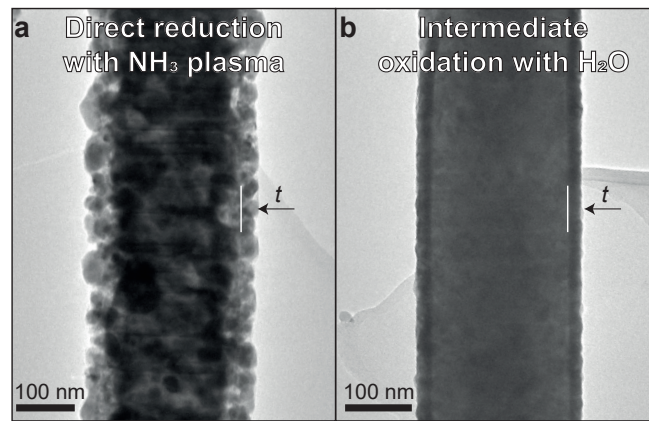


Figure 5.3 – Ni NTs prepared by depositing Ni onto GaAs NWs with (a) a one-step Ni ALD process based on the  $\text{NiCp}_2$  reduction via  $\text{NH}_3$  plasma and (b) a two-step ALD process based on the intermediate Ni oxidation with  $\text{H}_2\text{O}$  (described in Section 5.2).

## 5.2 ALD process 2, exploiting nickelocene, water and hydrogen plasma as reactants

### 5.2.1 Pub. I: Plasma-Enhanced Atomic Layer Deposition of Nickel Nanotubes with Low Resistivity and Coherent Magnetization Dynamics for 3D Spintronic

M. C. Giordano, K. Baumgaertl, S. Escobar Steinvall, J. Gay, M. Vuichard, A. Fontcuberta i Morral and D. Grundler

ACS Appl. Mater. Interfaces 2020, 12, 36, 40443–40452

Publication Date: August 12, 2020

doi: 10.1021/acsami.0c06879

*Reproduced from ACS Appl. Mater. Interfaces 2020, 12, 36, 40443–40452 with permission of ACS Publishing. For uniformity the layout was reformatted and the references were integrated into the thesis' bibliography.*

My contribution to this paper included the development of the nickel deposition processes by ALD, the materials characterization, the fabrication of nanotubes and the micro-devices to characterize them, the AMR measurements, the micro-BLS measurements and data analysis. The micro-BLS measurements and their analysis were supported by K. Baumgaertl, the TEM and STEM-EDX analysis were done with the help of S. Escobar Steinvall. The AMR measurements of nanotubes were conducted with the support of EPFL semester students J. Gay and M. Vuichard. I wrote the draft of the manuscript.

#### Abstract

We report plasma-enhanced atomic layer deposition (ALD) to prepare conformal nickel thin films and nanotubes by using nickelocene as a precursor, water as the oxidant agent and an in-cycle plasma enhanced reduction step with hydrogen. The optimized ALD pulse sequence, combined with a post-processing annealing treatment, allowed us to prepare 30 nm thick metallic Ni layers with a resistivity of  $8\ \mu\Omega\text{cm}$  at room temperature and good conformality both on the planar substrates and nanotemplates. Thereby we fabricated several micrometer-long nickel nanotubes with diameters ranging from 120 to 330 nm. We report on the correlation between ALD growth and functional properties of individual Ni nanotubes characterized in terms of magneto-transport and the confinement of spin wave modes. The findings offer novel perspectives for Ni-based spintronics and magnonic devices operated in the GHz frequency regime with a 3D device architecture.



### Introduction

Magnetic nanostructures find applications in data storage devices [7], magnetic sensors [181, 182] and biomedical applications [12]. The demand of high-density technologies [19] and the need of new applications are driving the expansion of nanomagnetism towards three-dimensional (3D) device architectures[20, 21]. Here, novel physical phenomena arising from complex spin textures become possible. However, the implementation of high-quality 3D nanomagnetic structures on large scales is lacking. A promising path is to magnetically coat 3D nanotemplates, e.g. polymeric scaffolds[23], self-assembled[24] or bottom-up grown[25, 26] nanostructures. Therefore, a technique for conformal coatings of high-quality ferromagnetic metals is of uttermost importance to advance 3D nanomagnetism. Atomic layer deposition (ALD) [27, 28] indeed offers a great potential. Here the material is deposited through self-limiting reactions between vapor phase metal-organic precursors (and co-reactants) and the exposed substrate surface, enabling conformal coatings and thickness control on the atomic scale. For the deposition of numerous oxides, ALD is a well-established technique. For metallic thin films, including ferromagnetic metals, ALD still faces challenges due to the limited number of suitable precursors, the difficulty in reducing the metal cations, and the tendency of metals to agglomerate to islands [35, 31]. Previous attempts to deposit the ferromagnetic metal nickel with ALD included one-step and two-step processes. In the first scenario, the nickel films were deposited directly through the reaction of the nickel precursor and a co-reactant. Amongst them there were molecular hydrogen [31], molecular ammonia[125], plasma-activated hydrogen[124] and ammonia [124, 32], as well as tert-butylamine[34]. The use of plasma offered the possibility to lower the deposition temperature and to increase the purity of the deposited material [152]. However, the recombination of plasma species limited the conformality of plasma-enhanced ALD (PE-ALD) on high aspect ratio (AR) nanotemplates [148, 152]. For the two-step process, the first step was based on nickel oxide deposition, where the oxidant co-reactant was ozone[25, 22, 183, 184] or water[122], and the second step relied on a reduction process, which transformed the oxide into pure nickel. The reduction was performed either within the ALD cycle with hydrogen plasma [122], or as post-deposition annealing in molecular hydrogen [25, 26], or by exploiting both processes. The two-step process ensured, in principle, good conformality on high aspect ratio nanotemplates due to the greater homogeneity of nickel oxide deposition via the thermal ALD growth. The usage of water as co-reactant resulted in Ni coatings with good conformality on nanotemplate substrates with an AR of about 3:1 [122]. Metallic Ni coatings achieved with ozone as the co-reactant exhibited appreciable surface roughness and inhomogeneities as Ostwald ripening was potentially induced by the annealing temperatures above 400 °C [25, 46, 185].

Nanotubes (NTs) prepared from ferromagnets represent prototypical 3D nanomagnetic structures [21]. They raised significant attention as they support stable flux-closure magnetic states [38] and avoid the Bloch point structure along the central axis. This results in a fast and controllable reversal process when compared to magnetic stripes [39]. The properties of these nanostructures are extremely versatile for applications as they change as a function of their geometry[83, 37], the angle at which the external field is applied [186] or due to the

interactions between them[154]. In addition, previously unforeseen dynamic effects are possible. Domain walls moving in nanotubes are predicted to avoid Walker breakdown and give rise to Cherenkov-like spin wave emission [40]. Their curvature generates non-reciprocal spin-wave dispersion [41]. Furthermore, the three geometric parameters, namely the length, the inner radius and external radius, offer the possibility to tailor spin-wave confinement. These characteristics make ferromagnetic NTs promising functional objects for 3D integrated spintronics and magnonics [13]. Experimental studies on individual NTs focused so far on the determination of their static magnetic properties, magnetization states and reversal magnetization mechanisms, by techniques such as SQUID magnetometry [88][107], cantilever magnetometry [106], anisotropic magnetoresistance measurements [25, 26, 105] and x-ray based magnetic imaging [111, 107]. Still, the dynamic magnetization of individual ferromagnetic NTs with the radius on the order of 100 nm has not yet been the subject of comprehensive experimental investigations. So far studies were limited to spin-wave resonances of large ensembles of ferromagnetic tubular structures [85] and of rolled up ferromagnetic layers on semiconductor membranes with micrometric radii[71, 115], where azimuthal interference of long-wavelength magnetostatic spin waves was found. Lenz et al.[187] recently reported the magnetization dynamics of an individual Fe nanorod embedded in a carbon nanotube, studied by ferromagnetic resonance (FMR) and Brillouin light scattering (BLS). Dynamics of individual nanotubes [40, 41] remain to be explored experimentally.

Atomic layer deposition (ALD) has selectively been used for the fabrication of ferromagnetic Ni NTs by coating GaAs nanowires [25, 26]. Weber *et al.* [106] demonstrated three stable magnetization states in individual ALD-grown Ni nanotubes measured by cantilever magnetometry. Rueffer *et al.* [26] measured an anisotropic magnetoresistance (AMR) effect of up to 1.4 % on such Ni nanotubes when applying fields of 1 T at room temperature. The presented NTs exhibited a rough surface after annealing and their magnetization dynamics were not reported. Wang *et al.* [32] reported PE-ALD to coat high aspect ratio (AR~ 13 : 1) Si nanopillars with Ni. They achieved a low resistivity of 11.8  $\mu\Omega\text{cm}$  in planar Ni layers after post-annealing enhancement, but did not report on functional properties of the high aspect ratio coatings.

In this work we present the fabrication of Ni NTs by PE-ALD on single-crystalline GaAs nanowires as 3D nanomagnetic structures. Adapting the two-step ALD process of Ref. [122] we employed nickelocene as the metallorganic precursor and water as the oxidant agent to first obtain nickel oxide. Subsequently, an in-cycle plasma enhanced reduction process with hydrogen was performed to get metallic nickel. We optimized the ALD sequence to enhance the functional properties and conformality of Ni in the nanotubular shape. We identified the deposition conditions that led to identical coverage on planar substrates and on the nanotemplates with an AR above 15:1. The optimized Ni NTs exhibited, after post-annealing enhancement, smooth surfaces and showed both a low resistivity of roughly 8  $\mu\Omega\text{cm}$  and a prominent AMR effect. We characterized the magnetization dynamics of individual NTs under microwave irradiation in the GHz frequency regime. We detected a series of resonances by micro-focused BLS which we attributed to spin-wave modes with discrete wave vectors  $k$  due to azimuthal confinement. To the best of our knowledge, this is the first experimental investigation of resonant modes in nanoscale ferromagnetic NTs. Our results prove the high quality of the

## 5.2. ALD process 2, exploiting nickelocene, water and hydrogen plasma as reactants

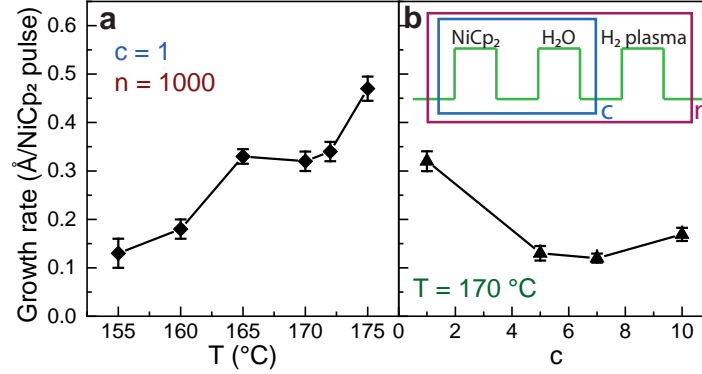


Figure 5.4 – (a) Dependence of the growth rate of Ni on the chamber temperature. Each sample was prepared with  $n = 1000$  cycles. (b) Dependence of growth rate on the number  $c$  of NiCp<sub>2</sub>/H<sub>2</sub>O steps in the ALD cycle (inset) for samples deposited at  $T = 170$  °C.

achieved 3D ferromagnetic coatings, promising to advance the realization and exploration of 3D spintronic device architectures such as the proposed racetrack memory.[19] They offer a novel avenue also for Ni-based nanotechnologies beyond nanomagnetism.[188, 189, 190]

## Results and discussion

### Growth of nickel thin films and nanotubes

We start by reporting on the PE-ALD growth of Ni thin films on planar Si (100) substrates and high aspect ratio nanotemplates. The planar wafers and GaAs nanowires with hexagonal cross-sections (Figure A.1), respectively, were coated with a few nanometers of alumina with the aim of growing Ni on the same surface, while focusing on the effect of different substrate geometries and aspect ratios. In order to optimize the composition and morphology we varied the chamber temperature  $T$  and the number of metal oxide deposition steps  $c$  prior to hydrogen-plasma reduction. Figure 5.4a shows the dependence of the growth rate of nickel on planar substrates on  $T$ . Here the number of nickel oxide was set to  $c = 1$  and the ALD cycle was repeated  $n = 1000$  times (inset of Figure 5.4b). The chamber temperature was varied from 155 °C to 175 °C. From  $T = 155$  °C to  $T = 165$  °C we observe that the growth rate increases from a value of 0.12 Å/(NiCp<sub>2</sub> pulse) to a value of 0.33 Å/(NiCp<sub>2</sub> pulse). It stays constant at  $0.33 \pm 0.01$  Å/(NiCp<sub>2</sub> pulse) for temperatures ranging from 165 to 172 °C. We attribute this temperature regime to the ALD window. The growth rate is at 0.47 Å/(NiCp<sub>2</sub> pulse) for  $T = 175$  °C. To explore how the growth rate varies at  $T = 170$  °C with changing the number of nickel oxide steps  $c$  in the ALD cycle, we varied the parameter  $c$  from 1 to 10, while the ALD cycle  $n$  was changed consistently in order to keep the product  $c \times n = 1000$ . In Figure 5.4b we report the growth rate estimated on the the number of total NiCp<sub>2</sub> pulses ( $c \times n$ ) as function of the parameter  $c$ , number of steps leading to nickel oxide formation. We observe that the growth rate drops from 0.33 Å/(NiCp<sub>2</sub> pulse) at  $c = 1$  to 0.13 Å/(NiCp<sub>2</sub> pulse) at  $c = 5$  and 7. It increases again

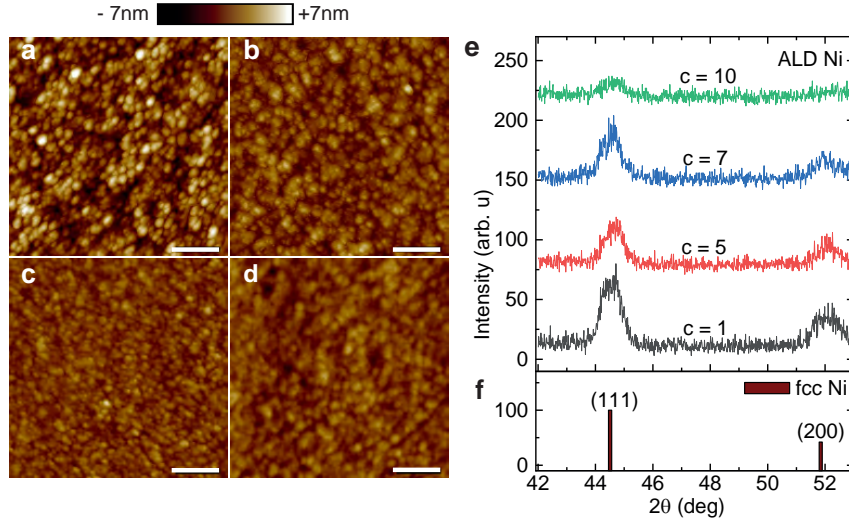


Figure 5.5 – Atomic force microscopy performed on a  $1\text{ }\mu\text{m} \times 1\text{ }\mu\text{m}$  area of samples with (a)  $c = 1$ , (b)  $c = 5$ , (c)  $c = 7$ , and (d)  $c = 10$  (scale bars:  $200\text{ nm}$ ). (e) X-ray diffractograms of  $30 \pm 2\text{ nm}$  thick nickel films prepared with  $c$  ranging from 1 to 10 (see labels). (f) The bars give the positions of the (111) and (200) reflections of cubic nickel (PDF 00-004-0850). The thin films were deposited at  $170^\circ\text{C}$  on a silicon substrate coated with  $5\text{ nm}$  of  $\text{Al}_2\text{O}_3$  and annealed at  $350^\circ\text{C}$ .

to  $0.17\text{ }\text{\AA}/(\text{NiCp}_2\text{ pulse})$  for  $c = 10$ . Thin films with a thickness of about  $30\text{ nm}$  were prepared with  $c$  set to 1, 5, 7 and 10, taking into account the values of growth rate reported in Figure 5.4b. They were then annealed under hydrogen flow (details in Methods). In the following we discuss the properties of annealed Ni films. Atomic force microscopy (Figure 5.5a-d) and X-ray diffraction (Figure 5.5e) were used to assess the roughness and the crystallographic structure, respectively, of the four planar Ni films. We extracted rms roughness values of  $2.1\text{ nm}$  for  $c = 1$  (Figure 5.5a),  $1.3\text{ nm}$  for  $c = 5$  (Figure 5.5b),  $0.9\text{ nm}$  for  $c = 7$  (Figure 5.5c) and  $1.2$  for  $c = 10$  (Figure 5.5d). Accordingly, the sample prepared with  $c = 7$  showed the smoothest surface, with a rms roughness amounting to the 3 % of the film thickness (compare Figure 5.8a). In Figure 5.5e we report the X-ray diffractograms acquired in a glancing incident angle configuration for the four annealed thin films. The measured peaks are consistent with the (111) and (200) reflections of cubic nickel (PDF 00-004-0850) shown in Figure 5.5f. The broadening and positions of peaks of the samples prepared with  $c = 1, 5$  and  $7$  suggest polycrystalline Ni films, with no preferential grain orientation. We ascribe the peak asymmetries to micro-strains induced by the synthesis-annealing process. The lattice parameter  $a$  was extracted from the XRD diffractograms and is provided in Table 1. The synthesis conditions in samples prepared with ALD parameter  $c$  equal to 5 or 7, compared to conditions  $c = 1$ , led to slightly larger cell parameters. The signal-to-noise ratio for  $c = 10$  was not adequate for extracting the lattice parameter.

The four depositions were performed simultaneously on Si wafers and GaAs nanowires (both coated with alumina). We employed different set of nanowires, with lengths between 7 and 15

## 5.2. ALD process 2, exploiting nickelocene, water and hydrogen plasma as reactants

Table 5.1 – Crystallographic information extracted from the XRD diffractograms of the annealed Ni thin films as a function of the synthesis parameter  $c$ .

Synthesis parameter $c$	Phase / Structure type	Lattice parameter $a$ (Å)
1	Ni / fcc	3.507
5	Ni / fcc	3.512
7	Ni / fcc	3.514
10	Ni / fcc	-

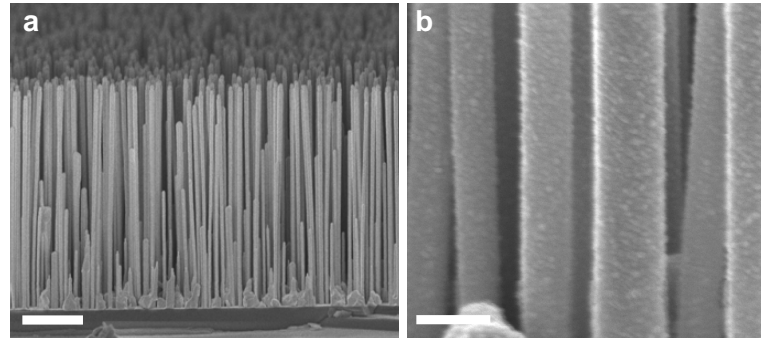


Figure 5.6 – Scanning electron microscopy (SEM) micrographs of (a) a large ensemble of vertical nanowires with ALD-grown Ni shells (scale bar: 1  $\mu\text{m}$ ) and (b) selected central regions of Ni NTs (scale bar: 200 nm).

$\mu\text{m}$  and diameters ranging from 100 to 270 nm. The aspect ratios of different nanotemplates were calculated following the convention for squared pillars [148] and range from 15:1 to 31:1 (Table A1). The nanotemplates allowed us to obtain arrays of millions of vertically oriented nickel nanotubes (Figure 5.6). To investigate the chemical composition and the structure of the Ni NTs we performed transmission electron microscopy (TEM). Figure 5.7a to 5.7d shows high-resolution (HR) TEM micrographs with insets of the corresponding selective area electron diffraction (SAED) patterns of the Ni nanotubes prepared with  $c = 1, 5, 7$  and 10, respectively. The images depict the interface between GaAs nanowires and the ALD-grown  $\text{Al}_2\text{O}_3/\text{Ni}$  shells. The Ni coating with  $c = 1$  (Figure 5.7a) exhibits a relatively large peak-to-peak roughness value of about 7 nm. The Ni shells deposited with  $c = 5, 7, 10$  (Figure 5.7b to d) show a continuous coverage and form ferromagnetic nanotubes with small roughness. The roughness variation of the NTs is qualitatively consistent with the characteristics found for the planar Ni films (Figure 5.8a). No preferential growth direction is observed in any of the samples, all made up of grains of different sizes and orientations. An epitaxial relationship between core and shells was not found. All shells exhibited a surface layer of nickel oxide of a few nanometers, attributed to oxidization in air after the annealing treatment. SAED images contain the typical ring patterns of a polycrystalline texture, which we attribute to the nickel shell, and a single crystal dot pattern of a zinc-blende structure, that we assign to the GaAs core, which was grown along the  $[111]\text{B}$  directions as previously reported [191]. Starting from the center, the diffraction rings were assigned to the (111), (200), (220) and (311) planes respectively,

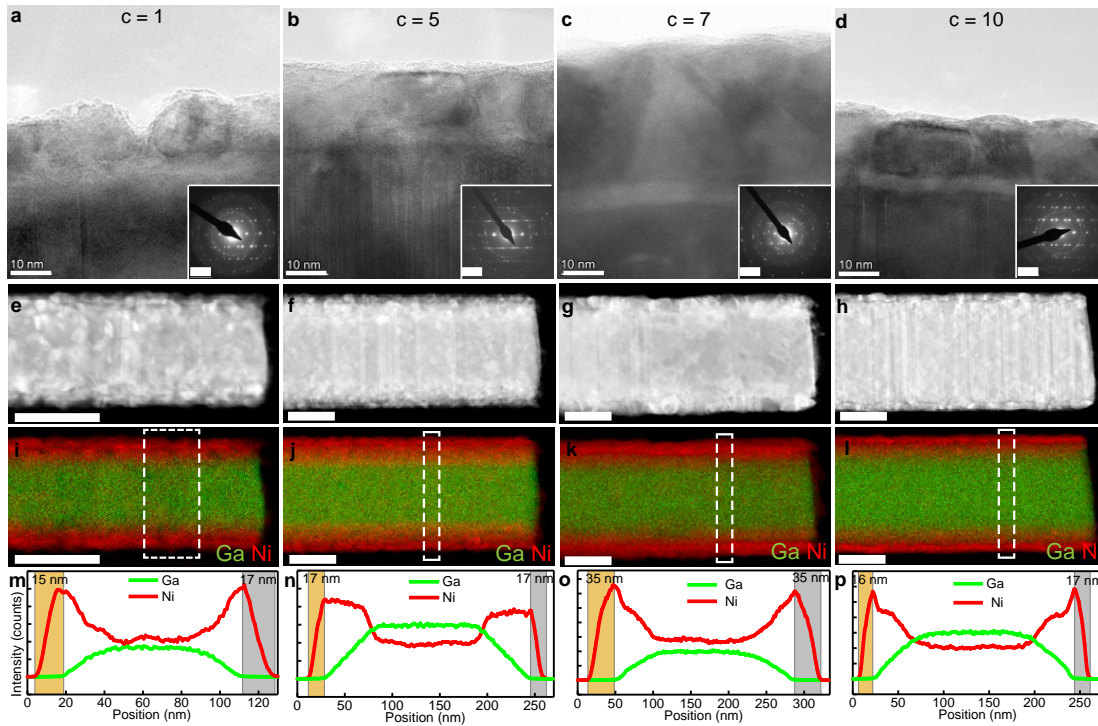


Figure 5.7 – (a-d) HRTEM images (scale bar: 10 nm) of interfaces between GaAs nanowires and the  $\text{Al}_2\text{O}_3/\text{Ni}$  shells. The insets show SAED patterns (scale bars: 5  $\text{nm}^{-1}$ ). (e-h) HADDAF images (scale bars: 100 nm). (i-l) Distribution of Ga and Ni. (m-p) Elemental analysis of Ni nanotubes on GaAs nanowires. Each column of panels represents one sample. The four samples were prepared with  $c$  set to 1, 5, 7 and 10 as indicated on top of each column. The chamber (annealing) temperatures were 170 °C (350 °C).

belonging to the face-centered cubic lattice of Ni crystals. Using scanning TEM (STEM) we performed high-angle annular dark-field (HAADF) and energy dispersive X-ray spectroscopy (EDS) analysis to study the composition and elemental distribution of the nanostructures. HADDAF images in Figure 5.7e to 5.7h display the edges of NTs which were cleaved and close to the Si(111) substrate. Corresponding element maps of Ga and Ni, as representative elements of inner core and outer shell, are shown in Figure 5.7i to 5.7l (and Figure A.1). Figure 5.7m to 5.7p show line scans of the Ni (red curve) and Ga (green curve) elemental distributions as a function of position along the NT diameter. The signals were extracted in the area enclosed by the dotted line and averaged along the NT long axis. These curves allowed us to quantify the thickness of the  $\text{Al}_2\text{O}_3/\text{Ni}$  shells on the nanotemplates (Methods). Thicknesses of the top and bottom edge of the cross section are highlighted by yellow and gray shaded regions in Figure 5.7m to 5.7p. Similar analysis was acquired at random spots of five NTs of each deposition, giving averaged thicknesses of  $11.5 \pm 2.4$  nm,  $14.0 \pm 2.1$  nm,  $29.4 \pm 4.1$  nm and  $12.2 \pm 1.5$  nm for depositions prepared with  $c = 1, 5, 7$  and 10, respectively. Only for  $c = 7$  did we observe that the Ni shell had a thickness that was comparable with the one deposited on the planar Si (100) substrate. In Figure A.2 we analyzed the step coverage as the ratio between sidewall and

## 5.2. ALD process 2, exploiting nickelocene, water and hydrogen plasma as reactants

top-surface film thickness for two samples. The values were  $\geq 88\%$ . The growth rates of shells were found to vary as a function of  $c$ . We explain the different growth rates and surface roughnesses by different growth mechanisms. The higher the number of nickel oxide steps  $c$  in the ALD sequence, the more the surface is oxidized, to which the hydrogen plasma pulse is applied. The drop in growth rate for  $c > 1$  in Figure 5.8a might indicate that we moved away from the PE-ALD regime, for which the growth rate is enhanced by reaction mechanisms involving plasma species, and entered a thermal ALD regime, which often exhibits a smaller growth rate [192, 193]. Furthermore, the decomposition of the metalorganic precursor is expected to be more pronounced on nickel than on nickel oxide [194]. Consequently the Ni-rich surface realized by  $c = 1$  promotes a larger growth rate. The discrepancies in growth rates for planar films and NT shells are attributed to the recombination of plasma species by collisions on the enlarged surface area provided by the nanotemplates. The recombination probability of hydrogen plasma species is higher on metallic nickel [195, 196] than on an oxidized surface [197, 198]. For  $c = 7$  we observed the lowest roughness in planar thin films and the highest growth rate on the high aspect ratio nanotemplates. We assume that in this deposition process a scenario was reached where, at each ALD cycle, a monolayer of nickel oxide was formed before the reducing hydrogen plasma step was inserted. Further studies on the growth rate of process with  $c = 7$  (Figure A.4) showed that the growth mechanism can be understood as ALD of  $\text{NiO}_x$  on a surface cyclically reduced to Ni by hydrogen plasma. For  $c = 10$ , the increase in growth rate in the planar film (Figure 5.4b) might suggest that a larger nickel oxide thickness was realized compared to samples with  $c = 5$  and  $c = 7$ , hence that the duration of the hydrogen plasma pulse was no longer optimized to reduce the deposited oxide layer. For the same reason, we speculate that the subsequent annealing treatment in hydrogen may have been less effective on the reduction-induced crystallization process of sample  $c = 10$  and thereby explain the less intense peaks observed in the X-ray diffractogram of Figure 5.5e.

### Magnetic properties of planar Ni thin films

In Figure 5.8a to 5.8e (and Figure A.3a and A.3b) we summarize different physical properties of Ni thin films measured as a function of the growth parameter  $c$ : the rms roughness measured by atomic force microscopy (AFM) (Figure 5.8a), the magnetization measured at room temperature by SQUID (Figure 5.8b), the room temperature resistivity measured by either a four-probe configuration or a van der Pauw configuration (Figure 5.8c), the AMR effect (Figure 5.8d) and the linewidth of the ferromagnetic resonance (FMR) (Figure 5.8e). In Figure 5.8f we depict the magnetoresistance measured on planar Ni thin films when an applied in-plane magnetic field  $\mu_0 H = 80$  mT was rotated (the angle  $\theta$  is defined between the current direction and  $\mathbf{H}$ ). We display the specific resistivity  $\rho(\theta)$  in terms of  $\frac{\Delta\rho(\theta)}{\rho} = \frac{\rho(\theta) - \rho(90^\circ)}{\rho(90^\circ)}$ . We observe a  $\cos^2(\theta)$  dependency as expected for the AMR effect. Depending on  $c$  we find maximum values of the relative AMR effect  $\frac{\Delta\rho(\theta)}{\rho}$  ranging from 4.7 down to 2.1 (Figure 5.8d). From field-dependent FMR measurement (Figure 5.8e) we extracted the effective magnetization  $M_{\text{eff}}$  by fitting the Kittel formula [57] to the observed resonance frequencies (white



branch in the color-coded spectra shown in Figure 5.8g). The spectra were taken by inductive measurements using a vector network analyzer (VNA) and reflected the scattering parameter  $S_{21}$  (Methods). Values of  $M_{\text{eff}}$  are summarized in Figure 5.8b. In Figure 5.8h we compare individual spectra taken at the same field of -80 mT for thin films deposited with different  $c$ . We observe a resonance frequency of 5.5 GHz and a narrow linewidth for  $c = 7$ . Extracted linewidths are summarized in Figure 5.8e. The narrowest FMR linewidth of  $\Delta f = 1.23$  GHz is

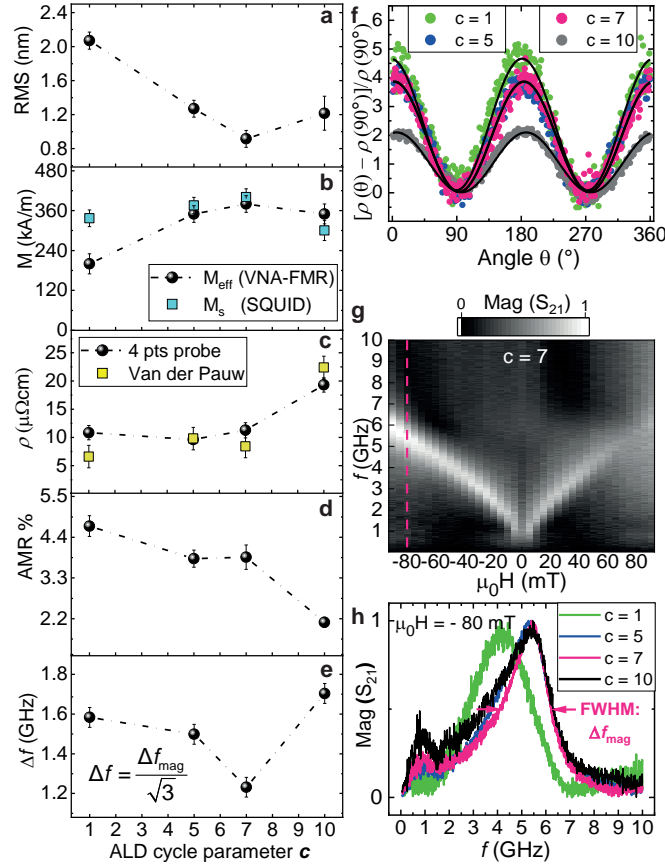


Figure 5.8 – Physical properties of the  $30 \pm 2$  nm thick Ni thin films as a function of  $c$ : (a) roughness, (b) effective and saturation magnetization  $M_s$  extracted from  $M(H)$  curves (Figure A.3b), (c) specific resistivity  $\rho$  extracted by two independent experiments, (d) relative AMR effect, and (e) linewidth  $\Delta f$ . (f) Magnetoresistance of four thin-film samples (see labels) measured at room temperature for a rotating in-plane field of 80 mT. (g) Magnitude of the scattering parameter  $S_{21}$  measured in an in-plane magnetic field by VNA-FMR on a thin film deposited with  $c = 7$ . White indicates large absorption. (h) Spectra taken at -80 mT on Ni thin films prepared with different  $c$  (see labels). For  $c \geq 5$  the resonance frequencies are found to be the same for different  $c$  but still the linewidth  $\Delta f_{\text{mag}}$  (indicated by horizontal arrows) varies as summarized in (e).

registered for a thin film prepared with  $c = 7$ . The same film exhibits the smallest rms roughness of 0.9 nm. We assume that the small roughness reduces the inhomogeneous linewidth broadening expected from two-magnon scattering induced by inhomogeneities and surface



## 5.2. ALD process 2, exploting nickelocene, water and hydrogen plasma as reactants

Table 5.2 – Geometrical parameters of NTs prepared with  $c = 7$ . S1 (S2) was used of magneto-transport (spin-dynamics) measurements.

Sample	$L$ ( $\mu\text{m}$ )	$D_{out}$ (nm)	$t$ (nm)
S1	$14.5 \pm 0.1$	$285 \pm 10$	$29.4 \pm 4.1$
S2	$14.5 \pm 0.1$	$280 \pm 20$	$29.4 \pm 4.1$

irregularities[180, 179]. Values of  $M_{\text{eff}}$  are found to be in good agreement with  $M_s$  measured by SQUID (Figure A.3b) in an in-plane magnetic field for  $c \geq 5$ . We measured a maximum effective magnetization  $M_{\text{eff}}$  of 380 kA/m for the sample deposited with  $c = 7$ . Within the error bar it agrees with an  $M_s$  of 400 kA/m measured by SQUID on the same sample. Consistent values indicate that additional magnetic anisotropies (magnetocrystalline anisotropy, surface anisotropy) do not play a significant role. The experimentally observed values are about 20 % smaller than the reported saturation magnetization of 490 kA/m of single-crystalline nickel [178]. For  $c = 1$ ,  $M_{\text{eff}}$  is found to be smaller than  $M_s$  by about 130 kA/m. The discrepancy indicates an out-of-plane anisotropy present in this sample. The lowest values of resistivity  $\rho$  that we measured on thin films with  $c = 1$  and  $c = 7$  amounted to about 7 to 8.4  $\mu\Omega\text{cm}$ . They were only slightly larger than the resistivity of 6.9  $\mu\Omega\text{cm}$  reported for bulk Ni at room temperature [177]. For  $c = 10$  we found  $\rho \sim 20 \mu\Omega\text{cm}$ . In the same sample we find the smallest AMR value of 2.1 %. We attribute the increased resistivity and the small AMR value for  $c = 10$  to inhomogeneities due to non-optimized ALD deposition.

### Transport properties of Ni nanotubes

Nickel NTs of the different sets of depositions were extracted from the nanotemplate substrates and transferred to either Si or glass substrates for further nanolithography and the integration of metallic leads. Then we performed magneto-transport and spin-dynamic experiments on individual NTs. In the following we report on data obtained on samples S1 and S2 (Tab. 5.1). In Figure 5.9 and Figure A.5, we report the field-dependent resistance  $R$  measured on different nanotubes. The data of nanotube S1 deposited with  $c = 7$  is displayed in Figure 5.9. The two voltage probes were separated by 7  $\mu\text{m}$ . The field was applied long the long axis. While decreasing the field from 80 mT (red curve), the magnetoresistance remains constant at about 27.4  $\Omega$  until  $\approx 30$  mT. From  $R$  we calculate a specific resistivity of  $7.8 \pm 2.8 \mu\Omega\text{cm}$ . This value is only about 13 % larger compared to the resistivity of bulk nickel. For further decreased  $H$ , the resistance decreases to a minimum value of 27.05  $\Omega$  at -2 mT. The maximum resistance is restored again for  $\mu_0 H \leq -30$  mT and remains constant until -80 mT. The blue curve is acquired with increasing field and shows hysteretic behavior near zero field. Considering the long axis of the NT to be the easy axis, a field of 80 mT is sufficient to saturate the spins along the current direction. This configuration corresponds to the scenario of maximum electron scattering for the AMR effect and the resistance is at its maximum value. For fields below 30 mT, the resistance decreases, which we attribute to the onset of reversal of the NT's magnetization. The reduced resistance suggests that spins tilt away from the current direction.

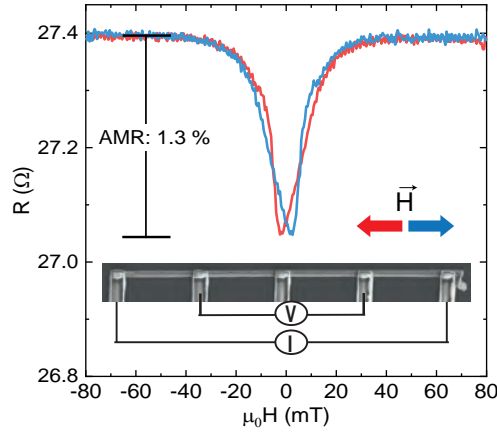


Figure 5.9 – Magnetoresistance of nanotube S1 measured as a function of a static magnetic field applied along the long NT axis. The inset shows an SEM micrograph of S1 contacted by 5 metallic leads made from a Au thin film via lift-off processing. Voltage ( $V$ ) and current ( $I$ ) probes are indicated.

For nanotubes of similar geometrical parameters the reversal of magnetization is predicted to occur via vortex domain wall formation [37]. Correspondingly spins would be aligned in an azimuthal direction around the NT, thereby taking an angle of 90 deg with respect to the current flow direction. This configuration corresponds to the scenario of minimum electron scattering for the AMR effect and is consistent with the observed reduction of  $R$  in the reversal regime. The relative variation of  $R$  corresponds to an AMR effect of about 1.3 % at room temperature in small fields. This value is larger by about 30 % compared to the best low-field AMR effect of Ni NTs reported previously (see the supplementary information of Ref. [26]).

### Spin dynamics in Ni nanotubes

The spin dynamics of individual NTs deposited with  $c = 7$  were studied after depositing them on a separate glass substrate (Figure 5.10a and Figure A.6). Coplanar waveguides (CPWs) made from 120 nm thick Au were fabricated by lift-off processing such that a NT was fully covered by the signal line of the CPW (Figure 5.10b). When a microwave current was applied to the CPW, a dynamic magnetic field  $h_{\text{rf}}$  was generated, which exerted a torque on the spins of the NT. To detect the induced spin precession we used microfocused BLS ( $\mu$ -BLS) [174]. We focused a laser beam through the glass substrate onto the NT from the backside. The backreflected light was analyzed by means of a Fabry-Perot interferometer for energy shifts due to inelastic scattering between the photon and the spin excitation. The chosen geometry with the NT covered by Au and the laser focused through the substrate prevented the NT from degrading due to the ambient atmosphere when heated by the focused laser beam. BLS measurements were performed in the central position of the NT. Figure 5.10c shows spectra obtained by  $\mu$ -BLS while sweeping the signal generator frequency from 1.5

## 5.2. ALD process 2, exploiting nickelocene, water and hydrogen plasma as reactants

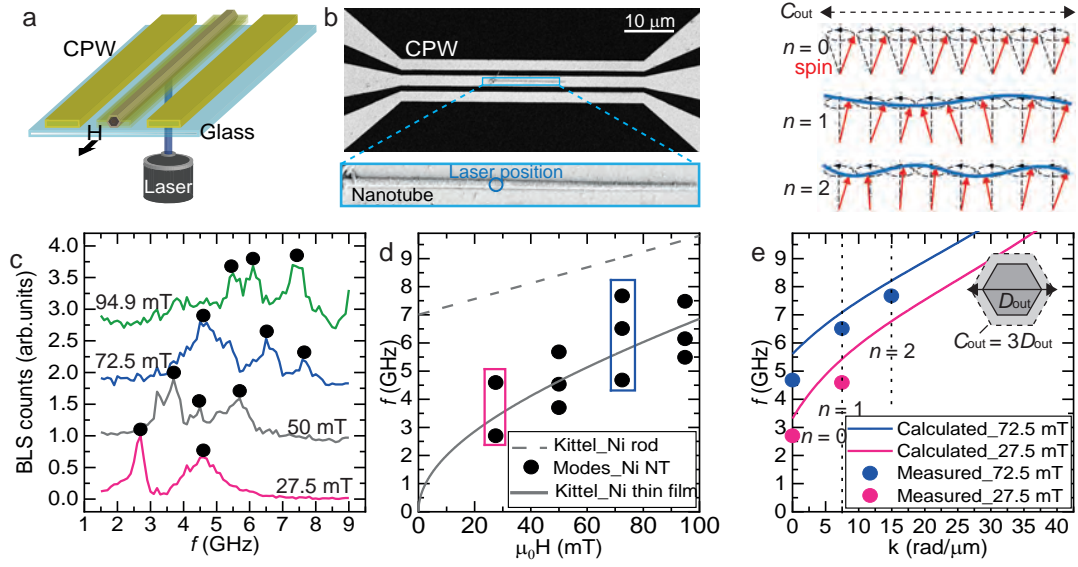


Figure 5.10 – (a) Sketch of the excitation-detection scheme to probe dynamic magnetization precession in individual NTs. The NT is covered by a coplanar waveguide (CPW) used for excitation. Laser light is focused through the transparent substrate onto the NT and the back reflected beam is analyzed by an interferometer. The field  $H$  is collinear with the long axis of the NT. (b) SEM micrograph of the gold CPW laying on the investigated Ni nanotube S2. Inset displays a magnified image of S2 under the signal line. (c) BLS spectra detected on S2 at different applied static magnetic fields. Black circles indicate peaks attributed to resonance frequencies (eigenmodes). (d) Extracted eigenmodes plotted as a function of the field and compared with the resonance frequency given by the Kittel equation [199] for a nickel rod (dotted gray line) and a nickel thin film (continuous gray line) using  $M_s = 380$  kA/m and a gyromagnetic ratio of 28.02 GHz/T. (e) Spin wave dispersion relations calculated for a 30 nm Ni thin film subjected to 27.5 mT (bottom line) and 72.5 mT (top line) by using the Kalinikos and Slavin formalism [68]. The resonance frequencies measured on S2 (boxes in d) are displayed as filled circles matching the color code of the calculated lines. The wave vector  $k = k_n$  was estimated assuming azimuthal confinement of DE modes with  $n = 0, 1, 2$  as illustrated above.

to 9 GHz in steps of 0.1 GHz. A static magnetic field was applied along the long axis and varied in steps from 27.5 (bottom curve) to 94.9 mT (top curve). At each increment we detect more than one peak in the spectrum, indicating multiple resonant magnon modes (black circles) whose eigenfrequencies vary systematically with  $H$ . In Figure 5.10d we summarize the resonance frequencies as a function of field. For comparison we show with a gray dotted and solid line the field-dependencies of FMR frequencies of a cylindrical nickel rod and a nickel film, respectively, which were calculated according to the Kittel formula [200] with a gyromagnetic ratio of 28.02 GHz/T and  $M_{\text{eff}} = 380$  kA/m, i.e. the value measured on the planar ALD-grown Ni film. Considering the shape-dependent demagnetization effects, we expect that the resonance frequency for uniform precession of a tube (FMR) resides below the FMR frequency of the rod. Indeed, measured eigenfrequencies of the NT fall below the

dashed curve. The observed field-dependencies of measured eigenmodes are similar to the slopes of the calculated curves (broken and dashed lines). In the following, we speculate on the origin of the multiple observed eigenmodes. We assume that the peculiar tubular shape of the NT gives rise to standing spin waves with wavelengths  $\lambda_n$  fulfilling the constructive interference condition  $n \times \lambda_n = 3 \times D$  along the azimuthal direction, where  $n$  is an integer number ( $n = 0, 1, 2, \dots$ ) and  $3 \times D$  is the circumference  $C$  of the hexagonal tube [25]. The allowed wave vectors amount to  $k_n = 2\pi/\lambda_n = n \times 2\pi/C$ . The mode with  $n = 0$  represents uniform spin precession. The wave vectors  $\mathbf{k}_n$  with  $n \geq 1$  point in azimuthal directions. They are orthogonal to the direction of magnetization  $\mathbf{M}$  of the NT which was found to be aligned with  $\mathbf{H}$  for  $\mu_0 H \geq 30$  mT (Figure 5.9). In such a configuration the eigenfrequency of a spin wave is expected to increase with increasing  $k$  (Damon-Eshbach mode configuration). In Figure 5.10e we plot the peak frequencies observed at 27.5 mT and 72.5 mT in that for each field value we attribute wavevectors  $k_n$  with increasing  $n$  to modes with increasing resonance frequency. The solid lines shown in Figure 5.10e reflect the spin wave dispersion relations  $f(k)$  calculated for a 30 nm-thick Ni film according to the formalism provided by Kalinikos and Slavin [68]. The experimental values follow the slope of  $f(k)$  expected for a thin film. However, the observed eigenfrequencies are smaller than the calculated ones at a given field. The remaining discrepancy could most likely be attributed to the different dynamic demagnetization effect of the tubular geometry compared to the planar film and the increased temperature of the NT in the laser focus. As the magnetization of Ni decreases with increasing temperature, lower resonance frequencies would indeed be expected. The results depicted in Figure 5.10 show that the Ni NTs form spin-wave nanocavities which impose discrete wave vectors and confine GHz microwave signals on the nanoscale. They can be produced in large ensembles of vertically aligned 3D nanomagnetic structures (Figure 5.6).

## Conclusions

Combining cycles of thermal ALD of nickel oxide with a single pulse of plasma-assisted hydrogen reduction, we both obtained the conformal growth typical of thermal ALD and exploited the low temperature reduction realized by a plasma treatment. The optimized ALD sequence resulted in conformal coating of vertically aligned nanotemplates with Ni where the growth rate was similar to the growth rate of the planar films. We achieved a specific resistivity of Ni of about  $8 \mu\Omega\text{cm}$  on both planar substrates and arrays of nanotemplates. The low-field AMR effect observed in the hysteretic regime of a nanotube amounted to 1.3 % at room temperature. The spin-wave damping was low allowing us to detect several standing spin wave modes which fulfilled the constructive interference condition in azimuthal direction of a nanotube. The Ni thin films and nanotubes thereby exhibited physical properties which make them promising for functional spintronic elements and magnonic applications in 3D device architectures.

### Methods

#### Plasma enhanced atomic layer deposition

Si (100) wafers were cleaved in pieces of circa 2 cm x 1 cm and employed as substrates for the deposition of planar Ni thin films. The Si substrates were cleaned using isopropanol, DI water and dried by blowing nitrogen. GaAs NWs were grown in a molecular-beam epitaxy reactor as previously reported [191] and used as nanotemplates for nanotubes depositions. They were inserted in the ALD chamber without previous treatment. Nickel growth experiments were performed in a hot wall Beneq TFS 200 ALD reactor, operated at a pressure of 4-5 mbar, under a 100 sccm constant flow of ultrahigh purity nitrogen, used both as carrier and purge gas. Prior to Ni growth, the Si (100) wafer pieces and GaAs nanowires were coated with 5 nm of  $\text{Al}_2\text{O}_3$  in the same ALD chamber, by alternating trimethylaluminium (TMA) and  $\text{H}_2\text{O}$  pulses for 65 cycles at a substrate temperatures of  $T = 170^\circ\text{C}$ . The pulse sequence was as follow: TMA/purge/ $\text{H}_2\text{O}$ /purge with durations of 200 ms/800 ms/500 ms/800 ms, respectively. The growth of nickel was performed using nickelocene ( $\text{Ni}(\text{C}_5\text{H}_5)_2$ ,  $\text{NiCp}_2$ ) as a precursor, water as the oxidant agent and an in-cycle plasma enhanced reduction step with hydrogen. Nickelocene and water were stored in stainless steel containers respectively at  $80^\circ\text{C}$  and room temperature to exploit their vapor pressure. The plasma was generated in a RF parallel plate system where one electrode with shower head was powered at 150 W, the other was grounded and hosted the sample substrates. Pure hydrogen was supplied through the plasma head with a flow rate of 300 sccm. An ALD cycle consisting of  $c$  steps of  $\text{NiCp}_2/\text{H}_2\text{O}$  leading to the formation of nickel oxide, followed by one step of plasma hydrogen, reducing nickel oxide to metallic nickel, was repeated  $n$  times. The ALD sequence can be summarized as follow:  $[(\text{NiCp}_2/\text{purge}/\text{H}_2\text{O}/\text{purge}) \times c + \text{H}_2 \text{ plasma}/\text{purge}] \times n$ . The pulse duration of nickelocene and water in the  $\text{NiCp}_2/\text{H}_2\text{O}$  part of the sequence was set as 2 and 6 s, respectively, and were followed by purge steps of 4 and 8 s. Hydrogen plasma was supplied for 4 s, followed by a nitrogen purge of 8 s. The thickness of the deposited thin films was measured imaging the films in cross section by SEM. The growth rate was calculated dividing the thickness by the total number of  $\text{NiCp}_2$  pulses  $c \times n$ . The first set of depositions was performed at different chamber temperatures of the range  $160 - 175^\circ\text{C}$ , keeping  $c = 1$  and  $n = 1000$ . A second set of samples was deposited at  $T = 170^\circ\text{C}$  to assess variations of growth rate on the number of  $\text{NiCp}_2/\text{H}_2\text{O}$  steps  $c$ , by keeping  $c \times n = 1000$ . To achieve thin films with thickness of around 30 nm, a third set of depositions was carried out where the ALD cycle number  $n$  was set as 1000, 475, 350, 175 for  $c$  set as 1, 5, 7, 10, respectively. After nickel deposition, the samples were annealed in the same ALD chamber at  $350^\circ\text{C}$ , for 5 hours, under a mixture of pure hydrogen and nitrogen with flow rates set to 50 sccm and 100 sccm, respectively. No significant thickness variations were registered in the planar thin films as a consequence of the annealing treatment.

#### Structural characterization and chemical analysis of the thin films and nanotubes

We report the properties of the annealed thin films. Their morphologies and thicknesses were investigated by scanning electron microscopy (SEM) and atomic force microscopy (AFM).

X-ray diffraction patterns were recorded in the glancing incidence mode, with incidence angle of  $2^\circ$ , on a Malvern Panalytical (Empyrean model) diffractometer using Cu K-alpha radiation. We used the HighScore plus software to determine the d-spacing between lattice planes and the peaks asymmetries. The analysis was based on a pseudo-Voigt fitting function. The lattice parameter  $a$  was derived from its geometrical relation with the d-spacing, assuming a cubic lattice. The morphology of the annealed nanotubes was investigated by both SEM and transmission electron microscopy (TEM), chemical element distribution was examined by scanning transmission electron microscopy (STEM) combined with energy dispersive X-ray spectroscopy (STEM-EDS). The TEM and STEM experiments were carried out using an FEI Talos electron microscope operated at 200 kV. The thicknesses of the NTs were extracted from EDS elemental 2D maps of Ga and Ni using Velox, which were analyzed along specific lines cutting the NT perpendicularly to the length. Line scans were smoothened by applying a Gaussian blur ( $\sigma = 1.0$ ) on the maps. The width of the line was 15-20 nm. Moving from the inner GaAs core towards the external NT radius, we assumed the ALD  $\text{Al}_2\text{O}_3/\text{Ni}$  shell to start at the point where the counts of the Ga element distribution (green curve) vanished to zero and to end at the point where the counts of the Ni element distribution (red curve) vanished to zero. We subtracted a nominal thickness of 5 nm ascribable to the  $\text{Al}_2\text{O}_3$  layer to obtain the Ni thickness.

### Investigation of physical properties

The static magnetic properties of the thin films were assessed using a SQUID system (MPMS-5, Quantum Design) operated at room temperature (300 K). Broadband spectroscopy of the deposited thin films was performed using a vector network analyzer (VNA) to sweep the frequency and record the ferromagnetic resonance (FMR) absorption spectra. The thin films were positioned on top of a CPW connected by microwave tips to a vector network analyzer (VNA). The 2-port VNA allowed us to generate a microwave magnetic field with frequencies ranging from 10 MHz to 10 GHz. The applied microwave current generated an in-plane rf-magnetic field perpendicular to the long axis of the CPW. The microwave with a power of  $-15$  dBm was applied at the port 1 of the CPW in order to excite magnetization precession. The precession-induced voltage was detected at port 2 via reading the scattering parameter  $S_{21}$  where the numbers 2 and 1 in the subscript denote the detection and excitation port. An external magnetic field  $\mu_0 H$  was swept from 90 mT to  $-90$  mT along the CPW's long axis. The linewidth of the resonant trace acquired at each field was divided by  $\sqrt{3}$  to obtain, with good approximation, the imaginary component of the FMR response. Resistivity measurements were performed with a KLA Tencor OmniMap RS75 four-point resistivity meter. Anisotropic magneto resistance (AMR) measurements were carried out in Van der Pauw four-point configuration [166]. The samples were bonded into a chip-carrier adapted for a room temperature probe station, equipped with a custom built 2D vector magnet assembly that allowed us to vary the in-plane applied field  $H$  under an angle  $\theta$ . AMR measurements were performed at room temperature applying a current of  $2 \mu\text{A}$  and a static in-plane magnetic field of 80 mT applied at an angle varying from 0 to 360 deg.

### Experiments on nanotubes with integrated leads and waveguides

The Ni nanotubes were transferred through an isopropyl alcohol solution on a 4-inch Si(100) wafer covered with 200 nm thick SiO<sub>2</sub> for the fabrication of metallic leads and on a 4-inch fused silica wafer for the fabrication of integrated coplanar waveguides (CPWs). On both wafers pre-patterned gold alignment markers were fabricated by photolithography via a custom developed software previously reported [45] to precisely localize randomly oriented nanotubes and generate the electron beam lithography pattern for integrated leads and CPWs. The metallic leads (CPWs) were prepared by electron beam lithography and a following sputtering (evaporation) of 5 nm Ti/ 400 (120) nm Au film. The CPWs' dimensions were chosen to enable impedance matching. The signal line, having a width of  $2.0 \pm 0.1 \mu\text{m}$  was separated by gaps of  $1.1 \pm 0.1 \mu\text{m}$  width from the  $2 \mu\text{m}$  wide ground lines. Magneto-transport properties of nanotubes were investigated at room temperature employing a probe station. The resistances were measured by 4 probe measurements with a magnetic field applied in parallel to the tube axis. Resistivities were calculated as  $\rho = \frac{R \times A}{l}$ , where  $l$  is the separation between the voltage leads and  $A$  is the cross-sectional area  $A$  of the shell around a NW. Correspondingly,  $A$  was calculated as the difference between an external hexagonal area with the hexagon's long diagonal  $D_{\text{out}}$  (measured by SEM) and an internal hexagonal area with diameter  $D_{\text{in}}$  (taken as  $D_{\text{out}} - 2 \times t$ , with  $t$  being the thickness of the Ni shell).

Spin wave eigenmodes were detected via Brillouin light scattering (BLS) microscopy at room temperature [174]. A coplanar microwave waveguide (CPW) was fabricated on the glass substrate on top of the NT and oriented in a way that the signal line covered the NT along its long axis. The end of the CPW was electrically bonded to a printed circuit board, which was connected to a signal generator (Anritsu MG3692C) applying a microwave current. The corresponding magnetic microwave field excited spin precession in the NT at a fixed frequency. The frequency was swept from 1.5 to 9 GHz. A monochromatic laser with a wavelength of 473 nm and power of 0.8 mW was focused through the sample backside to a diffraction limited spot using a specially corrected 100× objective lens with a large numerical aperture of NA = 0.85. The recorded BLS signal is proportional to the square of the amplitude of the dynamic magnetization at the position of the laser spot. The sample was mounted on a closed loop piezo stage which allowed a precise localization of the NT spots addressed in the experiments. The power was such that spin precession was excited in the linear regime. A magnetic field was applied parallel to the NT long axis via a permanent magnet.

### Acknowledgements

Funding by the German Science Foundation DFG via GR1640/5-2 in SPP1538 "Spin caloric transport" and SNF via grants 163016, BSCGI0\_157705, and NCCR QSIT is gratefully acknowledged. We thank Gözde Tütüncüoğlu and Didier Bouvet for excellent experimental support.





## 6 Atomic layer deposition of nickel-iron nanotubes and thin films

### 6.1 ALD process optimization for permalloy $\text{Ni}_{80}\text{Fe}_{20}$

#### 6.1.1 Pub. II: $\text{Ni}_{80}\text{Fe}_{20}$ nanotubes with optimized spintronic functionalities prepared by Atomic Layer Deposition

M. C. Giordano, S. Escobar Steinvall, S. Watanabe, A. Fontcuberta i Morral and D. Grundler

doi: arXiv:2105.01969

Publication Date: May 5, 2021

My contribution to this paper included the development of the nickel-iron deposition processes by ALD, the materials characterization, the fabrication of the nanotubes and of the electrical devices to characterize them, the AMR measurements, the micro-BLS measurements and data analysis. The TEM and STEM-EDX analysis were done with the help of S. Escobar Steinvall. The VNA-FMR data analysis was supported by Sho Watanabe.

#### Abstract

Permalloy  $\text{Ni}_{80}\text{Fe}_{20}$  is one of the key magnetic materials in the field of magnonics. Its potential would be further unveiled if it could be deposited in three dimensional (3D) architectures of sizes down to the nanometer. Atomic Layer Deposition, ALD, is the technique of choice for covering arbitrary shapes with homogeneous thin films. Early successes with ferromagnetic materials include nickel and cobalt. Still, challenges in depositing ferromagnetic alloys reside in the synthesis via decomposing the constituent elements at the same temperature and homogeneously. We report plasma-enhanced ALD to prepare permalloy  $\text{Ni}_{80}\text{Fe}_{20}$  thin films and nanotubes using nickelocene and iron(III) tert-butoxide as metal precursors, water as the oxidant agent and an in-cycle plasma enhanced reduction step with hydrogen. We have optimized the ALD cycle in terms of Ni:Fe atomic ratio and functional properties. We obtained

a Gilbert damping of 0.013, a resistivity of  $28 \mu\Omega\text{cm}$  and an anisotropic magnetoresistance effect of 5.6 % in the planar thin film geometry. We demonstrate that the process also works for covering GaAs nanowires, resulting in permalloy nanotubes with high aspect ratios and diameters of about 150 nm. Individual nanotubes were investigated in terms of crystal phase, composition and spin-dynamic response by microfocused Brillouin Light Scattering. Our results enable NiFe-based 3D spintronics and magnonic devices in curved and complex topology operated in the GHz frequency regime.

### Introduction

Magnetic thin films play an extremely important role in technologies such as data storage media[6], GMR sensors [8], spin valves[9] and magnetic MEMS [10, 11]. Among various magnetic materials, the NiFe alloy with stoichiometry  $\text{Ni}_{80}\text{Fe}_{20}$ , often referred as permalloy, is technologically relevant for the high permeability, low coercivity, near zero magnetostriction and significant anisotropic magnetoresistance (AMR). Permalloy plays a crucial role also in fundamental and applied research, as it is one of the standard materials chosen for the study of novel structures in nanomagnetism and magnonics[19, 13]. The latter is a modern branch of magnetism focused on the study of the spin waves, the collective excitations of magnetically ordered materials. Low energy consumption of spin waves and the potential compatibility with next-generation circuits beyond CMOS electronics make them a potential tool for non-charge based signal processing, communication and computation [13, 17, 14, 15]. In magnonics, the choice of magnetic materials would fall on those with low damping for spin waves, a property quantified by the phenomenological dimensionless Gilbert damping parameter  $\alpha$ . Standard materials would be insulating magnets as yttrium iron garnet (YIG) and polycrystalline metallic alloys as NiFe and CoFeB. While YIG offers the lowest spin wave damping, the choice of polycrystalline metallic alloys as NiFe and CoFeB meets better the needs for the industrial scalability of miniaturized and integrated systems[18].

So far,  $\text{Ni}_{80}\text{Fe}_{20}$  films have been mostly obtained by physical vapor deposition (PVD) methods, like sputtering [201, 202], electron beam evaporation and molecular beam epitaxy[203]. Other routes are electrodeposition[204, 205, 206, 207], spray coating and micromolding [208]. The PVD techniques are well suited for the production of planar nanostructures[209, 210]. However, they are limited by shadowing effects, which make them disadvantageous for the coating of three-dimensional (3D) nanostructures with high aspect ratios. Correspondingly, tetrapods for multi-branched 3D spintronics were prepared from polycrystalline cobalt by means of electrodeposition [211]. To further optimise the deposition of 3D permalloy coatings, it is a necessity to increase the step edge coverage. This enhances the deposition uniformity irrespective of the morphology of the deposited surface, and in turn opens up the study of new physical phenomena envisioned in 3D nanomagnetic systems [212, 18, 73, 20, 40, 21, 19, 39, 36]. Atomic layer deposition (ALD) is a chemical deposition technique offering the ideal conformality on 3D nanostructured surfaces. Here, the thin film formation is based on the repeated exposure of a substrate to separate precursors [27, 213]. These precursors react with the surface of a material one at a time in a sequential, self-limiting manner ensuring a good control of

thickness, excellent step coverage and conformality on substrates with different geometries and aspect ratios. The deposition of high- $\kappa$  gate oxides, such as  $\text{Al}_2\text{O}_3$ , has been one of the most widely examined areas of ALD and already advances microelectronics applications like metal-oxide semiconductor field effect transistors (MOSFET) and dynamic random access memories (DRAM)[30]. The processes for depositing metal layers using this technique, including ferromagnetic metals, still present technical challenges and are the subject of extensive research [31, 32, 33, 34, 35]. The main challenges are the limited number of suitable precursors, the difficulty in reducing metal cations and the tendency of metals to agglomerate into islands [35, 31]. We emphasize the difficulty, specific to a bi-metallic alloy, to identify a pair of precursors, one for each metal, which have a similar reactivity with the substrate surface, with a suitable co-reactant and in the same thermal range. Many works concern the use of ALD to obtain 3D nickel nanostructures such as nanotubes [22, 25, 88, 106, 26, 66]. The research on NiFe metallic alloys deposited by ALD is still in its infancy. Ferrimagnetic oxides  $\text{Ni}_x\text{Fe}_{3-x}\text{O}_4$  have been successfully prepared by exploiting the ALD process of the two binary oxides NiO and FeO [214]. In the work of Espejo *et al.* [46] a study was presented where a combination of supercyclic ALD with thermal reduction is used to achieve metallic alloy NiFe thin films. The process explored was based on nickelocene and ferrocene as Ni and Fe precursors, ozone as co-reactant to get an intermediate NiFe oxide and a further annealing in hydrogen. A linear dependency between the Ni : Fe precursors pulse ratio and the final stoichiometry was identified, leading to the achievement of a NiFe stoichiometry ( $\text{Ni}_{83}\text{Fe}_{17}$ ) very close to that of permalloy. The study showed how the initial amount of oxygen in the NiFe - oxide thin films obtained induces a significant dewetting phenomenon during the thermal reduction in hydrogen, compromising the morphology in the final metallic form.

In this work we present a different approach where the nickel (iron) sequence exploits nickelocene (iron(III) tert-butoxide) as metal precursors, water as the oxidant agent and an in-cycle plasma enhanced reduction step with hydrogen. Ni-rich NiFe thin films with different Ni:Fe atomic ratios were achieved by alternating  $m$  times the sequence for the deposition of nickel [215, 122] with a single sequence for the deposition of oxidized iron [101, 83, 84] and a post-deposition annealing treatment in hydrogen. The planar thin films so prepared were characterized in terms of a series of electric and magnetic properties considered significant for industrial applications and research. We quantitatively compare them with thin films that we prepared by the electron-beam evaporation using a commercial  $\text{Ni}_{80}\text{Fe}_{20}$  target material. The sequence with optimized Ni:Fe pulse ratio  $m$ , combined with the post-processing annealing treatment, allowed us to prepare thin films with the expected  $\text{Ni}_3\text{Fe}$  FCC phase ( $L1_2$ ) [216], stoichiometry extremely close to target permalloy ( $\text{Ni}_{80.4}\text{Fe}_{19.6}$ ) and physical properties unprecedentedly measured in permalloy thin films prepared by ALD. We measured a coercive field of 3.6 mT, a Gilbert damping of 0.013 and a resistivity of  $28 \mu\Omega\text{cm}$ . The process presented could contain the dewetting phenomenon on silicon substrates. As a proof of concept for the use of this technique to obtain nanostructured 3D coatings, we show the fabrication of NiFe nanotubes (NTs) using GaAs nanowires (NWs) with high aspect ratio and diameters lower than 100 nm as nanotemplates. We provide a chemical and structural characterization of the NiFe nanotubes, confirmed to have a permalloy shell. Lastly, the low damping of the

ferromagnetic shell allowed to measure several spin waves resonant modes in individual NTs investigated by micro-focused Brillouin Light Scattering ( $\mu$ -BLS). Our results show the remarkable potential of the ALD technique to venture the third dimension in nanomagnetism, magnonics and spintronics applications based on thin-film permalloy prepared by conformal coating technique.

### Results and discussion

#### Morphology of Nickel-Iron Thin Films and Nanotubes

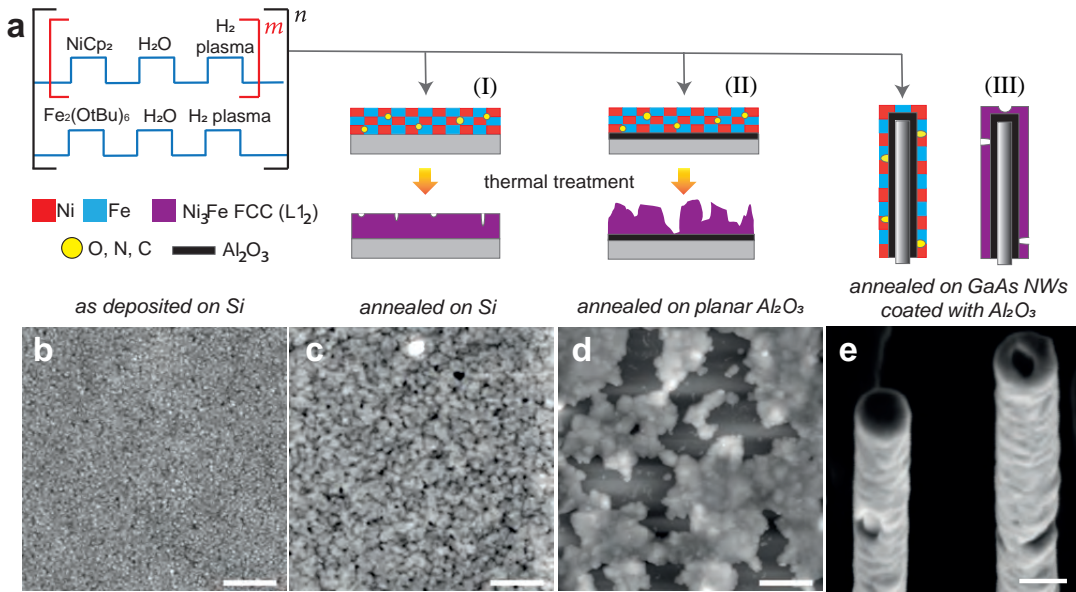


Figure 6.1 – Sketch describing the PEALD cycle for the deposition of  $\text{Ni}_{100-x}\text{Fe}_x$  originally contaminated by residual process elements (O, N, C); the annealing treatment to induce the  $\text{Ni}_3\text{Fe}$  FCC phase ( $L_{12}$ ) [216] formation and the observed morphology of the final thin films achieved, on different substrates. Atomic force microscopy performed on a  $2\ \mu\text{m} \times 2\ \mu\text{m}$  area of the sample prepared with samples with  $m = 6$  (b) as-deposited, (c) annealed on a bare Si substrate (color code range:  $-7\ \text{nm} \div +7\ \text{nm}$ ; scale bar: 400 nm), (d) annealed on a Si substrate pre-coated by 5 nm of  $\text{Al}_2\text{O}_3$  (color code range:  $-70\ \text{nm} \div +70\ \text{nm}$ ; scale bar: 400 nm). (e) SEM micrograph of  $\text{Ni}_{100-x}\text{Fe}_x$  nanotubes on GaAs nanowires pre-coated by 5 nm of  $\text{Al}_2\text{O}_3$ , after the annealing treatment (scale bar: 100 nm)

In Figure 6.1a we show schematically the process followed to prepare  $\text{Ni}_{100-x}\text{Fe}_x$  thin films by plasma enhanced atomic layer deposition (PEALD) on different substrates. The PEALD cycle combines a sequence for the deposition of nickel [122, 215] and a sequence for the deposition of  $\text{Fe}_2\text{O}_3$  [101, 83, 84], to which we have added a plasma hydrogen step. The Ni:Fe atomic ratio is controlled by the number  $m$  of the Ni sequence repetition between each Fe step. The NiFe process was tested on relevant substrates like planar Si wafers, both uncoated and coated with few nm of alumina  $\text{Al}_2\text{O}_3$ , and GaAs NWs encapsulated in a capping layer of

$\text{Al}_2\text{O}_3$ . The as-deposited films were annealed aiming at the  $\text{Ni}_3\text{Fe}$  FCC phase. We show the AFM analysis performed on the sample prepared with  $m = 6$  in its as-deposited (Figure 6.1b) and annealed state (Figure 6.1c) on a bare Si substrate. In Figure 6.1d we report the AFM analysis on the annealed thin film obtained with the same process, exploiting  $m = 6$ , on a Si substrate coated with 5 nm of alumina. Lastly, the SEM micrograph in Figure 6.1e depicts the morphology of the thin films deposited on GaAs/ $\text{Al}_2\text{O}_3$  nanowires, once the annealing treatment is performed. Depending on the type of substrate, the thermal treatment was found to have different effects on the final morphology of the thin films. In general, on a bare Si substrate, we observe that the annealing process is accompanied by a thin film thickness shrinkage of about 15 %, the formation of nanopores and a higher surface roughness with respect to the as-deposited thin film. For the reported sample the rms roughness increased from 1.2 nm to 2.1 nm in thin films with a thickness of 27 nm and 23 nm, respectively, in the as-deposited (Figure 6.1b) and annealed form (Figure 6.1b). For the Si substrate coated with alumina we observe that the thermal treatment is accompanied by a dewetting of the thin film. Here, the thin film arranges in agglomerates to reduce the film-substrate interface area and minimize the system energy. In Fig. 6.1e, we observe the formation of random localized small holes in the 3D shells achieved by coating GaAs/ $\text{Al}_2\text{O}_3$  NWs. Despite the unfavorable adhesion of  $\text{Ni}_{100-x}\text{Fe}_x$  on the alumina layer, the encapsulation of GaAs nanowires by few nm of this material was necessary to prevent the As evaporation during the annealing and to use them as a template for  $\text{Ni}_{100-x}\text{Fe}_x$  nanotubes.

The same experiments were done with Ni : Fe pulse ratio  $4 \leq m \leq 7$ . The thermal treatment was performed for all the compositions. All the samples were amorphous and contained remaining oxygen, nitrogen and carbon in their as-deposited state (Figure A.7). The types of morphology described are common to the samples obtained with the synthesis parameter  $m = 4, 5$  and  $6$ . For the sample prepared with  $m = 7$ , more nanoholes are observed (Figure A.8). For this sample, we speculate that phase segregation might have further increased its roughness and the number of holes during the annealing treatment and subsequent cooling, as its composition might be close to the  $\text{Ni}_{90}\text{Fe}_{10}$  phase segregation line in the Ni-Fe phase diagram [216].

### Growth rates

The choice of the homoleptic dinuclear iron(III) tert-butoxide complex ( $\text{Fe}_2(\text{OtBu})_6$ ) as iron precursor is motivated by its capability to react with water in a self-limiting manner. Furthermore, it reacts at temperatures ( $T = 130 - 180^\circ\text{C}$  [101, 83, 84]) compatible with the one for the deposition of nickel using nickelocene ( $\text{NiCp}_2$ ), water and plasma hydrogen as reactants ( $T = 170^\circ\text{C}$  in our system [215]). The growth rate of the processes exploiting  $m = 4, 5, 6$  and  $7$  was estimated to be (0.15, 0.17, 0.18 and 0.20) Å/ cycle, respectively. The recorded values were lower than those that would be obtained for the Ni and  $\text{Fe}_2\text{O}_3$  processes individually. We hypothesize that the deposition of Ni in the presence of  $\text{Fe}_2\text{O}_3$  is slower than in the presence of Ni alone and that a partial reduction of  $\text{Fe}_2\text{O}_3$  in the presence of Ni and plasma hydrogen during the deposition sequence occurs. The in-depth study of these co-deposition mecha-

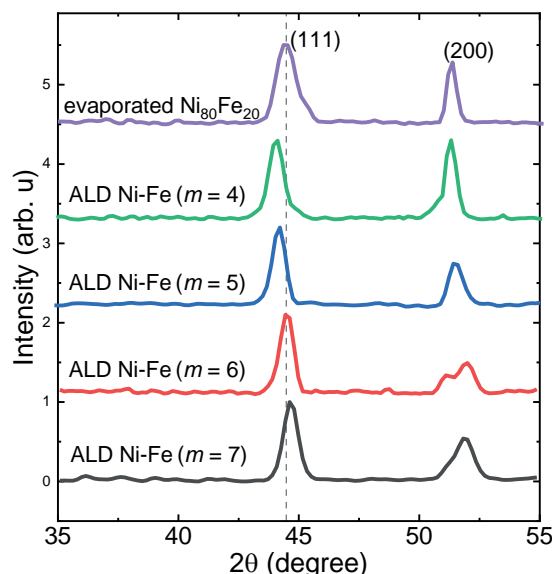


Figure 6.2 – X-ray diffractograms of 50 nm thick evaporated commercial  $\text{Ni}_{80}\text{Fe}_{20}$  thin film and of  $22 \pm 3$  nm thick  $\text{Ni}_{100-x}\text{Fe}_x$  films prepared by PEALD with  $m$  ranging from 4 to 7 (see labels). The position of the (111) reflection of the evaporated  $\text{Ni}_{80}\text{Fe}_{20}$  is marked by a dotted line. The ALD thin films were deposited at 170 °C on a silicon substrate and annealed at 380 °C.

nisms is not the subject of this work.

### Stoichiometry and XRD Analysis of $\text{Ni}_{100-x}\text{Fe}_x$ Thin Films

Figure 6.2 shows the X-ray diffractograms (XRD) of the annealed planar thin films prepared by PEALD with  $m = 4, 5, 6$  and 7, compared with the diffractogram of an electron-beam evaporated thin film of commercial permalloy  $\text{Ni}_{80}\text{Fe}_{20}$ , displayed at the top of the graph. The XRD results show mainly two peaks compatible with the (111) and (200) reflections of the  $\text{Ni}_3\text{Fe}$  FCC phase (ICSD code: 632930). The gray dotted line marks the position of the (111) reflection of the permalloy thin film evaporated from commercial target material. The (111) peak linewidth and position are reported in Table 6.1 for each sample. The small linewidth of the ALD thin films, compared to the reference permalloy sample, reflects a larger average crystallite size. We attribute this observation to the higher temperatures experienced both during the deposition and the annealing process by the samples prepared by ALD. The shift towards a lower angle of the (111) peak, going from the sample prepared with  $m = 7$  to the one prepared with  $m = 4$ , reflects the lattice expansion caused by the incorporation of a higher atomic percentage of Fe. The EDS analysis on the samples (Table 6.1) confirms this hypothesis. Remarkably, the Fe incorporation in the lattice is accompanied by the appearance of stress in the film, which involves strains of the (200) plane. This is particularly visible in the

## 6.1. ALD process optimization for permalloy $\text{Ni}_{80}\text{Fe}_{20}$

Table 6.1 – Stoichiometry and Crystallographic Information Extracted from the Energy Dispersive Spectra and the X-Ray Diffractograms of the Annealed  $\text{Ni}_{100-x}\text{Fe}_x$  Thin Films as a Function of the Ni:Fe Pulse Ratio  $m$ .

Ni:Fe pulse ratio $m$	Ni (at%)	Fe (at%) $x$	Phase	(111) peak position ( $^{\circ}2\theta$ )	FWHM (111) peak ( $^{\circ}2\theta$ )	Lattice parameter $a(\text{\AA})$
4	$76 \pm 5$	$24 \pm 5$	FCC ( $L1_2$ )	44.063	0.634	3.557
5	$78 \pm 5$	$22 \pm 5$	FCC ( $L1_2$ )	44.167	0.543	3.549
6	$81 \pm 5$	$19 \pm 5$	FCC ( $L1_2$ )	44.493	0.544	3.524
7	$83 \pm 5$	$17 \pm 5$	FCC ( $L1_2$ )	44.666	0.615	3.511
Evaporated $\text{Ni}_{80}\text{Fe}_{20}$	$80 \pm 5$	$20 \pm 5$	FCC ( $L1_2$ )	44.666	0.802	3.525

diffractogram of the sample prepared with  $m = 6$  where we can distinguish two components of the (200) reflection, possibly indicating that the stress relaxation was achieved by the formation of two domains with different (200) spacing. The lattice parameter of the samples was determined based on the (111) position (Table 6.1). The lattice parameter is found to scale linearly with the iron content in this composition range. The lattice constant of the permalloy thin film reference, as well as the Ni:Fe atomic ratio measured by the SEM-EDS analysis, match closely the parameters obtained for the ALD sequence with Ni:Fe pulse ratio  $m = 6$ . For this pulse ratio in particular we verified the stoichiometry and the phase of the  $\text{Ni}_{100-x}\text{Fe}_x$  thin films obtained in the shape of nanotubes, with higher resolution techniques. In Figure 6.3 (and Figure A.9) we report on the elemental analysis by STEM-EDX of NiFe nanotubes deposited with the Ni:Fe precursor pulse ratio  $m = 6$ . In particular, Figure 6.3a and Figure 6.3b show a bright field TEM image and the HADDAF image of the nanotube, respectively. In Figure 6.3c-h the element distribution of Ni, Fe, Ga, As, Al and O are reported. In Figure 6.3i and Figure 6.3j we report the elements distribution along the Line 1 and the EDX spectra of the Area 1 depicted in Figure 6.3b, respectively. The NT images present a very smooth Ni-Fe shell, with no visible holes on a length of 350 nm. The core remained pristine despite the high-temperature annealing conditions. The elemental maps show a homogeneous intermixing of Ni and Fe in the outer shell (Figure 6.3c,d), a GaAs nanowire core (Figure 6.3e,f) and an intermediate alumina capping layer (Figure 6.3g,h). Apart from the expected presence of oxygen in the  $\text{Al}_2\text{O}_3$  layer at the interface between the GaAs core and Ni-Fe shell, the oxygen is almost absent in the outer shell, indicating that the thermal treatment in hydrogen successfully reduced the oxidized metal atom (Figure 6.3h). The elemental distribution along Line 1 shows at which position, in the 3D object, we measure the higher counts of each element. This analysis confirms that the elements of the three layers did not intermix with each other. The chemical analysis of Area 1 gives the following composition: 77.4 at% Ni, 19.1 at% Fe, 3.5 at% O. The final NT material has, therefore, a Ni:Fe atomic ratio equal to 80.2 : 19.8 and a content of oxygen equal to 3.5 at%. For this batch of NTs, we estimated an average stoichiometry of  $\text{Ni}_{80.4 \pm 0.3}\text{Fe}_{19.6 \pm 0.3}$ , based on the analysis of five elements (Figure A.9, Table A.3). The amount of oxygen within the shell of the NTs has been quantified as  $(3.5 \pm 0.1)$

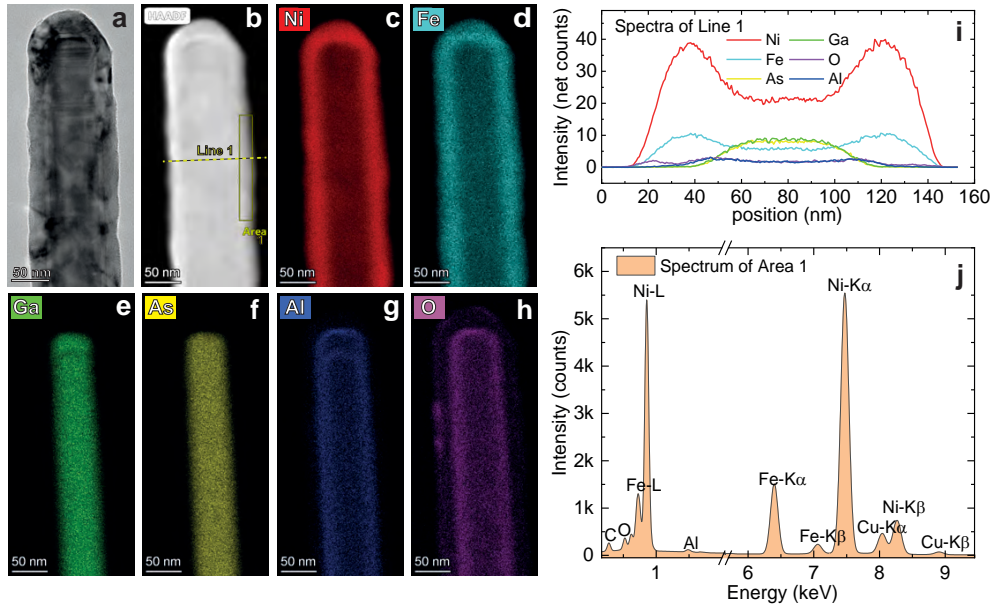


Figure 6.3 – (a)BF-TEM image and (b) HADDAF image of the extremity of a  $\text{Ni}_{100-x}\text{Fe}_x / \text{Al}_2\text{O}_3$  nanotube prepared by ALD on a GaAs nanowire. STEM-EDX maps of (c,d) the  $\text{Ni}_{100-x}\text{Fe}_x$  outer shell, (e,f) the GaAs nanowire core and (g,h) the  $\text{Al}_2\text{O}_3$  spacing layer (scale bars: 50 nm). The HADDAF image applies to all the STEM-EDX maps. (i) Elements distribution along the Line 1 and (j) elemental analysis of the Area 1 depicted in (b). The outer  $\text{Ni}_{100-x}\text{Fe}_x$  thin film were achieved with a deposition at 170 °C, using a Ni:Fe pulse ratio  $m = 6$ , and a further annealing treatment at 380 °C.

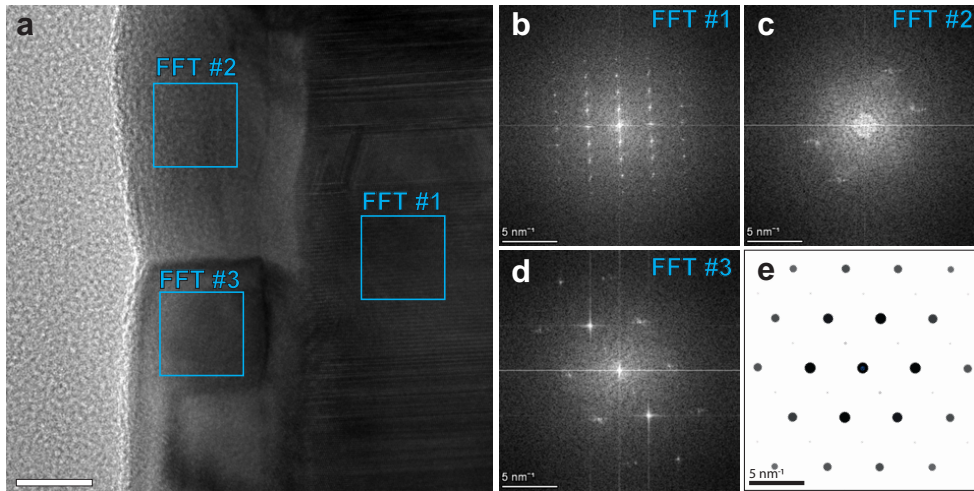


Figure 6.4 – (a) HR-TEM image showing the single-crystal GaAs core, the  $\text{Al}_2\text{O}_3$  spacer and the nanocrystalline  $\text{Ni}_{80}\text{Fe}_{20}$  outer shell (scale bar: 10 nm). Power spectra were extracted for the core (b) and the outer shell (c-d). (e) Simulated diffraction patterns for the  $\text{Ni}_3\text{Fe}$  FCC phase along the [101] zone axis, exhibiting the same symmetry as (d).



at% and is compatible with a small superficial passivation of the shell. After having verified the NTs stoichiometry, we analyzed the crystal phase of the 3D coatings by high resolution transmission electron microscopy (HR-TEM). Figure 6.4a shows an HR-TEM image of the interface between the  $\text{NiFe} / \text{Al}_2\text{O}_3$  nanotube, prepared by ALD, and the GaAs nanowire core. The NiFe shell results locally compact and smooth. We took the fast Fourier transform (FFT) of the HR-TEM image in correspondance of the regions highlighted by blue squares. The extracted power spectra of the spatial frequencies are reported in Figure 6.4 b-d, and show the single-crystal GaAs core (Fig. 6.4b), and the nanocrystalline  $\text{Ni}_{80}\text{Fe}_{20}$  shell (Fig. 6.4c,d). The observed pattern, and thus the orientation, varies between the  $\text{Ni}_{80}\text{Fe}_{20}$  grains in the shell, indicative of a random crystal orientation. The symmetry of the pattern from the bottom grain (Fig. 6.4d) can be matched to a simulated SAED pattern of  $\text{Ni}_3\text{Fe}$  (Fig. 6.4e) along a  $[101]$  zone axis. This shows that the nanotube growth occurs in a randomly oriented nanocrystalline fashion with the standard  $\text{Ni}_3\text{Fe}$  FCC permalloy crystal structure ( $L1_2$ ).

### Magnetic Properties of $\text{Ni}_{100-x}\text{Fe}_x$ Thin Films

The magnetic hysteresis of the as-deposited and annealed planar  $\text{Ni}_{100-x}\text{Fe}_x$  thin films prepared by PEALD was acquired at room temperature using a vibrating-sample magnetometer (VSM). The ALD thin films show a weak magnetization in their as-deposited state (Figure A.10). Here we focus on the hysteresis of the annealed thin films prepared with Ni:Fe pulse ratios  $m = 4, 5, 6$  and  $7$  and compare the results with the hysteresis of the reference  $\text{Ni}_{80}\text{Fe}_{20}$  thin film. Figure 6.5a (Figure A.11) shows the hysteresis obtained with the field applied in plane at zero (45) degrees with respect to the edge of a squared sample. In Figure 6.5b we report the extrapolated values of coercive field as a function of the synthesis parameter  $m$ . As a reference we report, in yellow, the range of coercive field values reported for permalloy in literature [217, 218] and, marked with a dotted line, the value measured of the reference  $\text{Ni}_{80}\text{Fe}_{20}$  thin film. The four ALD-prepared samples were ferromagnetic at room temperature and exhibited a coercive field which stayed constant with the angle of the applied field (Figure A.11). A hysteresis squareness  $M_r / M_s$  above 0.9 for samples prepared with  $m = 4, 5$  and  $6$  and equal to 0.8 for the sample prepared with  $m = 7$  indicated that the magnetocrystalline anisotropy overall was small in the alloys [62]. The coercive fields measured for ALD-prepared  $\text{Ni}_{100-x}\text{Fe}_x$  thin films ranged from 3.6 to 10 mT, with the minimum value being measured for the thin film prepared with Ni:Fe pulse ratio  $m = 6$ . The coercive field of 3.6 mT was close to the values of 0 to 3 mT expected for permalloy [217, 218] and one order of magnitude smaller than the value of 47.5 mT reported earlier for ALD-prepared  $\text{Ni}_{100-x}\text{Fe}_x$  thin films [46]. The evaporated reference  $\text{Ni}_{80}\text{Fe}_{20}$  thin film exhibited a coercive field of 0.36 mT. We attribute the discrepancy between the coercive fields of ALD-prepared  $\text{Ni}_{100-x}\text{Fe}_x$  and evaporated commercial  $\text{Ni}_{80}\text{Fe}_{20}$  thin films to the nanoholes induced by the annealing treatment of the ALD-prepared thin films. These defects might act, in fact, as domain wall pinning centers in the ALD-grown material, affecting the magnetization reversal. In Figure 6.5c, the saturation magnetization values  $M_s$  extracted from the hysteresis are shown as a function of  $m$ . The values of  $\mu_0 M_s$  rang from 0.80 to 1.22 T and are found to scale linearly with the content of iron, i.e.  $\mu_0 M_s$  decreases with

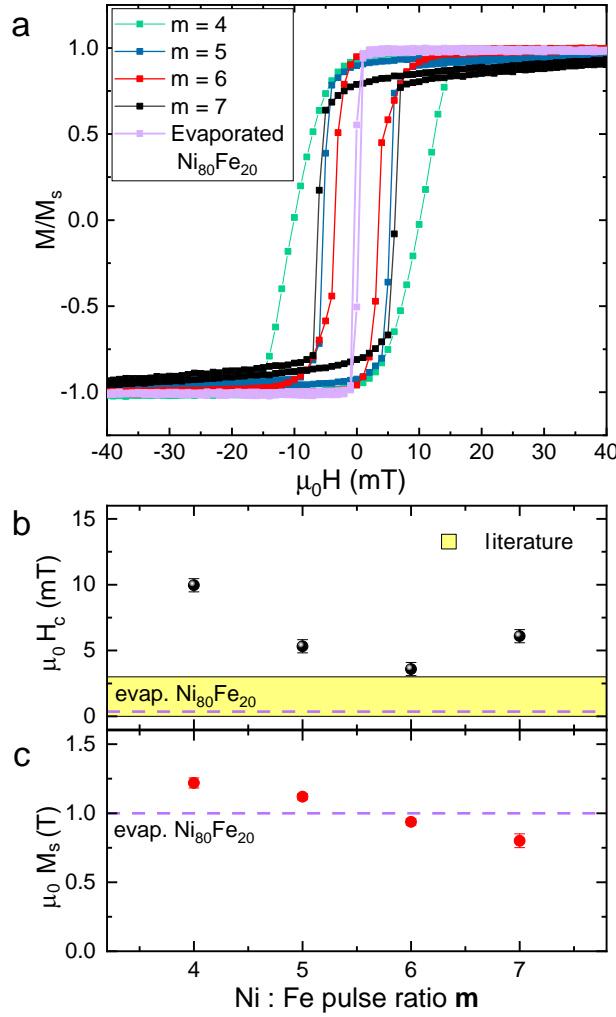


Figure 6.5 – (a) Hysteresis loops measured by VSM at room temperature of annealed  $\text{Ni}_{100-x}\text{Fe}_x$  thin films prepared by PEALD with Ni:Fe pulse ratios  $m = 4, 5, 6$  and  $7$  and of the reference  $\text{Ni}_{80}\text{Fe}_{20}$  thin film. Values of (b) coercive fields  $H_c$  and of (c) saturation magnetization  $M_s$  are plotted as a function of the ALD process parameter  $m$ . The literature values for permalloy  $H_c$  are indicated with a yellow range, while the values of  $H_c$  and  $M_s$  measured for the evaporated permalloy, prepared as a reference are displayed with a dashed line.

the Ni:Fe pulse ratio  $m$ . The sample prepared with  $m = 6$  exhibits a saturation magnetization  $\mu_0 M_s$  of 0.94 T, which is close to the value measured for permalloy (1T). In Figure 6.6a we show the measured values for the resistivity both in the as-deposited and in the annealed thin films, as a function of the parameter  $m$ . The resistivities measured for the annealed  $\text{Ni}_{100-x}\text{Fe}_x$  thin films have been obtained with a commercial 4-point probe station and a custom-built Van der Pauw configuration measurement setup. The dashed lines correspond to the resistivity values measured on a 20 nm thin film of evaporated  $\text{Ni}_{80}\text{Fe}_{20}$ . In Figure 6.6b, we depict the magnetoresistance measured on planar NiFe thin films when an applied in-plane magnetic field  $\mu_0 H = 80$  mT was rotated. The angle  $\theta$  was defined between the current direction and  $\mathbf{H}$ .

We display the anisotropic magnetoresistance (AMR) as  $\frac{\Delta\rho(\theta)}{\rho} = \frac{\rho(\theta) - \rho(90^\circ)}{\rho(90^\circ)}$ . The relative AMR effect is reported in Figure 6.6c as a function of the synthesis parameter  $m$ . We obtain resistivity values ranging from 154 to 172  $\mu\Omega\text{cm}$  for the as-deposited thin films. The resistivity is found to decrease with increasing  $m$ , hence with the nickel content. Our resistivity values are much lower when compared with those obtained in the process that used ozone as a co-reactant [46, 66]. We attribute this observation to the reduced amount of oxygen in the as-deposited material, that we achieved by the specific choice of precursors and reactants. The values of resistivity range from 23 to 34  $\mu\Omega\text{cm}$  in the annealed samples and do not vary significantly with  $m$ . At  $m = 6$  we get  $\rho = 28 \mu\Omega\text{cm}$ . The values measured match closely the ones measured for the evaporated commercial  $\text{Ni}_{80}\text{Fe}_{20}$ , marked by the dashed lines. Hence, we speculate that the nanoholes in the thin films seem to affect the magnetization reversal but do not have a significant impact on the current percolation paths. For the magnetotransport measurements we observe the  $\cos^2(\theta)$  dependency expected for the AMR effect. Depending on  $m$ , we find values of the relative AMR effect ranging from 4.4 to 9.5 %. In particular, for the samples prepared with Ni:Fe precursors pulse ratio  $m = 4, 5$  and 6, we register AMR% values in agreement with both what is expected for NiFe alloys in this compositional range [219] and the value measured on a reference thin film of evaporated commercial permalloy (dashed line). The process with  $m = 6$  results in the lowest spin-wave damping as will be discussed below. Here, we extract a relative AMR effect amounting to 5.6 %. This value is larger than the one found for low-damping ALD-grown Ni which was 3.9 % [215]. We register an anomalous high AMR% value for the NiFe sample prepared with  $m = 7$ , and we attribute it to the different morphology and the larger number of holes in the thin film.

Now we report on the magnetization dynamics of the annealed NiFe samples, investigated by broadband ferromagnetic resonance (VNA-FMR) spectroscopy (Figure 6.7). Figure 6.7a and b (Figure A.12) show the spectra of the evaporated commercial  $\text{Ni}_{80}\text{Fe}_{20}$  thin film and of the PEALD-grown thin films prepared with  $m = 6$  ( $m = 4, 5$  and 7), respectively. The spectra were taken by inductive measurements on a coplanar wave guide (CPW) using a vector network analyzer (VNA) and reflected the magnitude of the scattering parameter  $S_{21}$ . The black branches in the color-coded spectra represent resonant absorption at different values of the in-plane magnetic field. In Figure 6.7c we compare resonance frequencies for  $H > 0$  extracted from spectra of the PEALD prepared NiFe thin films and the evaporated permalloy. In Figure 6.7d we compare the individual spectra taken at the same field of 50 mT for thin films prepared with Ni : Fe pulse ratios  $m = 4, 5, 6$  and 7 and for the evaporated permalloy thin film used as a reference. The linewidth, extracted from a Lorentz fit, were employed to determine the damping parameter  $\alpha$  of the materials (Methods). In Figure 6.7e we report the linewidth  $\Delta$  of the imaginary component of  $S_{21}$  plotted as a function of the resonance frequency for the PEALD sample prepared with  $m = 6$  and the reference permalloy sample. The curves are fitted by a linear function, whose slope is twice the damping parameter  $\alpha$ . The estimated value is displayed in proximity of each curve. In Figure 6.7f we report the imaginary component of the scattering parameter  $S_{21}$  measured by VNA-FMR in a NiFe thin film prepared with  $m = 6$ , compared with the resonance spectra of the NT prepared with the same PEALD process, mea-

sured at its central position by microfocused Brillouin Light Scattering ( $\mu$ -BLS). The resonance frequencies are indicated with open red circles. Both curves were acquired at  $\mu_0 H = 90$  mT. Figure 6.7g shows a SEM micrograph of the coplanar wave guide (CPW) employed to excite spin waves in an individual NT and the NT investigated lying parallel to the CPW's signal line. The blue circle indicates the position of the  $\mu$ -BLS blue laser employed to detect the excited spin waves modes. The direction of the external applied field is indicated with a yellow arrow. Our results show that in the case where we employed a Ni : Fe pulse ratio  $m = 6$  in the ALD deposition process, we achieve the closest values of field-dependent frequencies (Figure 6.7c) and Gilbert damping  $\alpha$  (Figure 6.7d) to those measured for a standard permalloy thin film of stoichiometry  $\text{Ni}_{80}\text{Fe}_{20}$ . These results agree with the chemical and structural analysis presented for this sample. The hole like features in the PEALD film certainly increase the value of the Gilbert damping due to two-magnon scattering [180, 179]. A higher  $\alpha$  value in sample  $m = 6$  is therefore explained. The permalloy NTs achieved with this process show much richer spectra when compared to the PEALD-prepared nickel nanotubes [215] and we attributed this result to the lower damping. We attribute this to the amount of oxygen in the as deposited material, that has been drastically reduced with this choice of precursors and reactants. The values of resistivity range from 23 to 34  $\mu\Omega\text{cm}$  in the annealed samples and do not show a significant dependence on the parameter  $m$ . At  $m = 6$  we get  $\rho = 28 \mu\Omega\text{cm}$ . The values measured match really closely the ones measured for the evaporated commercial  $\text{Ni}_{80}\text{Fe}_{20}$ , marked by dashed lines. Hence, we hypothesize that the presence of nanopores in the thin films, which seems to affect their magnetization, does not have a significant impact on the amount of current percolation paths. For the magnetotransport measurements we observe the  $\cos^2(\theta)$  dependency expected for the AMR effect. Depending on  $m$ , we find maximum values of the relative AMR effect ranging from 4.4 to 9.5. In particular, for the samples prepared with Ni:Fe precursors pulse ratio  $m = 4, 5$  and 6, we register AMR% values in agreement both with what expected for NiFe alloys in this compositional range [219] and with the value measured in a reference thin film of evaporated commercial permalloy (dashed line). We register an anomalous high value for the NiFe sample prepared with  $m = 7$  and we attribute it to the different morphology achieved and the larger presence of holes in the thin film. Now we report on the magnetization dynamics of the annealed NiFe samples, investigated by broadband ferromagnetic resonance (FMR) spectroscopy (Figure 6.7). Figure 6.7a and b (Figure A.12) show the spectra of the evaporated commercial  $\text{Ni}_{80}\text{Fe}_{20}$  thin film and of the PEALD-grown thin films prepared with  $m = 6$  ( $m = 4, 5$  and 7), respectively. The spectra were taken by inductive measurements on a coplanar wave guide (CPW) using a vector network analyzer (VNA) and reflected the magnitude of the scattering parameter  $S_{21}$ . The black branches in the color-coded spectra represent resonant absorption at different values of the in-plane magnetic field. In Figure 6.7c we compare resonance frequencies for  $H > 0$  extracted from spectra of the PEALD prepared NiFe thin films and the evaporated permalloy. In Figure 6.7d we compare the individual spectra taken at the same field of 50 mT for thin films prepared with Ni:Fe pulse ratios  $m = 4, 5, 6$  and 7 and for the evaporated permalloy thin film used as a reference. The linewidths  $\Delta f$ , extracted from fitting a Lorentzian function to the spectra  $S_{21}$ , were employed to determine the damping parameter  $\alpha$  of the materials (Methods). In Figure 6.7e we report

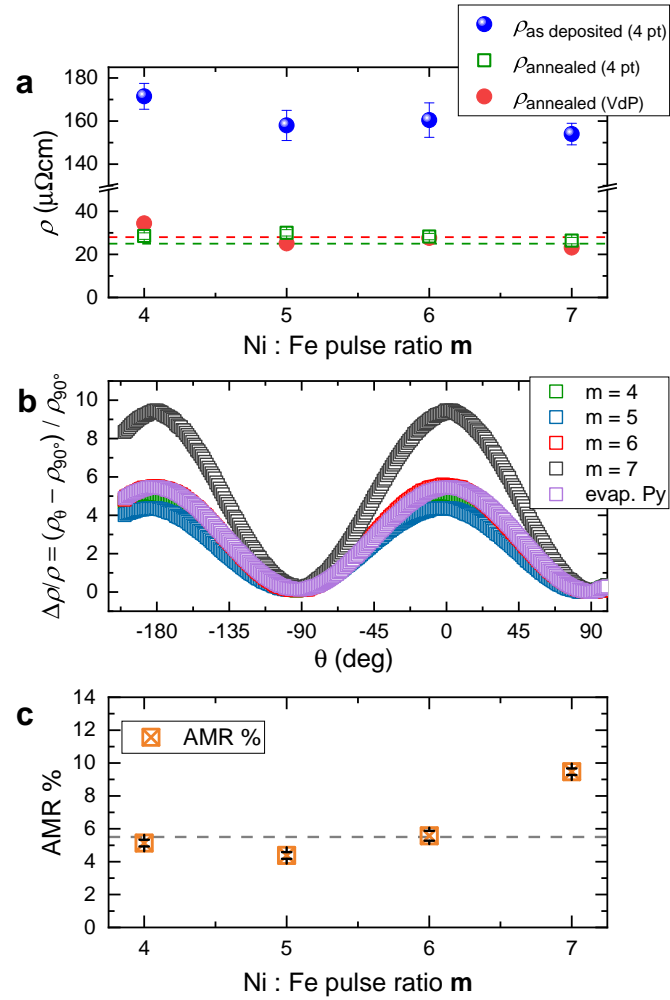


Figure 6.6 – (a) Resistivity values of the as-deposited and annealed ALD-prepared  $\text{Ni}_{100-x}\text{Fe}_x$  thin films, compared with the value measured for a 20 nm evaporated permalloy thin film (dashed line). (b) Magnetoresistance measured at room temperature for a rotating in-plane field of 80 mT and (c) relative AMR effect extrapolated of the ALD-prepared  $\text{Ni}_{100-x}\text{Fe}_x$  thin films and a 20nm - thick evaporated commercial  $\text{Ni}_{80}\text{Fe}_{20}$  thin film used as a reference.

$\Delta f$  as a function of the resonance frequency for the PEALD sample prepared with  $m = 6$  (upper curve) and the reference permalloy sample (lower curve). The curves are fitted by a linear function, whose slope is twice the damping parameter  $\alpha$  [199]. The extracted values  $\alpha$  are displayed next to the curves. The value  $\alpha = 0.013$  obtained for the ALD-grown thin film is larger than 0.009 detected on the reference NiFe film. The hole like features in the PEALD film most likely induce two-magnon scattering [180, 179] and increase  $\alpha$  beyond 0.009. In Figure 6.7f we show the imaginary component of the scattering parameter  $S_{21}$  measured on a NiFe thin film prepared with  $m = 6$  by VNA-FMR and compare it with the spectrum obtained by microfocused Brillouin Light Scattering ( $\mu$ -BLS) on a nanotube prepared with the same PEALD process. The spectrum was measured at the central position of the NT as depicted in

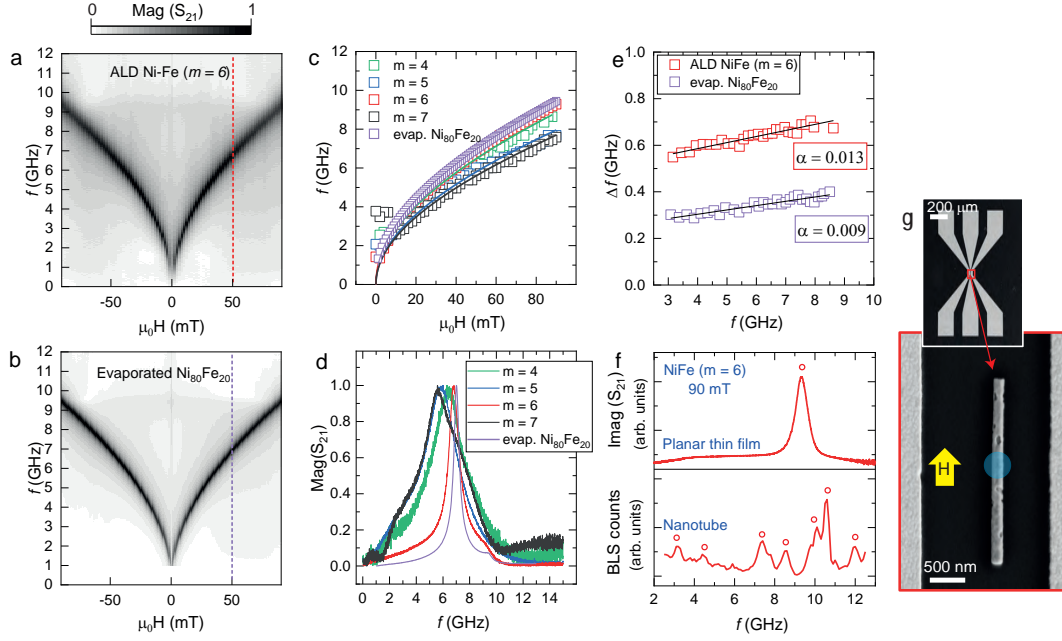


Figure 6.7 – Magnitude of the scattering parameter  $S_{21}$  measured at  $T = 300$  K in an in-plane magnetic field by VNA-FMR on (a) the NiFe thin film prepared by PEALD with  $m = 6$  and (b) the e-beam evaporated thin film of  $\text{Ni}_{80}\text{Fe}_{20}$  used as a reference. Black indicates large absorption. (c) Field dependent resonance frequencies (symbols) extracted from VAN-FMR spectra. The lines depict fits using the Kittel equation [57] and are guides to the eye. (d) Individual spectra extracted at +50 mT and fitted by a Lorentzian function for the NiFe thin films prepared by PEALD using  $m = 4, 5, 6$  and  $7$  and the evaporated (evap.)  $\text{Ni}_{80}\text{Fe}_{20}$  thin film. (e)  $\Delta f$  reflecting the linewidth of the imaginary component of  $S_{21}$  for the PEALD film prepared with  $m = 6$  and the reference permalloy film plotted as a function of the resonance frequency. Each dataset is fitted by a linear function, whose slope is twice the damping parameter  $\alpha$ . (f) Imaginary component of the scattering parameter  $S_{21}$  measured by VNA-FMR on the NiFe thin film prepared with  $m = 6$  (top) and  $\mu$ -BLS spectrum acquired on the central position of the NT prepared with the same process (bottom). The planar thin film is magnetized with an in-plane magnetic field of 90 mT, while the nanotube is magnetized along its long axis with a field of 90 mT. The resonance frequencies are indicated with red circles. (g) SEM micrographs of both the CPW employed to excite spin waves and the investigated NT lying parallel to the CPW's signal line. The blue circle indicates the position of the blue laser employed to detect the excited spin waves eigenmodes. The yellow arrow represents the direction of the in-plane magnetic field.

Figure 6.7g. Both spectra were acquired at  $\mu_0 H = 90$  mT. Resonance frequencies are indicated with open red circles. Figure 6.7g shows a SEM micrograph of both the coplanar wave guide (CPW) employed to excite the spin precession in the individual NT and the NT parallel to the CPW's signal line. The blue circle indicates the position of the blue laser employed to detect the excited spin waves modes via  $\mu$ -BLS. The direction of the external applied field is indicated with a yellow arrow. The  $\mu$ -BLS spectrum of the permalloy NT is much richer than the ones

reported for PEALD-prepared nickel nanotubes [215]. The series of resonance peaks indicate confined spin waves as previously reported for Ni NTs [215]. We attribute the larger number of resolved spin-wave resonances in Figure 6.7f to the lower damping of NiFe compared to Ni. A detailed discussion about the nature of the additionally observed modes is beyond the scope of this paper.

Our results show that in the case of the Ni:Fe pulse ratio  $m = 6$  in the ALD deposition process we achieve field-dependent resonance frequencies (Figure 6.7c) and a Gilbert damping parameter  $\alpha$  (Figure 6.7d) which are close to those values measured for a standard permalloy thin film of stoichiometry  $\text{Ni}_{80}\text{Fe}_{20}$ . When studying the linewidths of field dependent resonant modes detected locally on the NT by means of  $\mu$ -BLS, we determined a Gilbert damping parameter of 0.01 (Figure A.13). The  $\mu$ -BLS technique allowed, in fact, to focus the laser on a defect-free region of the nanostructure. Thereby extrinsic contributions to the peak broadening were less dominant. The spin-wave spectroscopy confirmed the good quality of the ALD-grown permalloy and its reduced damping compared to ALD-grown Ni [215], opening new possibilities for applications in 3D nanomagnonics.

### Conclusions

NiFe thin films with different Ni:Fe atomic ratios were prepared by alternating  $m$  times the sequence for the deposition of nickel with a single sequence for the deposition of oxidized iron and a post-deposition annealing treatment in hydrogen. We achieved an optimized stoichiometry via the Ni:Fe pulse ratio  $m = 6$ . By a further annealing step the resistivity of the optimized permalloy (Py) thin films was  $28 \mu\Omega\text{cm}$  and the measured spin wave damping 0.013. A high relative AMR of 5.6 % was observed in the ALD-grown Py thin film with lowest spin wave damping. The high quality of the films allowed us to measure multiple resonant spin-wave eigenmodes in an individual Py nanotube. In the case of Py NTs the spectra were richer compared to the previously reported ALD-grown Ni NTs substantiating the lower damping of Py. The permalloy thin films and nanotubes thereby exhibited physical properties that make them promising for functional spintronic elements and magnonic applications in 3D device architectures.

### Methods

#### Plasma Enhanced Atomic Layer Deposition of NiFe and Subsequent Annealing

Si (100) wafers were cleaved in pieces of about 2 cm x 2 cm and employed as substrates for the deposition of planar NiFe thin films. The Si substrates were cleaned with the following procedure: 15 min in  $\text{H}_2\text{O} : \text{NH}_4\text{OH} (28\%) : \text{H}_2\text{O}_2 (5:1:1)$  at  $70^\circ\text{C}$ ; 10 s in  $\text{HF} (49\%) : \text{H}_2\text{O} (1:10)$  at room temperature; 15 min in  $\text{H}_2\text{O} : \text{HCl} (37\%) : \text{H}_2\text{O}_2 (6:1:1)$  at  $75^\circ\text{C}$ . GaAs NWs were grown on Si (111) substrates as fully described in references [161, 162] and used as nanotemplates. They were inserted in the ALD chamber without previous treatment. The Si wafers were used both as bare substrates and coated with a 5 nm - thick layer of ALD alumina ( $\text{Al}_2\text{O}_3$ ) as previ-

ously described [215]. GaAs NWs were employed pre-coated with alumina. Nickel-Iron growth experiments were performed in a hot wall Beneq TFS 200 ALD reactor, operated at a pressure of 4-5 mbar, under a 100 sccm constant flow of ultrahigh purity nitrogen, used both as carrier and purge gas. We used nickelocene ( $\text{NiCp}_2$ ), iron(III) tert-butoxide complex ( $\text{Fe}_2(\text{OtBu})_6$ ) and water as precursors and reactant. They were stored in stainless steel containers at 80°C, 100°C and room temperature, respectively, to exploit their vapor pressure. The chamber temperature was set as 170 °C. The plasma was generated in an RF parallel plate system and powered at 150 W. Pure hydrogen was supplied through the plasma head with a flow rate of 300 sccm. The PEALD sequence can be summarized as follows:  $[(\text{NiCp}_2/\text{purge}/\text{H}_2\text{O}/\text{purge}/\text{H}_2 \text{ plasma}/\text{purge}) \times m + (\text{Fe}_2(\text{OtBu})_6/\text{purge}/\text{H}_2\text{O}/\text{purge}/\text{H}_2 \text{ plasma}/\text{purge})] \times n$ . The corresponding steps duration was the following:  $[(2\text{s}/4\text{s}/4\text{s}/8\text{s}/4\text{s}/8\text{s}) \times m + (2\text{s}/4\text{s}/4\text{s}/8\text{s}/4\text{s}/8\text{s})] \times n$ . NiFe thin films with thickness of  $25 \pm 3$  nm were prepared setting  $m = 4, 5, 6$  and  $7$  and using  $n = 300, 250, 215$  and  $190$ , respectively, in order to keep the total number of precursors pulses  $(m + 1) \times n$  equal to  $\sim 1500$ , for each process. The thickness of the deposited thin films was measured by imaging the films in cross section by SEM. The growth rate was calculated by dividing the thickness by the total number of precursors pulses  $(m + 1) \times n$ . Thin films prepared on Si, Si /  $\text{Al}_2\text{O}_3$  planar substrates and GaAs /  $\text{Al}_2\text{O}_3$  NWs were thermally treated at 380°C for 2h 30 min under forming gas  $\text{N}_2 - \text{H}_2$  with flow 300 sccm. This temperature was reported to be sufficient to activate the reduction of iron oxide in the presence of nickel [46].

Reference permalloy thin films were prepared in an electron-beam evaporator Leybold Optics LAB 600H, using commercial targets of  $\text{Ni}_{80}\text{Fe}_{20}$ . A 50 nm - thick thin film was used as a reference for all the comparative analysis shown in the paper, except for the measurements of resistivity and anisotropic magnetoresistance. Here we employed a reference  $\text{Ni}_{80}\text{Fe}_{20}$  sample with a thickness of 20 comparable to the one of annealed NiFe samples prepared by ALD.

### **Structural Characterization and Chemical Analysis of the Thin Films and Nanotubes**

We report the properties of the annealed thin films. Their morphologies and thicknesses were investigated by scanning electron microscopy (SEM) from Zeiss and atomic force microscopy (AFM) from Bruker. Chemical analysis of thin films were performed by SEM combined with energy dispersive X-ray spectroscopy (SEM-EDS) on a Zeiss Merlin system. X-ray diffraction spectra were recorded in the glancing incidence mode on a Malvern Panalytical (Empyrean model) diffractometer with incidence angle of  $0.8^\circ$ . The morphologies of the annealed nanotubes was investigated by both SEM and transmission electron microscopy (TEM), chemical element distribution was examined by scanning transmission electron microscopy (STEM) combined with energy dispersive X-ray spectroscopy (STEM-EDS). The TEM and STEM experiments were carried out using an FEI Talos electron microscope operated at 200 kV. The thicknesses of the NTs were extracted from EDS elemental 2D maps of Ga and Ni using the software Velox, as previously discussed [215]. The diffraction pattern was simulated using the software JEMS, for the Ni:Fe crystal structure with atomic ratio 75:25.



### Investigation of Physical Properties of Thin Films

The static magnetic properties of the thin films were assessed using a Microsense EZ-7 vibrating sample magnetometer (VSM) operated at room temperature. The saturation magnetization  $M_s$  values were determined from the VSM hysteresis by normalizing the magnetization  $M$  (emu) measured at 150 mT by the volume of the material  $V_m$ . For the calculation of  $V_m$  the estimated volume of holes measured by AFM has been subtracted. Resistivity measurements were performed with a KLA Tencor OmniMap RS75 four-point resistivity meter. Anisotropic magnetoresistance (AMR) measurements were carried out in the van der Pauw four-point configuration [166] in a custom-built set-up described previously [215]. AMR measurements were performed at room temperature applying a current of 10  $\mu\text{A}$  and a static in-plane magnetic field of 80 mT applied at an angle varying from 0 to 360°. Broadband spectroscopy of the deposited thin films was performed using a vector network analyzer (VNA), sweeping the frequency and recording the ferromagnetic resonance (FMR) absorption spectra. The thin films were positioned on top of a CPW connected by microwave tips to the VNA. The 2-port VNA generates a microwave current providing an in-plane rf-magnetic field perpendicular to the long axis of the CPW. The frequency of the microwave magnetic field was swept from 10 MHz to 15 GHz. The microwave with a power of –10 dBm was applied at port 1 of the CPW in order to excite magnetization precession. The precession-induced voltage was detected at port 2 via the scattering parameter  $S_{21}$  where the numbers 2 and 1 in the subscript denote the detection and excitation port. An external magnetic field  $\mu_0 H$  was swept from 90 mT to –90 mT along the CPW's long axis. The field dependent frequency behavior was assessed by fitting the data by the Kittel equation [200]. The Gilbert damping parameter  $\alpha$  was determined by plotting the linewidth  $\Delta f$  against the corresponding resonance frequencies. The curve was fitted by a linear function, whose slope is twice the damping parameter  $\alpha$ . The  $\Delta f$  of the imaginary component of the scattering parameter  $S_{21}$  was estimated dividing by  $\sqrt{3}$  the linewidth of the magnitude component of  $S_{21}$  ( $\Delta f_{\text{Mag}}$ ) [13]. The metallic coplanar wave guide (CPW) for the investigation of the NT was fabricated by electron beam lithography and a following evaporation of 5 nm Ti/ 120 nm Au film. The signal line, having a width of  $2.5 \pm 0.1 \mu\text{m}$  was separated by gaps of  $1.7 \pm 0.1 \mu\text{m}$  width from the ground lines. The CPW was fabricated around individual NTs placed parallel to the signal line and electrically bonded to a printed circuit board, which was connected to a signal generator (Anritsu MG3692C) applying a microwave current. The corresponding magnetic microwave field excited spin precession in the NT at a fixed frequency. Spin wave eigenmodes were detected via microfocused Brillouin light scattering (BLS) microscopy at room temperature [174]. A monochromatic laser with a wavelength of 473 nm and power of 0.5 mW was focused directly on top of the NT.

### Acknowledgements

We thank SNF for funding our research via grants 163016, BSCGI0\_157705, NCCR QSIT and 197360. We thank Didier Bouvet, Bi Wen Hua and Ivica Zivkovic for the excellent experimental support.

## 6.2 Static and dynamic magnetization in $\text{Ni}_{80}\text{Fe}_{20}$ nanotubes

### 6.2.1 Pub.III: Dipolar-exchange spin waves confinement in ALD-prepared permalloy $\text{Ni}_{80}\text{Fe}_{20}$ nanotubes

The following chapter focuses on the study of spin dynamics in individual permalloy nanotubes prepared by the plasma-enhanced atomic layer deposition process discussed in the previous section.

Here a draft version of a manuscript is reproduced.

M. C. Giordano, M. Hamdi, A. Mucchietto and D. Grundler

My contribution to this work included the fabrication of permalloy nanotubes by means of an ALD process optimized in the framework of this thesis, the fabrication of the electrical devices to characterize them, the design and execution of the micro-focused Brillouin Light Scattering ( $\mu$ -BLS) measurements, the coordination of the micromagnetic simulation work with the experimental research plan and the data analysis. The micromagnetic simulations were executed by Mohammad Hamdi. The micro-BLS measurements were supported technically by Andrea Mucchietto. The analysis of experimental and simulation data was partially supported by both M. Hamdi and A. Mucchietto.

### Introduction

Advances in magnonics [17, 13, 220, 18] fostered new ideas for information processing concepts based on the propagation of spin waves with a characteristic wavelength of few nanometer. This sets new grounds for novel and smaller logic elements which, not relying on charge transport, have the great advantage of operating with low energy consumption. Among these elements, three-dimensional magnetic nanostructures (3D) are very promising for miniaturizing and achieving the highest integration density in magnonic devices [18, 221]. The potential of these new 3D building blocks will materialize only when the underlying spin wave dynamics is understood. Nanotubes (NTs) prepared from ferromagnets represent prototypical 3D nanomagnetic structures [21]. The properties of these nanostructures are extremely versatile for applications as they change as a function of their geometrical properties [83, 37]. NTs raised significant attention for hosting stable flux-closure magnetic states [38], which results in a fast and controllable domain wall motion when compared to magnetic stripes [39, 40]. The three geometric parameters, namely the length, the inner radius and external radius, offer the possibility to tailor and manipulate spin-wave confinement in 3D space. Curvature-induced magnetochiral effects originating from the dipole-dipole interaction are expected to arise in such structures and are predicted to generate non-reciprocal spin-wave dispersion [41]. Previous experimental studies on spin wave resonances of ferromagnetic tubular structures have been limited to large arrays formed in porous alumina templates or to rolled-up ferromagnetic

layers (RUFLs) with micrometric radii. Investigating individual RUFLs the authors of Refs. [71, 115] transferred spin wave physics from the planar to the tubular form. This model is not valid for radii below 100 nm due to the increased relevance of the short-range exchange interaction. Dispersion relations have also been calculated using models for cylindrical systems with ultra thin tube walls [69]. Few experimental studies focused so far on the magnetization dynamics of ferromagnetic NTs with a hexagonal cross section. A recent work [42] studied the spin wave dynamics in a permalloy (Py) NT using time-resolved scanning transmission X-ray microscopy. The study concerned a single magnetic state (vortex state) induced by the specific magnetic anisotropy which was given by incident angle growth conditions during the Py evaporation process. The authors showed that the asymmetric spin-wave transport, originally predicted for cylindrical nanotubes, it is also observable in a NT with a hexagonal cross-section. We reported azimuthally confined spin waves in Ni NTs which were magnetized along the axis [215].

Here we demonstrate ferromagnetic hexagonal cross-sectional NTs as tubular cavities for dipole-exchange spin waves. Combining Brillouin Light Scattering (BLS) experiments and micromagnetic simulations, we focus in particular on identifying the nature of the modes that are possible in this geometry and understand how they vary for different NT magnetic states. We chose permalloy ( $\text{Ni}_{80}\text{Fe}_{20}$ ) as material for the NT shell, as permalloy is of utmost relevance in magnetoelectronics, spintronics and magnonics [18]. The recently developed atomic layer deposition process for permalloy [222] avoids growth-induced anisotropies in the ferromagnetic shell, enabling different effective fields compared to Ref. [42].

### Results and discussion

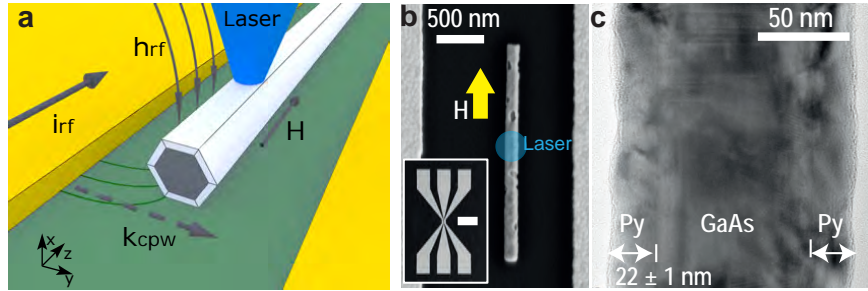


Figure 6.8 – (a) Sketch of the spin waves excitation-detection scheme based on a coplanar wave guide (CPW) and microfocus Brillouin light scattering microscopy. (b) SEM image of the nanotube placed between signal and ground line of a CPW, parallel to the signal line (inset: CPW at a smaller magnification: scale bar: 200  $\mu\text{m}$ ). (c) TEM image of a Py nanotube on a GaAs core, indicating a shell thickness of  $22 \pm 1$  nm.

In Figure 6.8a we report a schematic drawing of the device operated at room temperature. An rf-current  $i_{rf}$  applied to the CPW generates a dynamic magnetic field  $h_{rf}$  around it. This magnetic microwave field excites spin precession in the adjacent ferromagnetic NT, at the given frequency. Spin wave eigenmodes of the NT are detected via BLS microscopy, by fo-

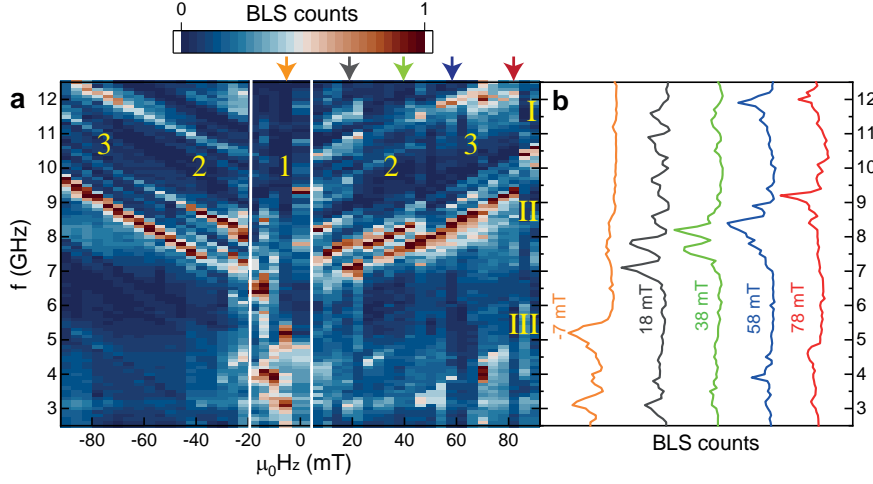


Figure 6.9 – (a) BLS spectra detected at room temperature at the NT center, plotted as a function of an external static magnetic field  $\mu_0 H$  applied along the NT axis. Colored arrows indicate spectra extracted at given fields (78, 58, 38, 18, -7 mT), which are shown in (b).

cusing a monochromatic blue laser on the sample top surface. An external static magnetic field depicted as  $H$  in Fig. 6.8a is applied along the NT axis ( $z$  direction). The Py nanotube is positioned parallel to the CPW (Fig. 6.8b). The sample consists of a 22 nm thick permalloy (Py) layer coated around a non-magnetic GaAs nanowire. The position of the BLS laser spot is marked with a blue circle of a diameter comparable with the one of the real laser (about 350 - 400 nm). The laser spot was positioned in the center of the NT, between two defects of the NT shell spaced by 560 nm. In Figure 6.8c a transmission electron micrograph of a NT is shown where we observe in the lateral view a 22 nm thick Py layer covering the GaAs NW core and the 5 nm thin spacer of  $\text{Al}_2\text{O}_3$  used to separate them. The investigated NT has an outer radius  $r_o = 80$  nm and internal an radius  $r_i = 58$  nm. These values are extracted from assumed circular cross-sections that best fit at the inner and outer surface, respectively, of the Py shell. In Figure 6.9a (Figure A.14) we show the BLS spectra detected for microwave frequencies in the range 2.5 - 12.5 GHz for the sample NT-s1 (NT-s2), as a function of  $H$ . The data were acquired for static fields ranging from +90 mT to -90 mT. Colored arrows indicate spectra extracted at specific fields (78, 58, 38, 18, -7 mT) and displayed in Figure 6.9b. The NTs investigated show richer spectra compared to Ni NTs [215]. Several branches of distinguished eigenmodes are observed. A nearly linear dependency  $\frac{df}{dH}$  on the applied magnetic field is registered for the main identified resonance modes for  $|\mu_0 H| > 50$  mT (field regime 3 in Fig 6.9a). In this field range, we categorize the observed branches in three groups I to III as indicated. In group II we notice an increase of intensity for certain branches at fields below +42 mT, suggesting a change in the NT magnetization (field regime 2 in Fig 6.9a). Similar behavior is observed for the spectra detected at negative magnetic fields in regime 2. The low frequency branches resolved in the field range from 0 to -18 mT (field regime 1 in Fig 6.9a), together with the lack of mirror symmetry with respect to  $\mu_0 H = 0$  suggest a reversal process

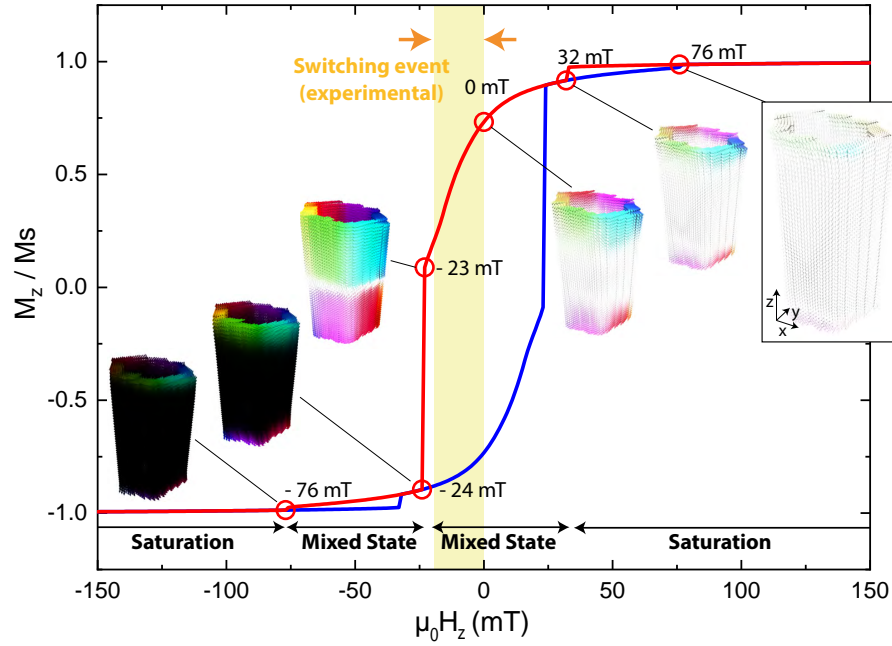


Figure 6.10 – Simulated static magnetization hysteresis of a Py NT magnetized along its axis ( $z$  direction) when the field is swept from positive to negative values (red curve) and from negative to positive values (blue curve). Magnetic configurations are extracted from the simulations at specific fields and displayed for +76, +32, 0, -23, -24 and -76 mT.

of the nanotube near  $H=0$  which is completed at around -18 mT when coming from positive  $H$ .

### Simulated static magnetization

To understand the field dependent magnetic configurations and the resonant modes in the investigated Py NTs with hexagonal cross section, we performed micromagnetic simulations. To consider the local demagnetization introduced by the defects in the permalloy shell, we assumed a NT length  $L$  of 560 nm which is the separation between the two defects seen in Fig. 6.8. In the simulation the ends of the NT were slightly tilted to simulate the irregular orientation of the defects.

In Figure 6.10 we report the results of the simulated static magnetization of a Py NT initially magnetized along its axis ( $z$  direction). The figure shows the magnetic hysteresis obtained by extracting the magnetization along  $z$  ( $M_z$ ) as a function of the static magnetic field  $\mu_0 H_z$  along the same direction. The field was swept from positive to negative values (red curve) and from negative to positive values (blue curve). Depictions of the simulated NT magnetization are given at specific values of magnetic field selected on the red curve. For high positive magnetic fields  $\mu_0 H_z > 33$  mT a magnetic state approximated by a saturated state is found, where most

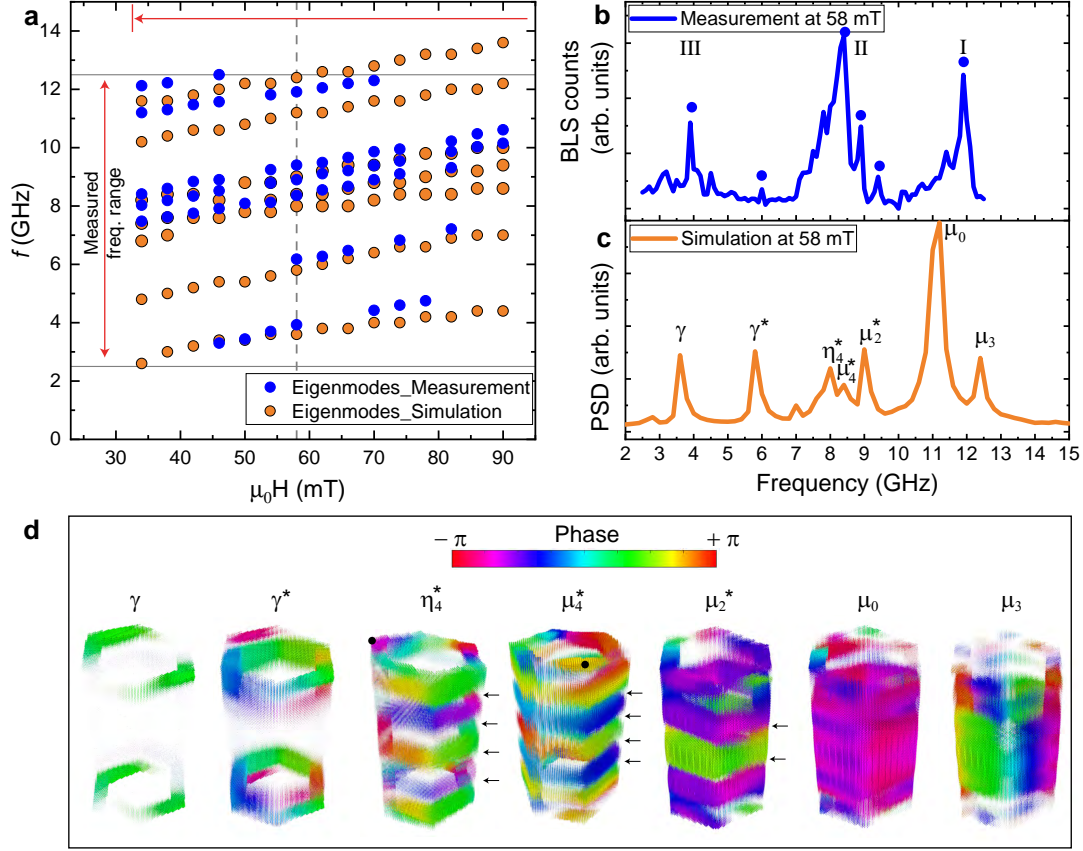


Figure 6.11 – (a) Eigenmode frequencies detected by  $\mu$ -BLS in the central part of a Py NT (blue circles) and simulated resonance frequencies (orange circles) plotted as a function of the magnetic field applied along the NT axis. The field range shown corresponds to the saturated state according to simulations. (b) BLS spectrum and (c) simulated spectrum obtained for a field of 58 mT. The principal eigenmodes are labeled by different letters and corresponds to the dynamic magnetization profile (mode profile) reported in (d). The color scale bar represents values of the spin wave phase ranging from  $-\pi$  to  $+\pi$ .

of the spins are aligned along  $\mathbf{z}$ . The spin configuration is depicted for an applied field of 76 mT. Moving from high positive magnetic field towards zero, we observe that the relative magnetization stays at almost 1 until +33 mT and then drops to a value of 0.9 at +32 mT. At 32 mT the magnetization curls at the ends of the tube to minimize the stray field and remains axially in the center to minimize the exchange energy. The end-vortices show opposite chirality as expected for thick tubes with  $t/r_0 > 0.2$  [87]. This magnetic configuration is known as the mixed state. With  $\mu_0 H_z$  decreasing from 32 mT to 0 mT,  $M_z/M_s$  is found to decrease monotonously down to 0.7. At  $\mu_0 H_z = 0$  the ground state is still the mixed state. The relative magnetization reduces to zero for a magnetic field value of -23 mT. Here, the end-vortices having opposite senses of rotations, have expanded such that they are separated by a Néel-type domain wall located in the center. At -24 mT a switching event occurs whereby the central

magnetization changes sign, leading to the formation of a mixed state with magnetization aligned along the negative  $z$  axis in the central part of the nanotube approaching  $M_z/M_s = -0.9$ . The formation of the saturated magnetic state is observed starting from -76 mT. The magnetic field range where the BLS data suggest a decrease of relative NT magnetization terminating in a switching event (from 0 to -18 mT) is highlighted in yellow for comparison with the simulated hysteresis. A reversal mechanism occurring via the formation of a Néel-type domain wall has been proved for short cylindrical NTs with length  $L$  up to  $1\ \mu\text{m}$  [88] and it is validated for short hexagonal cross-section NTs with lengths up to  $1\ \mu\text{m}$  by our simulations.

### Simulated dynamic magnetization in saturation state

We start analyzing the spin wave modes in the field regime (33 - 90) mT corresponding to the saturated state of the NT according to the simulations and attributed to the regime 3 in Figure 6.9. In Figure 6.11a we report the eigenmode frequencies resolved by  $\mu$ -BLS in the central part of the Py NT-s1 (blue circles) and the simulated resonance frequencies (orange circles) plotted as a function of the magnetic field applied along the NT axis  $z$ . Representative spectra measured in this field regime are shown in Figure 6.11b and c for the BLS measurement and simulation, respectively, at  $\mu_0 H_z = 58$  mT. The relevant frequencies in Fig. 6.11b are marked with blue circles and grouped as I, II, III accordingly to Fig. 6.9a. In Figure 6.11c the principal eigenmodes are labeled with different letters corresponding to the dynamic magnetization profile of the modes shown in Fig. 6.9d. The experimental results match with good approximation the outcome of the simulations in terms of eigen frequencies (Fig. 6.9a), but show different relative peak intensities (Fig. 6.9b). The different types of confinement shown in Fig. 6.9d are found for all the fields of the saturated state and will be here described for  $\mu_0 H_z = 58$  mT. Consistent with the frequencies measured by BLS in the group I, we find two simulated modes labeled  $\mu_0$  and  $\mu_3$  with eigen frequencies of 11.2 and 12.4 GHz, respectively. The mode profile of  $\mu_0$  corresponds to a in-phase spin precession, nearly uniform over the 3D geometry body, which can thereby be considered as the ferromagnetic resonance(FMR) of the NT with wave vector  $k_0 = 0$ . The eigenmode  $\mu_3$  shows the dynamic magnetization profile of a standing spin wave confined azimuthally, hence in Damon-Eshbach (DE) configuration ( $M \perp k$ ), with a wavelength fulfilling the constructive interference condition  $n \lambda_n = C$  with  $n$  being the number of nodes and  $C$  the circumference of the hexagonal NT. The quantization observed in the simulations corresponds to  $n = 3$ , hence the  $k$  vector is given by  $k_3 = 3 \cdot 2\pi / C$ . The eigenfrequency of the spin wave is found to increase with increasing  $k$ , as expected for the DE configuration. In the range of the BLS detected resonance frequencies of group II, we find three simulated modes labeled as  $\mu_2^*$ ,  $\mu_4^*$  and  $\eta_4^*$  with eigenfrequencies of 9, 8.4 and 8 GHz, respectively. The mode profile of  $\mu_2^*$  is that of a standing wave confined along the NT length  $L$  with  $k$  vector parallel to the magnetization of the NT, hence in backward volume (BWV) configuration. As the amplitude of the standing wave is found to be uniform along the six facets having slightly different lengths, we simplify the constructive interference condition fulfilled by the wavelength as  $\lambda_n = 2L_{av}/n$  with  $L_{av}$  being the average length of the the NT

and  $n$  the number of nodes, which is equal to 2 in Fig. 6.11d, ( $\mu_2^*$  profile). The quantized  $k$  vector is thereby  $k_2 = 2\pi/L_{av}$ . In Fig. 6.11d the mode profiles of  $\mu_4^*$  and  $\eta_4^*$  are rotated to show the facet with predominant spin wave amplitude on the right side. The profile of  $\eta_4^*$  was rotated by  $120^\circ$  anticlockwise around the NT  $z$  axis with respect to the profile of  $\mu_4^*$ . The same edge corner is marked with a black circle as a reference. It emerges that the mode profile of  $\mu_4^*$  and  $\eta_4^*$  is that of a standing wave confined along the hexagon facet of length  $L'$  and  $L''$ , respectively, with quantization  $n = 4$  and  $L' > L''$ . The quantized spin wave  $k$  vectors of  $\mu_4^*$  and  $\eta_4^*$  are hence  $k_{4'} = 4\pi/L'$  and  $k_{4''} = 4\pi/L''$ , respectively. For this group of eigenmodes we found that  $k_2 < k_{4'} < k_{4''}$ . The eigen frequency of the spin wave is found to decrease with increasing  $k$ , accordingly to what is expected for the BWV mode. Lastly, the modes labeled  $\gamma$  and  $\gamma^*$  with resonant frequencies 3.6 and 5.8 GHz, are found to be generated at the NT edges:  $\gamma$  being the ferromagnetic resonance of the hexagon corners at the NT edges and  $\gamma^*$  a spin wave confined azimuthally along the NT edges in BWV mode. The resonance of the edge corners has a much lower frequency compared to the modes of the NT body due to the demagnetization lowering locally the internal field of the NT edges.

In the light of the simulation results, the differences evidenced in the measured peak intensities with respect to simulation peak intensities are attributed to the experimental technique employed. While the micromagnetic simulations allow to get the spin wave spectra of the full 3D structure,  $\mu$ -BLS is a space-resolved technique where the spatial resolution is given by the laser spot diameter. The presence of  $\gamma$  and  $\gamma^*$  eigenmodes in the BLS spectra, categorized as group III, implies that a portion of the BLS laser area has investigated a region close to one of the two defects. The different intensity of these modes in the experimental data might indicate that the laser only partially overlapped with the mode. Furthermore, the excitation scheme based on electrically bonded CPW is expected to provide lower microwave power for higher frequencies. This might be the reason why the FMR mode measured experimentally doesn't have the highest intensity. Finally, the intensity of spin waves detected by  $\mu$ -BLS also depends on the size of the cross-section for magnon-photon scattering. The latter might vary between the top three facets of the hexagonal tube illuminated by the laser, hence influencing the relative intensities of the eigenmodes of the group II.

Now we discuss the mixed state of the NT. As the external magnetic field along  $z$  is reduced and the vortices extend towards the center, we observe that the hybridization of the edge modes  $\gamma$  and  $\gamma^*$  and the axial modes occurs. Furthermore, due to the tilt of the NT edges and the increased local demagnetization, the more the external field is reduced to zero, the more the  $\gamma^*$  mode confinement varies from azimuthal to that along a helix extending from the edges to the center of the NT. This is particularly visible in the ground state (Figure A.16). The standing wave modes hybridized with the helical one of the ends have a very complex dynamic magnetization profile and are here not discussed.

### **Simulated dynamic magnetization in presence of a Néel-type domain wall**

In this section we report on the spin wave confinement measured for a very extreme case of the mixed state, namely the state preceding the magnetization switch, here presented at  $\mu_0 H_z$



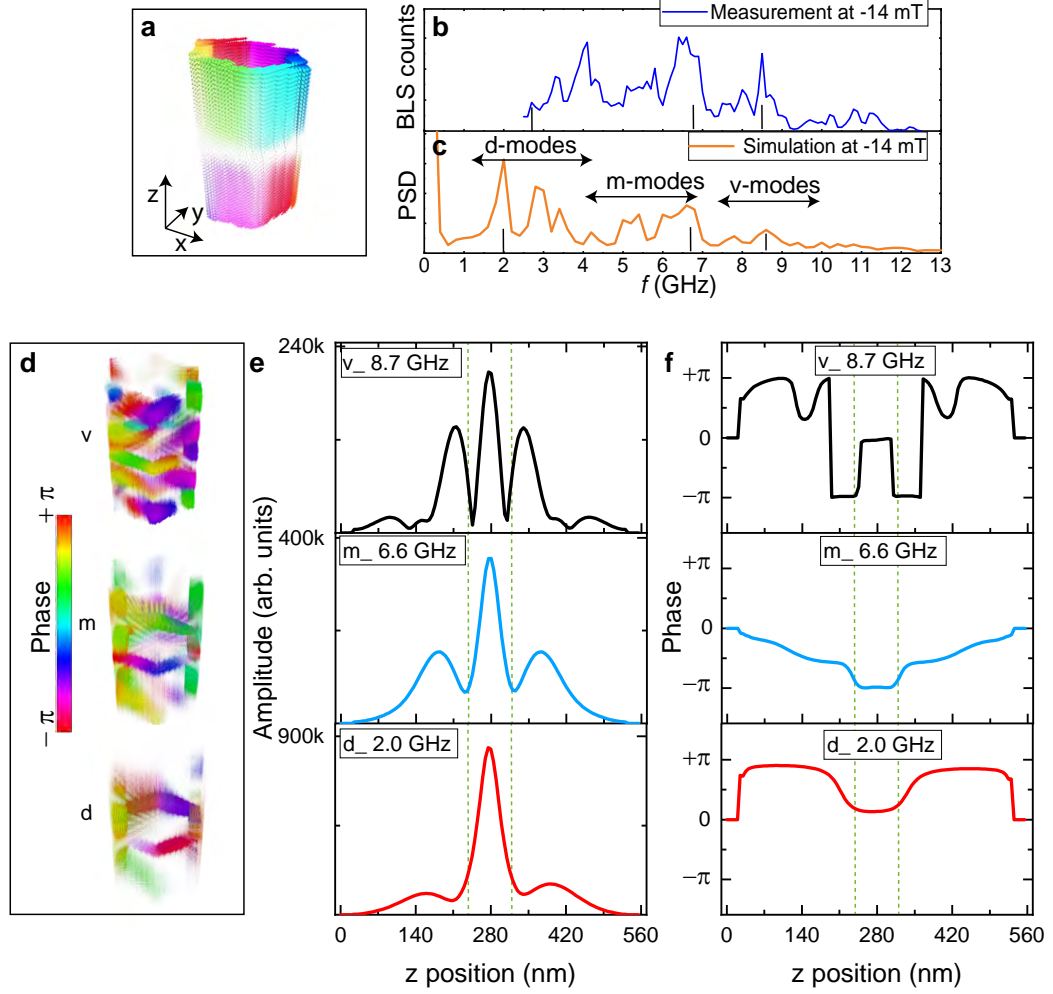


Figure 6.12 – (a) Simulated static magnetization profile of the NT at  $\mu_0 H_z = -14$  mT. (b) BLS spectrum and (c) simulated spectrum at  $\mu_0 H_z = -14$  mT. The principal eigenmodes in (c) are subdivided in three groups (d, m and v). Eigenfrequencies marked by black ticks in each group correspond to the mode profiles reported in (d). The color scale bar represents values of the spin wave phase ranging from  $-\pi$  to  $+\pi$ . (e) Amplitude and (f) phase of the mode profiles shown in (d), plotted as a function of the  $z$  position for a fixed position in the  $x$ - $y$  plane of the Py shell.

$= -14$  mT. In Fig. 6.12a we report the magnetic configuration simulated at  $-14$  mT where the two NT end vortices with opposite chirality meet at the center of the NT length, forming a Néel-type domain wall (DW) (white region). The detected BLS spectrum and the simulated power spectral density (PSD) for  $\mu_0 H_z = -14$  mT are reported in Fig. 6.12b and Fig. 6.12c, respectively. In the simulated spectra, three types of spin wave confinement are found that are indicated as d, m and v modes in Fig. 6.12c and will be described qualitatively. Selective frequencies of the three groups are marked with a black tick and correspond to the mode profile reported in Fig. 6.12d. The complexity of the 3D mode profiles require to analyze them

along individual lines in the  $z$  direction. In Fig. 6.12e and in Fig. 6.12f amplitude and phase of the mode profiles shown in Fig. 6.12d are plotted as a function of the  $z$  position for a fixed point of the  $x$ - $y$  plane belonging to the Py shell. Green dotted lines give the extension of the domain wall, located at  $(280 \pm 35)$  nm. Analyzing the space-resolved amplitude profiles in Fig. 6.12e from top to bottom we can see that for the v-mode the spin wave is distributed over the entire NT length with higher amplitudes registered in the segment from 140 nm to 420 nm and maximum amplitude in correspondence of the DW centered at 280 nm. For the m-mode we find a relatively similar amplitude distribution with the relative maximum at 280 nm increasing in intensity with respect to the v-mode. The amplitude profile of the d-mode shows a spin wave mostly confined at the DW. Analyzing the space resolved phase profiles of Fig. 6.12f we observe, for the v-mode at 8.7GHz, a phase modulation between  $|\pi|$  and 0.9 in the two NT halves defined by the presence of the DW. The phase profile is found to be specular with respect to the DW  $z$  position 280 nm and constant for the  $z$  range  $(280 \pm 35)$  nm associated to the DW presence. The phase profile of the m-mode at 6.6 GHz presents same symmetry with respect to the DW position, but here the wave modulation between NT extremities and central DW is very weak. Lastly, for the d-mode at 2 GHz, the phase is constant to around  $|\pi|$  outside the DW region and constant to 0.4 in the DW region. By combining the analysis of the 3D results in Fig. 6.12d with the spatially resolved phase profiles of Fig. 6.12f along  $z$ , we identify three possibilities for the spin wave confinement in this magnetic configuration: 1) standing waves traveling along the vortices in DE mode, symmetrical with respect to the NT center and confined between the NT edge and the DW (v-mode); 2) spin waves confined azimuthally along the DW perimeter (d-mode) and 3) an hybridization of the two (m-modes).

## Conclusions

In summary, we measured different confinements of standing spin waves in nanoscale ALD-prepared permalloy nanotubes using the microfocus BLS technique. The rich spectra of eigenmodes were analyzed using micromagnetic simulations and attributed to the interference of dipolar-exchange standing spin waves along both the azimuthal and axial direction. At low fields, for the specific NT geometry and size analyzed, low frequency modes were attributed to the eigenmodes of Néel DWs and helical waves originating from the NT tilted edges. The good match between experimental results and those simulated with standard parameters for permalloy, validate the good quality of the material deposited by the ALD process developed. Our study show the possibility of manipulate the spin wave confinement in ferromagnetic NTs with hexagonal cross section by changing their magnetic state. From the technical perspective, our study shows the top table technique of microfocus BLS as suitable for the study of the magnetization dynamics and magnetochiral textures as helix and DWs also in 3D magnetic systems. Our results pave the way to advance the research in the emerging fields of 3D nanomagnetism and magnonics.

### Methods

#### Permalloy Nanotubes and Microwave Antennas Fabrication

Nanotubes were fabricated by coating, via a plasma enhanced atomic layer deposition (PE-ALD) process, the ferromagnetic permalloy  $\text{Ni}_{80}\text{Fe}_{20}$  (Py) onto GaAs nanowires (NWs) previously grown on Si (111) substrates in a molecular-beam epitaxy reactor as reported in refs.[161, 162]. The PE-ALD process was performed in a hot wall Beneq TFS 200 ALD reactor, operated at a pressure of 4-5 mbar, under a 100 sccm constant flow of nitrogen, used both as carrier and purge gas. We used nickelocene ( $\text{NiCp}_2$ ), iron(III) tert-butoxide complex ( $\text{Fe}_2(\text{OtBu})_6$ ) and water as precursors and reactant, respectively. The chamber temperature was set to 170 °C. The plasma was generated in an rf parallel plate system and powered at 150 W. Pure hydrogen gas was supplied through the plasma head with a flow rate of 300 sccm. The PE-ALD sequence is summarized as follows:  $[(\text{NiCp}_2/\text{purge}/\text{H}_2\text{O}/\text{purge}/\text{H}_2 \text{ plasma}/\text{purge}) \times 6 + (\text{Fe}_2(\text{OtBu})_6/\text{purge}/\text{H}_2\text{O}/\text{purge}/\text{H}_2 \text{ plasma}/\text{purge})] \times 215$ . The corresponding step durations were the following:  $[(2\text{s}/4\text{s}/4\text{s}/8\text{s}/4\text{s}/8\text{s}) \times 6 + (2\text{s}/4\text{s}/4\text{s}/8\text{s}/4\text{s}/8\text{s})] \times 215$ . Nanotubes were annealed at 380 °C for 2h 30 min under forming gas  $\text{N}_2 - \text{H}_2$  with a flow of 300 sccm to further reduce the deposited material. The coplanar wave guides (CPWs) employed to excite spin precession in the Py NTs were prepared by electron beam lithography and evaporation of 5 nm thick Ti and 120 nm thick Au layer. The CPW's dimensions were chosen to enable impedance matching. The signal line, having a width of  $2.5 \pm 0.1 \mu\text{m}$  was separated by gaps of  $1.7 \pm 0.1 \mu\text{m}$  width from the ground lines.

#### Micro-focused Brillouin Light Scattering experiments

Spin wave eigenmodes were detected via microfocus Brillouin light scattering ( $\mu$ -BLS) microscopy at room temperature [174]. The CPW was electrically connected via wire bonding and a printed circuit board to a signal generator (Anritsu MG3692C) applying current. The corresponding magnetic microwave field excited spin precession in the NT at a fixed frequency. The frequency was varied in a step-wise from 2.5 to 12.5 GHz. A monochromatic laser with a wavelength of 473 nm and power of 0.5 mW was focused on the top surface of the NT. The recorded BLS signal was proportional to the square of the amplitude of the dynamic magnetization at the position of the laser spot. The sample was mounted on a closed loop piezo-electrical stage which allowed a precise positioning of the NT. The power was such that spin precession was excited in the linear regime. A magnetic field was applied parallel to the NT long axis (z axis) via a permanent magnet.

#### Micromagnetic Simulations

Micromagnetic simulations using OOMMF[223] were performed to obtain a microscopic insight into SW excitations in NTs. A bitmap containing the required hexagonal geometry of the NT cross section in xy-plane was imported into OOMMF. This hexagonal cross section

was rotated along z-axis by 15 degree in order to distribute the systematic roughness due to pixelization on all facets of NTs as uniform as possible (see Figure A.15). This cross section was extended to  $L=560$  nm as the length of the simulated NTs. The two ends of the NT is terminated at an angle of 15 degree with respect to xy-plane to emulate the irregular orientation of the defects in the measured NT. The geometry is discretized on a grid of  $2.5 \text{ nm} \times 2.5 \text{ nm} \times 5 \text{ nm}$ . A uniform DC magnetic field was applied along the z direction (NT axis), and equilibrium magnetization configuration was determined for each DC field value. Subsequently, a spatially uniform Sinc pulse of the form

$$\mathbf{h}_e = \frac{h_0 \sin[2\pi f_c(t - t_0)]}{2\pi f_c(t - t_0)} [\cos(45^\circ)\hat{x} + \sin(45^\circ)\hat{y}] \quad (6.1)$$

with amplitude of  $h_0 = 2$  mT, cut-off frequency of  $f_c = 50$  GHz and  $t_0 = 500$  ps was applied at an angle of  $45^\circ$  in the xy-plane. A total simulation duration of  $T = 5$  ns was considered. The dynamic magnetization was recorded as a function of x, y, z every time step of  $\delta t = 5$  ps. A fast Fourier transformation (FFT) was performed on the magnetization of each pixel along the time axis to obtain the resonance spectrum. Then sums of power and phase of complex dynamic magnetization  $m_d = m_x + im_y$  were calculated to display the SW spatial profile for relevant frequencies.  $|m_d|$  was then integrated over the whole geometry (defined as PSD), and plotted as a function of frequency  $f$  in order to observe the microwave absorption (e. g. Fig. 6.11c and Fig. 6.12c). The input parameters used in the simulations were as follows: saturation magnetization  $M_s = 800$  kA/m, exchange constant  $A = 13$  pJ/m, and damping constant  $\alpha = 0.005$ . The dynamic magnetization profiles are visualized using "Mayavi: 3D Visualization of Scientific Data"[224].

### 6.3 Comparison between $\text{Ni}_{80}\text{Fe}_{20}$ nanotubes and Ni nanotubes

Static and spin dynamic magnetization studies were performed on ferromagnetic nanotubes prepared out of two different materials, Ni and permalloy (Py,  $\text{Ni}_{80}\text{Fe}_{20}$ ). In this section, we focus on the spectra of the  $\mu$ -BLS experiments to highlight differences and common aspects analyzed in Ni and Py nanotubes.

In Figure 6.13 we report the BLS spectra measured for individual Ni (orange curve) and Py (green curve) NTs, axially magnetized with external fields of similar intensities: 50 and 46 mT, respectively. The peak position and the linewidth of the ferromagnetic resonance (FMR) mode were analyzed by a Lorentzian fit and are marked for the two spectra. A general observation is that the two sets of resonance frequencies fall in two different frequency ranges. For the Ni NT the peaks with higher intensity are located in the range 1.5 - 7 GHz, while for the Py NT they appear for  $f \geq 7$  GHz. A larger number of resonance peaks is resolved in the Py NT, compared to the Ni NT. The resonance peaks exhibit large (small) linewidth when they are measured in the Ni (Py) NT, respectively. For instance, the FMR mode resonates at 3.6 GHz and at 11.5 GHz in the Ni and Py NT, respectively. To compare the two linewidths  $\Delta f$ , quality factors  $Q = \frac{f}{\Delta f}$

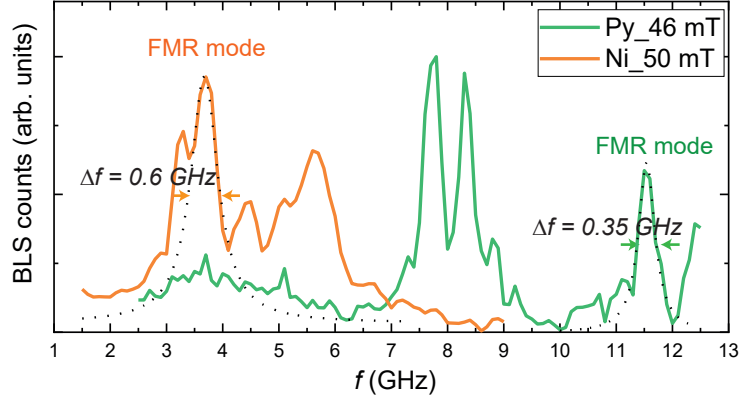


Figure 6.13 –  $\mu$ -BLS spectra detected for a Ni NT (orange curve) and a Py NT (green curve) axially magnetized with  $\mu_0 H = 50$  and 46 mT, respectively.

are evaluated. Thereby the frequency dependance of the FMR (Eq. 2.26) is considered. For Ni we find  $Q_{\text{Ni}} \approx 5$  and for permalloy we evaluate  $Q_{\text{Py}} \approx 33$ . Thereby, the magnetic resonances are considerably sharper for Py NTs than for Ni NTs in qualitative agreement with the differences in Gilbert damping parameter  $\alpha$ .

In Figure 6.14 a and b we display the geometrical parameters of the type of nanotubes measured in this thesis. The direction along which the NTs were magnetized is indicated with an arrow. The conditions for quantized  $k$  vectors are recalled in the yellow box of Fig. 6.14 b. In Figure 6.14 c and d, we compare the extracted eigenmodes for a Ni and a Py NT, respectively, plotted as a function of field in their saturation state. For each material, we also report the resonance frequency given by the Kittel equation [57] for a cylindrical rod (upper curve in Fig. 6.14 c and d) and a planar thin film (bottom curve in Fig. 6.14 c and d). For the FMR mode, the frequency values of a second sample of each material is reported (squared symbols). The y-error bar corresponds to the linewidth of the FMR resonances. For the Py NTs they are roughly consistent with the size of the symbols. In 6.14 d, we have focused on the peaks with highest intensities. The geometrical parameters of the samples and the properties measured for the ALD-grown materials are summarized in Table 6.2. The Ni NTs have diameters of either 260 or 280 nm. The Ni NTs did not contain nanotroughs along the full length of about 15  $\mu\text{m}$ . The Ni NTs, probed with a  $\mu$ -BLS laser focused in their central position and with aspect ratios larger than 50, can be hence be approximated by a NT of infinite length. Permalloy NTs have diameters in the order of 150 - 160 nm. The nanotroughs in the ALD-grown shell were proven to pose boundary conditions for the spin waves confinement, hence we approximated these NTs' lengths to the spacing between the defects ( $L = 560 \mu\text{m}$  in Fig. 6.14 b). Accordingly we modeled them as finite-length NTs. For Ni NTs we detected standing spin waves confined only in azimuthal direction ( $\phi$ - modes in Fig. 6.14 c). For Py NTs eigenmodes were attributed to an confinement also along  $L$ , together with the azimuthally confined modes. The azimuthally confined modes have eigenfrequencies above the FMR frequency branch, as  $f$  increases with the module of the  $k$  vector when this is perpendicular to the direction of the magnetization

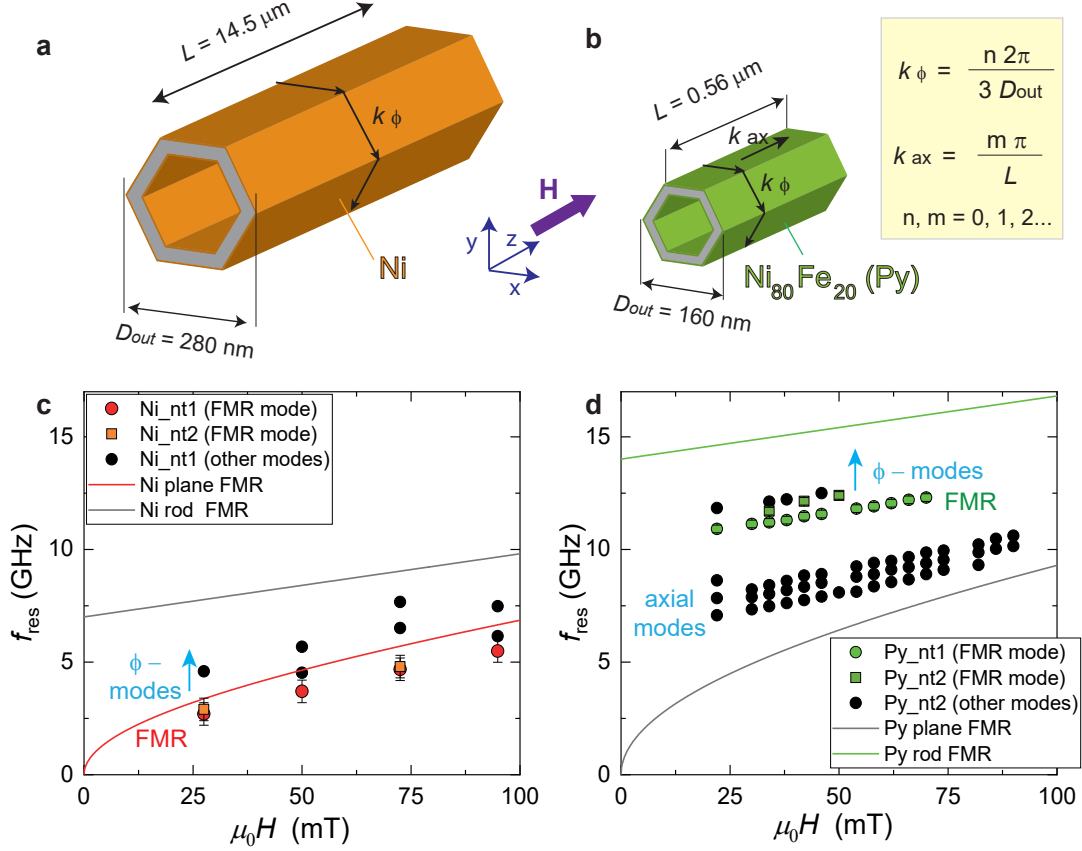


Figure 6.14 – Sketches of (a) Ni and (b) Py NTs with relevant geometrical parameters considered in the text and modeling. The discrete  $k$  vectors possible for this geometry along the azimuthal direction ( $k_\phi$ ) and along the axis ( $k_{\text{ax}}$ ) are given in the yellow inset in (b). Eigenmodes extracted from the  $\mu$ -BLS measurements are reported as a function of the applied field  $\mu_0 H$  in (c) and (d) for a Ni and a Py NTs samples, respectively. The FMR curves of a cylindrical rod and a planar thin film are reported for comparison, for each material.

(DE mode). The eigenfrequencies of the axially confined modes are below the FMR branch. They are found to decrease with increasing  $k$  (See Section 6.2), accordingly to what is expected for  $\mathbf{k} // \mathbf{M}$  (BWV mode).

Finally, we note that the frequency branch attributed to the FMR mode in the case of the Ni NTs (red and orange symbols in Fig. 6.14 c) lies slightly below the FMR curve for a thin Ni film (red curve) and shows a similar squared-field dependency. In case of the Py NTs, the frequency branch attributed, by micromagnetic simulations, to the FMR mode (Fig. 6.14 d) resides at intermediate frequency values between those of a planar Py film (gray curve) and those of a cylindrical Py rod (green curve). The slope  $\frac{df}{dH}$  of the measured FMR modes is similar to the linear field dependency of the rod resonance. To interpret these observations,

### 6.3. Comparison between $\text{Ni}_{80}\text{Fe}_{20}$ nanotubes and Ni nanotubes

we consider two geometrical factors: one is the radii ratio  $\beta = \frac{r_i}{r_o}$ , the other is the curvature of the magnetic shell which is expressed as  $r_o^{-2}$ . Values of  $\beta$  are reported in Table 6.2 for the four samples,  $r_o$  is considered as half of the longer diameter of the hexagonal section  $D_{out}$ . As reported for cylindrical nanotubes [61], and mentioned in Chapter 2 (Section 2.2, Eq. (2.11)), with increasing  $\beta$  ratio, the transverse demagnetization factor of a NT decreases, going from that of a non-hollow cylindrical rod ( $Nx = Ny = \frac{1}{2}$ ) towards the values of the in the plane thin film ( $Nx = Ny = 0$ ). Hence the permalloy nanotubes, having a smaller  $\beta$  ratio, have relative higher demagnetization values than the one for planar thin films, if compared to the Ni nanotubes. We attribute this observation to the smaller outer diameter, and the concomitant curvature-induced exchange effect. We argue that the observed shift to higher eigen-frequencies as modeled by Leblond et al. [69] and Otalora et al. [41] (Eq. (2.31) and Eq. (2.35) in Chapter 2, Sec. 2.3.3, respectively) is a consequence of the exchange energy contribution due to increased curvature in our Py NTs compared to the Ni NTs. For Ni NTs we were able to interpret the data, by approximation, with the dispersion relation of a thin film, by posing periodical boundary conditions, hence a quantization of  $k_\phi$ . However, none of the models listed in Chapter 2, Sec. 2.3.3 were adequate to substantiate the resonance frequencies of Py NTs. Instead, micromagnetic simulations were necessary to interpret the data. In conclusion, our experimental results show that the set of resonance frequencies of a tubular spin wave nanocavity with hexagonal cross section are nanoengineered by the selected material and geometrical parameters, e.g. the radii ratio (tunable by varying the NT's thickness), the NT's length and its curvature.

Table 6.2 – Geometrical parameters of the nanotubes investigated and relevant physical properties of the ALD-grown materials.

Sample	Material	$M_s$ (kA/m) in thin film	$\alpha$ in thin film (in NT)	$L$ ( $\mu\text{m}$ )	$D_{out}$ ( $2r_o$ ) (nm)	$\beta = \frac{r_i}{r_o}$
Ni_nt1 (S2 in Sec. 5.2)	Ni	$400 \pm 50$	0.045	$14.5 \pm 0.1$	$280 \pm 20$	0.79
Ni_nt2 (s4 in App. A.1)	Ni	$400 \pm 50$	0.045	$13.7 \pm 0.1$	$260 \pm 10$	0.77
Py_nt1 (NT_s1 in Sec. 6.2)	$\text{Ni}_{80}\text{Fe}_{20}$	$750 \pm 50$	0.013 (0.01)	$0.56 \pm 0.1$	$160 \pm 10$	0.73
Py_nt2 (NT_s2 in App. A.3)	$\text{Ni}_{80}\text{Fe}_{20}$	$750 \pm 50$	0.013	$0.55 \pm 0.1$	$153 \pm 10$	0.72

Notes: the names of the samples are labeled with an unified nomenclature. Names used in other sections/appendixes are reported in parenthesis. The inner radius  $r_i$  has been estimated by subtracting the shell thickness from the outer radius  $r_o$ . The thicknesses, measured by TEM microscopy, are  $(29.4 \pm 4.1)$  nm and  $(21.6 \pm 1.0)$  nm for the Ni and Py NTs, respectively.





## 7 Summary and Outlooks

In this thesis a combined approach based on material science and engineering, the physical sciences and nanotechnology was followed to advance 3D spintronics and 3D magnonics. These technologies will be based on three-dimensional device architectures prepared from ferromagnetic nanostructures. As prototypical nanotemplates we chose semiconductor nanowires and fabricated large ensembles of vertically standing nanotubes consisting of Ni and  $\text{Ni}_{80}\text{Fe}_{20}$ . They exhibited low resistivity, large anisotropic magnetoresistance and low spin wave damping evidencing promising spintronic and magnonic functionalities. The steps taken and the results achieved are summarized in the following.

### **ALD-prepared Ni and NiFe coatings: process development and materials properties**

To achieve conformal 3D coatings consisting of Ni we combined cycles of thermal ALD of nickel oxide with a single pulse of plasma-assisted hydrogen reduction. We particularly aimed at polycrystalline Ni to avoid magnetocrystalline anisotropy and explore shape anisotropy effects. Nickelocene and water were used as metal precursor and co-reactant, respectively, and hydrogen as reactant for the plasma step. We both obtained the conformal growth typical of thermal ALD and exploited the low temperature reduction enabled by a plasma treatment. The optimized ALD sequence provided conformal coating of vertically aligned GaAs nanowires, resulting in a dense array of Ni NTs. We achieved a specific resistivity of Ni of about  $8 \mu\Omega\text{cm}$  on both planar substrates and arrays of nanowires. The low-field AMR effect observed at room temperature in the hysteretic regime of a nanotube amounted to 1.3 % , 3.9 % in the corresponding planar thin film. The spin wave damping was low enough to enable spin waves measurements. The excellent physical properties measured were due to a low content of contaminating elements, linked to the optimization of the ALD reactions, the polycrystalline nature of the ferromagnetic coatings and a low surface roughness. These chemical and morphological properties were studied by scanning transmission electron microscopy, coupled with energy dispersive X-ray imaging (STEM-EDX), X-ray diffraction (XRD), transmission electron microscopy (TEM) and atomic force microscopy (AFM). Our

process avoided the nanotroughs and the grainy surface observed in previously reported Ni films and nanotubes, ensuring a step coverage  $\geq 90\%$  on nanowires with high aspect ratios. NiFe thin films with different Ni:Fe atomic ratios were prepared by alternating  $m$  times the sequence for the deposition of nickel with a single sequence for the deposition of oxidized iron and a post-deposition annealing treatment in hydrogen. Nickelocene (iron(III) tert-butoxide) and water were used as Ni (Fe) precursors and co-reactant, respectively, and hydrogen as the reactant for the plasma step. This combination of Ni and Fe precursors was selected based on their capability to react in a self-limiting manner with the chosen substrate and water at the same temperature. We achieved an optimized permalloy (Py,  $\text{Ni}_{80}\text{Fe}_{20}$ ) stoichiometry via the Ni : Fe pulse ratio  $m = 6$ . By a further annealing step the resistivity of the optimized Py thin films was  $28 \mu\Omega\text{cm}$  and the measured spin wave damping  $\alpha$  0.013 in the thin films and 0.01 in an individual nanotube. The saturation magnetization  $\mu_0 M_s$  amounted to 0.94 T. This value is within the experimental error comparable to bulk permalloy. As intended, the  $M_s$  and the damping constant  $\alpha$  measured for ALD-grown Py were larger and smaller, respectively, than the ones of Ni. A high relative AMR of 5.6 % was observed in the ALD Py thin film with the lowest spin wave damping. As in the case of Ni NTs, the high quality of the ferromagnetic films allowed us to measure multiple spin-wave resonances in individual NTs, indicating confined magnon modes. The specific ALD-based process has been explored for the first time. To the best of our knowledge, this thesis contains the second study reported in the literature for the deposition of ALD-prepared metallic NiFe coatings. The functional and morphological properties of the permalloy coatings obtained show a significant step forward compared to what previously reported. However, we still foresee room for improvement for the surface morphology. The source of nanotroughs is identified in the stress caused by the removal of oxygen and the  $\text{Ni}_3\text{Fe}$  FCC ( $L1_2$ ) phase formation occurring in the annealing processes. These structural features could be overcome by stress relaxation studies, optimization of the thin film thickness combined with modifications of heating/cooling protocols and/or the use of capping layers. As another option, one should look into processes leading to the direct co-deposition of metallic Ni and Fe, which would eliminate oxygen incorporation, which we see as one of the two causes for defects formations. In the lights of the recent ALD Ni progresses, a promising alternative route to achieve this result would be to combine the lately developed process exploiting  $\text{Ni}(\text{acac})_2$  (tmeda) and  $\text{N}_2\text{H}_4$  [132] (Table 3.1, Chapter 3) with the one employing  $\text{Fe}(\text{tBuAMD})_2$  and  $\text{H}_2$  [31] (See Table 3.2, Chapter 3). The resulting shells of both materials were polycrystalline and magnetically isotropic. This aspect was particularly relevant when addressing shape-dependent magnetic properties in the nanotubes.

### Ni and NiFe nanotubes static and dynamic magnetization properties

Ni and NiFe nanotubes were obtained as large ensembles of vertically aligned 3D nano-magnetic structures. They were then transferred on separate substrates and integrated in characterization devices designed by electron beam lithography to be characterized individually. In Ref. [215] we published the results obtained on individual Ni NTs by performing

---

both anisotropic magnetoresistance (AMR) measurements and Brillouin light scattering spectroscopy (BLS), while exciting spin waves via a microwave antenna. Consistently with the theoretical predictions, our AMR results indicated a mixed state as the ground magnetization state and a reversal mechanism mediated by the formation of flux-closure magnetic states. The predominance of the shape anisotropy over other material-induced anisotropies it is found only for the optimized ALD sequence. In the optimized material, the spin-wave damping was low allowing us to detect several dipolar-exchange standing spin waves modes, which fulfilled the constructive interference condition in the azimuthal direction of the nanotube.

Analog BLS studies were performed to investigate standing spin wave confinement in permalloy NTs. Here, we supported the experimental data with complementary static and dynamic micromagnetic simulations. Given the short length and peculiar geometry of the NTs analyzed, the simulations suggested a mixed state at remanance and a reversal magnetization occurring via the formation of a Néel-type domain wall (DW). The BLS measurements under microwave irradiations were performed for different magnetic configurations of the nanotubes. When the NT was axially magnetized, the rich spectra of eigenmodes was attributed to the interference of dipolar-exchange standing spin waves along both the azimuthal and axial directions. At low fields, for the specific NT geometry and size analyzed, low frequency modes were attributed to the eigenmodes of the Néel DW and helical waves originating from the NT's tilted edges. The good match between experimental results and those simulated with standard parameters for permalloy and the absence of other magnetic anisotropies contributions than shape anisotropy, validate the good quality of the material deposited by ALD and its isotropic magnetic properties. In the case of Py NTs, when compared to the Ni NTs, a larger set of resonances was resolved due to both different boundary conditions imposed by a shorter length of the nanotubes and, above all, a lower spin wave damping achieved compared to Ni NTs. Furthermore, by only comparing the frequencies attributed to the ferromagnetic resonance (FMR) in the two types of NTs, we observe that in Ni NTs with diameters of about 280 nm, the frequencies follow a field dependency closer to the one expected for a Ni thin film, while in Py NTs with a reduced diameter of about 160 nm the resonance frequencies of the FMR mode have a field dependency approaching the one of a Py cylindrical rod. This observation confirms that in the explored nanotubular systems the allowed resonant frequencies were tailored by the geometrical parameters, like for instance the NT's curvature.

To conclude, our BLS measurements, performed while irradiating NTs with microwaves, show that these nanotubes form spin-wave nanocavities which impose discrete wave vectors and confine GHz microwave signals on the nanoscale. Furthermore, it has been shown that this confinement can be manipulated by engineering the geometrical parameters and magnetic states of the ferromagnetic nanotubes. From the technical perspective, this thesis shows the table top technique of micro-focused BLS as suitable for the study of the magnetization dynamics and magnetochiral textures as helix and DWs, also in 3D magnetic systems. To the best of our knowledge our studies represent the first spatially resolved BLS spectra obtained on ferromagnetic NTs with diameters in the order of hundreds of nanometers. The same approach have been recently exploited by other research groups investigating other types of 3D magnetic structures [211, 221], witnessing the emerging interest in 3D magnonics. Future

perspectives for the research presented in this thesis go in the direction of expanding the number of nanostructured 3D surfaces on which we apply the developed ALD processes. The conformal coating with ferromagnets of curved surfaces will result in non-collinear spin configurations with novel spintronics properties to explore. By employing complex nanoscaffolds with specifically designed periodicities in different spatial directions as nanotemplates, the superstructures can serve as 3D magnonic crystals with defined symmetry directions for the propagation of spin waves.

# A Appendix

## A.1 Supplementary information of Pub.I

Supplementary information of "Plasma-Enhanced Atomic Layer Deposition of Nickel Nanotubes with Low Resistivity and Coherent Magnetization Dynamics for 3D Spintronics".

M. C. Giordano, K. Baumgaertl, S. Escobar Steinvall, J. Gay, M. Vuichard, A. Fontcuberta i Morral and D. Grundler

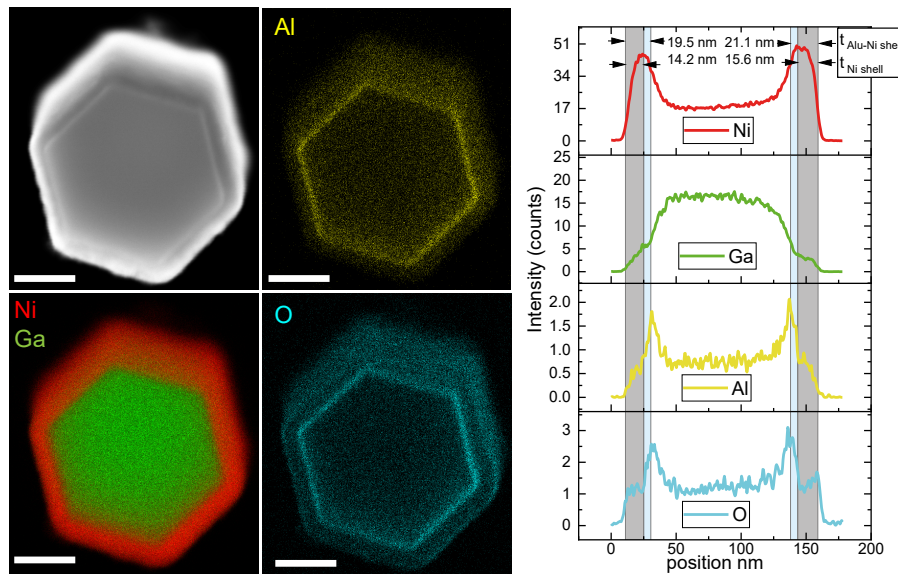


Figure A.1 – (a) HADDAF and elemental distribution of (b) Ni, Ga, (c) Al and (d) O of a cross section of a Ni shell deposited on a GaAs nanowire covered with a 5 nm thick Al<sub>2</sub>O<sub>3</sub> layer (scale bars: 100 nm). (e) Elemental analysis along the white dotted lines. The asymmetric appearance of the shell thickness is due to the misalignment of the nanotube's long axis with the electron beam.

## Appendix A. Appendix

Table A.1 – Geometrical parameters employed to determine the aspect ratio (AR) of the nanowires templates. The minimum, maximum and average spacing among nanowires are indicated as  $w_{min}$ ,  $w_{max}$  and  $w_{ave}$ , respectively.  $L_{max}$  represents the maximum length of the nanowires.

Deposition set	$w_{min}$ ( $\mu\text{m}$ )	$w_{max}$ ( $\mu\text{m}$ )	$w_{ave}$ ( $\mu\text{m}$ )	$L_{max}$ ( $\mu\text{m}$ )	$AR = L_{max} / w_{ave}$
c = 1	$0.43 \pm 0.1$	$0.78 \pm 0.1$	$0.61 \pm 0.25$	$15.0 \pm 0.1$	$\sim 25 : 1$
c = 5	$0.17 \pm 0.1$	$1.00 \pm 0.1$	$0.54 \pm 0.59$	$8.0 \pm 0.1$	$\sim 15 : 1$
c = 7	$0.88 \pm 0.1$	$0.06 \pm 0.1$	$0.49 \pm 0.58$	$15.0 \pm 0.1$	$\sim 31 : 1$
c = 10	$0.50 \pm 0.1$	$0.20 \pm 0.1$	$0.35 \pm 0.21$	$7.0 \pm 0.1$	$\sim 20 : 1$

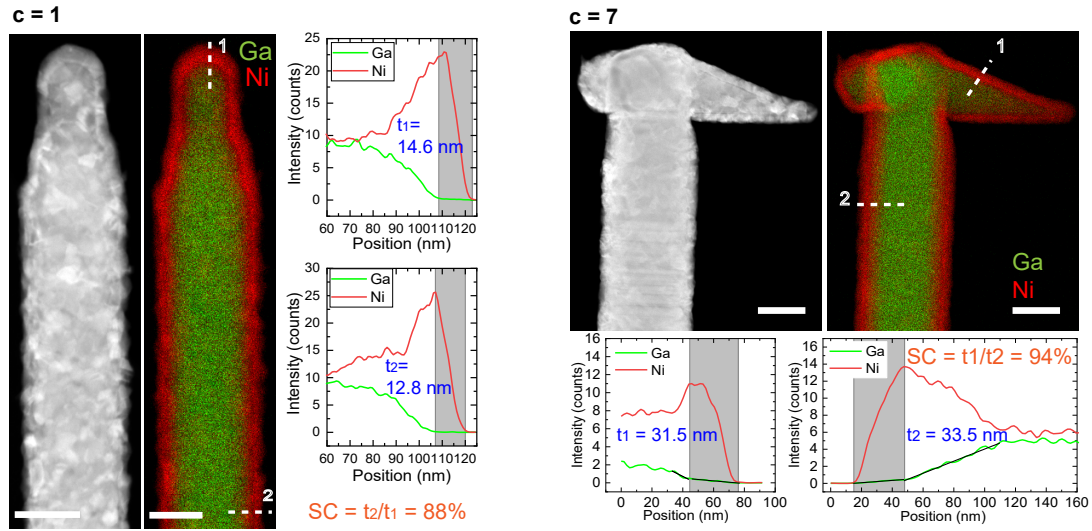


Figure A.2 – STEM-EDS images taken on ALD-grown Ni shells of depositions sets with (a)  $c = 1$  (scale bar: 100 nm) and (b)  $c = 7$  (scale bar: 200 nm) deposited on GaAs nanowires after depositing 5 nm of  $\text{Al}_2\text{O}_3$ . The core/shell systems were annealed at 350 °C. The ratio  $t_2/t_1$  of thicknesses  $t_1$  and  $t_2$  taken at positions 1 and 2 respectively, provide the step coverage ratio SC. The two positions are separated by about 900 nm. SC is given in the panels.

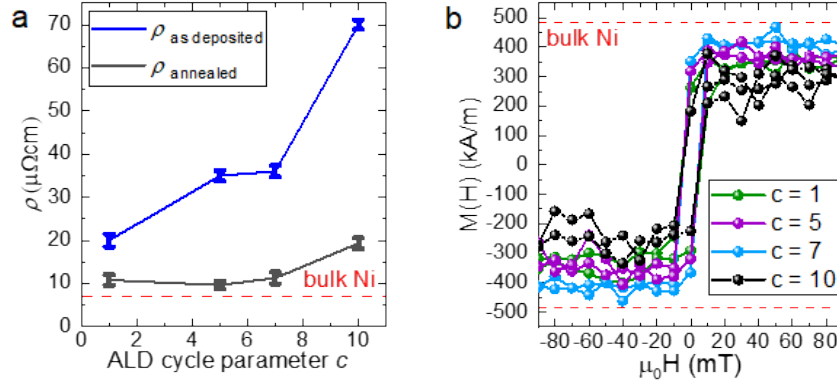


Figure A.3 – (a) Values of resistivity of the four planar ALD-grown Ni films as deposited on a Si substrate, displayed as a function of the ALD cycle parameter  $c$  (blue curve). The values are compared with the ones reported in the main manuscript for the corresponding annealed samples (dark gray curve). The resistivity was measured at room temperature in a 4-point probe configuration. (b) Magnetic hysteresis curves  $M(H)$  of the annealed planar ALD Ni films. Ni films grown with  $c = 5$  and  $c = 7$  exhibit the largest saturation magnetization  $M_s$  extracted at 85 mT. Values are reported in Fig. 5 of the main manuscript. The data were obtained at room temperature using a SQUID magnetometer with the external magnetic field  $H$  applied in the plane of the films.

Table A.2 – Parameters of ALD-grown Ni NTs for which measured data are reported in Figures A.5 and A.6

Sample	$L$ ( $\mu\text{m}$ ) ( $\mu\text{m}$ )	$D_{\text{out}}$ (nm)	$t$ (nm)	Deposition set
s_1	$14.0 \pm 0.1$	$260 \pm 10$	$11.5 \pm 2.4$	$c = 1$
s_2	$5.0 \pm 0.1$	$220 \pm 10$	$13.7 \pm 1.0$	$c = 5$
s_3	$14.4 \pm 0.1$	$265 \pm 10$	$29.4 \pm 4.1$	$c = 7$
s_4	$13.7 \pm 0.1$	$260 \pm 10$	$29.4 \pm 4.1$	$c = 7$

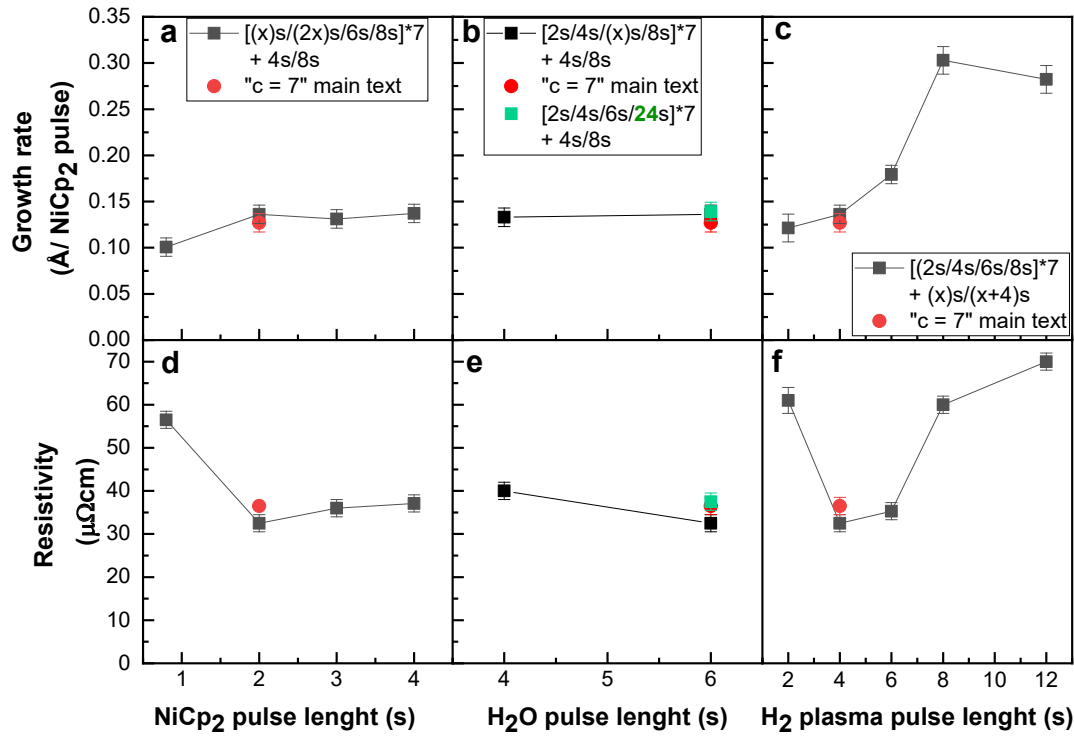


Figure A.4 – Growth rates for  $c = 7$  depending on pulse lengths of (a) nickelocene, (b) water, and (c) hydrogen used for the plasma-enhanced reduction. The black symbols are obtained by deposition processes performed independently of the processes reported in the manuscript. The thin films were deposited at a temperature  $T = 170$  °C. In the bottom row we display the resistivities measured on the planar films reported in (a) to (c). Resistivities depending on pulse lengths of (d) nickelocene, (e) water, and (f) hydrogen. The durations specified in the legends refer to the precursors and purge lengths in the sequence (NiCp<sub>2</sub>/purge/H<sub>2</sub>O/purge)\*7 + H<sub>2</sub> plasma/purge. The parameter  $x$  refers to the quantity displayed on the x-axis. The values of growth rate and resistivity were measured on the as-deposited thin films. The red circle represents the separate sample of optimized properties discussed in the manuscript.



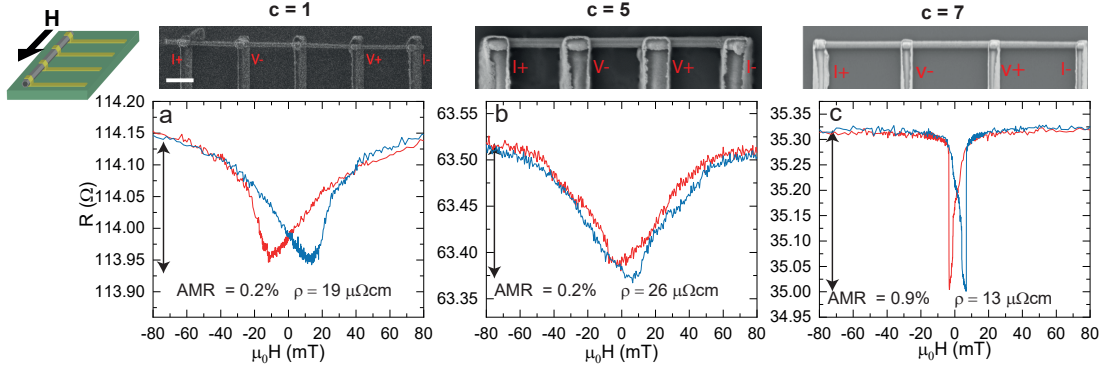


Figure A.5 – Magnetoresistance  $R(H)$  measured on the Ni NTs (a)  $s_1$ , (b)  $s_2$  and (c)  $s_3$  described in Table S1 and corresponding SEM images. The resistance was measured at room temperature with the external magnetic field  $H$  applied along the long axes (sketched on the left), by using the metallic leads sketched in the SEM images. Relative resistance changes (AMR) between maximum and minimum values of  $R$  are stated in each figure. From values  $R$  measured at 80 mT we calculated the specific resistivities  $\rho$  as stated in the figures. Scale bars are 1  $\mu\text{m}$ . The core/shell systems were annealed at 350 °C.

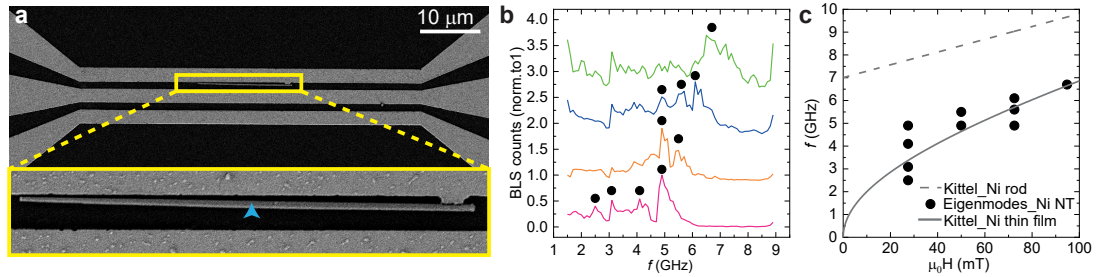


Figure A.6 – (a) SEM image of an individual nanotube ( $s_4$ ) positioned in the gap of a coplanar waveguide (CPW) between signal and ground lines. The nanotube was grown with  $c = 7$ . (b) BLS data obtained when focusing the laser onto the center of the nanotube and exciting spin-precessional motion by microwave magnetic fields with frequencies between 1.5 and 9 GHz. We show spectra taken at fields 27.5, 50, 72.5 and 94.9 mT (from bottom to top) applied along the long axis. We mark peaks that we identify as magnon resonances with filled circles. (c) Summary of resonance frequencies extracted from (b) plotted as a function of applied field  $H$ . We compare the resonance frequencies with the field-dependent resonance frequencies expected for a planar Ni film (solid line) and a Ni nanorod with a diameter consistent with the nanotube (broken line). The resonance frequencies are grouped close to the solid curve consistent with the nanotube discussed in the main text.

## A.2 Supplementary information of Pub.II

Supplementary information of "Low Gilbert Damping Permalloy Thin Films and Nanotubes Prepared by Plasma-Enhanced Atomic Layer Deposition"

M. C. Giordano, S. Escobar Steinvall, S. Watanabe, A. Fontcuberta i Morral and D. Grundler

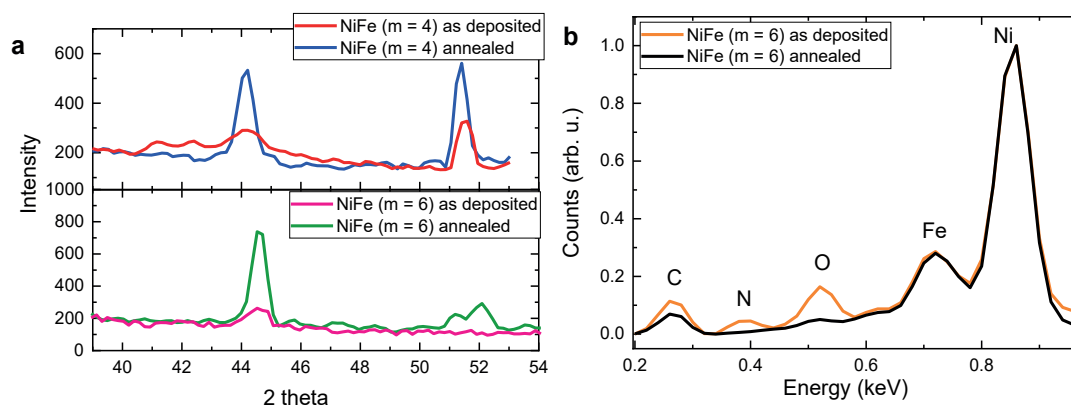


Figure A.7 – (a) X-Ray diffractograms of the samples prepared with  $m = 4$  and  $m = 6$  in their as deposited and annealed state. (b) Energy dispersive spectroscopy of the NiFe sample prepared with  $m = 6$  as deposited and annealed in the energy range 0.2-1 keV. The annealing treatment was performed at 380 °C.

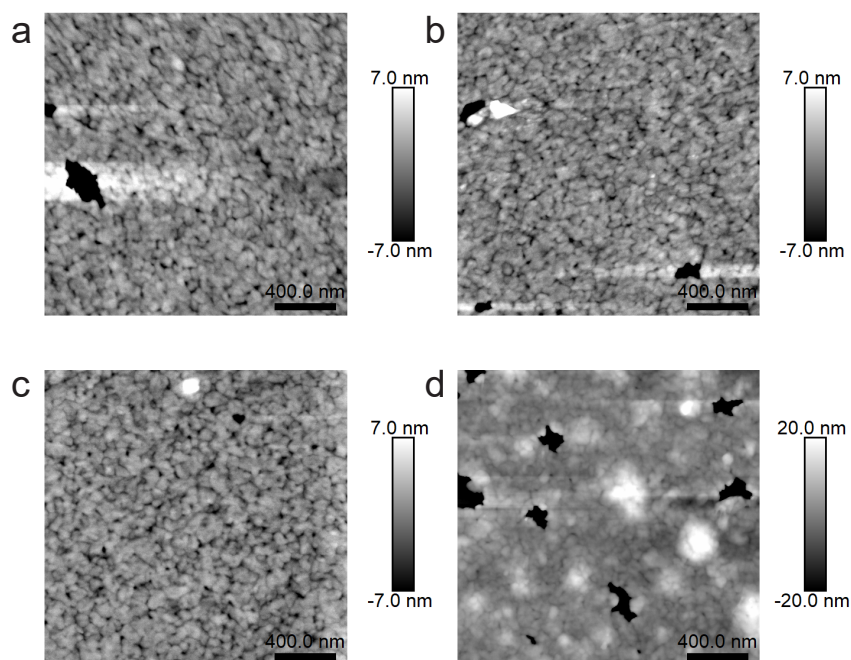


Figure A.8 – (a) Atomic force microscopy performed on a  $2\text{ }\mu\text{m} \times 2\text{ }\mu\text{m}$  area of samples prepared with (a)  $m = 4$ , (b)  $m = 5$ , (c)  $m = 6$ , and (d)  $m = 7$  on bare silicon substrates, after the annealing treatment at  $380\text{ }^{\circ}\text{C}$ .

Table A.3 – Thickness and compositional values of NiFe NTs prepared by ALD with Ni:Fe pulse ratio  $m = 6$ . The values were extrapolated from STEM-EDX analysis, reported in Fig. A.9.

Sample	Permalloy thickness(nm)	Ni (at%) in NiFe ratio	Fe (at%) in NiFe ratio	O (at%) in the shell
NT1 (main text)	21.1	80.2	19.8	3.5
NTS1	23.3	80.7	19.3	3.4
NTS2	20.2	80.5	19.5	3.6
NTS3	23.3	80.7	19.3	3.5
NTS4	22.1	80.8	19.2	3.5
Average	$21.6 \pm 1$	$80.4 \pm 0.3$	$19.6 \pm 0.3$	$3.5 \pm 1$

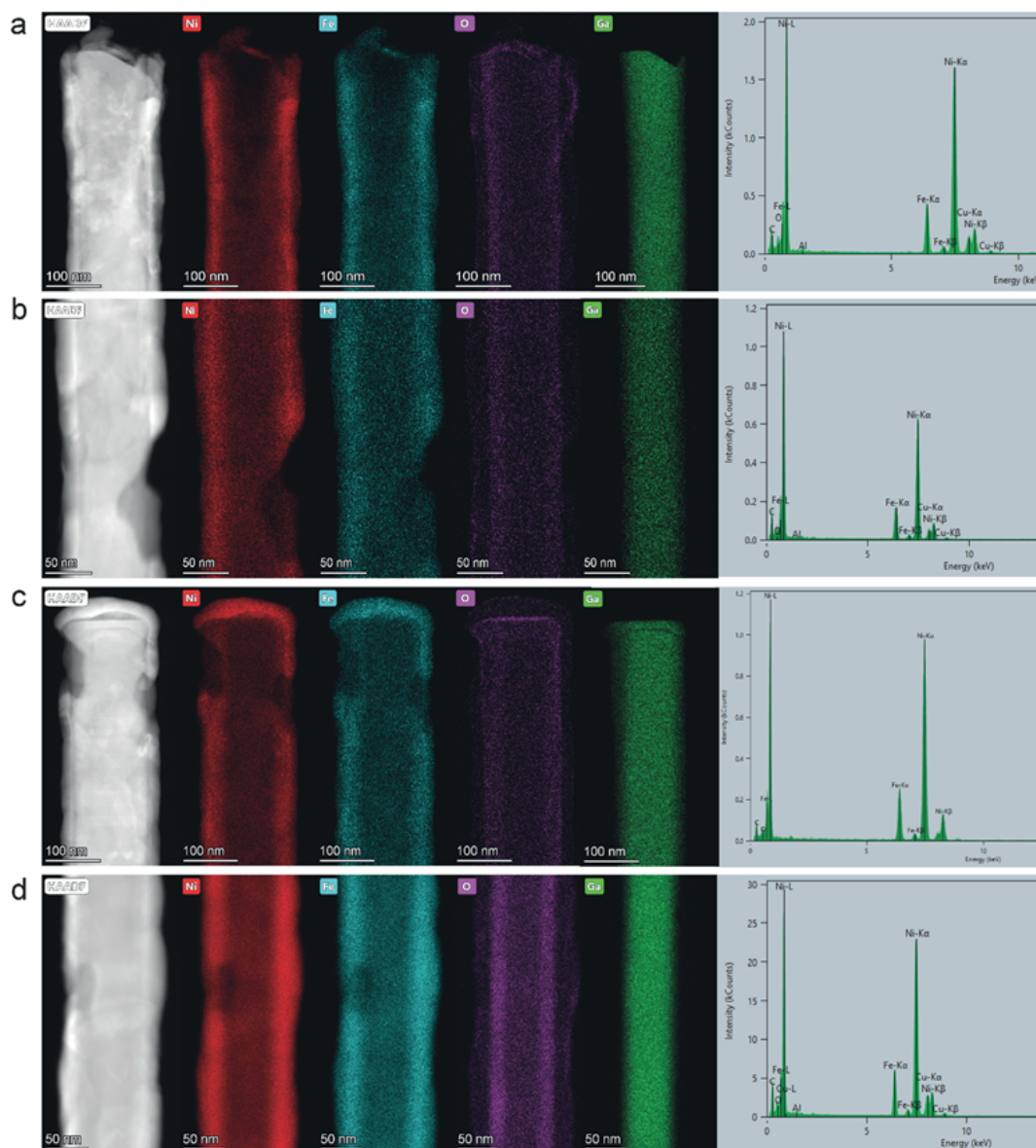


Figure A.9 – HADDF images and elemental maps of the NiFe nanotube samples (a-d) NTS1-4, prepared with Ni:Fe pulse ratio  $m = 6$ , annealed at  $380\text{ }^{\circ}\text{C}$ , and corresponding energy dispersive spectroscopy analysis of the external shell. The composition and NiFe shell thickness values measured for the four nanotubes are summarized in Table S1.

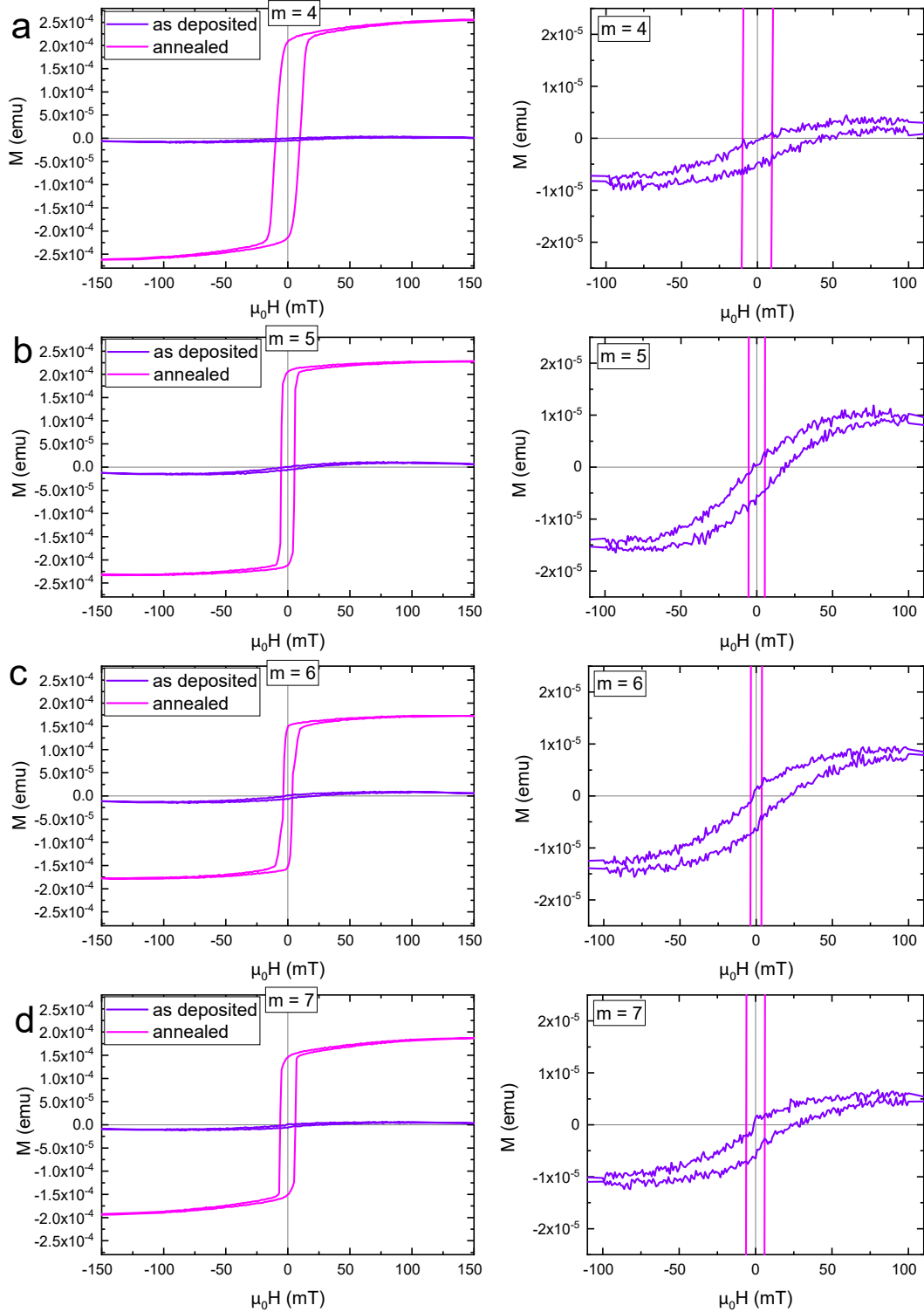


Figure A.10 – Hysteresis curves measured with a VSM, at room temperature, of as deposited (purple curve) and annealed (magenta curve) NiFe thin films prepared by ALD, using Ni:Fe pulse ratio (a)  $m = 4$ , (b)  $m = 5$ , (c)  $m = 6$  and (d)  $m = 7$ . The hysteresis were acquired with an applied field oriented at  $0^\circ$  *irc* degrees in the plane of the sample. On the right panel the same curves are reported zoomed.

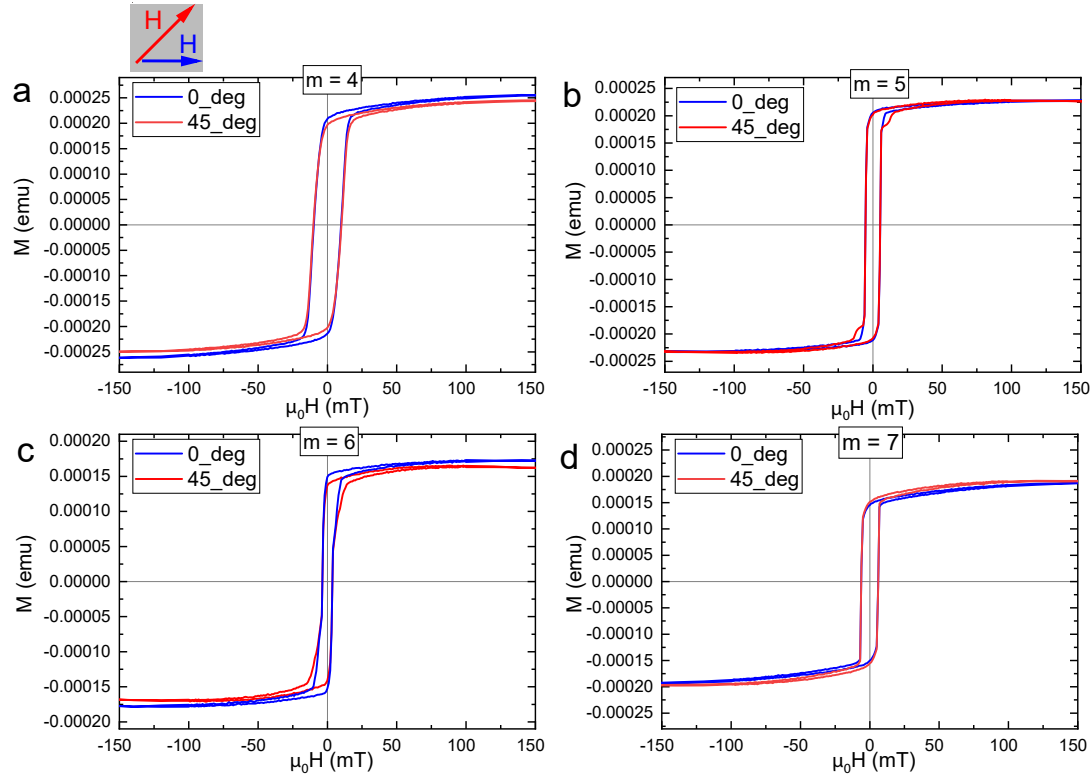


Figure A.11 – Hysteresis curves measured with a VSM at room temperature of annealed NiFe thin films prepared by ALD, using Ni:Fe pulse ratio (a)  $m = 4$ , (b)  $m = 5$ , (c)  $m = 6$  and (d)  $m = 7$ . The blue (red) curves were acquired with an applied field oriented at  $0^\circ$  ( $45^\circ$ ) in the plane of the sample.

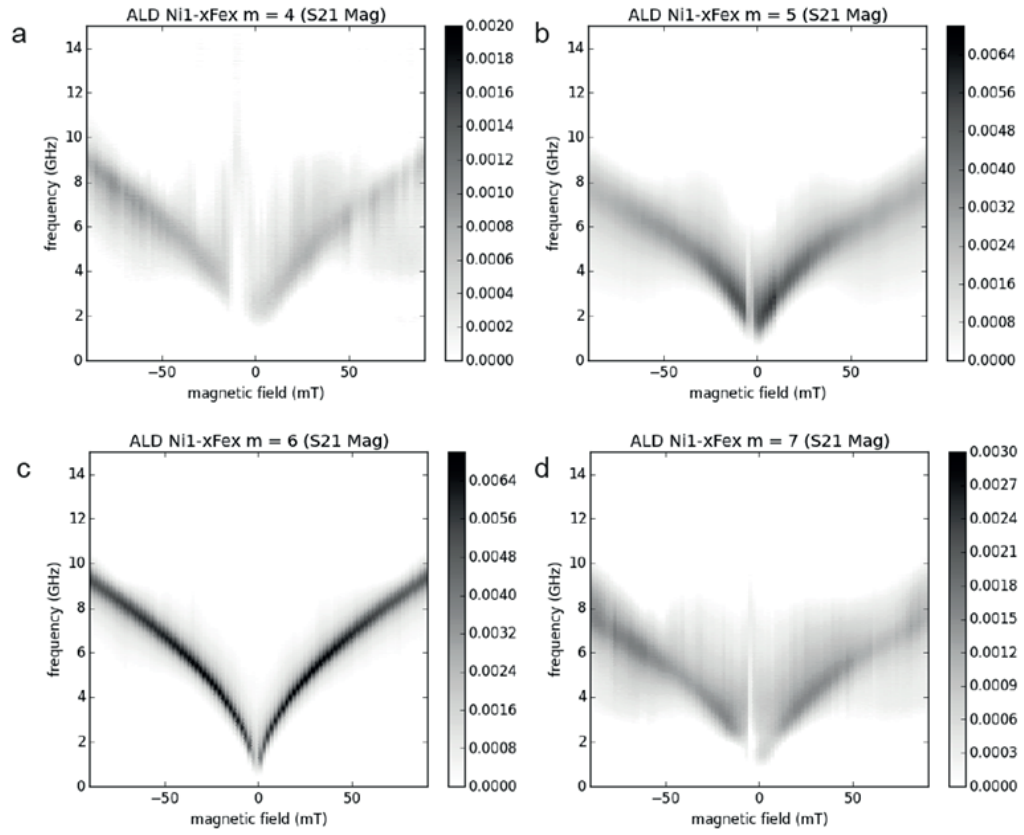


Figure A.12 – VNA-FMR measurements of annealed NiFe thin films prepared by ALD, using Ni:Fe pulse ratio (a)  $m = 4$ , (b)  $m = 5$ , (c)  $m = 6$  and (d)  $m = 7$ . The resonance measurements were acquired while sweeping the magnetic field from 90 to -90 mT in the plane of the sample.

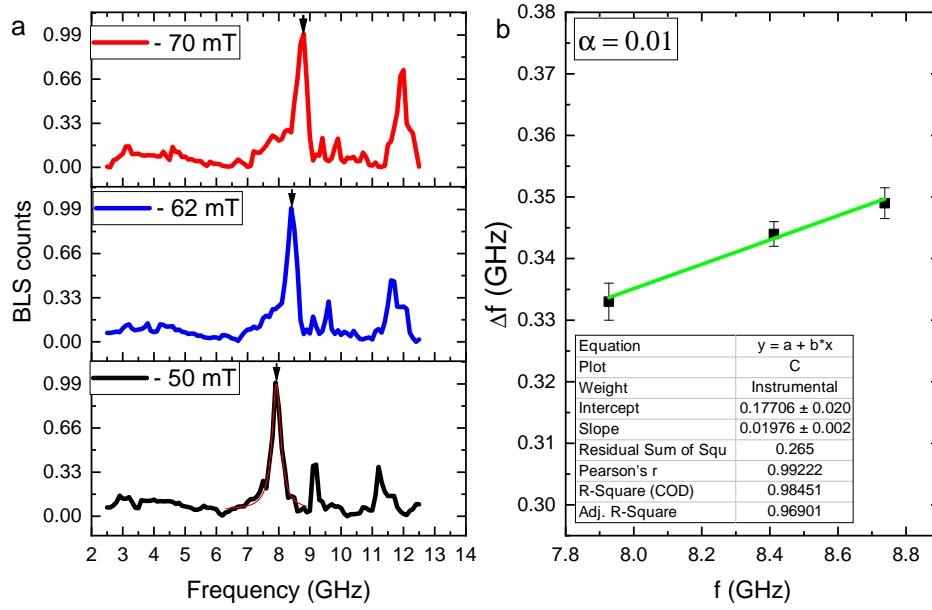


Figure A.13 – (a) BLS spectra detected, at different applied static magnetic fields, on a individual permalloy NT prepared by PEALD using Ni : Fe pulse ratio  $m = 6$ . Black arrows indicate the peak (eigenmode) whose linewidth was used to assess the NT damping parameter. (b) Linewidth  $\Delta f$  plotted as function of the resonance frequency of the mode selected. The data are fitted with a linear function whose slope is twice the Gilbert damping parameter  $\alpha$ , that is found to be 0.01. Note that the frequency regime is small in (b), and further experiments over a broader frequency regime are needed to obtain an improved estimation for  $\alpha$  in the nanotubes.



### A.3 Supplementary information of Pub.III

Supplementary information of "Dipolar-exchange spin waves confinement in ALD-prepared permalloy  $\text{Ni}_{80}\text{Fe}_{20}$  nanotubes"

M. C. Giordano, M. Hamdi, A. Mucchietto, A. Fontcuberta i Morral and D. Grundler

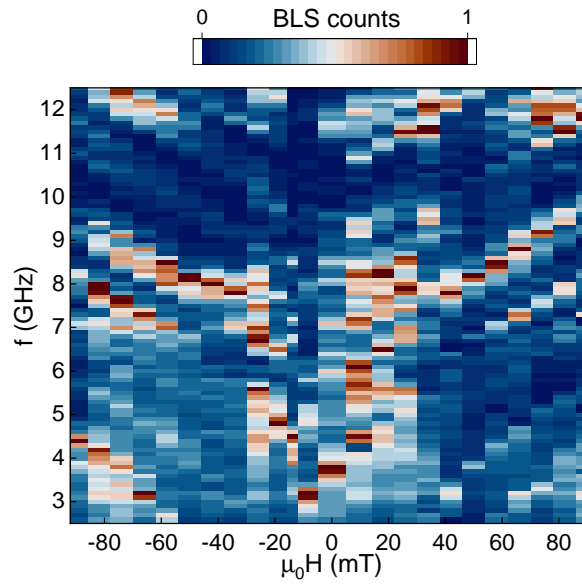


Figure A.14 – BLS spectra detected at room temperature at the center of sample NT-s2, plotted as a function of an external static magnetic field  $\mu_0 H$  applied along the NT axis.

Table A.4 – Geometrical parameters of the NiFe NTs investigated.

Sample name	Py shell thickness (nm)	External diameter $D_{out}$ (nm)	NT full lenght $l$ ( $\mu\text{m}$ )	Distance between defects $L$ (nm)
NT-s1 (main text)	$21.6 \pm 1.0$	$160 \pm 10$	$2.4 \pm 0.1$	$560 \pm 10$
NT-s2	$21.6 \pm 1.0$	$153 \pm 10$	$2.8 \pm 0.1$	$550 \pm 10$

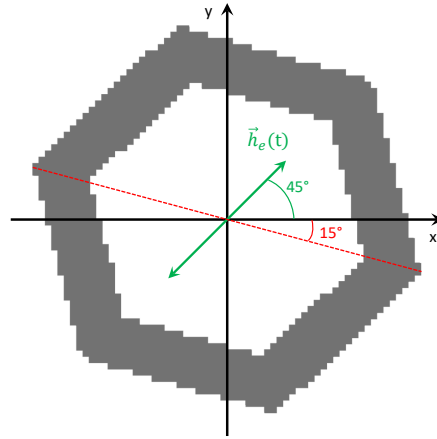


Figure A.15 – NT cross section set as input for the micromagnetics simulations. The two ends of the NT are tilted at an angle of  $15^\circ$  with respect to  $xy$ -plane to emulate the irregular orientation of the defects in the measured NT. A spatially uniform sinc pulse  $\vec{h}_e$  is applied at  $45^\circ$  with respect to  $xy$ -plane. The geometry is discretized on a grid of  $2.5 \text{ nm} \times 2.5 \text{ nm} \times 5 \text{ nm}$ .

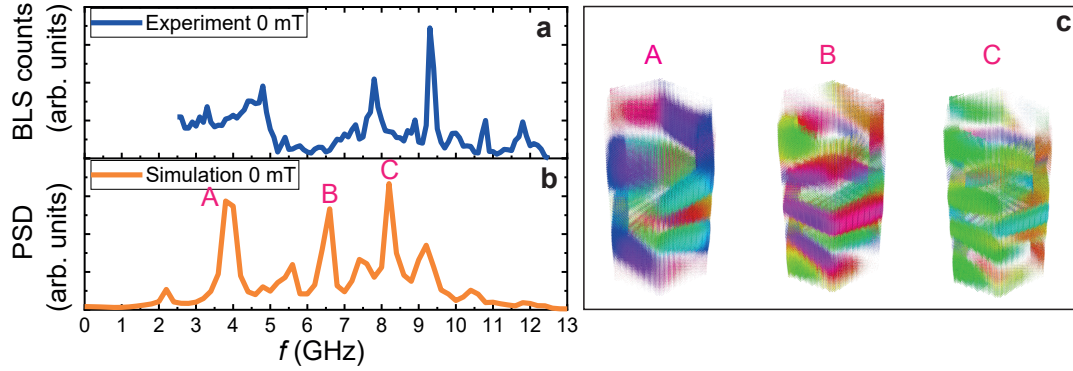


Figure A.16 – (a) NT-s1 BLS spectrum and (b) simulated spectrum obtained in absence of static magnetic field (0 mT). Specific eigenmodes are labeled by A, B, C and corresponds to the dynamic magnetization profile reported in (c). The color scale bar represents values of the spin wave phase ranging from  $-\pi$  to  $+\pi$ .

# Bibliography

- [1] J. M. D. Coey. *Magnetism and Magnetic Materials*. Cambridge University Press, 2010.
- [2] M. Julliere. Tunneling between ferromagnetic films. *Physics Letters A*, 54(3):225–226, 1975. doi: 10.1016/0375-9601(75)90174-7.
- [3] M. N. Baibich, J. M. Broto, A. Fert, F. N. Van Dau, F. Petroff, P. Etienne, G. Creuzet, A. Friederich, and J. Chazelas. Giant magnetoresistance of (001) Fe/(001) Cr magnetic superlattices. *Physical Review Letters*, 61(21):2472, 1988. doi: 10.1103/PhysRevLett.61.2472.
- [4] G. Binasch, P. Grünberg, F. Saurenbach, and W. Zinn. Enhanced magnetoresistance in layered magnetic structures with antiferromagnetic interlayer exchange. *Physical Review B*, 39(7):4828, 1989. doi: 10.1103/PhysRevB.39.4828.
- [5] Y. Tian and S. Yan. Giant magnetoresistance: history, development and beyond. *Science China Physics, Mechanics and Astronomy*, 56(1):2–14, 2013. doi: 10.1007/s11433-012-4971-7.
- [6] M. H. Kryder. Magnetic thin films for data storage. *Thin Solid Films*, 216(1):174 – 180, 1992. doi: 10.1016/0040-6090(92)90890-N.
- [7] D. Makarov, M. Melzer, D. Karnaushenko, and O. G. Schmidt. Shapeable magnetoelectronics. *Applied Physics Reviews*, 3(1):011101, 2016. doi: 10.1063/1.4938497.
- [8] J. Lenz and S. Edelstein. Magnetic sensors and their applications. *IEEE Sensors Journal*, 6(3):631–649, 2006. doi: 10.1109/JSEN.2006.874493.
- [9] J. C. S. Kools. Exchange-biased spin-valves for magnetic storage. *IEEE Transactions on Magnetics*, 32(4):3165–3184, 1996. doi: 10.1109/20.508381.
- [10] D. Niarchos. Magnetic MEMS: key issues and some applications. *Sensors and Actuators A: Physical*, 106(1):255 – 262, 2003. doi: 10.1016/S0924-4247(03)00179-1.
- [11] S. Venkateshwaran, E. Selvakumar, P. Senthamil Selvan, M. Selvambikai, R. Kannan, and A. S. Pradeep. Corrosion and magnetic characterization of electroplated NiFe and NiFeW soft magnetic thin films for MEMS applications. pages 447–454, Singapore, 2019. Springer Singapore. doi: 10.1007/978-981-13-1780-4\_43.

- [12] R. Chen, G. Romero, M. G. Christiansen, A. Mohr, and P. Anikeeva. Wireless magnetothermal deep brain stimulation. *Science*, 347(6229):1477–1480, 2015. doi: 10.1126/science.1261821.
- [13] S. Neusser and D. Grundler. Magnonics: Spin Waves on the Nanoscale. *Advanced Materials*, 21(28):2927–2932, 2009. doi: 10.1002/adma.200900809.
- [14] S. A. Nikitov, D. V. Kalyabin, I. V. Lisenkov, A. Slavin, Y. N. Barabanenkov, S. A. Osokin, A. V. Sadovnikov, E. N. Beginin, M. A. Morozova, Y. A. Filimonov, Y. V. Khivintsev, S. L. Vysotsky, V. K. Sakharov, and E. S. Pavlov. Magnonics: a new research area in spintronics and spin wave electronics. *Physics-Uspekhi*, 58(10):1002–1028, 2015. doi: 10.3367/ufne.0185.201510m.1099.
- [15] D. Stancil and A. Prabhakar. *Spin Waves: Theory and Applications*. Springer, 2009.
- [16] H. Yu, O. Kelly, V. Cros, R. Bernard, P. Bortolotti, A. Anane, F. Brandl, F. Heimbach, and D. Grundler. Approaching soft x-ray wavelengths in nanomagnet-based microwave technology. *Nature Communications*, 7:11255, 2016. doi: <https://doi.org/10.1038/ncomms11255>.
- [17] V. V. Kruglyak, S. O. Demokritov, and D. Grundler. Magnonics. *Journal of Physics D: Applied Physics*, 43(26), 2010. doi: 10.1088/0022-3727/43/26/264001.
- [18] G. Gubbiotti. *Three-Dimensional Magnonics: Layered, Micro-and Nanostructures; 1st ed.* Jenny Stanford Publishing, 2019.
- [19] S.S.P. Parkin, M. Hayashi, and L. Thomas. Magnetic Racetrack Memory. *Science*, 320(5873):190–194, 2008. doi: 10.1126/science.1145799.
- [20] R. Streubel, P. Fischer, F. Kronast, V. P. Kravchuk, D. D. Sheka, Y. Gaididei, O. G. Schmidt, and D. Makarov. Magnetism in Curved Geometries. *Journal of Physics D: Applied Physics*, 49(36):363001, 2016. doi: 10.1088/0022-3727/49/36/363001.
- [21] A. Fernández-Pacheco, R. Streubel, O. Fruchart, R. Hertel, P. Fischer, and R. P. Cowburn. Three-dimensional nanomagnetism. *Nature Communications*, 8:15756, 2017. doi: 10.1038/ncomms15756.
- [22] M. Daub, M. Knez, U. Goesele, and K. Nielsch. Ferromagnetic nanotubes by atomic layer deposition in anodic alumina membranes. *Journal of Applied Physics*, 101(9):09J111, 2007. doi: 10.1063/1.2712057.
- [23] C. Donnelly, M. Guizar-Sicairos, V. Scagnoli, M. Holler, T. Huthwelker, A. Menzel, I. Vartiainen, E. Müller, E. Kirk, S. Gliga, J. Raabe, and L. J. Heyderman. Element-specific x-ray phase tomography of 3D structures at the nanoscale. *Physical Review Letters*, 114:115501, 2015. doi: 10.1103/PhysRevLett.114.115501.

- [24] R. Streubel, V. P. Kravchuk, D. D. Sheka, D. Makarov, F. Kronast, O. G. Schmidt, and Y. Gaididei. Equilibrium magnetic states in individual hemispherical permalloy caps. *Applied Physics Letters*, 101(13):132419, 2012. doi: 10.1063/1.4756708.
- [25] D. Rüffer, R. Huber, P. Berberich, S. Albert, E. Russo-Averchi, M. Heiss, J. Arbiol, A. Fontcuberta i Morral, and D. Grundler. Magnetic States of an Individual Ni Nanotube Probed by Anisotropic Magnetoresistance. *Nanoscale*, 4(16):4989–4995, 2012. doi: 10.1039/c2nr31086d.
- [26] D. Rüffer, M. Slot, R. Huber, T. Schwarze, F. Heimbach, G. Tütüncüoğlu, F. Matteini, E. Russo-Averchi, A. Kovács, R. Dunin-Borkowski, R. R. Zamani, J. R. Morante, J. Arbiol, A. Fontcuberta i Morral, and D. Grundler. Anisotropic magnetoresistance of individual CoFeB and Ni nanotubes with values of up to 1.4 % at room temperature. *APL Materials*, 2(7):076112, 2014. doi: 10.1063/1.4891276.
- [27] R. W. Johnson, A. Hultqvist, and S. F. Bent. A brief review of atomic layer deposition: From fundamentals to applications. *Materials Today*, 17(5):236–246, 2014. doi: 10.1016/j.mattod.2014.04.026.
- [28] S. M. George. Atomic Layer Deposition: An Overview. *Chemical Reviews*, 110(1):111–131, 2010. doi: 10.1021/cr900056b.
- [29] K. Nielsch, J. Bachmann, M. Daub, J. Jing, M. Knez, U. Gösele, S. Barth, S. Mathur, J. Escrig, and D. Altbir. Ferromagnetic nanostructures by atomic layer deposition: from thin films towards core-shell nanotubes. *ECS Transactions*, 11(7):139, 2007. doi: 10.1149/1.2779078.
- [30] M. Ritala and J. Niinistö. Industrial applications of atomic layer deposition. *ECS Transactions*, 25(8):641–652, 2009. doi: 10.1149/1.3207651.
- [31] B. S. Lim, A. Rahtu, and R. G. Gordon. Atomic layer deposition of transition metals. *Nature Materials*, 2(11):749–754, 2003. doi: 10.1038/nmat1000.
- [32] Y. P. Wang, Z. J. Ding, Q. X. Liu, W. J. Liu, S. J. Ding, and D. W. Zhang. Plasma-assisted atomic layer deposition and post-annealing enhancement of low resistivity and oxygen-free nickel nano-films using nickelocene and ammonia precursors. *Journal of Materials Chemistry C*, 4(47):11059–11066, 2016. doi: 10.1039/c6tc03606f.
- [33] J. P. Klesko, M. M. Kerrigan, and C. H. Winter. Low temperature thermal atomic layer deposition of cobalt metal films. *Chemistry of Materials*, 28(3):700–703, 2016. doi: 10.1021/acs.chemmater.5b03504.
- [34] M. M. Kerrigan, J. P. Klesko, K. J. Blakeney, and C. H. Winter. Low temperature, selective atomic layer deposition of nickel metal thin films. *ACS Applied Materials & Interfaces*, 10(16):14200–14208, 2018. doi: 10.1021/acsami.8b03074.

- [35] D. J. Hagen, M. E. Pemble, and M. Karppinen. Atomic layer deposition of metals: precursors and film growth. *Applied Physics Reviews*, 6(4):041309, 2019. doi: 10.1063/1.5087759.
- [36] J. Escrig, P. Landeros, D. Altbir, E.E. Vogel, and P. Vargas. Phase diagrams of magnetic nanotubes. *Journal of magnetism and magnetic materials*, 308(2):233–237, 2007. doi: 10.1016/j.jmmm.2006.05.019.
- [37] P. Landeros, O. J. Suarez, A. Cuchillo, and P. Vargas. Equilibrium states and vortex domain wall nucleation in ferromagnetic nanotubes. *Physical Review B*, 79:024404, 2009. doi: 10.1103/PhysRevB.79.024404.
- [38] M. Staño and O. Fruchart. Magnetic nanowires and nanotubes. In *Handbook of Magnetic Materials*, volume 27, pages 155–267. Elsevier B.V., 2018. doi: 10.1016/bs.hmm.2018.08.002.
- [39] P. Landeros, S. Allende, J. Escrig, E. Salcedo, D. Altbir, and E. E. Vogel. Reversal modes in magnetic nanotubes. *Applied Physics Letters*, 90(10):102501, 2007. doi: 10.1063/1.2437655.
- [40] M. Yan, C. Andreas, A. Kákay, F. García-Sánchez, and R. Hertel. Fast Domain Wall Dynamics in Magnetic Nanotubes: Suppression of Walker Breakdown and Cherenkov-like Spin Wave Emission. *Applied Physics Letters*, 99(12):122505, 2011. doi: 10.1063/1.3643037.
- [41] J. A. Otálora, M. Yan, H. Schultheiss, R. Hertel, and A. Kákay. Curvature-induced asymmetric spin-wave dispersion. *Physical Review Letters*, 117(22):227203, 2016. doi: 10.1103/PhysRevLett.117.227203.
- [42] L. Körber, M. Zimmermann, S. Wintz, S. Finizio, M. Weigand, J. Raabe, J. A. Otálora, H. Schultheiss, E. Josten, J. Lindner, C. H. Back, and A. Kákay. Experimental observation of the curvature-induced asymmetric spin-wave dispersion in hexagonal nanotubes. *arXiv*, 2020. doi: arXiv:2009.02238.
- [43] M. Vázquez. *Magnetic nano-and microwires: design, synthesis, properties and applications. 2nd Edition*. Woodhead Publishing, 2020.
- [44] A. Mehlin, B. Gross, M. Wyss, T. Schefer, G. Tütüncüoglu, F. Heimbach, A. Fontcuberta i Morral, D. Grundler, and M. Poggio. Observation of end-vortex nucleation in individual ferromagnetic nanotubes. *Physical Review B*, 97(13), 2018. doi: 10.1103/PhysRevB.97.134422.
- [45] D. Rueffer. *Magnetic States and Spin-Wave Modes in Single Ferromagnetic Nanotubes*. PhD thesis, EPFL, 2014.
- [46] A. P. Espejo, R. Zierold, J. Gooth, J. Dendooven, C. Detavernier, J. Escrig, and K. Nielsch. Magnetic and electrical characterization of nickel-rich NiFe thin films synthesized by

- atomic layer deposition and subsequent thermal reduction. *Nanotechnology*, 27(34): 345707, 2016. doi: 10.1088/0957-4484/27/34/345707.
- [47] T. Sebastian, K. Schultheiss, B. Obry, B. Hillebrands, and H. Schultheiss. Micro-focused Brillouin light scattering: imaging spin waves at the nanoscale. *Frontiers in Physics*, 3: 35, 2015. doi: 10.3389/fphy.2015.00035.
- [48] W. Nolting and A. Ramakanth. *Quantum Theory of Magnetism*. Springer Berlin Heidelberg, 2009.
- [49] A.G. Gurevich and G.A. Melkov. *Magnetization Oscillations and Waves*. Taylor & Francis, 1996.
- [50] C. G. Stefanita. *Magnetism*. Springer Berlin Heidelberg, 2012. doi: 10.1007/978-3-642-22977-0.
- [51] C. M. Hurd. Varieties of magnetic order in solids. *Contemporary Physics*, 23(5):469–493, 1982. doi: 10.1080/00107518208237096.
- [52] J. Fidler, R.W. Chantrell, T. Schrefl, and M.A. Wongsam. Micromagnetics: Basic principles. pages 5642–5650. Elsevier, Oxford, 2001. doi: 10.1016/B0-08-043152-6/00984-0.
- [53] W. F. Brown. Theory of the approach to magnetic saturation. *Physical Review*, 58: 736–743, 1940. doi: 10.1103/PhysRev.58.736.
- [54] W. F. Brown. Thermal fluctuations of a single-domain particle. *Physical Review*, 130: 1677–1686, 1963. doi: 10.1103/PhysRev.130.1677.
- [55] C. Herring and C. Kittel. On the theory of spin waves in ferromagnetic media. *Physical Review*, 81:869–880, 1951. doi: 10.1103/PhysRev.81.869.
- [56] G. S. Abo, Y. Hong, J. Park, J. Lee, W. Lee, and B. Choi. Definition of magnetic exchange length. *IEEE Transactions on Magnetics*, 49(8):4937–4939, 2013. doi: 10.1109/TMAG.2013.2258028.
- [57] C. Kittel. On the theory of ferromagnetic resonance absorption. *Physical Review*, 73: 155–161, 1948. doi: 10.1103/PhysRev.73.155.
- [58] A. Aharoni. Demagnetizing factors for rectangular ferromagnetic prisms. *Journal of Applied Physics*, 83(6):3432–3434, 1998. doi: 10.1063/1.367113.
- [59] R. Moskowitz and E. Della Torre. Theoretical aspects of demagnetization tensors. *IEEE Transactions on Magnetics*, 2(4):739–744, 1966. doi: 10.1109/TMAG.1966.1065973.
- [60] D. X Chen, J. A. Brug, and R. B. Goldfarb. Demagnetizing factors for cylinders. *IEEE Transactions on magnetics*, 27(4):3601–3619, 1991. doi: 10.1109/20.102932.

- [61] J. Prat-Camps, C. Navau, D. X. Chen, and A. Sanchez. Exact analytical demagnetizing factors for long hollow cylinders in transverse field. *IEEE Magnetics Letters*, 3:0500104–0500104, 2012. doi: 10.1109/LMAG.2012.2198617.
- [62] L. F. Yin, D. H. Wei, N. Lei, L. H. Zhou, C. S. Tian, G. S. Dong, X. F. Jin, L. P. Guo, Q. J. Jia, and R. Q. Wu. Magnetocrystalline anisotropy in permalloy revisited. *Physical Review Letters*, 97:067203, 2006. doi: 10.1103/PhysRevLett.97.067203.
- [63] L. D. Landau and E. Lifshitz. On the theory of the dispersion of magnetic permeability in ferromagnetic bodies. *Phys. Z. Sowjet.*, 8:153, 1935. doi: 10.1016/B978-0-08-036364-6.50008-9.
- [64] T. L. Gilbert. A Lagrangian formulation of the gyromagnetic equation of the magnetization field. *Physical Review*, 100:1243, 1955.
- [65] F. Giesen. *Magnetization Dynamics of Nanostructured Ferromagnetic Rings and Rectangular Elements*. Cuvillier Verlag, 2005.
- [66] R. Huber. *Control of Spin Waves on the Nanoscale in One-Dimensional Magnonic Crystals and Atomic Layer Deposition of Metallic Ferromagnets for Second Generation of Nanomaterials*,. PhD thesis, Munich University of Technology, 2013.
- [67] F. Brandl. *Thermal effects in laser-heated freestanding permalloy and multiferroic hybrid structures forming magnonic grating couplers and prototype spin wave multiplexers*. PhD thesis, Technische Universität München, 2014.
- [68] B. A. Kalinikos and A. N. Slavin. Theory of dipole-exchange spin wave spectrum for ferromagnetic films with mixed exchange boundary conditions. *Journal of Physics C: Solid State Physics*, 19:7013–7033, 1986. doi: 10.1088/0022-3719/19/35/014.
- [69] H. Leblond and V. Veerakumar. Magnetostatic spin solitons in ferromagnetic nanotubes. *Physical Review B*, 70:134413, 2004. doi: 10.1103/PhysRevB.70.134413.
- [70] F. Balhorn, S. Mansfeld, A. Krohn, J. Topp, W. Hansen, D. Heitmann, and S. Mendach. Spin-wave interference in three-dimensional rolled-up ferromagnetic microtubes. *Physical Review Letters*, 104:037205, 2010. doi: 10.1103/PhysRevLett.104.037205.
- [71] F. Balhorn, S. Jeni, W. Hansen, D. Heitmann, and S. Mendach. Axial and azimuthal spin-wave eigenmodes in rolled-up permalloy stripes. *Applied Physics Letters*, 100(22):222402, 2012. doi: 10.1063/1.3700809.
- [72] S. Mendach, J. Podbielski, J. Topp, W. Hansen, and D. Heitmann. Spin-wave confinement in rolled-up ferromagnetic tubes. *Applied Physics Letters*, 93(26):262501, 2008. doi: 10.1063/1.3058764.
- [73] J. A. Otálora, M. Yan, H. Schultheiss, R. Hertel, and A. Kákay. Asymmetric spin-wave dispersion in ferromagnetic nanotubes induced by surface curvature. *Physical Review B*, 95(18), 2017. doi: 10.1103/PhysRevB.95.184415.



- 
- [74] A.P. Espejo, N. Vidal-Silva, J.A. López-López, D. Goerlitz, K. Nielsch, and J. Escrig. Current-driven vortex domain wall motion in wire-tube nanostructures. *Applied Physics Letters*, 106(13):132405, 2015. doi: 10.1063/1.4916666.
- [75] F. G. Mertens and A. R. Bishop. Dynamics of vortices in two-dimensional magnets. *Nonlinear Science at the Dawn of the 21st Century*, pages 137–170, 2007. doi: 10.1007/3-540-46629-0\_7.
- [76] H. Wang and C. E Campbell. Spin dynamics of a magnetic antivortex: micromagnetic simulations. *Physical Review B*, 76(22):220407, 2007. doi: 10.1103/PhysRevB.76.220407.
- [77] A. Fert, V. Cros, and J. Sampaio. Skyrmions on the track. *Nature nanotechnology*, 8(3): 152–156, 2013. doi: 10.1038/nnano.2013.29.
- [78] A. Fert, N. Reyren, and V. Cros. Magnetic skyrmions: advances in physics and potential applications. *Nature Reviews Materials*, 2(7):1–15, 2017.
- [79] E. H. Frei, S. Shtrikman, and D. Treves. Critical size and nucleation field of ideal ferromagnetic particles. *Physical Review*, 106:446–455, 1957. doi: 10.1103/PhysRev.106.446.
- [80] G.C. Han, B.Y. Zong, P. Luo, and Y.H. Wu. Angular dependence of the coercivity and remanence of ferromagnetic nanowire arrays. *Journal of Applied Physics*, 93(11):9202–9207, 2003. doi: 10.1063/1.1572197.
- [81] J. Escrig, M. Daub, P. Landeros, K. Nielsch, and D. Altbir. Angular dependence of coercivity in magnetic nanotubes. *Nanotechnology*, 18(44):445706, 2007. doi: 10.1088/0957-4484/18/44/445706.
- [82] S. Allende, J. Escrig, D. Altbir, E. Salcedo, and M. Bahiana. Angular dependence of the transverse and vortex modes in magnetic nanotubes. *The European Physical Journal B*, 66(1):37–40, 2008. doi: 10.1140/epjb/e2008-00385-4.
- [83] J. Escrig, J. Bachmann, J. Jing, M. Daub, D. Altbir, and K. Nielsch. Crossover between two different magnetization reversal modes in arrays of iron oxide nanotubes. *Physical Review B*, 77:214421, 2008. doi: 10.1103/PhysRevB.77.214421.
- [84] J. Bachmann, J. Escrig, K. Pitzschel, J. M.M. Moreno, J. Jing, D. Görlitz, D. Altbir, and K. Nielsch. Size effects in ordered arrays of magnetic nanotubes: pick your reversal mode. *Journal of Applied Physics*, 105(7), 2009. doi: 10.1063/1.3074109.
- [85] Z. K. Wang, H. S. Lim, H. Y. Liu, S. C. Ng, M. H. Kuok, L. L. Tay, D. J. Lockwood, M. G. Cottam, K. L. Hobbs, P. R. Larson, J. C. Keay, G. D. Lian, and M. B. Johnson. Spin waves in nickel nanorings of large aspect ratio. *Physical Review Letters*, 94:137208, 2005. doi: 10.1103/PhysRevLett.94.137208.
- [86] A.P. Chen, K.Y. Guslienko, and J. Gonzalez. Magnetization configurations and reversal of thin magnetic nanotubes with uniaxial anisotropy. *Journal of Applied Physics*, 108(8): 083920, 2010. doi: 10.1063/1.3488630.

- [87] A. P. Chen, J. M. Gonzalez, and K. Y. Guslienko. Magnetization configurations and reversal of magnetic nanotubes with opposite chiralities of the end domains. *Journal of Applied Physics*, 109:073923, 4 2011. doi: 10.1063/1.3562190.
- [88] A. Buchter, J. Nagel, D. Ruffer, F. Xue, D. P. Weber, O. F. Kieler, T. Weimann, J. Kohlmann, A. B. Zorin, E. Russo-Averchi, R. Huber, P. Berberich, A. Fontcuberta i Morral, M. Kemmler, R. Kleiner, D. Koelle, D. Grundler, and M. Poggio. Reversal mechanism of an individual ni nanotube simultaneously studied by torque and squid magnetometry. *Physical Review Letters*, 111:067202, 2013. doi: 10.1103/PhysRevLett.111.067202.
- [89] P. Landeros and A. S. Núñez. Domain wall motion on magnetic nanotubes. *Journal of Applied Physics*, 108(3):33917, 2010. doi: 10.1063/1.3466747.
- [90] J. A. Otálora, J. A. López-López, P. Landeros, P. Vargas, and A. S. Nunez. Breaking of chiral symmetry in vortex domain wall propagation in ferromagnetic nanotubes. *Journal of Magnetism and Magnetic Materials*, 341:86–92, 2013. doi: 10.1016/j.jmmm.2013.04.014.
- [91] M. Yan, C. Andreas, A. Kákay, F. García-Sánchez, and R. Hertel. Chiral symmetry breaking and pair-creation mediated Walker breakdown in magnetic nanotubes. *Applied Physics Letters*, 100:252401, 2012. doi: 10.1063/1.4727909.
- [92] J. Hurst, A. De Riz, M. Staño, J. C. Toussaint, O. Fruchart, and D. Gusakova. Theoretical study of current-induced domain wall motion in magnetic nanotubes with azimuthal domains. *Physical Review B*, 103:024434, 2021. doi: 10.1103/PhysRevB.103.024434.
- [93] J. A. Otálora, JA López-López, AS Núñez, and P Landeros. Domain wall manipulation in magnetic nanotubes induced by electric current pulses. *Journal of Physics: Condensed Matter*, 24(43):436007, 2012.
- [94] J. A. Otálora, J. A. López-López, P. Vargas, and P. Landeros. Chirality switching and propagation control of a vortex domain wall in ferromagnetic nanotubes. *Applied Physics Letters*, 100(7):072407, 2012. doi: 10.1063/1.3687154.
- [95] M. Yan, A. Kákay, C. Andreas, and R. Hertel. Spin-Cherenkov effect and magnonic Mach cones. *Physical Review B*, 88(22):220412, 2013. doi: 10.1103/PhysRevB.88.220412.
- [96] T. M. Nguyen and M. G. Cottam. Spin-wave excitations in ferromagnetic nanotubes. *Surface science*, 600(18):4151–4154, 2006. doi: 10.1016/j.susc.2006.01.138.
- [97] T. K. Das and M. G Cottam. Theory of dipole-exchange spin waves in metallic ferromagnetic nanotubes of large aspect ratio. *Journal of Applied Physics*, 109(7):07D323, 2011. doi: 10.1063/1.3554208.
- [98] A. L. González, P. Landeros, and Á. S. Núñez. Spin wave spectrum of magnetic nanotubes. *Journal of magnetism and magnetic materials*, 322(5):530–535, 2010. doi: 10.1016/j.jmmm.2009.10.010.

- 
- [99] J. A. Otálora, A. Kákay, J. Lindner, H. Schultheiss, A. Thomas, J. Fassbender, and K. Nielsch. Frequency linewidth and decay length of spin waves in curved magnetic membranes. *Physical Review B*, 98(1), 2018. doi: 10.1103/PhysRevB.98.014403.
- [100] O. Albrecht, R. Zierold, S. Allende, J. Escrig, C. Patzig, B. Rauschenbach, K. Nielsch, and D. Görlitz. Experimental evidence for an angular dependent transition of magnetization reversal modes in magnetic nanotubes. *Journal of Applied Physics*, 109(9):093910, 2011. doi: 10.1063/1.3583666.
- [101] J. Bachmann, J. Jing, M. Knez, S. Barth, H. Shen, S. Mathur, U. Gösele, and K. Nielsch. Ordered iron oxide nanotube arrays of controlled geometry and tunable magnetism by atomic layer deposition. *Journal of the American Chemical Society*, 129(31):9554–9555, 2007. doi: 10.1021/ja072465w.
- [102] A. Rudolph, M. Soda, M. Kiessling, T. Wojtowicz, D. Schuh, W. Wegscheider, J. Zweck, C. Back, and E. Reiger. Ferromagnetic GaAs/GaMnAs core-shell nanowires grown by molecular beam epitaxy. *Nano Letters*, 9(11):3860–3866, 2009. doi: 10.1021/nl9020717.
- [103] Y. T. Chong, D. Görlitz, S. Martens, M. Y. E. Yau, S. Allende, J. Bachmann, and K. Nielsch. Multilayered core/shell nanowires displaying two distinct magnetic switching events. *Advanced Materials*, 22(22):2435–2439, 2010. doi: 10.1002/adma.20090432.
- [104] J. Escrig, S. Allende, D. Altbir, and M. Bahiana. Magnetostatic interactions between magnetic nanotubes. *Applied Physics Letters*, 93:023101, 2008. doi: 10.1063/1.2956681.
- [105] K. Baumgaertl, F. Heimbach, S. Maendl, D. Rueffer, A. Fontcuberta i Morral, and D. Grundler. Magnetization reversal in individual Py and CoFeB nanotubes locally probed via anisotropic magnetoresistance and anomalous Nernst effect. *Applied Physics Letters*, 108(13):132408, 2016. doi: 10.1063/1.4945331.
- [106] D. P. Weber, D. Rüffer, A. Buchter, F. Xue, E. Russo-Averchi, R. Huber, P. Berberich, J. Arbiol, A. Fontcuberta I Morral, D. Grundler, and M. Poggio. Cantilever magnetometry of individual ni nanotubes. *Nano Letters*, 12(12):6139–6144, 2012. doi: 10.1021/nl302950u.
- [107] D. Vasyukov, L. Ceccarelli, M. Wyss, B. Gross, A. Schwarb, A. Mehlin, N. Rossi, G. Tütüncüoglu, F. Heimbach, R. R. Zamani, A. Kovács, A. Fontcuberta I Morral, D. Grundler, and M. Poggio. Imaging stray magnetic field of individual ferromagnetic nanotubes. *Nano Letters*, 18(2):964–970, 2018. doi: 10.1021/acs.nanolett.7b04386.
- [108] M. Wyss, A. Mehlin, B. Gross, A. Buchter, A. Farhan, M. Buzzi, A. Kleibert, G. Tütüncüoglu, F. Heimbach, Morral A.I. Fontcuberta, D. Grundler, and M. Poggio. Imaging magnetic vortex configurations in ferromagnetic nanotubes. *Physical Review B*, 96(2), 2017. doi: 10.1103/PhysRevB.96.024423.
- [109] J. Liang, J. Wang, A. Paul, B. J. Cooley, D. W. Rench, N. S. Dellas, S. E. Mohny, R. Engel-Herbert, and N. Samarth. Measurement and simulation of anisotropic magnetore-

- pistance in single GaAs/MnAs core/shell nanowires.
- Applied Physics Letters*
- , 100(18):182402, 2012. doi: 10.1063/1.4710524.
- [110] C. Butschkow, E. Reiger, A. Rudolph, S. Geißler, D. Neumaier, M. Soda, D. Schuh, G. Woltersdorf, W. Wegscheider, and D. Weiss. Origin of negative magnetoresistance of GaAs/(Ga,Mn)As core-shell nanowires. *Physical Review B*, 87(24):245303, 2013. doi: 0.1103/PhysRevB.87.245303.
  - [111] M. Zimmermann, T. N. Gerhard Meier, F. Dirnberger, A. Kákay, M. Decker, S. Wintz, S. Finizio, E. Josten, J. Raabe, M. Kronseder, D. Bougeard, J. Lindner, and C. H. Back. Origin and manipulation of stable vortex ground states in permalloy nanotubes. *Nano Letters*, 18(5):2828–2834, 2018. doi: 10.1021/acs.nanolett.7b05222.
  - [112] J. Nagel, A. Buchter, F. Xue, O. F. Kieler, T. Weimann, J. Kohlmann, A. B. Zorin, D. Ruffer, E. Russo-Averchi, R. Huber, et al. Nanoscale multifunctional sensor formed by a Ni nanotube and a scanning Nb nanoSQUID. *Physical Review B*, 88(6):064425, 2013. doi: 10.1103/PhysRevB.88.064425.
  - [113] A. Buchter, R. Wölbing, M. Wyss, O. F. Kieler, T. Weimann, J. Kohlmann, A. B. Zorin, D. Ruffer, F. Matteini, G. Tütüncüoglu, et al. Magnetization reversal of an individual exchange-biased permalloy nanotube. *Physical Review B*, 92(21):214432, 2015. doi: 10.1103/PhysRevB.92.214432.
  - [114] B. Gross, D.P. Weber, D. Ruffer, A. Buchter, F. Heimbach, A. Fontcuberta i Morral, D. Grundler, and M. Poggio. Dynamic cantilever magnetometry of individual CoFeB nanotubes. *Physical Review B*, 93(6):064409, 2016. doi: 10.1103/PhysRevB.93.064409.
  - [115] F. Balhorn, C. Bausch, S. Jeni, W. Hansen, D. Heitmann, and S. Mendach. Azimuthal spin-wave modes in rolled-up permalloy microtubes: Tuneable mode frequency, mode patterns, and mode splitting. *Physical Review B*, 88(5):054402, 2013. doi: 10.1103/PhysRevB.88.054402.
  - [116] F. Giesen, J. Podbielski, T. Korn, M. Steiner, A. Van Staa, and D. Grundler. Hysteresis and control of ferromagnetic resonances in rings. *Applied Physics Letters*, 86(11):112510, mar 2005. doi: 10.1063/1.1886247.
  - [117] M. Zimmermann. *Static and dynamic properties of hexagonally shaped magnetic nanotubes*. PhD thesis, 2018.
  - [118] M. Leskelä. Atomic layer deposition of nanostructured materials. pages 401–421. Wiley-VCH, 2012. doi: 10.1002/9783527639915.ch17.
  - [119] H. Kim, T. Koseki, T. Ohba, T. Ohta, Y. Kojima, H. Sato, and Y. Shimogaki. Cu wettability and diffusion barrier property of Ru thin film for Cu metallization. *Journal of The Electrochemical Society*, 152(8):G594, 2005. doi: 10.1149/1.1939353.

- [120] D. J. Hagen, I. M. Povey, S. Rushworth, J. S. Wrench, L. Keeney, M. Schmidt, N. Petkov, S. T. Barry, J. P. Coyle, and M. E. Pemble. Atomic layer deposition of cu with a carbene-stabilized cu(i) silylamide. *Journal of Materials Chemistry C*, 2:9205–9214, 2014. doi: 10.1039/C4TC01418A.
- [121] M. Kim, S. Nabeya, D. K. Nandi, K. Suzuki, H. M. Kim, S. Y. Cho, K. B. Kim, and S. H. Kim. Atomic layer deposition of nickel using a heteroleptic Ni precursor with NH<sub>3</sub> and selective deposition on defects of graphene. *ACS Omega*, 4(6):11126–11134, 2019. doi: 10.1021/acsomega.9b01003.
- [122] J. Chae, H. S. Park, and S. W. Kang. Atomic layer deposition of nickel by the reduction of preformed nickel oxide. *Electrochemical and Solid-State Letters*, 5(6):C64, 2002. doi: 10.1149/1.1475199.
- [123] K. W. Do, C. M. Yang, I. S. Kang, K. M. Kim, K. H. Back, H. I. Cho, H. B. Lee, S. H. Kong, S. H. Hahm, D. H. Kwon, J. H. Lee, and J. H. Lee. Formation of low-resistivity nickel silicide with high temperature stability from atomic-layer-deposited nickel thin film. *Japanese Journal of Applied Physics*, 45(4B):2975–2979, 2006. doi: 10.1143/jjap.45.2975.
- [124] H. B. R. Lee, S. H. Bang, W. H. Kim, G. H. Gu, Y. K. Lee, T. M. Chung, C. G. Kim, C. G. Park, and H. Kim. Plasma-Enhanced Atomic Layer Deposition of Ni. *Japanese Journal of Applied Physics*, 49(5 PART 3):05FA11, 2010. doi: 10.1143/JJAP.49.05FA11.
- [125] W. H. Kim, H. B. R. Lee, K. Heo, Y. K. Lee, T. M. Chung, C. G. Kim, S. Hong, J. Heo, and H. Kim. Atomic layer deposition of ni thin films and application to area-selective deposition. *Journal of The Electrochemical Society*, 158(1):D1–D5, 2011. doi: 10.1149/1.3504196.
- [126] C.M. Yang, S.W. Yun, J.B. Ha, K.I. Na, H.I. Cho, H.B. Lee, J.H. Jeong, S.H. Kong, S.H. Hahm, and J.H. Lee. Effectiveness of self-carbon and titanium capping layers in NiSi formation with Ni film deposited by atomic layer deposition. *Japanese Journal of Applied Physics*, 46(4B):1981–1983, 2007. doi: 10.1143/jjap.46.1981.
- [127] L. C. Kalutarage, P. D. Martin, M. J. Heeg, and C. H. Winter. Volatile and thermally stable mid to late transition metal complexes containing  $\alpha$ -imino alkoxide ligands, a new strongly reducing coreagent, and thermal atomic layer deposition of Ni, Co, Fe, and Cr metal films. *Journal of the American Chemical Society*, 135(34):12588–12591, 2013. doi: 10.1021/ja407014w.
- [128] M. Sarr, N. Bahlawane, D. Arl, M. Dossot, E. McRae, and D. Lenoble. Tailoring the properties of atomic layer deposited nickel and nickel carbide thin films via chain-length control of the alcohol reducing agents. *The Journal of Physical Chemistry C*, 118(40):23385–23392, 2014. doi: 10.1021/jp5068318.
- [129] G. Yuan, H. Shimizu, T. Momose, and Y. Shimogaki. Kinetic study on hot-wire-assisted atomic layer deposition of nickel thin films. *Journal of Vacuum Science & Technology A: Vacuum, Surfaces, and Films*, 32(1):01A104, 2014. doi: 10.1116/1.4829361.

## Bibliography

---

- [130] P. Motamedi, K. Bosnick, K. Cui, K. Cadien, and J. D. Hogan. Growth and characterization of metastable hexagonal nickel thin films via plasma-enhanced atomic layer deposition. *ACS Applied Materials & Interfaces*, 9(29):24722–24730, 2017. doi: 10.1021/acsami.7b05571.
- [131] J. M. Park, S. Kim, J. Hwang, W. S. Han, W. Koh, and W. J. Lee. Plasma-enhanced atomic layer deposition of nickel thin film using bis(1,4-diisopropyl-1,4-diazabutadiene)nickel. *Journal of Vacuum Science & Technology A: Vacuum, Surfaces, and Films*, 36(1):01A119, 2018. doi: 10.1116/1.5003388.
- [132] Y. Zhang, L. Du, X. Liu, and Y. Ding. High growth per cycle thermal atomic layer deposition of Ni films using an electron-rich precursor. *Nanoscale*, 11(8):3484–3488, 2019. doi: 10.1039/c8nr08040b.
- [133] G. Cacciamani, J. De Keyzer, R. Ferro, U.E. Klotz, J. Lacaze, and P. Wollants. Critical evaluation of the Fe–Ni, Fe–Ti and Fe–Ni–Ti alloy systems. *Intermetallics*, 14(10):1312–1325, 2006. doi: 10.1016/j.intermet.2005.11.028.
- [134] Alex B. F. Martinson, Michael J. DeVries, Joseph A. Libera, Steven T. Christensen, Joseph T. Hupp, Michael J. Pellin, and Jeffrey W. Elam. Atomic layer deposition of Fe<sub>2</sub>O<sub>3</sub> using ferrocene and ozone. *The Journal of Physical Chemistry C*, 115(10):4333–4339, 2011. doi: 10.1021/jp110203x.
- [135] M. Lie, H. Fjellvåg, and A. Kjekshus. Growth of Fe<sub>2</sub>O<sub>3</sub> thin films by atomic layer deposition. *Thin Solid Films*, 488(1):74–81, 2005. doi: 10.1016/j.tsf.2005.04.063.
- [136] J. R. Avila, D. W. Kim, M. Rimoldi, O. K. Farha, and J. T. Hupp. Fabrication of thin films of  $\alpha$ -Fe<sub>2</sub>O<sub>3</sub> via atomic layer deposition using iron bisamidinate and water under mild growth conditions. *ACS Applied Materials & Interfaces*, 7(30):16138–16142, 2015. doi: 10.1021/acsami.5b04043.
- [137] H.C.M. Knoops, S.E. Potts, A.A. Bol, and W.M.M. Kessels. Atomic layer deposition. In *Handbook of Crystal Growth*, pages 1101–1134. North-Holland, second edition edition, 2015. doi: 10.1016/B978-0-444-63304-0.00027-5.
- [138] M. Leskelä and M. Ritala. Atomic layer deposition (ALD): from precursors to thin film structures. *Thin Solid Films*, 409(1):138–146, 2002. doi: 10.1016/S0040-6090(02)00117-7.
- [139] E. Ahvenniemi, A. R. Akbashev, S. Ali, M. Bechelany, M. Berdova, S. Boyadjiev, D. C. Cameron, R. Chen, M. Chubarov, V. Cremers, et al. Review Article: Recommended reading list of early publications on atomic layer deposition—Outcome of the “Virtual Project on the History of ALD”. *Journal of Vacuum Science & Technology A: Vacuum, Surfaces, and Films*, 35(1):010801, 2017. doi: 10.1116/1.4971389.
- [140] A. A. Malygin, V. E. Drozd, A. A. Malkov, and V. M. Smirnov. From v. b. aleskovskii’s “framework” hypothesis to the method of molecular layering/ atomic layer deposition. *Chemical Vapor Deposition*, 21(10-11-12):216–240, 2015. doi: 10.1002/cvde.201502013.

- [141] S. I. Kol'tsov and V. B. Aleskovskii. Silica gel: Its structure and chemical properties. *Goskhimizdat, Leningrad*, page 94, 1963.
- [142] V. B. Aleskovskii. Chemistry and technology of solids. *Journal of Applied Chemistry of the USSR*, 47(10):2207–2217, 1974.
- [143] R. L. Puurunen. A short history of atomic layer deposition: Tuomo Suntola's atomic layer epitaxy. *Chemical Vapor Deposition*, 20(10-11-12):332–344, 2014. doi: 10.1002/cvde.201402012.
- [144] J. Suntola, T. and Antson. Method for producing compound thin films, November 15 1977. US Patent 4,058,430.
- [145] G. N. Parsons, J. W. Elam, S. M. George, S. Haukka, H. Jeon, W. M. M. Kessels, M. Leskelä, P. Poodt, M. Ritala, and S. M. Rossmagel. History of atomic layer deposition and its relationship with the American Vacuum Society. *Journal of Vacuum Science & Technology A: Vacuum, Surfaces, and Films*, 31(5):050818, 2013. doi: 10.1116/1.4816548.
- [146] K. Mistry, C. Allen, C. Auth, B. Beattie, D. Bergstrom, M. Bost, M. Brazier, M. Buehler, A. Cappellani, R. Chau, et al. A 45 nm logic technology with high-k+ metal gate transistors, strained silicon, 9 Cu interconnect layers, 193 nm dry patterning, and 100% Pb-free packaging. In *2007 IEEE International Electron Devices Meeting*, pages 247–250, 2007. doi: 10.1109/IEDM.2007.4418914.
- [147] F. Zaera. The surface chemistry of atomic layer depositions of solid thin films. *The Journal of Physical Chemistry Letters*, 3(10):1301–1309, 2012. doi: 10.1021/jz300125f.
- [148] V. Cremers, R. L. Puurunen, and J. Dendooven. Conformality in atomic layer deposition: Current status overview of analysis and modelling. *Applied Physics Reviews*, 6:21302, 2019. doi: 10.1063/1.5060967.
- [149] J. W. Elam, D. Routkevitch, P. P. Mardilovich, and S. M. George. Conformal coating on ultrahigh-aspect-ratio nanopores of anodic alumina by atomic layer deposition. *Chemistry of Materials*, 15(18):3507–3517, 2003. doi: 10.1021/cm0303080.
- [150] J. Dendooven, D. Deduytsche, J. Musschoot, R. L. Vanmeirhaeghe, and C. Detavernier. Modeling the conformality of atomic layer deposition: The effect of sticking probability. *Journal of The Electrochemical Society*, 156(4):P63, 2009. doi: 10.1149/1.3072694.
- [151] H. C. M. Knoops, E. Langereis, M. C. M. van de Sanden, and W. M. M. Kessels. Conformality of plasma-assisted ALD: Physical processes and modeling. *Journal of The Electrochemical Society*, 157(12):G241, 2010. doi: 10.1149/1.3491381.
- [152] H. B. Profijt, S. E. Potts, M. C. M. van de Sanden, and W. M. M. Kessels. Plasma-Assisted Atomic Layer Deposition: Basics, Opportunities, and Challenges. *Journal of Vacuum Science & Technology A: Vacuum, Surfaces, and Films*, 29(5):050801, 2011. doi: 10.1116/1.3609974.

- [153] H. C. M. Knoop, T. Faraz, K. Arts, and W. M. M. Kessels. Status and prospects of plasma-assisted atomic layer deposition. *Journal of Vacuum Science & Technology A: Vacuum, Surfaces, and Films*, 37(3):030902, 2019. doi: 10.1116/1.5088582.
- [154] M.P. Proenca, C. T. Sousa, J. Escrig, J. Ventura, M. Vazquez, and J.P.) Araujo. Magnetic interactions and reversal mechanisms in co nanowire and nanotube arrays. *Journal of Applied Physics*, 113:093907, 2013. doi: <https://doi.org/10.1063/1.4794335>.
- [155] C. Y. Han, G. A. Willing, Z. Xiao, and H. H. Wang. Control of the anodic aluminum oxide barrier layer opening process by wet chemical etching. *Langmuir*, 23(3):1564–1568, 2007. doi: 10.1021/la060190c.
- [156] Y. Velázquez-Galván, J. M. Martínez-Huerta, J. De La Torre Medina, Y. Danlée, L. Piraux, and A. Encinas. Dipolar interaction in arrays of magnetic nanotubes. *Journal of Physics: Condensed Matter*, 26(2):026001, 2013. doi: 10.1088/0953-8984/26/2/026001.
- [157] D. Zhang, Z. Liu, S. Han, C. Li, B. Lei, M. P. Stewart, J. M. Tour, and C. Zhou. Magnetite Fe<sub>3</sub>O<sub>4</sub> core shell nanowires: synthesis and magnetoresistance. *Nano Letters*, 4(11):2151–2155, 2004. doi: 10.1021/nl048758u.
- [158] M. Hilse, Y. Takagaki, J. Herfort, M. Ramsteiner, C. Herrmann, S. Breuer, L. Geelhaar, and H. Riechert. Ferromagnet-semiconductor nanowire coaxial heterostructures grown by molecular-beam epitaxy. *Applied Physics Letters*, 95(13):133126, 2009. doi: 10.1063/1.3240405.
- [159] R. S. Wagner and W. C. Ellis. Vapor-liquid-solid mechanism of single crystal growth. *Applied Physics Letters*, 4(5):89–90, mar 1964. doi: 10.1063/1.1753975.
- [160] A. Fontcuberta i Morral, C. Colombo, G. Abstreiter, J. Arbiol, and J. R. Morante. Nucleation mechanism of gallium-assisted molecular beam epitaxy growth of gallium arsenide nanowires. *Applied Physics Letters*, 92:063112, 2 2008. doi: 10.1063/1.2837191.
- [161] F. Matteini, V. G. Dubrovskii, D. Ruffer, G. Tütüncüoğlu, Y. Fontana, and A. Fontcuberta i Morral. Tailoring the diameter and density of self-catalyzed GaAs nanowires on silicon. *Nanotechnology*, 26(10):105603, 2015. doi: 10.1088/0957-4484/26/10/105603.
- [162] F. Matteini, G. Tütüncüoğlu, D. Mikulik, J. Vukajlovic-Plestina, H. Potts, J. B.e Leran, W. C. Carter, and A. Fontcuberta i Morral. Impact of the Ga droplet wetting, morphology, and pinholes on the orientation of GaAs nanowires. *Crystal Growth & Design*, 16(10):5781–5786, 2016. doi: 10.1021/acs.cgd.6b00858.
- [163] C. Colombo, D. Spirkoska, M. Frimmer, G. Abstreiter, and A. Fontcuberta i Morral. Ga-assisted catalyst-free growth mechanism of GaAs nanowires by molecular beam epitaxy. *Physical Review B*, 77(15), 2008. doi: 10.1103/PhysRevB.77.155326.
- [164] L.J. van der Pauw. A method of measuring specific resistivity and hall effect of discs of arbitrary shape. *Philips Research Reports*, 13(1):1–9, 1958.



- 
- [165] W. Thomson. On the electro-dynamic qualities of metals: Effects of magnetization on the electric conductivity of nickel and of iron. *Proceedings of the Royal Society of London*, (8):546–550, 1857.
- [166] M. Kateb, E. Jacobsen, and S. Ingvarsson. Application of an extended van der Pauw method to anisotropic magnetoresistance measurements of ferromagnetic films. *Journal of Physics D: Applied Physics*, 52(7):075002, 2019. doi: 10.1088/1361-6463/AAF4C9.
- [167] B.C. Wadell. *Transmission Line Design Handbook*. Artech House, 1991.
- [168] S. Neusser. *Spin waves in antidot lattices: From quantization to magnonic crystals*. PhD thesis, Technische Universität München, 2011.
- [169] W. F. Egan. *Practical RF Design*. John Wiley and Sons, 2003.
- [170] L. Brillouin. Diffusion de la lumière et des rayons x par un corps transparent homogène. *Annales de Physique*, 9(17):88–122, 1922. doi: 10.1051/anphys/192209170088.
- [171] Michael Cottam. *Light scattering in magnetic solids*. Wiley, New York, 1986.
- [172] JR Sandercock. *Light scattering in solids*, edited by m. balkanski, 1971. Paris: Flammarion Press.
- [173] B. Hillebrands. Progress in multipass tandem fabry–perot interferometry: I. a fully automated, easy to use, self-aligning spectrometer with increased stability and flexibility. *Review of Scientific Instruments*, 70(3):1589–1598, 1999. doi: 10.1063/1.1149637.
- [174] S. O. Demokritov and V. E. Demidov. Micro-brillouin light scattering spectroscopy of magnetic nanostructures. *IEEE Trans. Magn.*, 44:6–12, 2008.
- [175] V. E. Demidov and S. O. Demokritov. Magnonic waveguides studied by microfocus brillouin light scattering. *IEEE Transactions on Magnetics*, 51(4):1–15, 2015. doi: 10.1109/tmag.2014.2388196.
- [176] V. E. Demidov, O. Dzyapko, S. O. Demokritov, G. A. Melkov, and A. N. Slavin. Observation of spontaneous coherence in Bose-Einstein condensate of magnons. *Physical Review Letters*, 100:047205, 2008. doi: 10.1103/PhysRevLett.100.047205.
- [177] J. A Dean. *LANGE'S HANDBOOK OF CHEMISTRY*. McGraw-Hill, 1999.
- [178] J. Crangle and G. M. Goodman. The magnetization of pure iron and nickel. *Proceedings of the Royal Society A : Mathematical, Physical and Engineering Sciences*, 321(1547): 477–491, 1971. doi: 10.1098/rspa.1971.0044.
- [179] R. Arias and D. L. Mills. Extrinsic contributions to the ferromagnetic resonance response of ultrathin films. *Physical Review B*, 60(10):7395–7409, 1999. doi: 10.1103/PhysRevB.60.7395.

## Bibliography

---

- [180] Y. Tserkovnyak, A. Brataas, G. E.W. Bauer, and B. I. Halperin. Nonlocal magnetization dynamics in ferromagnetic heterostructures. *Reviews of Modern Physics*, 77(4):1375–1421, 2005. doi: 10.1103/RevModPhys.77.1375.
- [181] I. Koh and L. Josephson. Magnetic nanoparticle sensors. *Sensors*, 9(10):8130–8145, 2009. doi: 10.3390/s91008130.
- [182] W. P. McCray. How spintronics went from the lab to the iPod. *Nature Nanotechnology*, 4: 2–4, 2009. doi: 10.1038/nnano.2008.380.
- [183] G. Wang, Z. Gao, S. Tang, C. Chen, F. Duan, S. Zhao, S. Lin, Y. Feng, L. Zhou, and Y. Qin. Microwave absorption properties of carbon nanocoils coated with highly controlled magnetic materials by atomic layer deposition. *ACS Nano*, 6(12):11009–11017, 2012. doi: 10.1021/nn304630h.
- [184] J. Rojas-Nunez, F. Valencia, R. I. Gonzalez, E. M. Bringa, S. Allende, J. L. Palma, A. Pereira, J. Escrig, and S. E. Baltazar. Mechanical performance of lightweight polycrystalline Ni nanotubes. *Computational Materials Science*, 168:81 – 86, 2019. doi: 10.1016/j.commatsci.2019.05.062.
- [185] A.L. Kozlovskiy, D. I. Shlimas, I. E. Kenzhina, and M. V. Zdorovets. The influence of thermal annealing on structural properties of Ni nanotubes. *Vacuum*, 153:254 – 261, 2018. doi: 10.1016/j.vacuum.2018.04.033.
- [186] M. P. Proenca, J. Sousa, C. T. Ventura, J. P. Araujo, J. Escrig, and M. Vazquez. Crossover between magnetic reversal modes in ordered ni and co nanotube arrays. *SPIN*, 2: 1250014, 2012. doi: <https://doi.org/10.1142/S2010324712500142>.
- [187] K. Lenz, R. Narkowicz, K. Wagner, C. F. Reiche, J. Körner, T. Schneider, A. Kákay, H. Schultheiss, U. Weissker, D. Wolf, D. Suter, B. Büchner, J. Fassbender, T. Mühl, and J. Lindner. Magnetization dynamics of an individual single-crystalline Fe-filled carbon nanotube. *Small*, 15(49):1904315, 2019. doi: 10.1002/sml.201904315.
- [188] A. Kozlovskiy, D. Shlimas, and M. Zdorovets. Investigation of the effect of ionizing radiation on the structural and conductive characteristics of Ni nanostructures. *Vacuum*, 163:103 – 109, 2019. ISSN 0042-207X. doi: 10.1016/j.vacuum.2019.02.015.
- [189] A. Kozlovskiy, S. Akhmetzhan, N. Ivanitskaya, I. Kenzhina, and M. Zdorovets. Study of the effect of irradiation with  $Ca^{5+}$  ions on the increase in ni nanotubes lifetime, applicable as the basis for lithium-ion batteries. *Materials Research Express*, 6(8):085074, 2019. doi: 10.1088/2053-1591/ab20ec.
- [190] A. Kozlovskiy, D. Shlimas, I. Kenzhina, and M. Zdorovets. Study of the use of ionizing radiation to improve the efficiency of performance of nickel nanostructures as anodes of lithium-ion batteries. *Materials Research Express*, 6(5):055026, 2019. doi: 10.1088/2053-1591/ab043b.

- [191] E. Uccelli, J. Arbiol, C. Magen, P. Krogstrup, E. Russo-Averchi, M. Heiss, G. Mugny, F. Morier-Genoud, J. Nygård, J. R. Morante, and A. Fontcuberta i Morral. Three-dimensional multiple-order twinning of self-catalyzed GaAs nanowires on Si substrates. *Nano Letters*, 11(9):3827–3832, 2011. doi: 10.1021/nl201902w.
- [192] S. Sioncke, A. Delabie, G. Brammertz, T. Conard, A. Franquet, M. Caymax, A. Urbanzyk, M. Heyns, M. Meuris, J. L. Van Hemmen, W. Keuning, and W. M. M. Kessels. Thermal and plasma enhanced atomic layer deposition of  $\text{Al}_2\text{O}_3$  on GaAs substrates. *Journal of The Electrochemical Society*, 156:H255–H262, 2009. doi: 10.1149/1.3076143.
- [193] J. L. Van Hemmen, S. B. S. Heil, J. H. Klootwijk, F. Roozeboom, C. J. Hodson, M. C. M. Van De Sanden, and W. M. M. Kessels. Plasma and thermal ALD of  $\text{Al}_2\text{O}_3$  in a commercial 200 mm ALD reactor. *Journal of The Electrochemical Society*, 154(7), 2007. doi: 10.1149/1.2737629.
- [194] F. A. Ospina-Acevedo, S. Perez Beltran, and P. B. Balbuena. Mechanisms of alumina growth via atomic layer deposition on nickel oxide and metallic nickel surfaces. *Physical Chemistry Chemical Physics*, 21(44):24543–24553, 2019. doi: 10.1039/c9cp05688b.
- [195] B. J. Wood and H. Wise. Kinetics of hydrogen atom recombination on surfaces. *Journal of Physical Chemistry*, 65:1976–1983, 1961. doi: 10.1021/j100828a015.
- [196] M. Kariniemi, J. Niinistö, M. Vehkamäki, M. and Kemell, M. Ritala, M. Leskelä, and M. Putkonen. Conformality of remote plasma-enhanced atomic layer deposition processes: An experimental study. *Journal of Vacuum Science & Technology A: Vacuum, Surfaces, and Films*, 30(1):01A115, 2012. doi: 10.1116/1.3659699.
- [197] R. K. Grubbs and S. M. George. Attenuation of hydrogen radicals traveling under flowing gas conditions through tubes of different materials. *Journal of Vacuum Science & Technology A: Vacuum, Surfaces, and Films*, 24(3):486–496, 2006. doi: 10.1116/1.2191862.
- [198] A. D. Tserepi and T. A. Miller. Two-photon absorption laser-induced fluorescence of H atoms: A probe for heterogeneous processes in hydrogen plasmas. *Journal of Applied Physics*, 75(11):7231–7236, 1994. doi: 10.1063/1.356680.
- [199] A. G. Gurevich and G. A. Melkov. *Magnetization Oscillations and Waves*. CRC Press, 1996.
- [200] C. Kittel. Theory of the Structure of Ferromagnetic Domains in Films and Small Particles. *Physical Review*, 70:11–12, 1946.
- [201] S. Wang, T. Gao, C. Wang, and J. He. Studies of anisotropic magnetoresistance and magnetic property of  $\text{Ni}_{81}\text{Fe}_{19}$  ultra-thin films with the lower base vacuum. *Journal of Alloys and Compounds*, 554:405 – 407, 2013. doi: 10.1016/j.jallcom.2012.12.004.
- [202] M. Ohtake, Y. Nonaka, and M. Futamoto. Metastable bcc-Ni and bcc-NiFe single-crystal films prepared on GaAs single-crystal substrates with different orientations. *IEEE Transactions on Magnetics*, 48(4):1589–1592, 2012. doi: 10.1109/TMAG.2011.2173316.

- [203] M. Ohtake, T. Tanaka, K. Matsubara, F. Kirino, and M. Futamoto. Epitaxial growth of permalloy thin films on MgO single-crystal substrates. *Journal of Physics: Conference Series*, 303:012015, 2011. doi: 10.1088/1742-6596/303/1/012015.
- [204] I. Tabakovic, J. Gong, S. Riemer, and M. Kautzky. Influence of surface roughness and current efficiency on composition gradients of thin NiFe films obtained by electrodeposition. *Journal of The Electrochemical Society*, 162(3):D102–D108, 2014. doi: 10.1149/2.0351503jes.
- [205] R. Balachandran, H.K. Yow, B.H. Ong, R. Manickam, V. Saaminathan, and K.B. Tan. Effects of ultrasonic field in pulse electrodeposition of NiFe film on Cu substrate. *Journal of Alloys and Compounds*, 481(1):336 – 339, 2009. doi: 10.1016/j.jallcom.2009.02.129.
- [206] J. de la Torre Medina, T. da Câmara Santa Clara Gomes, Y. G. Velázquez Galván, and L. Piraux. Large-scale 3-D interconnected Ni nanotube networks with controlled structural and magnetic properties. *Scientific Reports*, 8:14555, 2018. doi: 10.1038/s41598-018-32437-8.
- [207] A.M. Białostocka, U. Klekotka, and B. Kalska-Szostko. Modulation of iron–nickel layers composition by an external magnetic field. *Chemical Engineering Communications*, 206(6):804–814, 2018. doi: 10.1080/00986445.2018.1528239.
- [208] M. Cortes, J. Moulin, M. Couty, T. Peng, O. Garel, T. H. N. Dinh, Y. Zhu, M. Souadda, M. Woytasik, and E. Lefeuvre. Micromolding of NiFe and Ni thick films for 3D integration of MEMS. *ECS Transactions*, 58(40):41–53, 2014. doi: 10.1149/05840.0041ecst.
- [209] M. Pancaldi, N. Leo, and P. Vavassori. Selective and fast plasmon-assisted photo-heating of nanomagnets. *Nanoscale*, 11:7656–7666, 2019. doi: 10.1039/C9NR01628G.
- [210] V. S. Bhat, S. Watanabe, K. Baumgaertl, A. Kleibert, M. A. W. Schoen, C. A. F. Vaz, and D. Grundler. Magnon modes of microstates and microwave-induced avalanche in kagome artificial spin ice with topological defects. *Physical Review Letters*, 125:117208, 2020. doi: 10.1103/PhysRevLett.125.117208.
- [211] S. Sahoo, S. Mondal, G. Williams, A. May, S. Ladak, and A. Barman. Ultrafast magnetization dynamics in a nanoscale three-dimensional cobalt tetrapod structure. *Nanoscale*, 10(21):9981–9986, 2018. doi: 10.1039/C7NR07843A.
- [212] P. Fischer, D. Sanz-Hernández, R. Streubel, and A. Fernández-Pacheco. Launching a new dimension with 3D magnetic nanostructures. 8(1):10701, 2020. doi: 10.1063/1.5134474.
- [213] P. O. Oviroh, R. Akbarzadeh, D. Pan, R. A. M. Coetzee, and T. C. Jen. New development of atomic layer deposition: processes, methods and applications. *Science and Technology of Advanced Materials*, 20(1):465–496, 2019. doi: 10.1080/14686996.2019.1599694.
- [214] Y. T. Chong, E. M. Y. Yau, K. Nielsch, and J. Bachmann. Direct atomic layer deposition of ternary ferrites with various magnetic properties. *Chemistry of Materials*, 22(24):6506–6508, 2010. doi: 10.1021/cm102600m.

- 
- [215] M. C. Giordano, K. Baumgaertl, S. Escobar Steinvall, J. Gay, M. Vuichard, A. Fontcuberta i Morral, and D. Grundler. Plasma-enhanced atomic layer deposition of nickel nanotubes with low resistivity and coherent magnetization dynamics for 3D spintronics. *ACS Applied Materials & Interfaces*, 12(36):40443–40452, 2020. doi: 10.1021/acsami.0c06879.
- [216] I. Vernyhora, V. Tatarenko, and S. Bokoch. Thermodynamics of f.c.c.-Ni-Fe Alloys in a Static Applied Magnetic Field. *ISRN Thermodynamics*, 2012, 05 2012. doi: 10.5402/2012/917836.
- [217] B. Glaubitz, S. Buschhorn, F. Brüssing, R. Abrudan, and H. Zabel. Development of magnetic moments in  $\text{Fe}_{1-x}\text{Ni}_x$  alloys. *Journal of Physics: Condensed Matter*, 23(25):254210, 2011. doi: 10.1088/0953-8984/23/25/254210.
- [218] L. J. Gao, P. Ma, K. M. Novogradez, and P. R. Norton. Characterization of Permalloy thin films electrodeposited on Si(111) surfaces. *Journal of Applied Physics*, 81(11):7595–7599, 1997. doi: 10.1063/1.365305.
- [219] T. McGuire and R. Potter. Anisotropic magnetoresistance in ferromagnetic 3d alloys. *IEEE Transactions on Magnetism*, 11(4):1018–1038, 1975. doi: 10.1109/TMAG.1975.1058782.
- [220] K. Vogt, F. Fradin, and J. et al. Pearson. Realization of a spin-wave multiplexer. *Nature Communication*, 5(3727), 2014. doi: 10.1038/ncomms4727.
- [221] S. Sahoo, A. May, A. van Den Berg, A. K. Mondal, S. Ladak, and A. Barman. Observation of coherent spin waves in a three-dimensional artificial spin ice structure. *arXiv*, 2021. doi: arXiv:2102.10270.
- [222] M. C. Giordano, S. Escobar Steinvall, S. Watanabe, A. Fontcuberta i Morral, and D. Grundler.  $\text{Ni}_{80}\text{Fe}_{20}$  nanotubes with optimized spintronic functionalities prepared by atomic layer deposition. *arXiv*, 2021. doi: arXiv:2105.01969.
- [223] M. J. Donahue and M. J. Donahue. *OOMMF user's guide, version 1.0*. US Department of Commerce, National Institute of Standards and Technology, 1999.
- [224] P. Ramachandran and G. Varoquaux. Mayavi: 3D visualization of scientific data. *Computing in Science & Engineering*, 13(2):40–51, 2011.



## PERSONAL INFORMATION

Maria Carmen Giordano



📍 1020 Renens, VD - Switzerland

☎ +41 789455190

✉ [mcgiordano8@gmail.com](mailto:mcgiordano8@gmail.com)

🌐 <https://it.linkedin.com/pub/maria-carmen-giordano/45/a55/173>

📅 **Date of birth** 28.08.1987 | 📍 **Place of birth** San Giuseppe Vesuviano (Naples), Italy |

🇮🇹 **Nationality** Italian

## WORK EXPERIENCE

Oct.2016 – present **Doctoral Assistant**

Clean room fabrication and testing of micro-devices for the investigation of nanomagnetic elements operating in the GHz frequency regime. Research on atomic layer deposition (ALD) processes for the obtainment of magnetic low-roughness 3D conformal thin films with tailored microwave and electronic properties. ALD materials investigated: Ni, NiFe alloys, several oxides.

**École polytechnique fédérale de Lausanne (EPFL)** 1015 Lausanne- Switzerland

**Name of organization unit:** "Laboratory of Nanoscale Magnetic Materials and Magnonics - LMGN"

Feb.2015 - Jul.2016 **Scientific Assistant**

**Paul Sherrer Institut (PSI)** 5232 Villigen – Switzerland

**Name of organization unit:** " Bioenergy and Catalysis Laboratory (LBK) / Chemical Processes and Materials Group".

Dec.2013 –Dec.2014 **R&D Engineer**

**IMAST s.c.a.r.l. technological district**, 80133 Naples – Italy

(office based at **ST Microelectronics** 80022 Arzano, Naples – Italy)

**Name of organization unit in ST Microelectronics:** "Analog, Mems & Sensors - R&D department"

Jun.2013 – Dec.2013 **Process Engineer (Internship)**

**Procter & Gamble** 00040 Pomezia (RM) – Italy

**Name of organization unit:** "HDL making – Pomezia Plant"

Jan.2013 – Jun.2013 **Junior Consultant (Internship)**

**Confindustria** 00144 Rome (Italy)

**Name of organization unit:** "Federalimentare"

## EDUCATION AND TRAINING

Nov. 2014 **Qualification to the Profession of Industrial Engineer**

**University of Naples – Federico II**, 80125, Naples – Italy

Mar.2010 – Jul.2012 **Master's Degree in Materials Engineering, final grade: 110/110 cum laude**

**Polytechnic of Turin**, 10129, Turin – Italy

**Thesis:** "Synthesis and characterization of a silica-polysaccharide new hybrid material with catalytic and adsorbent properties, produced from renewable sources".

Organization: University of York, Green Chemistry Department, YO10 5DD York – U

Sep.2006 – Dec.2009 **Bachelor's Degree in Materials Science & Engineering, final grade: 110/110**

**University of Naples – Federico II**, 80125, Napoli – Italy

Erasmus Exchange Project at the Universitat Rovira i Virgili, 43007, Tarragona – Spain (Fall 2008/09).  
147

## SKILLS

Job-related skills	Solid background in materials science and engineering. Able to use and to interpret the output of the most common chemical, mechanical, functional characterization techniques for materials and devices. Good micro and nanofabrication skills. Used to work in clean room environments. Able to write research and technical reports. Basic knowledge of the patent draft process flow. Basic knowledge of lean manufacturing tools and good practice manufacturing (GPM).
Informatic skills	Good command of Microsoft Office tools and Latex. Good command of data analysis programs as Origin and Python. Previous use of Comsol for heat transfer simulations. Basic use of Matlab, Labview and of the common 3D CAD tools.
Language (level)	Italian (mother tongue), English (B2/C1), French (B1/B2), Spanish (B1).

## ADDITIONAL INFORMATION

Publications	<ul style="list-style-type: none"><li>• M.C. Giordano et al., <math>\text{Ni}_{80}\text{Fe}_{20}</math> Nanotubes with Optimized Spintronic Functionalities, arXiv 2021, arXiv:2105.01969.</li><li>• M.C. Giordano et al., Plasma-Enhanced Atomic Layer Deposition of Nickel Nanotubes with Low Resistivity and Coherent Magnetization Dynamics for 3D Spintronics, ACS Appl. Mater. Interfaces 2020, 12, 36, 40443–40452.</li><li>• M.C. Giordano et al., Confined spin waves in ferromagnetic nanotubes detected by Brillouin light-scattering spectroscopy, Annual Meeting of the Swiss Physical Society, 2018 (conference).</li><li>• G.P. Pepe et al., Flexible thermoelectric modules based on Bi-Te nanocomposites, Nanotech Italy, 2014 (conference)</li></ul>
--------------	--